Interface Engineering of Quantum Dot Heterostructures for Optoelectronic Applications and/or Magnetic Properties

A Thesis

Submitted for the Degree of

Doctor of Philosophy

In the Faculty of Science

by

Avijit Saha

New Chemistry Unit
Jawaharlal Nehru Centre for Advanced Scientific Research
(A Deemed University)
Bangalore – 560064

December 2016

Dedicated to my parents & family

DECLARATION

I hereby declare that the matter embodied in this thesis entitled "**Interface Engineering of Quantum Dot Heterostructures for Optoelectronic Applications and/or Magnetic Properties"** is the result of the research carried out by me at the New Chemistry Unit, Jawaharlal Nehru Centre for Advanced Scientific Research, Bangalore, India, under the supervision of Dr. Ranjani Viswanatha and it has not been submitted elsewhere for the award of any degree or diploma.

In keeping with the general practices of reporting scientific observation, due acknowledgements have been made whenever the work described is based on the findings of other investigators. Any omission which might have occurred by oversight or error in judgement is regretted.

Bangalore

……

Avijit Saha

CERTIFICATE

I hereby certify that the matter embodied in this thesis entitled **"Interface Engineering of Quantum Dot Heterostructures for Optoelectronic Applications and/or Magnetic Properties"** has been carried out by Mr. Avijit Saha at the New Chemistry Unit, Jawaharlal Nehru Centre for Advanced Scientific Research, Bangalore, India under my supervision and that has not been submitted elsewhere for the award of any degree or diploma.

Bangalore _____

Dr. Ranjani Viswanatha

(Research Supervisor)

ACKNOWLEDGEMENTS

First and foremost, I would like to express my sincere gratitude to my advisor Dr. Ranjani Viswanatha for enormous freedom, constant motivation and excellent guidance throughout my Ph.D. I am extremely fortunate to have her as my advisor, who gave me the freedom to explore on my own, and at the same time monitored my progress with patience and offered constructive criticism to recover when my steps faltered. I am thankful to her for giving me an opportunity to work under her guidance.

I would like to thank Prof. C. N. R. Rao for being a constant source of inspiration throughout my PhD life. Contagious enthusiasm and vision of Prof. Rao for science has motivated me at various times. I also convey my heartfelt gratitude to him for excellent experimental resources he has provided for our department.

I would like to thank Council of Scientific and Industrial Research, CSIR-India for my scholarship. I thank Department of Science and Technology (DST), International Centre for Materials Science (ICMS), SSL (Sheikh Saqr Laboratory), Synchrotron and neutron facility project, DST, JNCASR for Funding in different scientific aspects.

I would also like to thank Prof. K. S. Narayan (JNCASR), Dr. Ranjan Datta (JNCASR), Dr. Kishore V. Chellappan (JNCASR), Dr. Jay Ghatak (JNCASR), Dr. Soma Chattopadhyay (Argonne National Lab), Dr. Tomohiro Shibata (Argonne National Lab) and Dr. Syed Khalid (BNL NSLS-II/SSRL, USA) for fruitful scientific collaborations and insightful discussions. I have been greatly benefited from their expertise, and learned a lot in the process.

I would like to thank all my Ph.D. course instructors, Prof. Shobhana Narasimhan, Prof. Umesh Waghmare, Dr. Ranjani Viswanatha, Dr. Ranjan Datta, Prof. A. Sundaresan, Dr. Sebastian Peter, Prof. Subi J. George, Dr. Kaniska Biswas, Prof. T. Govindaraju, Dr. Ujjal K. Gautam and Prof. T. K. Maji for their instructive and enjoyable courses, and stimulating scientific interactions.

I owe my sincere thanks to my present and past lab mates Murthy, Renu, Suguna, Kushagra, Mahima, Pradeep, Amitha, Pallabi, Mahesh and Anur for their wonderful

company and scientific discussions. I also thank all the visiting students, Siddhartha, Bibhuti, Felix, Pratyusha, Sumitha and Subhadra who worked with me.

I would like to thank Dr. Rana, Somnath, and Chandan for magnetic measurement.

I thank all the technical staff of JNCASR, especially Mr. Anil, Mr. Vasu, Dr. Jay, Kannan, Mr. Karthik, Mr. Siva Kumar, Mrs. Usha, Mr. Peer, Mr. Mune Gowda and Mr. Dileep.

I extend my sincere thanks to the entire Academic and Administrative staff of JNCASR for their efficiency and helpfulness. Special thanks are due to the members of computer laboratory and library.

I would also like to thank the Hostel staff, Mess workers and Canteen stuffs and Raju for keeping me well fed. I would also like to thank Garden Staff, Security staff, Electrical Staff and my Gym instructor for give me such a nice environment in my daily life here.

I thank all my friends in JNC and IISc: Satya, Moumita, Sunita, Tarak, Nivedita, Somnath, Syamantak, Dheeraj, Arpan, Subhajit, Jiya, Saikat, Atanu, Lokesh, Nabaduti, Riteshda, Arpanda, Ranada, Jiada, Suresh, Venki, Divakar and many others. My special thank to Atanu, Moumita, Somnath, Ranada and Sohamda for helping me in understanding various scientific problems.

Last, but not the least, my parents for their unending support and encouragement during my up and downs. They have always believed in me, and never tied me down in any of my endeavors. I would like to thank Hemlata for her constant support in my academic and non-academic affairs.

Finally, I express my sincere gratitude to all those who helped me directly or indirectly.

Avijit Saha

Preface

Interface between two materials plays a very significant role in determining the materials property. In case of quantum dots (QDs) heterostructures it becomes even more critical due to quantum confinement and high surface volume ratio. In this thesis we have modeled the interface of heterostructured QDs from core shell to graded alloy to uniformly doped system and studied their optical, electronic and magnetic properties.

Chapter 1 gives a literature overview of interface engineering from bulk heterostructures to QD heterostructures. Further the localization of the optical charge carriers and magnetic domain walls are discussed in presence of various interfaces ranging from sharp interface to graded to completely diffuse interface specifically in the case of quantum dot heterostructures. Towards the end of chapter, the challenges and difficulties involved in the synthesis of QD heterostructures, specifically with the required interface has been discussed.

Chapter 2 describes the general synthesis methodologies used in this thesis to obtain heterostructure QDs, different characterization techniques used to characterise these QDs and other relevant experimental details.

Part 1. Heterostructure quantum dots for optical applications: Introduction of core shell QDs and engineering their interface can make them more efficient for various optical applications.Here, we have shown, that the control of interfacial defects in core-shell QDscan be used to enhance the photo physical properties, device performance and provide efficient applications for contrasting properties from same materials. These studies are discussed in next two chapters.

Chapter 3 introduces the interface modification in type-I heterostructure to develop high quantum yield QDs. Controlling the interfacial defects in CdSe/CdS, near unity quantum yield has been achieved. We showed that quantum yield of these QDs increase with the decrease of defects in the microstructure. Apart from that, these high QY(94%) QDs when used as an active layer, even in an un-optimized LED, shows luminescence above 7000 Cd/m^2 with a power conversion efficiency 1.5 lm/ W.

Chapter 4 demonstrates that interface alloying in type-II heterostructure can transform a well known photovoltaic material into a good photo emitting materials. Controlling the surface passivation in the core nanocrystals and tuning the synthesis parameter we demonstrate that CdTe/CdS core shell and graded alloy QDs shows completely contrasting properties. We study the local environment to confirm the internal structure and showed that X-ray absorption fine structure (XAFS) spectroscopy can be a very useful tool to study the internal structure in heterostructured QDs and their application.

Part II. Modifying the internal structure for magnetic properties: Hybrid ferromagnetic/semiconductor or ferromagnetic/antiferromagnetic materials are the potential candidates for emerging spin based electronic devises due to the opportunities to manipulate charge and electron spin in these systems. Controlled diffusion of a magnetic core in a semiconductor matrix can exhibit multifunctionality like room temperature ferromagnetism, exchange anisotropy, photoluminescence etc. Next three chapters discusses about the correspondence between internal structure and their multifunctional properties of these materials.

Chapter 5 deals with the diffusion of magnetic core in semiconductor heterostructure. It is divided into four sections.

Section-A demonstrates the extreme case of interface modeling i.e. the complete diffusion of a magnetic core (Fe_3O_4) inside CdS matrix to obtain highly crystalline, single domain Fe-doped CdS, where Fe is uniformly distributed inside CdS matrix. We show that, this technique rules out the well known problem of clustering of magnetic ions in dilute magnetic semiconductor (DMS) and opens up a new possibility to understand the origin of magnetism in DMS QDs. In addition, the versatility of this technique can be utilized in synthesizing uniformly doped nanocrystals with ultra-large size variation (~5-60 nm) by the modification of core size and reaction conditions using wet chemical method.

Section B deals with the variation local structure of Fe during the evolution from core shell to doped QDs during overcoating of Fe_3O_4 core with CdS. Studies reveal the presence of Fe_3O_4/CdS core-shell structure, followed by an alloying at the interface eventually forming to homogeneously Fe-doped CdS QDs with excellent control over size and size distribution.

Section C probes the variation of magnetic property of the core-shell Fe_3O_4/CdS QDs specifically at the interface during thin shell growth. We identify an unusual exchange bias phenomenon manifested at the interface of a magnetic/nonmagnetic heterostructure for thin CdS shells. Local structure study using XAFS reveals the formation of an antiferromagnetic exchange pinning layer at the interface, identified here as FeS which arises at the initial stage of CdS overcoating due to interface alloying. We showed that interface alteration for an optimized core size can give rise to significant exchange bias from a magnetic/nonmagnetic heterostructure.

Section D describes the effect of particle size and magnetic ion concentration on their magnetic property in magnetic semiconductor QDs. Here, we demonstrate magnetization/ion and blocking temperature in Fe-doped CdS nanocrystal (Fe-5%) increases with the increasing particles size due to increase of domain size and decrease of canted spin on the surface. While magnetization/ion and blocking temperature remains almost constant with the increasing dopant (12 nm size) concentration upto a concentration of 10%, identified as dilute doping regime, above which magnetization as well as blocking temperature changes due to clustering of magnetic ions inside the semiconducting matrix.

Chapter 6 deals with the synthesis of multifunctional doped QDs and the role of thermodynamics in diffusion doping. It contains two different sections.

In **Section A**we demonstrate that bond dissociation energy of the core and the diffusivity of the magnetic ions inside the semiconducting matrix are the two important factors in diffusion doping to achieve a very small size doped nanocrystals. By modulating these two factors we have shown the formation of small size (6-10 nm) uniformly doped (Fe/Ni/Co/Mn doped CdS) nanocrystals with controlled dopant concentration (<5%) and having superior optical and magnetic properties compared to earlier literature report.

Section B demonstrates the synthesis of transition metal co-doped nanocrystals and its effect on magnetic property in competition with doped nanocrystals. We have synthesized Mn, Ni co-doped CdS by following diffusion doping and a comparison of magnetic property with Mn doped CdS and Ni-doped CdS having similar percentage of doping showed an enhancement in the magnetization due to co-doping effect.

Chapter 7 demonstrates a strong exchange bias effect, which is commonly manifested by the hysteresis loop shift observed in a ferromagnetic/antiferromagnetic heterojunction. This

effect is a cornerstone of the design and development of spin valve, magnetic storage devices. Here, we show that a sharp core shell interface between an antiferromagnetic CoO and a ferrimagnetic $CoFe_2O_4$ gives rise to a strong exchange shift of about 5.5kOe, similar with the highest observed values in literature for quantum dots.

Abbreviations

AFM-Antiferromagnetic

DMS-Dilute Magnetic Semiconductor

DMSQDS-Dilute magnetic semiconductor quantum dots

FM- Ferromagnetic

FiM- Ferrimagnetic

LED- Light Emitting Diode

NQDs- Nanocrystal Quantum Dots

ODE- Octadecene

ODA- Octadecylamine

OlAm- Oleylamine

QY- Quantum Yield

SILAR- Successive ionic layer adsorption and reaction

TOP- Trioctylphosphine

TOPO- Trioctylphosphine oxide

TGA- Thermo gravimetric Analysis

Contents

5. Core-shell to Doped Quantum Dots

Chapter 1

A Brief Introduction to Quantum Heterostructures and Interfaces

1.1 Interface

An interface is a common boundary or layer that separates two condensed phases, exists usually in molecular dimension, composed of chemical compounds from the two surrounding phases. It has a great effect in determining materials physical and chemical properties, such as carrier dynamics,[1,2] electrics,[1] magnetism[3,4] etc. Various physical properties of materials in technological applications are determined by interfaces.[5-7] All these properties can be tuned by engineering the interface of heterostructure materials. A comprehensive understanding and optimization of the microstructure of the interface and precise control over it provides opportunities to develop technical advances in device architectures. With the advances of experimental and theoretical sciences, interface study and engineering have turned out to be one of the most interesting branch of material research.[6,8] The ability of designing engineered interfaces and obtaining desired properties in heterostructure materials have become an indispensable goal in material science. The structure, interaction between two different phases i.e. adhesion, interaction between same phases i.e. cohesion, thermodynamics, charge and spin dynamics of solid interfaces are the areas of recent research with far reaching applications. For example, spin injection across ferromagnetic/semiconductor junction in the field of spintronics,[9-11] charge dynamics between two semiconductors phases in semiconductor physics or the current dynamics in most of the Josephson junction used in sensor or other electronics devices rely on the interface.[12,13] Therefore a complete study and a comprehensive understanding would be necessary to achieve new heterostructure with desirable properties. Interface can be classified as liquid/vapor, solid/vapor, solid/liquid, liquid/liquid and solid/solid interfaces depending of the physical state of maters. In this thesis, we will be discussing only about solid-solid interface in detail.

Properties: Formation of the interface in heterojunction materials gives rise to interesting phenomena by effecting materials property depending on the nature of the materials. These effects are known to alter the effective behavior dramatically. When two crystalline solids form an interface, the following phenomena occur:-

(i) Strain at the interface due to different lattice constant.
(ii) Formation of new compound if the two solids react.
(iii) Inter-diffusion between two phases at high temperature.

The above mentioned phenomena affect various materials properties like thermodynamics, crystal structure, electronic structure and charge dynamics, conductivity, magnetoresistance etc.

Thermodynamics: Formation of interface in general changes the Gibbs free energy. Free energy at the interface becomes $\Delta G = \Delta W = 2\sigma A$ (1.1)

That is, energy required to change the interface is a free energy G, meaning work done W, which is proportional to σ interfacial tension and area of interfacial contact.

Crystal Structure: When two crystalline solids with different lattice constants form an interface, the lattice mismatch between the two surface leads to high strain at the interface. Depending on the lattice planes and lattice constant interfaces can be classified as (i) coherent interface, where the planes are continuous, (ii) incoherent interface, wherein there is no continuity between the planes and (iii) semi-coherent interface when it is neither fully coherent nor completely incoherent. The interfacial strain energy can lead to crystal defects such dislocations, stacking faults, which retains throughout the crystal lattice and alter the materials physical property. For example, the creation of dislocations in semiconductor heterostructure results in the formation of defect states, which act as a non-radiative recombination pathway for exciton carriers. Evelyn et al.[14] showed a spontaneous formation of a misfit dislocation arrays (as shown in figure 1.1) resulting a periodically varying strain field due to lattice mismatch at the interface in II-VI semiconductors (PbTe/ PbSe) give rise to an unusual pseudo magnetic field in the structure.

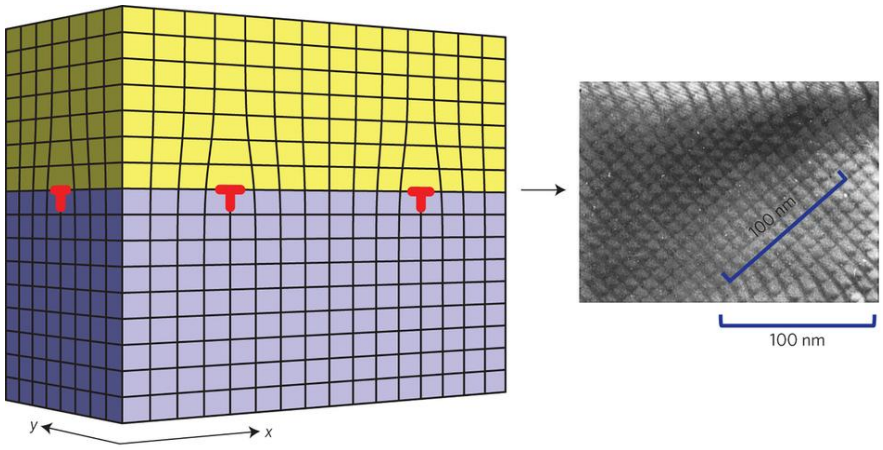

Figure 1.1: Formation of crystal strain and dislocation due to lattice mismatch. (Reprint by permission from ref[14] Nature Publishing Group, License No. 4000100347857)

Electronic Structure and Charge Dynamics: Formation of heterojunction between semiconductor / semiconductor or semiconductor / metal hybrid structure can alter the electronic states and charge dynamics at the interface.

Semiconductor / Semiconductor interface. When a p-type semiconductor is sandwiched with an n-type semiconductor, it creates a large charge density gradient resulting diffusion of charge carrier until the Fermi level of both the p and n-type semiconductor comes to equilibrium. This influences the band offsets and Fermi level position, as shown in Figure 1.2 (a), wherein the electron diffuses from p-side to n-side while hole diffuses from n-side to p-side.

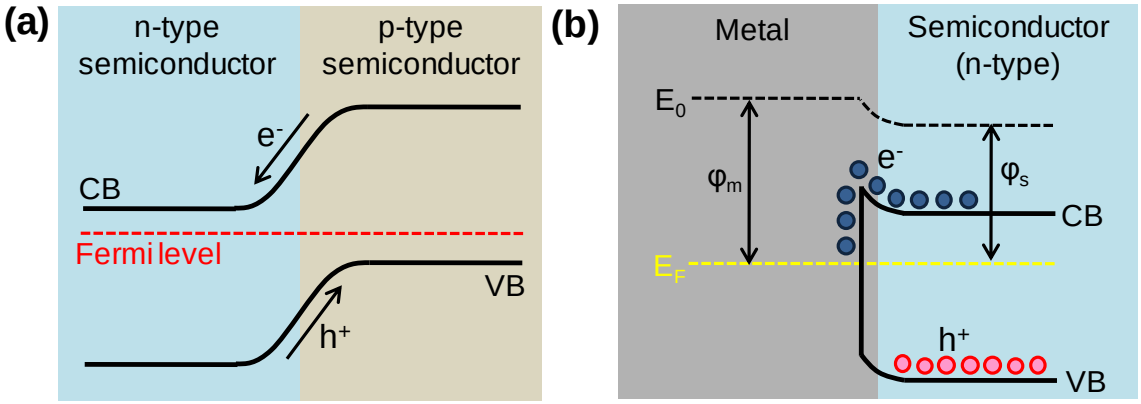

Figure 1.2 Schematic energy band diagrams of (a) semiconductor /semiconductor and (b) metal /semiconductor heterostructure and charge carrier dynamics at their interfaces. E_0 is the vacuum energy level, φ_m metal work function and φ_s semiconductor work function.

Metal / Semiconductor. Band bending effect can also be observed when a metal and an n-type semiconductor from a junction. Figure 1.2 (b) shows the band energy diagram of a metal semiconductor junction (Schottky junction), in which free electrons will traverse between metal and semiconductor due to the difference in work function. When metal work function (φ_m) is higher than the semiconductor (φ_s) as shown in Figure 1.2 (b), the electrons will flow from semiconductor to metal and when metal work function is lower than the semiconductor the electron will flow from semiconductor to metal. This charge flow continues until the Fermi level of both metal and semiconductor comes to an equilibrium. This charge imbalance gives rise to band bending at the interface. The energy bands move upward when $\varphi_m > \varphi_s$, while bend downward when $\varphi_s > \varphi_m$.[7]

Conductivity and Magnetoresistance: Formations of an interface, sometimes, can result in high conductivity or magnetoresistance even in non-magnetic insulating materials. Electronic

reconstruction at the interface of $SrTiO_3$ and $LaAlO_3$, which are well-known to be non-magnetic, insulating perovskite oxides, gives rise to high conductance and large negative magnetoresistance.[2,15] It was shown that formation of atomic interface presents an extra half electron or hole per unit shell, which takes part in conductivity and results high carrier mobility at the interface.

Hence, it is very important to study the interface effect, especially when the particle size approaches the quantum limit where the effects are enhanced and new properties arise. Here, in this thesis we have studied various hybrid quantum heterostructures and their interfaces. By engineering these interfaces we have shown their optical, electronic and magnetic properties can be tuned depending on the type of materials. Now a days, there is a great interest among the scientists to explore the materials properties with smaller and smaller dimension. This interest is due to the facts that as materials size approaches the quantum limit, new properties arises and materials gain potentials in wide range of efficient applications. The most effective example is Moore's law in integrated circuit, where it was predicted that the number of transistors doubles every two years. Another example is tunability of optical properties in various applications like optoelectronics,[16,17] photovoltaic[18-21] and bioimaging.[22-25] Moreover increase in surface area becomes beneficial for catalytic applications.[26,27]

The effects that are predominant with decrease in particle dimension from bulk to quantum dots are

(i) A large increase in surface to volume ratio giving rise to variation of surface phenomena.
(ii) In the case of semiconductor material when particles size is below excitonic Bohr radius, particles become confined in all three special directions due to quantum-confined effect.
(iii) For ferromagnetic materials, multidomain structure in bulk material becomes single domain below a critical size in nano regime and show superparamagnetism.[28,29]
(iv) For heterostructure QDs, the interface curvature increases; giving rise to enhanced interface effect and dislocations at the interface creates defects states.

However, one of the properties that has not been extensively studied in these materials is the effect if interfaces on their materials properties. Interfaces have been shown to induce

interesting properties in bulk materials. Specifically, we have focused on optically and magnetically active nanostructures and engineered their interfaces for novel properties.

1.2 Interface Engineering in Optically Active Semiconductor QD Heterostructures

QDs are zero dimensional semiconducting nanoparticles having size lesser than the excitonic Bohr radius (2-10 nm). It was first discovered by Alexi Ekimov[30,31] in semiconductor doped glasses and Louis Brus in solution.[32] Due to extremely small size, the excitons inside the QDs are confined in all the three spatial direction resulting size tunable photoluminescence spectra with narrow bandwidth. This quantum confined effect made QDs unique from bulk semiconductors and discreet molecules. The high luminescence, large absorption coefficient and size dependent optical property in QDs offers unprecedented opportunities in application from light emitting devices, photovoltaics and bioimaging.

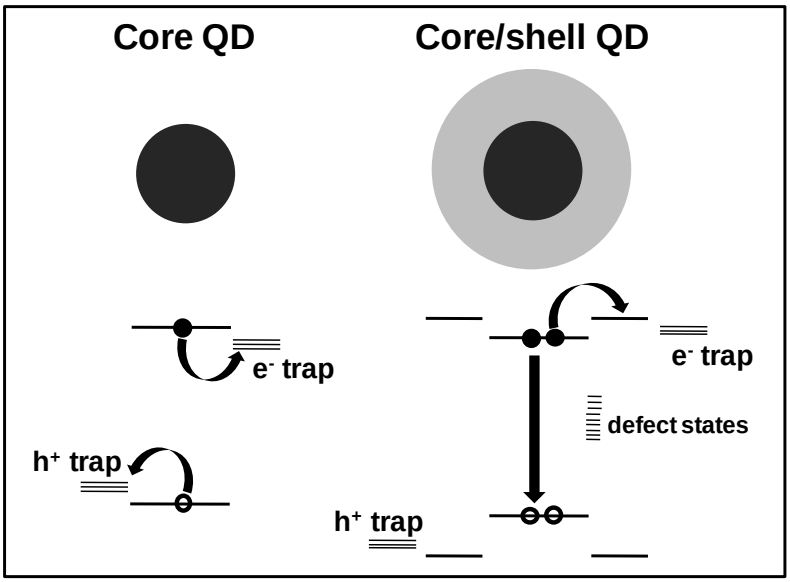

Figure 1.3 Variation of electronic structure and trap states from core to core-shell QDs.

However, due to very low dimension QDs properties suffer from major effects on these properties, as the surface to volume ratio is extremely high. Increase in surface area gives rise to a higher fraction of unsaturated dangling bonds which results in surface related defect or trap states between the valance and conduction band, providing a faster non-radiative de-excitation pathways for photogenerated charge carriers, thereby reduce the PL efficiency as shown in Figure 1.3. Trapping of electron or hole by the surface trap states under a constant

illuminescence results in charged QDs consequently giving rise to fluorescence intermittency or the so called blinking[33-37] in QDs. This effect further reduces the quantum efficiency. To avoid these detrimental effects a generic strategy is the overgrowth of a larger band gap semiconductor on the core QDs. For example CdSe, CdTe, ZnSe QDs overcoated with ZnS shell on top.[38-40] Use of larger band gap materials pushes the electron or hole trap states, associated with the surface, energetically far from the band gap of the core making them inaccessible for the photogenerated excitons pairs inside the core as demonstrated in Figure 1.3. This way, though it has been possible to improve the quantum efficiency, the lattice mismatch between the core and the shell materials introduce strain across the interface giving rise to defect states which again provides a non-radiative decay channel competing with the excitonic recombination. Another detrimental phenomenon, which reduces the quantum efficiency in these nanocrystals, is Auger recombination.[41,42] When these nanocrystals are illuminated with intense light source, it creates multi-excitons and the recombination energy of one exciton pair is used to promote the other electron or hole to reach to the continuum leaving out from the QDs instead of radiative emission. This way the QDs becomes charged and looses it emission efficiency. It has been observe from previous literature that at the barrier between the two semiconductors, their crystal structures and band edge discontinuities at the interface play a crucial role in determining their optical properties. Thus it has been observed theoretically that the only way to improve this problem is tuning their heterojunction by manipulating the interface and internal structure with atomic precision during shell growth. It has been studied extensively and found that slow compositional grading from core to shell at the interface is an effective way to control these two difficulties.[43] Firstly, this method eliminates the abruptness in the crystal lattice at the interface and thereby reduces the defect at the interface. Secondly, the effect of graded alloy structure reduces the discontinuities of band edge and effectively stops the Auger recombination as demonstrated in Figure 1.4. The figure shows a comparison between a sharp core-shell and a graded alloy structure and their effect on corresponding barrier potential. In case of sharp core shell structure, the variation of the potential at the interface is very abrupt and when an electron reflects back from the interface it suffers from a large change in momentum $\Delta k = k-(-k) = 2k$ as depicted in figure. However in case of smooth interface, the potential changes very smoothly and thus change in momentum at the interface is much lesser ($\Delta k \sim 0$). Now, when there is trion formation in sharp core-shell heterostructure

QDs due to the recombination of e-h pair as depicted in Figure 1.4 (a-b), large change in k value and the recombination energy during one exciton pair recombination allows the extra electron to go out to the continuum and giving rise to the Auger process. On the other hand, in case of graded alloy heterostructure as the change in k value is very small, momentum conservation principle does not allow the extra electron to go out of the QDs (Figure 1.4 b). So, less change in k value due to smooth interfacial potential suppresses the Auger recombination and consequently stops blinking in graded alloy QDs. Therefore, overcoating a core QDs with a larger bandgap semiconductor shell and engineering its interface can results blinking free highly luminescence QDs which can be very useful materials for light emitting applications like LED, LASER etc.

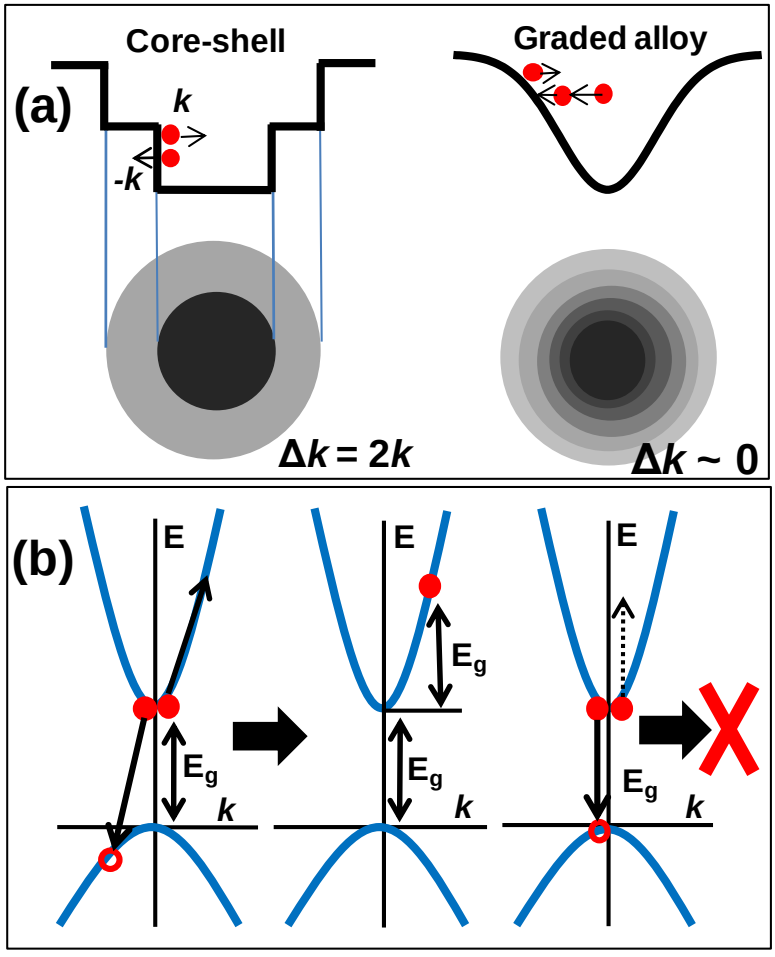

Figure 1.4: (a) Schematic of sharp and smooth interface potential in core-shell heterostructures. (b) Schematic of band diagram for large and very less change in k value.

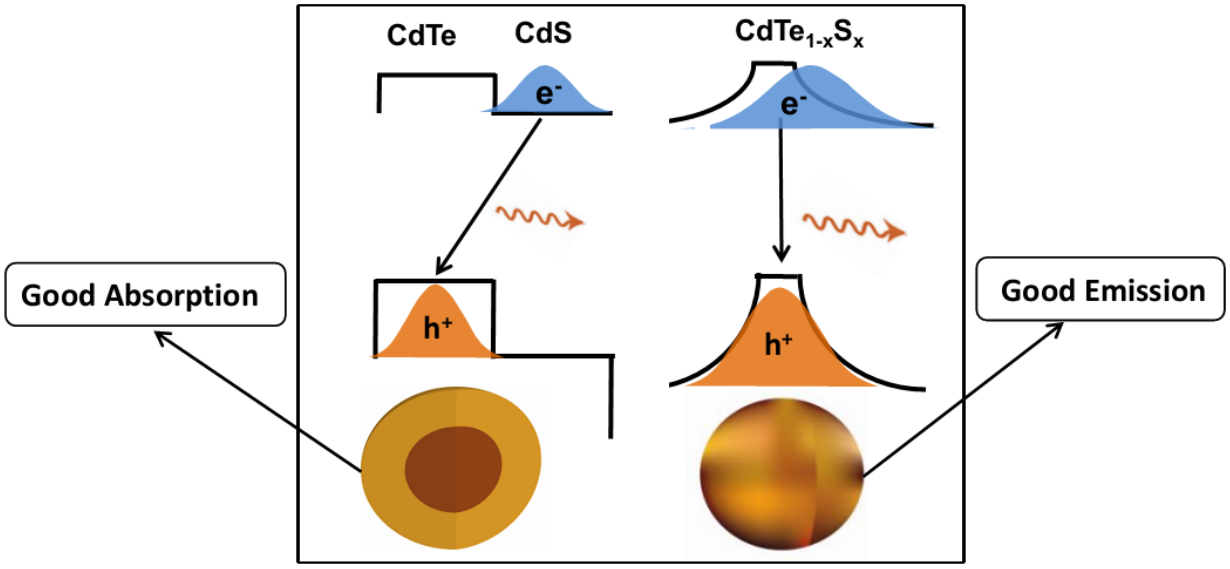

Figure 1.5 Schematic of band alignment for (a) core-shell and (b) and graded alloyed CdTe/CdS QDs.

However, overcoating the core QDs using another semiconductor such that their band edges are interspersed, as shown in Figure 1.5 can provide opportunities to spatially separate electron hole pair from each other and thereby can be used as a very good photovoltaic material. For example, CdTe QDs overcoated with CdS or CdSe forms this kind of band alignment, in which the hole remains localized inside core CdTe while the electron gets delocalized in shell. This type of band alignment provides extended exciton lifetime with low emission efficiency, however provides large absorption crosssection both from core and shell materials and enhances the carrier extraction probability for photovoltaic application. Understanding the electronic structure and interface engineering in this type of QDs heterostructure can lead to an excellent luminescent material for solid state light emitting application. Figure 1.5 shows the interface modification of CdTe/CdS graded alloy heterostructure resulting a more direct and easy recombination leading to high quantum efficiency. So, interface engineering can tune the properties of nano-heterostructures, which results a competing and contrasting properties from same materials, depending on the nature of the two QDs which is classified into different types based on their relative band alignment.

1.2.1 Classification of core-shell QDs

Depending on the band gap and relative band alignments of the semiconductors, core-shell heterostructured QDs can be classified into majorly three different categories namely type- I,

reverse type-I and type-II heterostructure. However, interfacial modeling of heterostructure can give rise to various other heterostructures like quasi type-II, core/shell/shell heterostructure etc.

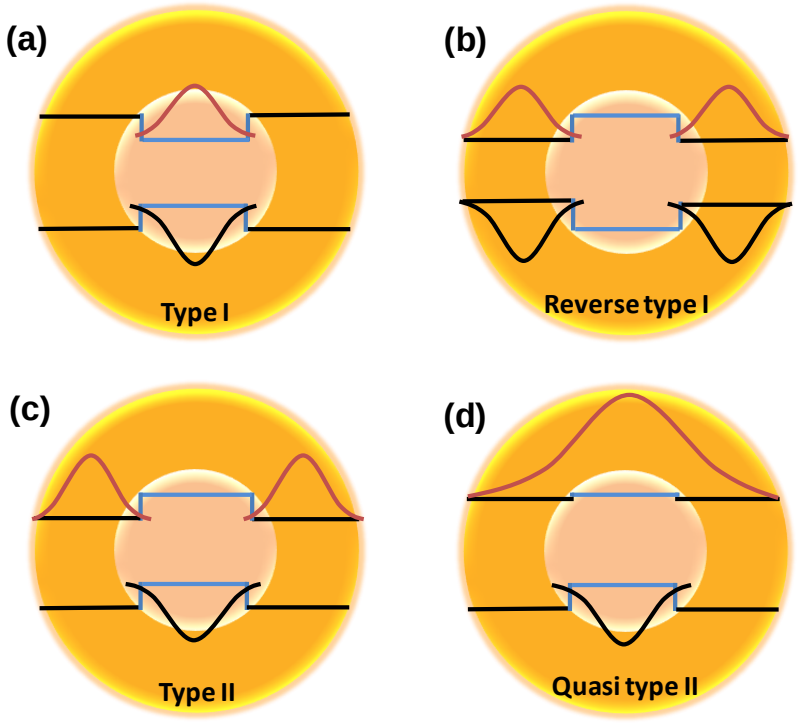

Figure 1.6: Schematic of various core-shell heterostructure and their band alignment for (a) type-I, (b) reverse type-I, (c) type-II and (d) quasi type-II.

Type-I Core-shell QDs: In this type of heterostructure, the band gap of the shell material is larger than the core band gap and both the band edges of core materials fall in between the band edges of the shell (described earlier) as demonstrated in the figure 1.6 (a). This typical arrangement of the band edges results in both the electron and hole wavefunctions of exciton pairs to be localized inside the core, while the shell acts a potential barrier. The shell material reduces the dangling bonds and energetically separates the surface traps from the optically active core and physically separates from its surrounding medium like oxygen or water molecule. As a consequence, type –I semiconductor heterostructure demonstrates enhanced luminescence as the exciton pair is spatially confined inside the core and recombines radiatively, giving rise to enhanced luminescence. CdSe/ZnS,[39] ZnSe/ZnS[38] core-shell QDs are the examples of type –I semiconductor heterostructure.

Reverse Type-I Core-shell QDs: In this type of heterostructure, the band gap of the shell material is smaller than the core band gap and both the band edges of the shell materials falls in

between the core band edges as shown in Figure 1.6 (b). This kind of band alignment results the electron and hole wavefunctions localized inside the shell, leading to tunability of the excitonic recombination energy. CdS/CdSe, ZnS/ZnSe core-shell structures are the example of reverse type-I semiconductor heterostructure.

Type-II Core-shell QDs: In this type, either the valence-band edge or the conduction band edge of the shell material is located within the band edges of the core as demonstrated in the Figure 1.6 (c). This staggered band alignment gives rise to spatial separation of electron and hole wavefunction in different region of core shell structure and the transition happens at lower energies than both the band gap of the semiconductors involved. Moreover, due to spatial separation in thicker shell QDs, the recombination probability decreases with an increase in lifetime increased. CdTe/CdSe, CdTe/CdS core-shell structures are the example of type-II semiconductor heterostructure.

Quasi Type-II QDs: This type of heterostructures allows either electron or hole to be delocalized throughout the nanocrystal, whereas the other to be localized inside the core due to one band edges of both the semiconductors fall on similar energy level (Figure 1.6 (d). CdSe/CdS with small CdSe seed as core forms quasi type–II heterostructure where the lowest energy hole wavefunction is localized in the core CdSe while the electron wavefunction is delocalized throughout the nanocrystals.

Core/Shell/Shell QDs: In this type heterostructure, core QD is overcoated with two different shell materials for example CdSe/ZnSe/ZnS[44] or CdSe/CdS/ZnS.[44,45] The large band gap outer shell stops the penetration of exciton carrier towards the surface while the intermediate shell reduces the lattice mismatch. An interesting example of core/shell/shell heterostructure is the so called quantum dot-quantum well structure,[46-48] in which a large band gap core is encapsulated with two shell material, the outer one with large band gap and the inner one with small band gap materials. This heterostructure provides high quantum yield under UV radiation.

Interface engineering of all these heterostructure QDs shows very high luminescence which are being used as solid state light emitting devices and bioimaging[49] or good charge separation which are being used in photovoltaics.[50]

1.3 Interface Engineering in Magnetic-Non-magnetic Semiconductor Nano-heterostructures

Introduction of magnetic materials with the semiconductors in integrated electronic devices has attracted a great attention of the scientific community and gave birth to a new exciting field, namely spintronics. The next generation electronics device combines the advantage of both magnetic spins and charge and paves the way towards non-volatile, fast and high capacity storage devices with very less energy consumption. The study of spin injection and electron transport property has been extensively carried out in ferromagnetic metal/semiconductor hybrid system.[51,52] This kind of heterostructure was first demonstrated in Fe/GaAs thin films[53-55] and thereafter many such systems like Fe/InAs,[56-58] Fe/MgO,[3,52] Fe/ZnO[59] thin films have been studied which showed high spin injection, mobility and magnetoresistance effect. Specific study by tuning their interface in these systems showed that the interface modeling can modulate their magnetic and semiconductor properties and provide valuable information for future electronic devices. Recently core-shell ferromagnetic/semiconductor heterostructure QDs have shown potential[43] in this research field due to quantum confinement effect on electronic states. In such systems, compared to bulk heterostructure the magnetic exchange interaction should be perturbed by the spatial confinement, which may affect the electronic structure and can give rise to the exchange of charge carriers between ferromagnetic and semiconducting phases by injecting spins from ferromagnetic to semiconducting phase. Also, the high surface to volume ratio enhances various interface-induced phenomena like magnetoresistance, exchange bias, electron transport. For example, Talapin's group has reported high mobility in charge transport and novel magnetic properties from FePt/PbX[60] (X=S or Se) and FePt/CdX[61] (X= S or Se) magnet/semiconductor core-shell nano-heterostructures with inorganic surface ligands. By controlling the spin, they have also demonstrated a large magnetoresistance from these heterostructure. Engineering the internal structure and interface in such system can give more insights into these studies.

1.4 Interface of hybrid magnetic/magnetic QD heterostructure

Similar to magnetic/semiconductor heterostructure, magnetic/magnetic hybrid heterostructure also receive much attention due to their fundamental scientific and technological importance. Formation of heterostructure with two different type of magnetism gives rise to new magnetic

phenomena due to exchange interaction at the interface. For example, presence of paramagnetic layer between two ferromagnetic layer show oscillatory exchange interaction as a function of paramagnetic layer thickness. However, the most attractive phenomena due to the proximity effect in magnetic heterostructure are the exchange coupling at the interface of a ferromagnetic and antiferromagnetic layer or the so called exchange bias effect.

1.4.1. Exchange Bias

The exchange coupling between a ferromagnetic (FM)/antiferromagnetic (AFM) interface gives rise to an unidirectional anisotropy in ferromagnetic layer below the Neel temperature (T_N) of the AFM material, causing coercivity increase of hysteresis loop, and a shift of the loop along the magnetic field axis, known as exchange bias effect. This effect was first observed by Meiklejohn and Bean[62,63] in the year of 1956, when studying Co nanoparticles embedded with CoO antiferromagnetic layer. The high anisotropy of the CoO AFM shell was considered to be the cause of increasing anisotropy of FM layer and the loop shift and it was recognized as a complete interfacial exchange phenomenon.

Phenomenology: The macroscopic origin of hysteresis loop shift is due to the pinning of domain wall on the surface of the ferromagnetic layer. A typical hysteresis loop shift along with different spin orientation at different stages of FM/AFM coupling has been depicted in the Figure 1.7. The measurement temperature should be below the Neel temperature of the antiferromagnetic layer. Above T_N, AFM spins remain randomly oriented and there is no proximity effect by the AFM layer. After field cooling below T_N, the pins of both orient parallel to each other at the interface (Figure 1.7). With the increase of reverse magnetic field the FM spins starts orient themselves with the field. However due to high anisotropy of AFM layer, the AFM spins remain unchanged. The AFM spins at the interface interact with the FM spins and do not allow their rotation with the reverse field. Thus the magnetic field required to change the orientation of FM spins is much higher than uncoupled FM materials. Conversely, when the magnetic field applied back to the forward direction, the spin rotation occurs very easily as the AFM spins are then in favor of magnetization reversal. So, the field needed is much less comparing to the uncoupled FM materials. As a result, the coercivity along the negative magnetic field axis is more, while it is less along the positive axis resulting an overall displacement of hysteresis loop along the negative field axis. This shift of the hysteresis loop from the origin is called the exchange bias field (H_E).

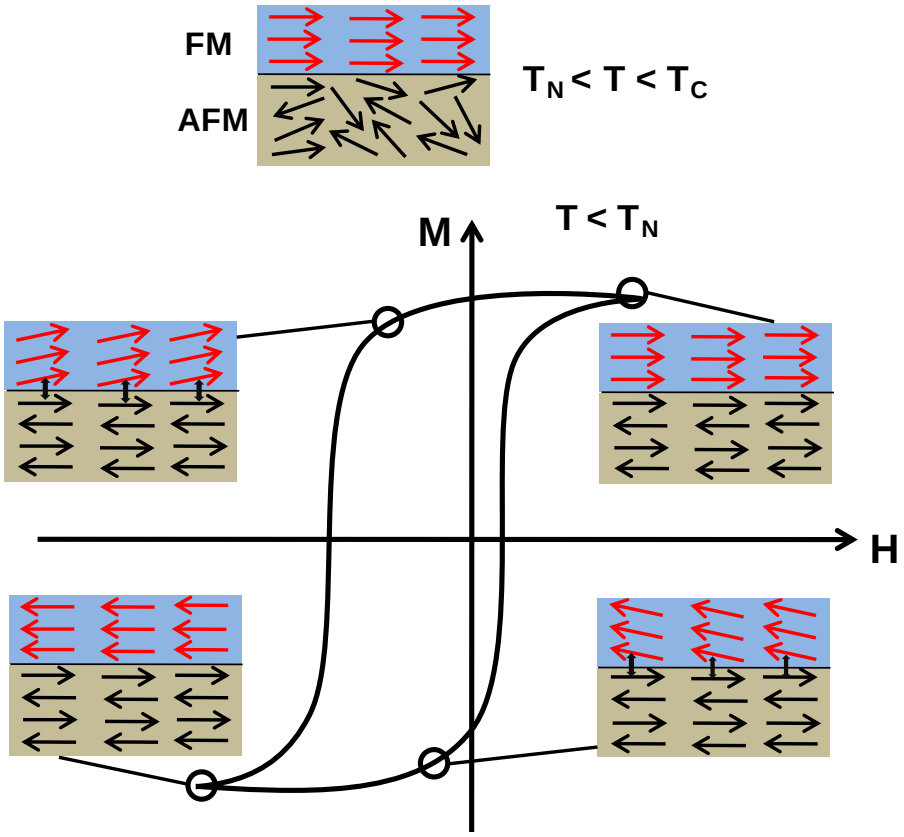

Figure 1.7 Schematic of spin configuration of FM/AFM heterostructure at different stages of applied magnetic field.

Exchange Bias in Core-shell Nano-heterostructure: Exchange bias effect has been mostly studied in thin films,[64,65] however recently there have been many reports on exchange bias in core shell heterostructure also.[66-69] Due to high surface to the volume ratio extremely high radius of curvature, the interface of FM/AFM nanostructure has become a subject of high interest to study the exchange bias. More interestingly in the case of core-shell QD heterostructure both the FM and AFM phases exist as single domain due to finite size effect, so the exchange interaction is solely the effect from two magnetic domains. The way to observe FM/AFM coupling is by overcoating a FM core with a distinct AFM shell with sharp core shell interface. The ability to control the internal structure and modifying the interface by chemical methods has important significance in understanding exchange bias in nanoparticles. After the discovery of exchange bias in Co/CoO[62,63] core-shell nanoparticle there have been many reports from various FM/AFM combination were observed.[67-71] Various core-shell structure having Co and Fe based core and other oxide as shell have been studied such as Co/MnO,[72]

NiCo/NiCoO,[73] Fe_3O_4/FeO,[74] Fe/Cr[75]. There are also reports on inverted AFM/FM core shell structure showing strong exchange bias effect such as FeO/Fe_3O_4,[71] MnO/Mn_3O_4.[66]

However, the interest in exchange bias study of nanoparticles is increasing due to its potential in nanotechnology and biological applications. The appearance of high coercivity due to exchange coupling leads to the development of rare-earth free permanent magnets in nanoparticles, which would be important for nanoparticle, based data storage devices. Moreover, large hysteresis loop area due to high coercivity from nanoparticles gives rise to more heat dissipation under high frequency alternating magnetic field has great promise in hyperthermia treatment.[28,76,77]

1.5 Magnetically Doped Semiconductor Nanostructure

The extreme case of interface modeling of magnetic core with semiconductor shell nano-heterostructure can be the complete diffusion of core and resulting magnetic ion doped semiconductor nanocrystals. Doped semiconductor materials with magnetic impurities or the so called "dilute magnetic semiconductor" (DMS) is one of the most interesting and emerging class of materials due to the existence of room temperature ferromagnetism and semiconductor properties and promise their potential use in spintronics, magnetic memory devices and other spin based information technologies. The idea of dilute magnetic semiconductor came from the "giant Zeeman splitting"[78] observed usually in semiconductors excitonic levels. It was observed that this effect could be enhanced significantly by dilute doping of paramagnetic impurities.[78-80] This high spin splitting in semiconductor leads to spin-resolved transport channels providing control over spin along with the charge of the electron. These novel characteristics made dilute magnetic semiconductor as a potential candidate for researchers to develop spin base electronic devices.

However, there are two key issues, which limit the DMS material to be used in practical application. Firstly, the Curie temperature of the DMS material is usually below room temperature; secondly, the origin of ferromagnetism mostly arises from secondary phase formation[81-83] or defects[84,85] and not due to dopant interaction with the host. Ideally, DMS material show ferromagnetism due to the sp-d exchange interaction between paramagnetic dopant ions and the host semiconductor charge carrier which gives rise to various effect such as "giant excitonic Zeeman splitting",[78,86] "Faraday effect",[87] zero field magnetization[88] etc. This

type of carrier mediated magnetic behavior has been demonstrated successfully in few DMS materials, like Mn doped GaAs,[89-91] Mn doped InAs,[92,93] however the Curie temperature in these system is far below the room temperature. Now a days, there are many reports claiming room temperature ferromagnetism from various DMS materials but the origin of ferromagnetism is not very clear due to the thermodynamic instability of the transition metal ions inside the semiconductor that leads to cluster formation. This cluster formation or the inhomogeneous dopant distribution has proved to be a bane for their application in spin injection and leads to many discrepancies in their fundamental properties.[78,94]

While the bulk DMS materials have already received much attention, now a day's its nano counterpart namely, diluted magnetic semiconductor quantum dots (DMSQDs) are in focus due to their capability of control over long spin coherence and spin polarization even under weak magnetic field. Along with the charge and spin manipulation, quantum confinement in DMS QDs also effects on impurity carrier binding energy[95] and magnetic exchange energies.[96] Moreover, the magnetic properties of the DMS QDs are strongly influenced by the doping site.[97,98] The influence of quantum confinement in DMS QDs' by probing their magnetic property with size variation below quantum confinement regime is a fascinating field of nanoscale research. However, synthesis of DMS QDs has become a major challenge in this field due large surface energy, finite size effect and self-purification.[99,100] In recent studies, though there have been many doping strategies reported, however the detection of phase separation is still very challenging.

1.6 Present Study

We observe that interplay between various heterostructure and their interfaces provide opportunities to play with nanocrystals properties. However it is nontrivial to engineer desired interface and heterostructure as high energetics involve due to finite size effect. The work in the present thesis focuses on three different aspects, namely (i) interface modeling in semiconductor/non-magnetic QD heterostructure for optical application, (ii) Interface modeling of magnetic/semiconductor hybrid structure and magnetic ion doped semiconductor for optical and magnetic properties and (iii) interface modeling for magnetic/magnetic heterostructure for magnetic properties. These studies are divided into two parts containing five chapters that follow a description of theoretical and experimental methods given in **Chapter 2**.

In **Part-I** of this thesis, we discuss the effect on electronic and optical properties of heterostructure QDs due to different kind of interface formation. It contains two chapters. **Chapter 3** discusses a technique to synthesize graded alloy structure in type-I core-shell QDs. It shows how to control the interfacial defects and alloying at the interface using different cores, having different amount of surface passivation can show a direction to synthesis of near unity quantum yield at room temperature. Further we show the high potentiality of these QDs in light emitting application by using them as an active layer of light emitting diode (LED). In **Chapter 4** we have shown how different internal structure type-II heterostructure can show different optical properties for competing and contrasting application like LED and photovoltaics.

In **Part-II**, we studied the synthesis and magnetic properties of various magnetic/ non-magnetic and magnetic/magnetic hybrid nano-heterostructures. It contains three Chapters. In **Chapter 5** we demonstrate a technique to synthesize uniformly doped dilute magnetic semiconductor QDs by diffusing the magnetic core into a non-magnetic semiconductor and studied the complete evolution from a core/shell heterostructure to doped semiconductor by probing the local structure using XAFS. We studied the evolution of magnetic property at different stages of evolution. Using this technique we synthesized DMS QDs varying percentage of magnetic ions and with controlled size or same magnetic ion concentration and established a correlation between the physical entities (size, doping concentration) with their magnetic properties. Universality of this diffusion doping has been shown in **Chapter 6,** where we have synthesized various optically as well as magnetically active doped and co-doped (Mn, Ni, Co) DMS QDs. Here, we discussed two factors, the core stability and the diffusion coefficient of the magnetic ions, which are very important to achieve desirable doping concentration or size of the doped nanocrystals. In **Chapter 7** we discussed the synthesis and characterization of an AFM/FM core-shell heterostructure and studied the magnetic exchange bias effect.

Bibliography

(1) Brown, K. A.; He, S.; Eichelsdoerfer, D. J.; Huang, M.; Levy, I.; Lee, H.; Ryu, S.; Irvin, P.; Mendez-Arroyo, J.; Eom, C.-B.; Mirkin, C. A.; Levy, J. *Nat. Commun.* **2016**, *7*, 10681.

(2) Ohtomo, A.; Hwang, H. Y. *Nature* **2004**, *427*, 423.

(3) Fan, Y.; Smith, K. J.; LupkeG; Hanbicki, A. T.; GoswamiR; Li, C. H.; Zhao, H. B.; Jonker, B. T. *Nature Nanotechnol.* **2013**, *8*, 438.

(4) Kalisky, B.; Bert, J. A.; Klopfer, B. B.; Bell, C.; Sato, H. K.; Hosoda, M.; Hikita, Y.; Hwang, H. Y.; Moler, K. A. *Nat. Commun.* **2012**, *3*, 922.

(5) Zanolli, Z. *Scientific Reports* **2016**, *6*, 31346.

(6) Allara, D. L. *Nature* **2005**, *437*, 638.

(7) Zhang, Z.; Yates, J. T. *Chem. Rev.* **2012**, *112*, 5520.

(8) Wang, S. Q.; Ye, H. Q. *Curr. Opin. Solid State Mater. Sci.* **2006**, *10*, 26.

(9) Sarma, S. D. *Nat. Mater.* **2003**, *2*, 292.

(10) Wolf, S. A.; Awschalom, D. D.; Buhrman, R. A.; Daughton, J. M.; von Molnar, S.; Roukes, M. L.; Chtchelkanova, A. Y.; Treger, D. M. *Science* **2001**, *294*, 1488.

(11) Felser, C.; Fecher, G. H.; Balke, B. *Angew. Chem. Int. Ed.* **2007**, *46*, 668.

(12) Johansson, G.; Tornberg, L.; Shumeiko, V. S.; Wendin, G. *J. Phys. Condens. Mat.* **2006**, *18*, S901.

(13) Shim, Y.-P.; Tahan, C. *Nat. Commun.* **2014**, *5*, 4225.

(14) Tang, E.; Fu, L. *Nature Phys.* **2014**, *10*, 964.

(15) Mathew, S.; Annadi, A.; Chan, T. K.; Asmara, T. C.; Zhan, D.; Wang, X. R.; Azimi, S.; Shen, Z.; Rusydi, A.; Ariando; Breese, M. B. H.; Venkatesan, T. *ACS Nano* **2013**, *7*, 10572.

(16) Yuan, X.; Ma, R.; Zhang, W.; Hua, J.; Meng, X.; Zhong, X.; Zhang, J.; Zhao, J.; Li, H. *ACS Appl. Mater. Interfaces* **2015**, *7*, 8659.

(17) Zhang, Y.; Xie, C.; Su, H.; Liu, J.; Pickering, S.; Wang, Y.; Yu, W. W.; Wang, J.; Wang, Y.; Hahm, J.-i.; Dellas, N.; Mohney, S. E.; Xu, J. *Nano Letters* **2011**, *11*, 329.

(18) Seo, G.; Seo, J.; Ryu, S.; Yin, W.; Ahn, T. K.; Seok, S. I. *J. Phys. Chem. Lett.* **2014**, *5*, 2015.

(19) Lan, X.; Masala, S.; Sargent, E. H. *Nat. Mater.* **2013**, *13*, 233.

(20) Ning, Z.; Voznyy, O.; Pan, J.; Hoogland, S.; Adinolfi, V.; Xu, J.; Li, M.; Kirmani, A. R.; Sun, J.-P.; Minor, J.; Kemp, K. W.; Dong, H.; Rollny, L.; Labelle, A.; Carey, G.;

Sutherland, B.; Hill, I.; Amassian, A.; Liu, H.; Tang, J.; Bakr, O. M.; Sargent, E. H. *Nat. Mater.* **2014**, *13*, 822.

(21) Jara, D. H.; Yoon, S. J.; Stamplecoskie, K. G.; Kamat, P. V. *Chem. Mater.* **2014**, *26*, 7221.

(22) Bharali, D. J.; Lucey, D. W.; Jayakumar, H.; Pudavar, H. E.; Prasad, P. N. *J. Am. Chem. Soc.* **2005**, *127*, 11364.

(23) Gu, Y.-P.; Cui, R.; Zhang, Z.-L.; Xie, Z.-X.; Pang, D.-W. *J. Am. Chem. Soc.* **2012**, *134*, 79.

(24) Gao, J.; Chen, K.; Luong, R.; Bouley, D. M.; Mao, H.; Qiao, T.; Gambhir, S. S.; Cheng, Z. *Nano Lett.* **2012**, *12*, 281.

(25) Rowland, C. E.; Susumu, K.; Stewart, M. H.; Oh, E.; Makinen, A. J.; O'Shaughnessy, T. J.; Kushto, G.; Wolak, M. A.; Erickson, J. S.; L. Efros, A.; Huston, A. L.; Delehanty, J. B. *Nano Lett.* **2015**, *15*, 6848.

(26) Wang, X.; Sun, G.; Li, N.; Chen, P. *Chem. Soc. Rev.* **2016**, *45*, 2239.

(27) Polshettiwar, V.; Luque, R.; Fihri, A.; Zhu, H.; Bouhrara, M.; Basset, J.-M. *Chem. Rev.* **2011**, *111*, 3036.

(28) Noh, S.-h.; Na, W.; Jang, J.-t.; Lee, J.-H.; Lee, E. J.; Moon, S. H.; Lim, Y.; Shin, J.-S.; Cheon, J. *Nano Lett.* **2012**, *12*, 3716.

(29) Richardson, J. T.; Yiagas, D. I.; Turk, B.; Forster, K.; Twigg, M. V. *J. Appl. Phys.* **1991**, *70*, 6977.

(30) Ekimov, A. I.; Efros, A. L.; Onushchenko, A. A. *Solid State Commun.* **1985**, *56*, 921.

(31) Ekimov, A. I.; Onushchenko, A. A.; Tzehomski, V. A. *Sov. Phys. Chem. Glass* **1980**, *6*, 2.

(32) Brus, L. E. *J. Chem. Phys.* **1983**, *79*, 5566.

(33) Efros, A. L.; Rosen, M. *Phys. Rev. Lett.* **1997**, *78*, 1110.

(34) Nirmal, M.; Dabbousi, B. O.; Bawendi, M. G.; Macklin, J. J.; Trautman, J. K.; Harris, T. D.; Brus, L. E. *Nature* **1996**, *383*, 802.

(35) Efros, A. L.; Nesbitt, D. J. *Nat. Nanotechnol.* **2016**, *11*, 661.

(36) Mahler, B.; Spinicelli, P.; Buil, S.; Quelin, X.; Hermier, J.-P.; Dubertret, B. *Nat. Mater.* **2008**, *7*, 659.

(37) Ye, M.; Searson, P. C. *Phys. Rev. B* **2011**, *84*, 125317.

(38) Song, K.-K.; Lee, S. *Curr. Appl. Phys.* **2001**, *1*, 169.

(39) Dabbousi, B. O.; Rodriguez-Viejo, J.; Mikulec, F. V.; Heine, J. R.; Mattoussi, H.; Ober, R.; Jensen, K. F.; Bawendi, M. G. *J. Phys. Chem. B* **1997**, *101*, 9463.

(40) Liu, Y.-F.; Yu, J.-S. *J. Colloid Interface Sci.* **2010**, *351*, 1.

(41) Galland, C.; Ghosh, Y.; Steinbruck, A.; Sykora, M.; Hollingsworth, J. A.; Klimov, V. I.; Htoon, H. *Nature* **2011**, *479*, 203.

(42) Klimov, V. I.; Mikhailovsky, A. A.; McBranch, D. W.; Leatherdale, C. A.; Bawendi, M. G. *Science* **2000**, *287*, 1011.

(43) Sarma, D. D.; Nag, A.; Santra, P. K.; Kumar, A.; Sapra, S.; Mahadevan, P. *J. Phys. Chem. Lett.* **2010**, *1*, 2149.

(44) Talapin, D. V.; Mekis, I.; Gotzinger, S.; Kornowski, A.; Benson, O.; Weller, H. *J. Phys. Chem. B* **2004**, *108*, 18826.

(45) Deka, S.; Quarta, A.; Lupo, M. G.; Falqui, A.; Boninelli, S.; Giannini, C.; Morello, G.; De Giorgi, M.; Lanzani, G.; Spinella, C. *J. Am. Chem. Soc.* **2009**, *131*, 2948.

(46) Mews, A.; Eychmueller, A.; Giersig, M.; Schooss, D.; Weller, H. *J. Phys. Chem.* **1994**, *98*, 934.

(47) Berezovsky, J.; Ouyang, M.; Meier, F.; Awschalom, D. D.; Battaglia, D.; Peng, X. *Phys. Rev. B* **2005**, *71*, 081309.

(48) Santra, P. K.; Viswanatha, R.; Daniels, S. M.; Pickett, N. L.; Smith, J. M.; O'Brien, P.; Sarma, D. D. *J. Am. Chem. Soc.* **2009**, *131*, 470.

(49) Jiang, W.; Singhal, A.; Zheng, J.; Wang, C.; Chan, W. C. W. *Chem. Mater.* **2006**, *18*, 4845.

(50) Romeo, A.; BÃ¤tzner, D. L.; Zogg, H.; Vignali, C.; Tiwari, A. N. *Sol. Energ. Mat. Sol. Cells* **2001**, *67*, 311.

(51) Xu, Y. B.; Freeland, D. J.; Kernohan, E. T. M.; Lee, W. Y.; Tselepi, M.; Guertler, C. M.; Vaz, C. A. F.; Bland, J. A. C.; Holmes, S. N.; Patel, N. K.; Ritchie, D. A. *J. Appl. Phys.* **1999**, *85*, 5369.

(52) Iovan, A.; Andersson, S.; Naidyuk, Y. G.; Vedyaev, A.; Dieny, B.; Korenivski, V. *Nano Lett.* **2008**, *8*, 805.

(53) Zakeri, K.; Kebe, T.; Lindner, J.; Farle, M. *J. Magn. Magn. Mater.* **2006**, *299*, L1.

(54) Florczak, J. M.; Dahlberg, E. D. *Phys. Rev. B* **1991**, *44*, 9338.

(55) Daboo, C.; Hicken, R. J.; Gu, E.; Gester, M.; Gray, S. J.; Eley, D. E. P.; Ahmad, E.; Bland, J. A. C.; Ploessl, R.; Chapman, J. N. *Phys. Rev. B* **1995**, *51*, 15964.

(56) Lee, W. Y.; Xu, Y. B.; Gardiner, S. M.; Bland, J. A. C.; Choi, B. C. *J. Appl. Phys.* **2000**, *87*, 5926.

(57) Moore, T. A.; Rothman, J.; Xu, Y. B.; Bland, J. A. C. *J. Appl. Phys.* **2001**, *89*, 7018.

(58) Hiroshi, O.; Kanji, Y.; Kazuhisa, S.; Koichi, M.; Atsushi, K.; Manfred, E. R. *Jpn J. Appl. Phys.* **2003**, *42*, L87.

(59) Lin, W.-C.; Chang, P.-C.; Tsai, C.-J.; Hsieh, T.-C.; Lo, F.-Y. *Applied Physics Letters* **2013**, *103*, 212405.

(60) Lee, J.-S.; Bodnarchuk, M. I.; Shevchenko, E. V.; Talapin, D. V. *J. Am. Chem. Soc.* **2010**, *132*, 6382.

(61) Son, J. S.; Lee, J.-S.; Shevchenko, E. V.; Talapin, D. V. *J. Phys. Chem. Lett.* **2013**, *4*, 1918.

(62) Meiklejohn, W. H.; Bean, C. P. *Phys. Rev.* **1956**, *102*, 1413.

(63) Meiklejohn, W. H.; Bean, C. P. *Phys. Rev.* **1957**, *105*, 904.

(64) Nogues, J.; Schuller, I. K. *J. Magn. Magn. Mater.* **1999**, *192*, 203.

(65) Allibe, J.; Fusil, S.; Bouzehouane, K.; Daumont, C.; Sando, D.; Jacquet, E.; Deranlot, C.; Bibes, M.; Barthelemy, A. *Nano Lett.* **2012**, *12*, 1141.

(66) Si, P. Z.; Li, D.; Choi, C. J.; Li, Y. B.; Geng, D. Y.; Zhang, Z. D. *Solid State Commun.* **2007**, *142*, 723.

(67) Kavich, D. W.; Dickerson, J. H.; Mahajan, S. V.; Hasan, S. A.; Park, J. H. *Phys. Rev. B* **2008**, *78*, 174414.

(68) Salazar-Alvarez, G.; Sort, J.; Surinach, S.; Baro, M. D.; Nogues, J. *J. Am. Chem. Soc.* **2007**, *129*, 9102.

(69) Baaziz, W.; Pichon, B. P.; Lefevre, C.; Ulhaq-Bouillet, C.; Greneche, J.-M.; Toumi, M.; Mhiri, T.; Begin-Colin, S. *J. Phys. Chem. C* **2013**, *117*, 11436.

(70) Si, P. Z.; Li, D.; Lee, J. W.; Choi, C. J.; Zhang, Z. D.; Geng, D. Y.; Bruck, E. *Appl. Phys. Lett.* **2005**, *87*, 133122.

(71) Sun, X.; Frey Huls, N.; Sigdel, A.; Sun, S. *Nano Lett.* **2012**, *12*, 246.

(72) van Lierop, J.; Schofield, M. A.; Lewis, L. H.; Gambino, R. J. *J. Magn. Magn. Mater.* **2003**, *264*, 146.

(73) Jeyadevan, B.; Chinnasamy, C. N.; Perales-Perez, O.; Iwasaki, Y.; Hobo, A.; Shinoda, K.; Tohji, K.; Kasuya, A. *IEEE Trans. Magn.* **2002**, *38*, 2595.

(74) Lak, A.; Kraken, M.; Ludwig, F.; Kornowski, A.; Eberbeck, D.; Sievers, S.; Litterst, F. J.; Weller, H.; Schilling, M. *Nanoscale* **2013**, *5*, 12286.

(75) Binns, C.; Qureshi, M. T.; Peddis, D.; Baker, S. H.; Howes, P. B.; Boatwright, A.; Cavill, S. A.; Dhesi, S. S.; Lari, L.; Kroger, R.; Langridge, S. *Nano Lett.* **2013**, *13*, 3334.

(76) Fortin, J.-P.; Wilhelm, C.; Servais, J.; Menager, C.; Bacri, J.-C.; Gazeau, F. *J. Am. Chem. Soc.* **2007**, *129*, 2628.

(77) Wu, L.; Mendoza-Garcia, A.; Li, Q.; Sun, S. *Chem. Rev.* **2016**, *116*, 10473.

(78) Norberg, N. S.; Parks, G. L.; Salley, G. M.; Gamelin, D. R. *J. Am. Chem. Soc.* **2006**, *128*, 13195.

(79) Beaulac, R.; Schneider, L.; Archer, P. I.; Bacher, G.; Gamelin, D. R. *Science* **2009**, *325*, 973.

(80) Barrows, C. J.; Vlaskin, V. A.; Gamelin, D. R. *J. Phys. Chem. Lett.* **2015**, *6*, 3076.

(81) Murali, G.; Amaranatha Reddy, D.; PoornaPrakash, B.; Vijayalakshmi, R. P.; Reddy, B. K.; Venugopal, R. *Physica B* **2012**, *407*, 2084.

(82) Singh, S. B.; Limaye, M. V.; Date, S. K.; Gokhale, S.; Kulkarni, S. K. *Phys. Rev. B* **2009**, *80*, 235421.

(83) Xiong, S.-J.; Du, Y. W. *Phys. Lett. A* **2008**, *372*, 2114.

(84) Madhu, C.; Sundaresan, A.; Rao, C. N. R. *Phys. Rev. B* **2008**, *77*, 201306.

(85) Lorite, I.; Kumar, Y.; Esquinazi, P.; Zandalazini, C.; de Heluani, S. P. *Small* **2015**, *11*, 4403.

(86) Sarkar, I.; Sanyal, M. K.; Kar, S.; Biswas, S.; Banerjee, S.; Chaudhuri, S.; Takeyama, S.; Mino, H.; Komori, F. *Phys. Rev. B* **2007**, *75*, 224409.

(87) Frey, J.; Frey, R.; Flytzanis, C. *Phys. Rev. B* **1992**, *45*, 4056.

(88) Gurung, T.; Mackowski, S.; Jackson, H. E.; Smith, L. M.; Heiss, W.; Kossut, J.; Karczewski, G. *J. Appl. Phys.* **2004**, *96*, 7407.

(89) Chiba, D.; Matsukura, F.; Ohno, H. *Appl. Phys. Lett.* **2006**, *89*, 162505.

(90) Matsukura, F.; Ohno, H.; Shen, A.; Sugawara, Y. *Phys. Rev. B* **1998**, *57*, R2037.

(91) Dietl, T. *Nat. Mater.* **2003**, *2*, 646.

(92) Ohno, H.; Chiba, D.; Matsukura, F.; Omiya, T.; Abe, E.; Dietl, T.; Ohno, Y.; Ohtani, K. *Nature* **2000**, *408*, 944.

(93) Chiba, D.; Yamanouchi, M.; Matsukura, F.; Ohno, H. *Science* **2003**, *301*, 943.

(94) Hoffman, D. M.; Meyer, B. K.; Ekimov, A. I.; Merkulov, I. A.; Efros, A. L.; Rosen, M.; Couino, G.; Gacoin, T.; Boilot, J. P. *Solid State Commun.* **2000**, *114*, 547.

(95) Norberg, N. S.; Dalpian, G. M.; Chelikowsky, J. R.; Gamelin, D. R. *Nano Lett.* **2006**, *6*, 2887.

(96) Bussian, D. A.; Crooker, S. A.; Yin, M.; Brynda, M.; Efros, A. L.; Klimov, V. I. *Nat. Mater.* **2009**, *8*, 35.

(97) Meulenberg, R. W.; Lee, J. R. I.; McCall, S. K.; Hanif, K. M.; Haskel, D.; Lang, J. C.; Terminello, L. J.; van Buuren, T. *J. Am. Chem. Soc.* **2009**, *131*, 6888.

(98) Kittilstved, K. R.; Gamelin, D. R. *J. Am. Chem. Soc.* **2005**, *127*, 5292.

(99) Dalpian, G. M.; Chelikowsky, J. R. *Phys. Rev. Lett.* **2006**, *96*, 226802.

(100) Karan, N. S.; Sarkar, S.; Sarma, D. D.; Kundu, P.; Ravishankar, N.; Pradhan, N. *J. Am. Chem. Soc.* **2011**, *133*, 1666.

Chapter 2
Methodology

2.1 Experimental Equipments and Principles

There are several types of experimental set ups and characterization techniques, which have been employed to study the various nanocrystal systems in present work: X-ray diffraction (XRD), transmission electron microscopy (TEM), UV-VIS absorption spectroscopy, Photoluminescence Spectroscopy, SQUID magnetometry and X-ray absorption of fine structure spectroscopy (XAFS). In this chapter, the details of all these techniques have be described.

2.1.1 X-ray diffraction

X-ray diffraction is most commonly used technique[1] for the determination of crystal structure and symmetry. In addition, this technique also provides an estimate of nanocrystal size. X-ray diffraction is based on constructive interference of monochromator radiation coming from different diffraction planes of the crystalline sample. X-rays are generated by a cathode ray tube, filtered to produce monochromatic radiation, collimated to concentrate and directed toward the sample. X-ray diffraction obeys Bragg's law which states that constructive interference would occur if the path difference between the x-rays scattered from parallel planes is an integer number of the wavelength of radiation. If the planes of atoms, separated by a distance'*d*', make an angle θ with incident beam as shown in figure, then the path difference would be $2d\sin\theta$. So, for constructive interference, the Braggs law must be satisfied

$$\text{i.e.} \qquad n\lambda = 2d\sin\theta \qquad n = 1, 2, 3, \ldots \qquad (2.1)$$

where λ= wavelength of the x-ray radiation

The particle size can be calculated using Scherrer equation,[2] which can be derived from Bragg's law of optical diffraction.

Lets consider a crystal having p number of planes, (*hkl*) of spacing '*d*' parallel to each other. So, the thickness of the crystal is $D_{hkl} = pd$.

Now, from Bragg's law the amplitude of the diffracted ray will be maximum when

$$\Delta l = 2d\sin\theta = n\lambda \qquad (2.2)$$

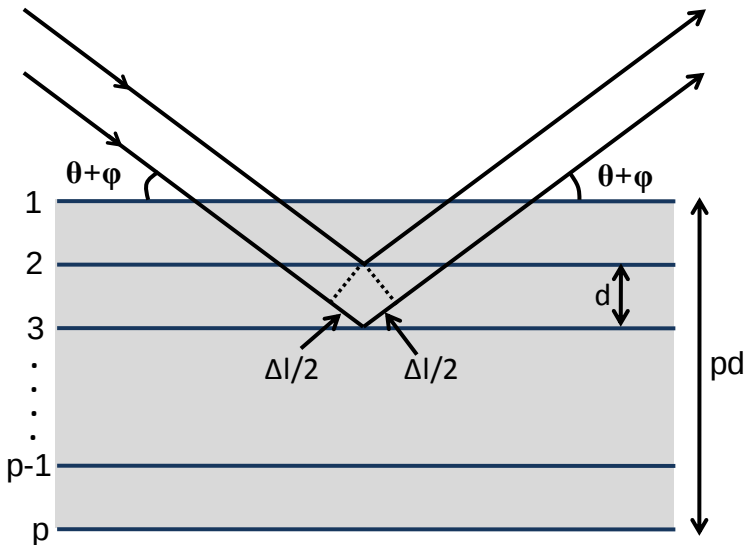

Figure 2.1: A schematic of X-ray diffraction.

When the incident angle θ changes by a small amount φ the path difference will be

$$\begin{aligned} \Delta l &= 2d\sin(\theta+\varphi) \\ &= 2d\,[\sin\theta\cos\varphi + \cos\theta\sin\varphi] \\ &= n\lambda\cos\varphi + \sin\varphi.2d\cos\theta \end{aligned} \tag{2.3}$$

As φ is very small then $\cos\varphi \sim 1$, $\sin\varphi \sim \varphi$

$$\Delta l = n\lambda + 2\varphi d\cos\theta \tag{2.4}$$

The corresponding phase difference

$$\begin{aligned} \frac{2\pi}{\lambda}\Delta l &= 2\pi n + \frac{4\pi}{\lambda}\varphi d\cos\theta \\ &= \frac{4\pi\varphi d\cos\theta}{\lambda} \end{aligned} \tag{2.5}$$

Now if n equal vectors differ in phase by successive uniform increments, the resultant amplitude is

$$an\frac{\sin\alpha}{\alpha} \tag{2.6}$$

where α is the half phase difference between the first and the last vectors of the series.

Now the phase difference of the first and the p th planes is

$$\xi = \frac{4\pi p\varphi d\cos\theta}{\lambda} \tag{2.7}$$

From equation (2.6) the resultant amplitude

$$A = \frac{ap\sin(\frac{2\pi p\varphi d\cos\theta}{\lambda})}{\frac{2\pi p\varphi d\cos\theta}{\lambda}} \tag{2.8}$$

The amplitude of the reflected rays from all p planes are in phase $A_0=ap$

The full width at the half maximum intensity can be calculated

$$\frac{A^2}{A_0^2} = \frac{1}{2} = \frac{sin^2\frac{\xi}{2}}{(\frac{\xi}{2})^2} \tag{2.9}$$

This equation is satisfied when $\frac{\xi}{2} = \pm 1.40$

Therefore $$\frac{4\pi p\varphi d\cos\theta}{2\lambda} = 1.40 \tag{2.10}$$

The full angular width at half maximum intensity of the reflection

$$\beta_{hkl} = 4\varphi = \frac{4\times 1.40\lambda}{2\pi pd\cos\theta}$$

$$= \frac{0.89\lambda}{pd\cos\theta} = \frac{0.89\lambda}{D_{hkl}\cos\theta}$$

Therefore $$D_{hkl} = \frac{0.89\lambda}{\beta_{hkl}\cos\theta} \tag{2.11}$$

This is known as Sherrer equation. We used this equation in many cases to get an estimate of nanocrystal size in this thesis.

We have carried out powder X-ray diffraction experiments on the samples using Bruker D8 Advance diffractometer using Cu-Kα radiation having wavelength 1.5406 Å. Powder or precipitates of sample were placed on a glass plate sample holder during measurement. As the diffraction peak intensity from the nanocrystal is very weak, we have taken scan for sufficiently long time to get a reasonable signal to noise ratio.

2.1.2 Transmission Electron Microscopy

The transmission electron microscopy (TEM) is one of the important tools in material science for characterization of microscopic structure of nanomaterials. A TEM image represents a two-dimensional projection of a three-dimensional (3D) object. TEM operates on the same principles as the visible light microscope, however uses electrons instead of light, having much lower wavelength, which makes it possible to get a resolution of about thousand times better than a visible light microscope. When the electron beam passes through a thin specimen, it get absorbed or diffracted by the specimen. The variation of intensity of electron diffraction across the specimen called the 'diffraction constant' is used in imaging of defects such as dislocation, interfaces and secondary phase particles. An image is formed from the interaction of the electrons transmitted through the specimen. The image is magnified and focused onto a fluorescent screen or a photographic film. Now a days, CCD camera is used to record the TEM images. TEM can be used in recording electron diffraction pattern. Although the XRD pattern provides more quantitative information than electron diffraction pattern, TEM has a greater advantage that the electron beam can be focused easily to any part of specimen. So this electron diffraction data from different area of specimen can give us more details about the accurate local structure of the sample study.

Samples for TEM were prepared by drop casting very dilute solution of the nanocrystal dissolved in a solvent (hexane) onto a carbon-coated copper grid. The grids were then dried under IR lamp for 2 hrs before taken imaging. TEM was carried out using Technai F30 UHR version electron microscope, using a field emission gun (FEG) operating at an acceleration voltage of 200 kV. High resolution transmission microscope (HRTEM) images were obtained from the FEI TITAN (cube) 80-300 kV double aberration corrected transmission electron microscope with a negative spherical aberration coefficient of Cs ~-30 μm to see the microstructure of core-shell QDs.

2.1.3 Scanning Transmission Electron Microscope- Energy-Dispersive X-ray Spectroscopy (STEM-EDX)

STEM-EDX is a technique which uses to characterize elemental distribution of materials. It combines principles of transmission electron microscopy and scanning electron microscopy. Here in this thesis we used STEM-EDX mapping inbuilt with Technai F30 UHR version electron microscope, to visualize the distribution of Fe ions in Fe-doped CdS QDs.

2.1.4 Electron Energy Loss Spectroscopy (EELS)

EELS is an analytical technique that measures the energy distribution of electron after they interact with a thin specimen and lost energy due to inelastic scattering. It provides information about the interacting atoms, including elemental identity, chemical bonding, valence and conduction band electronic properties. Chemical analysis in nanometer scale is a standard feature of Electron Energy Loss Spectroscopy (EELS). The strong points of EELS are the high spatial resolution of < 1 nm, the low detection limit of a few atoms.

Here in this thesis we used EELS with a gun monochromator in a FEI TITAN^{3TM} 80-300 KV aberration corrected transmission electron microscope and record the fine structures in the Fe $L_{2,3}$ absorption edge to determine the valance state of Fe in Fe_3O_4 and Fe-doped CdS QDs.

2.1.5 UV-VIS Absorption Spectroscopy

UV-VIS absorption spectroscopy is a powerful technique for the characterization of semiconductor nanocrystals. Absorption of ultraviolet and visible ray is associated with the excitation of electron from lower to higher energy level, specifically from valence band to conduction band in case of semiconductor. Beer-Lamberts law is used to determine the concentration of sample and it is given by

$$A = \varepsilon.c.l \qquad (2.12)$$

ε = molar absorption co-efficient, c = concentration, l = sample thickness

When light passes through a sample the Absorbance can be measured by the photodetector using formula

$$A = \log (I_0/I) \qquad (2.13)$$

The molar absorptivity can be calculated using the Beer-Lambert law.

The energy of the radiation should be equal or more than the band gap of the semiconductor nanocrystal. Semiconductor QDs shows size dependent confinement effect i.e. the band gap increases with the decrease of particle size. This change in band gap can be detected by the shift of the absorption edge.

In this work UV-Vis absorption spectroscopy has been used to monitor the band gap and absorption characteristics of different QDs. The measurements were carried out in Agilent 8453 UV-visible spectrometer.

2.1.6 Photoluminescence Spectroscopy

When a molecule or fluorophores absorbs a light, the molecule gets excited and creates exciton (electron-hole pair). The recombination of this exciton pairs results emission light known as photoluminescence (PL). PL spectroscopy is a kind of powerful and nondestructive technique which detects the intensity of emission at different wavelength. Here in this thesis, we used PL spectroscopy for analysis of optoelectronic properties of semiconductor QDs. Steady state PL spectra were obtained using a 450 W xenon lamp as the source on the FLSP920 spectrometer, Edinburgh instrument, while the photoluminescence decay dynamics (Time resolved PL) measurements were carried out using the EPL-405 ps pulsed diode laser.

Photoluminescence is defined as the spontaneous emission of light from material under optical excitation. The whole process occurs in three stages as described below (Figure 2.2).

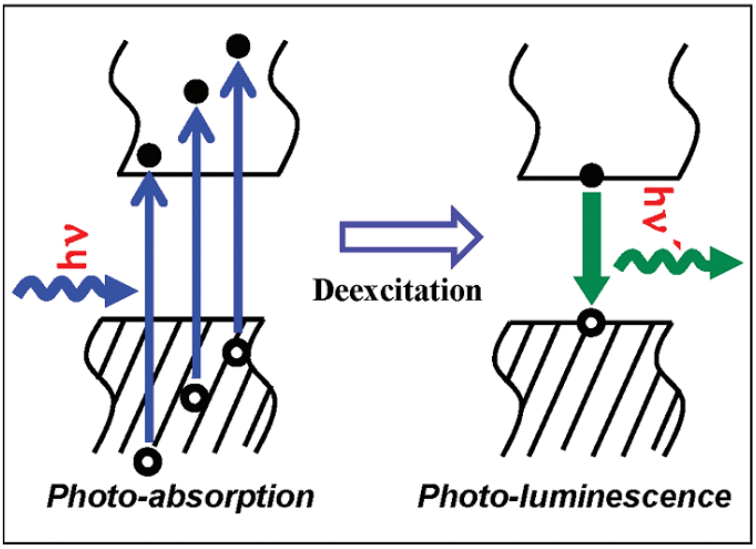

Figure 2.2: Schematic of Photoluminescence process. Reprinted with permission from ref [3] Copyright 2010 American Chemical Society.

Excitation: Excitation of molecule inside the materials occurs when an external light with energy $h\nu_{ex} > E_g$ (E_g is the band gap) incident on it. This process excites the electron to higher energy states in a time scale of 10^{-15} sec.

Non-radiative relaxation: The excited state exists for a finite time (typically picosecond). The excited electron slowly relaxed to the lowest level of first excited state. This process occurs in a time scale of 10^{-11}-10^{-14} sec and the electron loses energy in absence of any light radiation. The energy released in the forms of heat that absorb by the surroundings.

Fluorescence Emission: In this process the excited electron recombines with the ground state hole and releases a photon of energy $h\nu_{em}$. This process occurs in 10^{-9}-10^{-7} sec. As the excited electron dissipates some energy in form of heat, the energy of the emitted photon ($h\nu_{em}$) is always less than the excitation photon ($h\nu_{ex}$). This difference in energy or wavelength is called stokes shift.

Time Resolved Photoluminescence (TrPL): Time Resolved Photo-Luminescence (TrPL) is an experimental technique that provides the relaxation dynamics of charge carrier as a function of time after excitation using a short laser pulse. The time resolution can be obtained in a number of ways which depends on the required sensitivity and time resolution. TCSPC (Time-Correlated Single Photon Counting) is one of them and it is a digital counting technique which counts photons that are time-correlated in relation to a short excitation light pulse. This provides radiative and non-radiative lifetimes of exciton pairs in semiconductor materials. In this thesis, we have extensively used this technique to obtain average lifetimes of different QDs. Average lifetime is the time taken for the population of excited state molecules to become 37% of its original intensity after the excitation of QDs at time, t=0.

PL Quantum Yield: The photoluminescence quantum yield (PL QY) is the ratio of photons absorbed to photons emitted through fluorescence. It gives the information how the excited QD be deactivated either through radiative or non-radiative processes. PL QY will be 100% if all the excited photons decay radiatively to the ground state.

$$\text{PL QY} = \frac{\text{Number of photons emitted}}{\text{Number of photons absorbed}}$$

Experimentally, PL QY can be used measured by comparative method[4] or absolute method.[5]

"Comparative method" involves the use of well characterized standard samples with known QY values. This method is widely used and suitable for weakly absorbing samples in dilute solutions. The solutions of the reference and test samples with identical absorbance at the same excitation wavelength can be assumed to be absorbing the same number of photons. Hence, the ratio of the integrated PL intensities of the two solutions (recorded under same slit width, dwell time and other conditions) will yield the ratio of the QY values. Since QY for the reference sample is already known, it is straight forward to calculate the QY for the sample under measurement from the equation given below.

$$QY = QY_{ref} \frac{\eta^2}{\eta_{ref}^2} \frac{I}{A} \frac{A_{ref}}{I_{ref}}$$

where, I= integrated PL Intensity

A=absorbance at excitation wavelength

η= refractive index of the solvent

This method strongly relies on the reference sample and there are only few reference samples that are available in longer wavelengths which limit this method for measuring PL QY as the method requires similar optical properties for the standard as that of the sample.

These limitations can be overcome by use of integrating sphere which collects all the emission from the sample and this method is known as "Absolute method". We have used this method to calculate the PL QY of the QD samples in this thesis. The method involves measuring the scattering spectra of solvent and samples along with the emission spectrum of sample. The intensity of the scattering spectrum of the sample is less than that of solvent as the QDs present in the sample absorbs the incident light. The intensity difference in the scattering spectra of solvent and sample gives the number of photons absorbed by the sample. Then with the help of emission spectrum which gives the number of photons emitted and the intensity difference in the scattering spectra, the measurement of PL QY of the sample is trivial.

2.1.7 Inductively Coupled Plasma Optical Emission Spectrometry (ICP-OES)

ICP-OES is one of the most useful technique used in analytical laboratories to determine the composition of elements in a sample using plasma and a detector. It is based on Atomic Emission Spectroscopy in which the sample is excited with high temperature plasma (up to 8000 K), generated at the end of a quartz torch. When the excited electron returned to lower energy state, energy released as light and the corresponding photon wavelength is measured. Every element has its own characteristics emission spectrum. The element type is determined based on the wavelength of the photon rays, and the concentration of each element is determined based on the rays' intensity.

Sample introduced into the ICP should be liquid form. For solid samples, sample should be dissolved completely in Millipore water in acidic medium (2-5%). The plasma torch can be operated in vertical position, so that the observations though the plasma are done radially (side-

on viewing), or the torch can be put horizontally, allowing axial measurement (end-on viewing). Radial ICP's are less sensitive, but more robust and better resistant to the matrix, while axial ICPs are more sensitive, also to matrices.

Here, we have used Perkin Elmer optima 7000 DV ICP-OES machine to determine the elemental concentration in our samples. Samples were dissolved in 2-5% of HNO_3 solution, and different elemental concentrations were measured against high purity known standards.

2.1.8 SQUID Magnetometer

Samples magnetization *vs.* magnetic field and D. C. susceptibility measurement, presented in this thesis, were performed using Superconducting Quantum Interference Device (Quantum Design) at JNCASR, Bangalore.

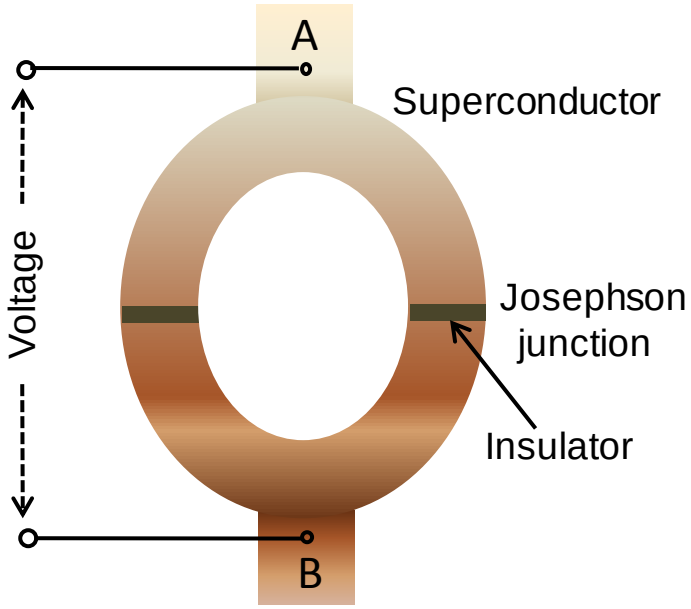

Figure 2.3: Schematic of SQUID device.

SQUID magnetometer[6] works on the principle of Faraday's law of electromagnetic induction, which states that a change in magnetic flux in a coil will induce an electromotive force (voltage) in the coil, which is equal to the rate of change of flux. SQUID magnetometer consists of a superconducting ring with two very narrow insulating gap, called Josephson junction, exists parallel to each other (shown in Figure 2.3). A superconducting current tunnel through the both junctions. A small change in magnetic flux can induce a voltage (Faraday's law), which increase the current in one side and decrease in the other side of the Josephson

junction. This results in appearance of a voltage between A and B points. So, change in each flux across the boundary of the rings gives rise to a voltage step. This SQUID device is usually kept inside helium bath and is linked to a superconducting pick up coil that detect the magnetic flux change due sample vibration (vertical) inside it. A superconducting magnet, which is used to generate the magnetic field, is equipped around the pickup coil. This coil along with the SQUID antenna transfers the magnetic flux from the sample to the SQUID device, which acts as a magnetic flux to voltage converter. This voltage is then amplified and read out by the electronics circuit attached with the device. As the SQUID device is very sensitive to the fluctuation of the magnetic field, it is kept inside a superconducting shielding to prevent from magnetic flux of superconducting magnet and the laboratory environment.

For M *vs.* H hysteresis curves presented in this thesis, the magnetizations of the samples were recorded at room temperature and at 2K as a function of swiping magnetic field. For DC susceptibility measurement, samples are first heated above their ordering temperature and then cooled down to low temperature (2K) without field (zero field cooled) or with field (field cooled) condition. The magnetization data due to a small magnetic field are then recorded during heating for both the cases. The blocking temperature is determined from the peak of the ZFC curve.

2.1.9 X-ray Absorption Fine Structure (XAFS) Spectroscopy

X-ray absorption fine structure spectroscopy[7-9] is an important tool to characterize the local structure of nanocrystals. This technique has been extensively used to probe the evolution of the local structure of various heterostructure and doped nanocrystal system in this thesis.

XAFS was developed in the early 1970 (Sayer *et. al*)[7] and is being widely used for characterizing various materials local atomic structure. It gives information about how X-rays are absorbed by a specific element (atoms) of its near and above the core binding energy through “photoelectric effect”. Usually, the energy range of X-ray used for the XAFS covers from 500 eV to 50 keV. When high energy X-rays incident on the sample (X-ray energy higher than the binding energy), the oscillating electric field of the electromagnetic radiation interacts with bound electrons of the absorbing atom and remove from its quantum level to the continuum. This results in absorption of X-ray energy and an emission of a photoelectron, from the atom. In XAFS we study the probability of X-ray absorption co-efficient (μ) as a function of X-ray energy.

According to Beer-Lambert law the energy absorption,

$$I=I_0\, e^{-\mu t} \tag{2.14}$$

Where I_0 and I are incident and transmitted x-ray intensity respectively, t is sample thickness as shown in Figure 2.4(a).

Usually the absorption co-efficient μ is can be expressed as,

$$\mu \approx \frac{\rho z^4}{AE^3} \tag{2.15}$$

Where ρ sample density, *z* atomic number, *A* atomic mass *E* energy of X-ray

XAFS measures the absorption coefficient as a function X-ray energy. At a certain energy where the X-ray energy matches with the binding energy of the core-electron, the absorption increased drastically giving rise to absorption edge. At this energy, the core electron is excited to the continuum state and produces a photoelectron. Thus the absorbed edges correspond to the binding energies of the electron in the K, L, M etc, shells of the specific absorbing atoms. The absorption edges are labelled as K, L_I, L_{II}, M_I… with the different energies.

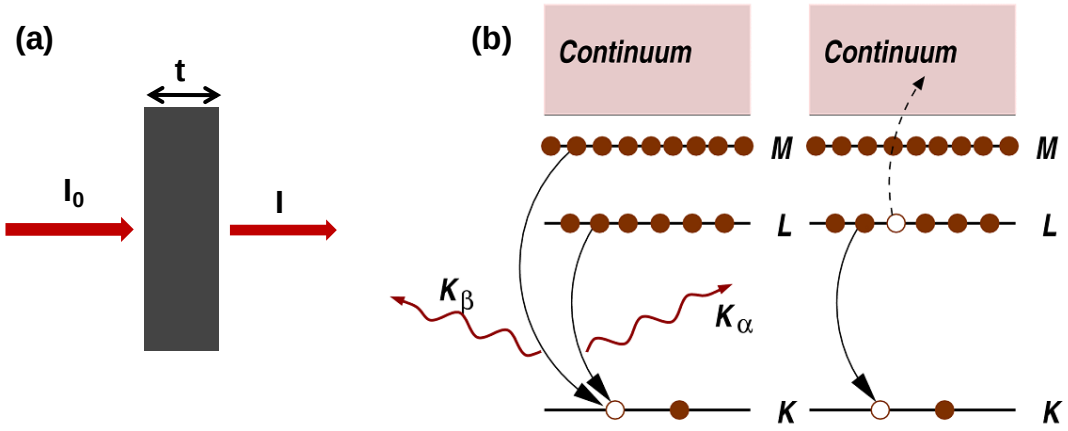

Figure 2.4: (a) A schematic of transmission of X-rat through a sample. (b) Schematic of X-ray fluorescence and Auger effect. (Adopted from Fundamental of XAFS, Matthew Newville).[10]

After the absorption process occurs, the atom goes to the excited state, having a core level empty and ejection of photoelectron as shown in Figure 2.4 (b). Thereafter two major processes occur, Firstly an electron from higher energy level comes down and fills the empty core level releasing an well-defined energy (k_α, k_β) known as X-ray fluorescence. The fluorescence energies are characteristic of the particular atom and can be used to identify atom. Secondly, as the electron from the higher level comes down to the empty core level, the relaxation energy

transferred to any other second electron in the same higher energy level. Absorbing the energy the second electron gets excited to the continuum or leaves the sample. This is known as Auger effect. In case of high energy, X-ray fluorescence dominates while at lower energy Auger process dominates.

XAFS is usually a measured in transmission or fluorescence mode geometries. The dependence of attenuation of absorption co-efficient $\mu(E)$ in transmission mode is

$$\mu(E) = \log(I_0/I) \qquad (2.16)$$

or in fluorescence mode is

$$\mu(E) = \log(I_f/I_0) \qquad (2.17)$$

where, I_0 = incident X-ray intensity, I= transmitted X-ray intensity and I_f = fluorescence X-ray intensity.

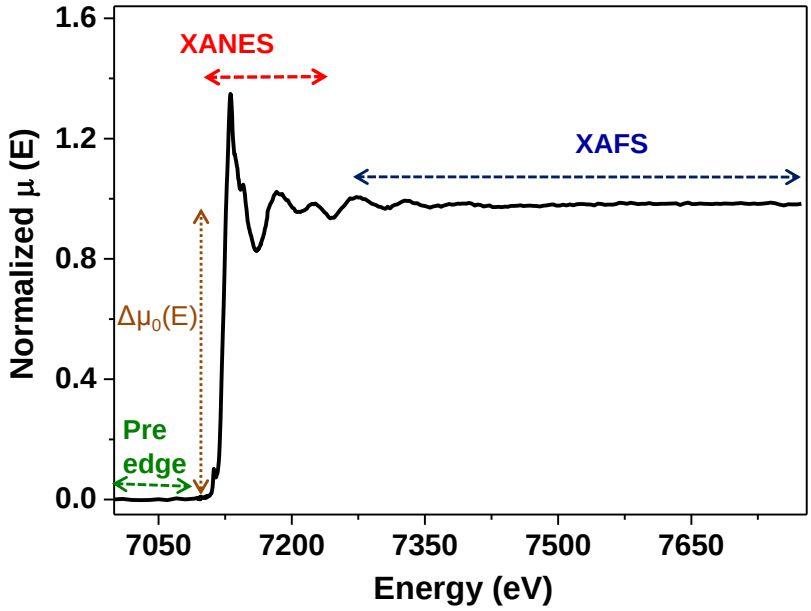

Figure 2.5 XAFS spectrum of Fe_3O_4 showing different region of energy.

A typical XAFS spectrum is shown in figure 2.5. It is generally divided into two sections (i) X-ray absorption near edge structure (XANES) which extend from just below the edge to about 30 eV and (ii) extended X-ray absorption fine structure spectroscopy (EXAFS) which starts after XANES and continues up to 1000 eV above the edge. As, XANES occurs at lower energy, when the transition happens, it provides information about electronic properties, oxidation states, the density available states etc. However, the EXAFS provides the most useful

information about the local structure around the absorbing atom. Moreover, it also gives the information about local defects and can extract site resolve structural information.

EXAFS represents an oscillatory behavior of absorption coefficient (μ) as a function of X-ray energy. Above the absorption edge, the X-ray energy used to excite a core level electron and the remaining energy is transformed to the photoelectron in form of kinetic energy (KE). So, the KE of the photoelectron is $KE= E-E_0$ where E= energy of X-ray, and E_0 =binding energy of the core electron. The photoelectron propagates outward from the absorbing atoms as spherical waves and interacts with the neighboring atoms and scatters from it. The relative phase of outgoing and scattered photoelectron changes the probability of absorption by the absorbing atoms. The constructing and destructing interference between the outgoing and backscattered photoelectron wave forms the oscillatory behavior of the XAFS spectra as shown in Figure 2.6.

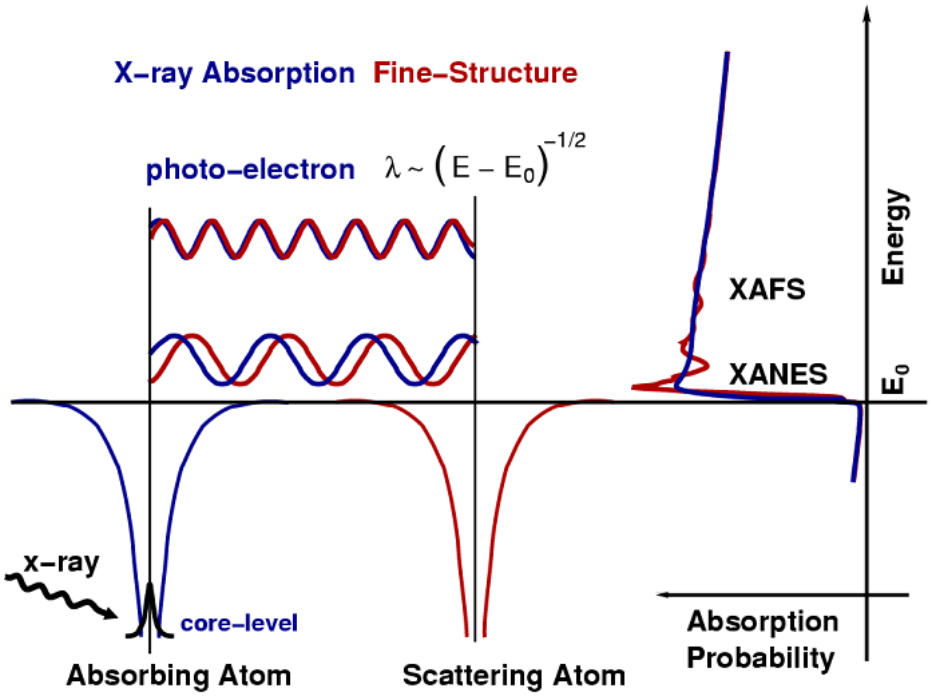

Figure 2.6 A schematic of XAFS oscillation formation due to interference of photoelectron and backscattered photoelectron. (Adopted from Fundamental of XAFS, Matthew Newville)[10]

All the atoms surrounding the absorbing atom take part in EXAFS signal formation. The nearest atoms form the first shell and the number of atoms in the first shell is called co-ordination number. This way it forms 2nd, 3rd nth number of shells having different co-ordination numbers.

The EXAFS spectra is defined as fine structure function

$$\chi(E) = \frac{\mu(E) - \mu_0(E)}{\Delta\mu_0(E)} \tag{2.18}$$

where, μ(E) is experimental absorption coefficient, μ_0(E) is slowly varying absorption from an isolated atom and $\Delta\mu_0$(E) is jump in the absorption co-efficient μ(E) at the threshold.

XAFS is an interference effect and depends on the wave nature of photoelectron. Therefore it is best to represent X-ray energy in terms of wave number k, of the photoelectron that can be defined as

$$k = \left(\frac{2m(E - E_0)}{\hbar^2}\right)^{\frac{1}{2}} \tag{2.19}$$

Where E_0 is absorption edge energy and m is mass of electron.

So, EXAFS can be represented as primary quantity χ(k), the oscillatory variation of photoelectron wavenumber. To emphasize the oscillation, χ(k) is often represented as k^2 or k^3.

Scattering from different surrounding neighbouring atoms give rise to different frequencies and the EXAFS oscillation χ(k) can be expressed as

$$\chi(k) = \sum \frac{N_j f_j(k) e^{-2k^2\sigma_j^2}}{kR_j^2} \sin[2k(R_j + \delta_j(k)] \tag{2.20}$$

where *f(k)* and *δ(k)* are scattering properties of the neighbouring atoms, R is the distance of the interacting neighbor, N is the coordination number and σ^2 is the Debye-Waller factor. By appropriate modeling of EXAFS spectra one can determine N, R, σ^2 from this equation knowing the scattering amplitude f(k) and phase shift δ(k).

XAFS data processing: The obtained data from synchrotron beamline represent the variation of μ as a function of energy which can be transformed in wavevector in k-space by changing energy to photoelectron wavenumber k [$k= (2m(E-E_0)/\hbar^2)^{1/2}$]. This spectrum has more physical consequence than when it represent in terms of radial function (R) i.e. in R-space by applying Fourier transformation on the k-space EXAFS.

However in this thesis we followed the following steps to process our data-

1. **Pre-edge background correction.** Due to intensity of the incident X-ray and detector efficiency there always exist some background intensity before absorption edge. This pre-

edge background should be removed before processing the data. The pre-edge spectrum should be fitted with some functional form and extrapolating this function into the post edge.

2. **Deglitching.**[11] The post absorption edge or the EXAFS region of the raw spectrum often consist of some sharp spikes due to reflection (Bragg scatter) from crystalline monochromator or the diffraction from the sample. These sharp spikes contributes a lot in Fourier transformed R-space spectrum and hence it is necessary to remove or deglitch them before processing further. This glitches can be removed by removing those defecting points carefully and fitting with a polynomial to interpolate the region of glitch.
3. **Normalization.** The EXAFS spectra recorded is contribution from multiple absorbing atoms. To obtain the contribution from a single atom and more quantitative information the data should be normalized. Normalization is usually done by following equation (2.18). Normalize μ(E) to go from 0 to 1, so that the EXAFS spectra is then normalized to an edge jump of 1.
4. **Conversion to k-space.** To convert the E-space spectrum to k-space χ(E) need to convert into χ(k). It can be changed by changing the x-axis using the relation $k= [(2m(E-E_0)/\hbar^2)^{1/2}]$.
5. **Conversion to R-space.** The k-space spectrum can be converted to R-space by Fourier transformation. The R-space spectrum represents the radial position of the neibouring atom. It should be noted that the peak position does not give exactly the bond length due to the phase shift term $\delta(k)$ in EXAFS equation 2.20. Typically the bond length is 0.3-0.5 Å shorter than the peak position.
6. **Fitting.** Finally the R-space data is modeled by providing known crystal structure information using known crystal structure information using abinitio calculation of FEFF code.[9]

Bibliography

(1) Klug, H. P.; Alexander, L. E. *X-Ray Diffraction Procedures: For Polycrystalline and Amorphous Materials*; Wiley, 1974.

(2) Patterson, A. L. *Phys. Rev.* **1939**, *56*, 978.

(3) Pradhan, N.; Sarma, D. D. *J. Phys. Chem. Lett.* **2011**, *2*, 2818.

(4) Williams, A. T. R.; Winfield, S. A.; Miller, J. N. *Analyst* **1983**, *108*, 1067.

(5) Porres, L.; Holland, A.; PÃ¥lsson, L.-O.; Monkman, A. P.; Kemp, C.; Beeby, A. *J. Fluoresc.* **2006**, *16*, 267.

(6) B. D. Cullity, C. D. G. *Introduction to Magnetic Materials*; Wiley-IEEE Press, 2008.

(7) Sayers, D. E.; Stern, E. A.; Lytle, F. W. *Phys. Rev. Lett.* **1971**, *27*, 1204.

(8) Rehr, J. J.; Albers, R. C. *Rev. Mod. Phys.* **2000**, *72*, 621.

(9) Newville, M. *J. Synchrotron Rad.* **2001**, *8*, 322.

(10) Newville, M. *Consortium for Advanced Radiation Sources, University of Chicago, Chicago, IL* **2004**.

(11) Zhuchkov, K. N.; Shuvaeva, V. A.; Yagi, K.; Terauchi, H. *J. Synchrotron Radiat.* **2001**, *8*, 302.

Chapter 3

Near Unity Quantum Yield in Semiconducting Quantum Dots: A Structural Perspective

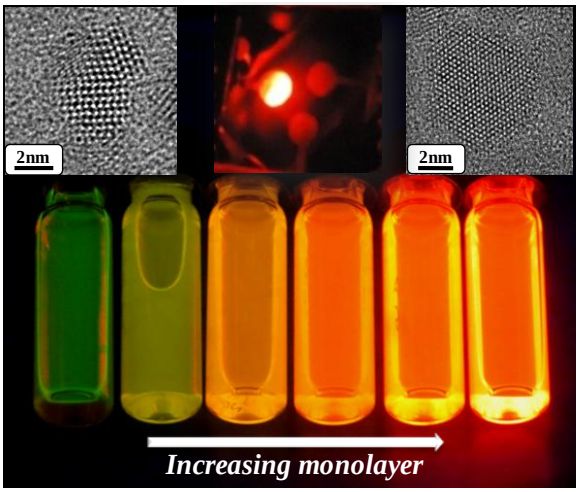

The following papers have been published based on the work presented here.

- J. Phys. Chem. Lett., 2013, 4, 3544–3549
- Patent Pub No. WO2014147555 (A2)

3.1 Summary

Core/shell nanocrystal QDs have shown great potential as efficient electroluminescent materials in devices like down conversion phosphors and light emitting diodes (LEDs). The efficiency of these devices is *non-linearly* enhanced by the use of high QY materials. Though relatively high QY materials with inherent advantages for use in device applications are achieved by thick shell CdSe/CdS NQDs, their QY is not anywhere near unity, due to lack of correlation of microstructure with their photo-physical properties. Here, in this report, we show that the control of interfacial defects are crucial to achieve near unity QY using microstructure studies of CdSe/CdS NQDs. Simple un-optimized LEDs obtained from these NQDs as active layer demonstrate performances in excess of 7,000 Cd/m^2 with power conversion efficiency of ~ 1.5 lm/W that is comparable to the best NQD based LEDs (1-3%) in spite of the absence of electron injecting buffer layer.

3.2 Introduction

Structural engineering of semiconducting nanocrystals have shown a lot of potential in improving various properties of the nanocrystals, specifically, the optical properties.[1-4] For example, the growth of a higher band gap shell material is known to be extensively used to passivate the core leading to high QY structures.[5] The high photoluminescence[6] (PL) QY without electric field induced charging in NQDs is a trade-off between the surface defects[7] and the core-shell interface.[8] However, among the multitude of methods available to obtain such core/shell[9] structures, the properties of the final materials obtained depends sensitively on various factors like the actual total coverage of the shell and if all nanocrystals are equally coated in addition to defects on the surface and/or at the shell interface.[8,10,11] Besides the lattice mismatch between the core and shell materials that is known to play an important role in the design of robust core/shell NQDs, in most cases the optical properties are mainly dominated by surface defects.[7,8] Core/shell NQDs have shown great potential as efficient electroluminescent materials in devices like down conversion phosphors and LEDs. The efficiency of these devices is *non-linearly* enhanced by the use of high QY materials. Though relatively high QY materials with inherent advantages, for use in device applications are achieved by thick shell CdSe/CdS NQDs, their QY is not anywhere near unity, due to lack of correlation of microstructure with their photo-physical properties. Recently, this frustrating dependence of optical properties on

surface chemistry and chemical environment was overcome by the growth of ultra thick inorganic shell of CdS over CdSe core particles.[12-15] Surprisingly, these particles were found to not only rid the dots of the detrimental effects of labile nature of organic ligands but were also shown to suppress a more intrinsic phenomenon, known as Auger recombination,[13,16-18] believed to give rise to blinking in NQDs.[12,15,19-21] Since then various advantages inherent in these ultra thick shell Auger engineered CdSe/CdS NQDs have been extensively studied and have justifiably drawn a lot of attention as prospective lasing materials,[17] efficient electroluminescent materials[22] and stable down conversion phosphors.[23,24] In the last couple of years, the properties of these compounds have been extensively studied starting from blinking statistics[15,20] to photostability to optical gain performance[17] as well as demonstration of LEDs.[22,24] Due to the large number of potential applications, modifying the chemistry in an effort to further optimize the QY is underway.[25] However in spite of a large effort, though incremental improvements in QY are reported, not surprisingly, recipe for high QY material is unknown. Specifically, the QY of these thick shell compounds have not improved much more than 30% except in a few rare cases leading up to 50% though high QY in thinner shell materials is now routine.[26] However, in spite of the fact that NQDs of single material or core/shell structures with a thin shell material have shown close to near unity QY,[26] the efficiency of devices have not improved substantially.

Latest efforts along this direction have attributed the low QY to the poor control of the crystal structure resulting in wurtzite rather than zinc-blende structure.[27] However, several fundamental theoretical studies on the electronic structure have emphasized that the crucial component is to suppress the Auger recombination in these materials. Calculations have shown that smoothening out the confinement potential reduces the efficiency of the Auger processes in low dimensional heterostructures[28] by several orders of magnitude compared to that in structures with abrupt boundaries and hence improve the QY.[28-30] Since then extended efforts have shown that it is non-trivial to translate such a theoretical demand to materials, specifically in a uniform defect-free manner, that would lead to nanocrystals with excellent photo-physical properties. Though it is well known that the effects of a single defect[7] or interface[28] on the properties of NQDs could have far-reaching consequences due to the high defect density, the control of defects in NQDs is very challenging as a result of the large number thermodynamic and kinetic factors involved.

Our studies in this direction have shown that the lack of a logical understanding and correlation of the microstructure with the photo physical properties of these core/shell structures is responsible for the sustained absence of high QY materials. In this chapter, we report for the first time an experimental correlation of the evolution of defects in NQDs to their photophysical properties. The control and minimization/elimination of the defects at the core/shell interface in CdSe/CdS NQDs leads to Auger-engineered[13,17] highly emissive QDs with excellent optical properties of near-unity QY. In the case of CdSe/CdS, a lattice mismatch of 3.9 % between CdSe and CdS poses a serious challenge in controlling defects at the interface of the core-shell during the synthesis of a thick uniform shell. Defect free graded alloy at interface was achieved using a counter-intuitive approach of a highly surface defective core that is demonstrated using PL lifetime studies and high resolution microscopy. This unusual observation can not only be explained using the well-studied sharp/smooth interface model, but a direct correlation between the QY and number of defective particles has been established by studying samples with varying QY. So, this work discusses a very counter-intuitive mechanism of decreasing defect density and shows that contradictory to the expected belief, high quality cores with low or nil surface defects are not ideally suited to yield high QY core/shell particles even in low lattice mismatch core and shell materials. In fact, we show that cores with large number of surface defects are better suited to obtain high QY materials.

Further the advantages of these NQDs could be directly translated into device performance in LED. A proof of concept verification of device efficiency was carried out by fabricating a simple LED using near unity QY nanocrystals as the active layer. As anticipated, the performance of these un-optimized simple devices was comparable to the best NQD based LED devices (1-3%) in spite of the absence of electron injecting buffer layer. The devices retained all the advantages of the earlier devices like remarkably low turn on voltage as well as possibility of driving the device to yield luminance to a range of 7,000 Cd/m^2. The sizable luminance at low input power leading to efficient devices (~ 1.5 Lm/W) is comparable to the efficiency of that obtained for solution processed LEDs; 2.4 Lm/W for cross-linked colloidal dots[31] and 4.2 lm/W for a transfer printed LED.[32]

3.3 Experimental Details

3.3.1 Synthesis

The successive ion layer adsorption and reaction (SILAR) technique was used to synthesize a thick uniform shell of CdS on CdSe nanocrystals while retaining the crystallinity of the samples. The defects in these nanocrystals were controlled by varying extent of surface passivation of the CdSe cores.

Synthesis of CdSe cores. Cadmium oleate ($CdOl_2$) was prepared using modified literature methods and 2 M TOP/Se solution by dissolving Se in TOP inside a glove box. In a typical synthetic method, 500 mg of TOPO, 5ml of ODE and 1 ml of 0.2 M $CdOl_2$ were taken in a 50 ml round-bottom flask equipped with a temperature controller probe and degassed in vacuum under constant stirring. After 1h of evacuation at 80°C the temperature of the reaction mixture was raised to 290°C under Ar atmosphere. 1 ml of 2 M TOP/Se, mixed with 1.5 ml of OlAm and 0.5 ml of ODE, was quickly injected into the reaction system at high temperature. For the growth of nanocrystals, the temperature of the system was then lowered to 260°C. After 1 minute, the solution was cooled down to room temperature to get NQDs of 3 nm size. Samples were washed by centrifugation once with acetone and followed by hexane/methanol mixture and redispersed in hexane. Highly defective CdSe cores were prepared by reducing the amount of TOPO (~300 mg) and OlAm (~1 ml).

Synthesis of CdSe/CdS core-shell QDs. The core-shell CdSe/CdS QDs were synthesized using the successive ionic layer adsorption and reaction (SILAR) technique. The amount of Cd and S precursors required for each individual layer were calculated considering CdSe and CdS being present in wurtzite structure and the average thickness of each monolayer was assumed to be 0.35 nm. In a typical experiment ~2×10^{-7} mol CdSe cores (size ~ 3 nm), 5ml of ODE and 5ml of OlAm were taken into a round-bottom flask and degassed at 80°C. After 1 h of evacuation the temperature was raised to 240°C under Ar flow. 0.2 M of sulfur dissolved in ODE and 0.2 M $CdOl_2$ were used as S and Cd precursors respectively. At 240°C the required amounts of $CdOl_2$ followed by S precursor were injected into the reaction mixture for each cycle of monolayer (ML) formation and the sample aliquots were taken out after the completion of each cycle.

After the addition of Cd precursors, the sample was annealed for 2.5 hrs and 1 h after the S precursor addition. All the samples were washed using a hexane methanol mixture and centrifuged to obtain precipitation and then redissolved in distilled hexane.

3.3.2 LED Fabrication

Poly(3,4-ethylenedioxythiophene): polystyrene sulphonate (PEDOT:PSS) (Baytron P) (~50 nm) was spin coated on to pre-cleaned indium tin oxide anode (ITO) substrate and annealed at 150^{o}C for 1 hour under low vacuum (0.1 Torr.). A layer of poly(3-hexylthiophene) (P3HT) (~40 nm) was spin coated on top of the PEDOT:PSS layer and annealed at 140^{o}C for 1 hour under N_2 atmosphere. The emissive layer of CdSe/CdS NQDs (~120 nm) was then spin coated on the P3HT layer followed by 12 h drying under N_2, the device was completed by depositing aluminium top electrode (~100 nm) by physical vapour deposition.

3.3.3 LED Characterization

Current-voltage characteristics were acquired using a Keithley 2400 Source Measure Unit as the voltage source and a Keithley 6512 electrometer. Spectral measurements were done using a fiber coupled Hamamatsu mini spectrophotometer (Model: TM-VIS/NIR). Luminance measurements were done using a calibrated silicon photodiode, which collected the emission from the ITO side of the device. The light lost through wave guiding and absorption in the various layers within the device was not accounted for in the estimation of luminescence.

3.4 Results and Discussion

The 3 nm cores of nanocrystals were synthesized using different concentrations of surface ligands as tabulated in Table 3.1. Starting from these cores, the growth of a shell of CdS was carried out by identical multiple steps of sequential addition of Cd and S precursors followed by annealing at high temperatures as shown in the scheme in Figure 3.1(a). A typical TEM of the large NQDs is shown in Figure 3.1(b) depicting presence of large spherical nanocrystals with relatively small size distribution (< 10%). The inset to Figure 3.1(b) shows the absorption and steady state PL data of the core as well as the overcoated nanocrystals showing the presence of highly emitting nanocrystal in the red region. The X-ray diffraction patterns, shown in Figure 3.1(c), on comparison with the bulk wurtzite and zinc blende CdSe and CdS

patterns reveal the formation of wurtzite core and core/shell nanostructures obtained both from cores with low as well as with high surface passivation with no traces of zinc-blende structure.

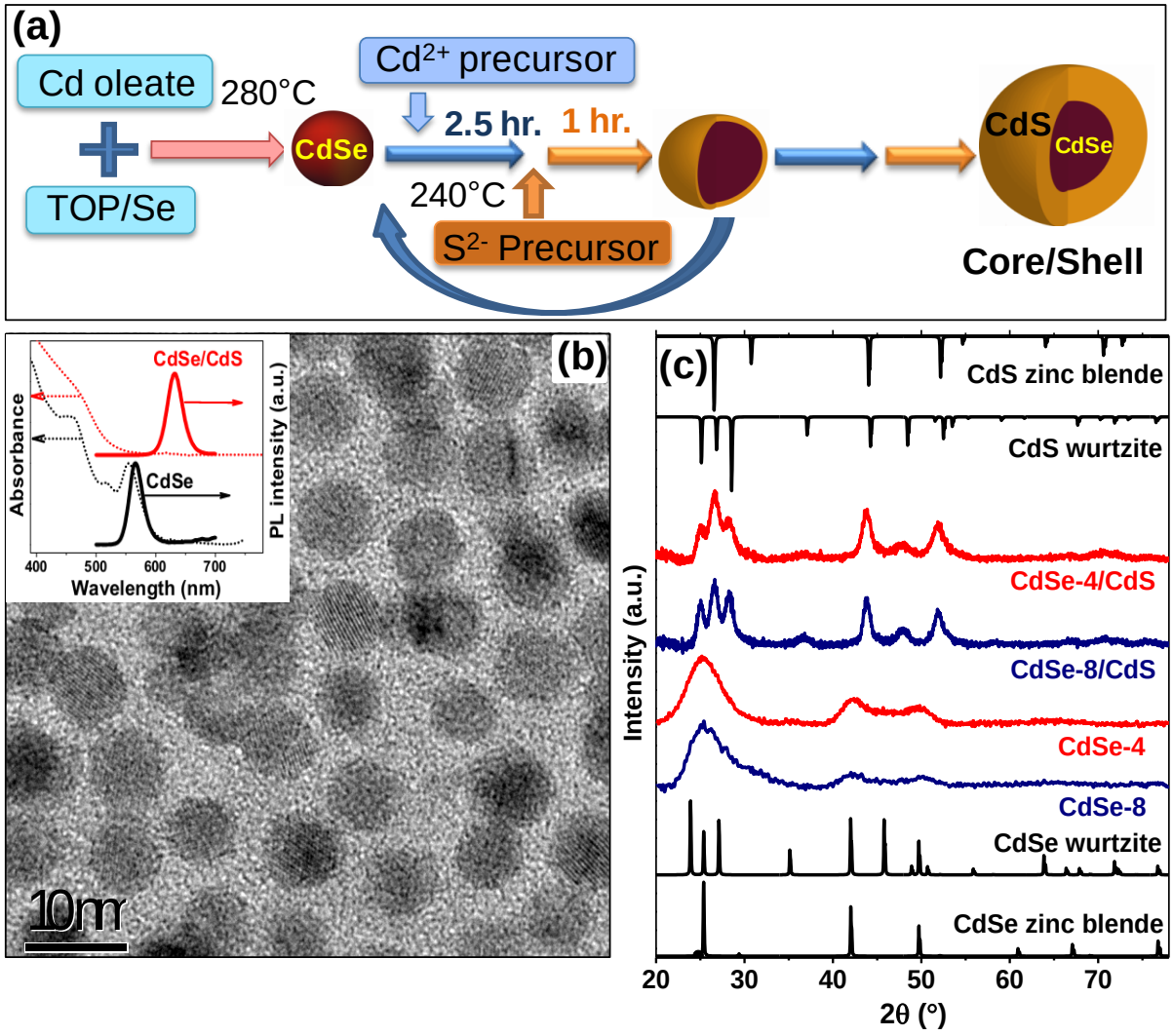

Figure 3.1: Synthesis and characterization of core-shell QDs: (a) Schematic showing the synthesis technique followed for obtaining high QY core/shell nanocrystals. (b) Typical TEM image of the core/shell nanocrystals showing the formation of spherical nanocrystals with a small size distribution. The inset shows the typical absorption and PL of the core and the core/shell nanocrystals. (c) Typical X-ray diffraction patterns obtained for the core and the core/shell nanocrystals for the case of defective surface (CdSe-4) and a smooth surface (CdSe-8) of the core along with the bulk CdS and CdSe.

Table 3.1 Influence of ligand concentration on average lifetime

Core	TOPO (mmol)	OlAm (mmol)	TOP (mmol)	Avg. Lifetime (ns)	QY (%)
CdSe-4	0.08	3	2.2	8.08	4
CdSe-6.5	0.10	4	2.2	24.2	6.5
CdSe-8	0.13	4.5	2.2	27	8
CdSe-14	0.13	3 (ODA)	2.5	28.1	14
CdSe-16	0.076	2.8 (ODA)	1.5 (TBP)	29	16

3.4.1 Optical Properties

The QY of the CdSe cores and the core/shell NQDs are characterized using steady state and time resolved PL studies. In recent literature[7] the relatively low QY in these thick shell NQDs has been attributed to the presence of high rate of non-radiative recombination through Auger process[30] and it is proposed that an effective means of reducing Auger recombination is to efficiently form an alloy layer at the interface to smoothen the potential. Here, in this study, we deliberately prepared 3 nm CdSe cores with differing extent of surface defects by modifying the concentration of surface ligands.[33] The extent of surface defects was characterized by time resolved fluorescence at the emission maxima as shown in Figure 3.2. The decrease in average lifetime is taken as a measure of increase in the non-radiative decay channels and hence an increase in the number of surface defects as shown for the case CdSe-4 to CdSe-16 in the Table 3.1. The lifetime decay plots for the case of less defective core (CdSe-8) and the core/shell structure obtained from this core (CdSe-8/CdS) is shown in Figure 3.3(a) while the corresponding steady state PL data is shown in the inset to the figure. From the Figure 3.3(a), it is evident that CdSe-8 nanocrystals show a nearly single exponential decay and the QY of these cores were found to be ~7-8 % while that in Figure 3.3(b) (CdSe-4) showed a large percentage of non-radiative decay channels as well as the <5% QY. This is not surprising since the CdSe-4 nanocrystals were made highly defective by purposely lowering the concentration of surface ligands. However, upon overcoating the material with a thick shell of CdS for both high and low surface defective CdSe (respectively shown in Figure 3.3(a) and 3.3(b)), the QY

increased to greater than 50% and unexpectedly > 90% respectively. Along with the earlier claims of interesting optical properties like high stability, reduced Auger recombination and suppressed blinking, to our knowledge, this is the first claim to near unity QY in thick shell CdSe based QDs although near unity QY has been obtained for thinner shell NQDs.[26] The advantages of thick shell QDs, as will be shown later in the report is clearly in being able to translate this efficiency into device.

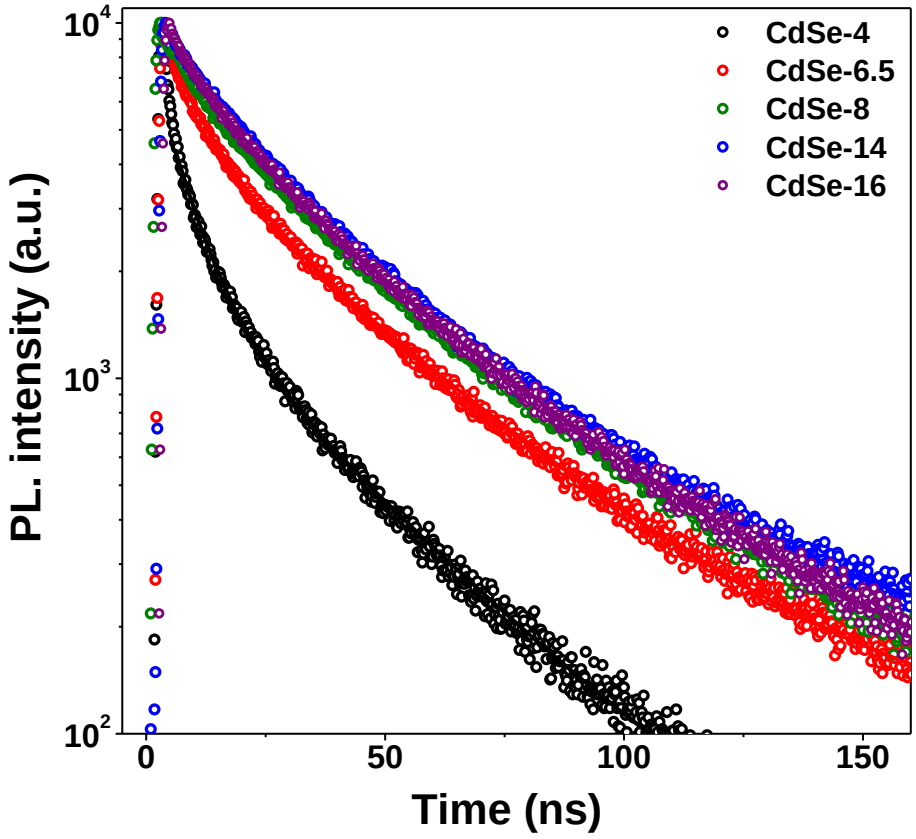

Figure 3.2: Lifetime decay of various core CdSe QDs prepared by changing ligand/ ligand concentrations**.** Solid lines show a bi-exponential fits to these data.

In order to verify the validity of the QY measurement, we excited the sample as well as known dye, Rhodamine-101 in ethanol (QY > 95%) with a 520 nm light and measure the QY using an integrating sphere. The results of this measurement are shown in the main panel of Figure 3.3(c) while the photograph of this emission is shown in the inset. From the figure, it is evident that not only the brightness of the NQDs is similar to that of the dye, but for a similar absorption, the area under the curve for the NQD and dye emission are identical thus verifying the QY of this sample.

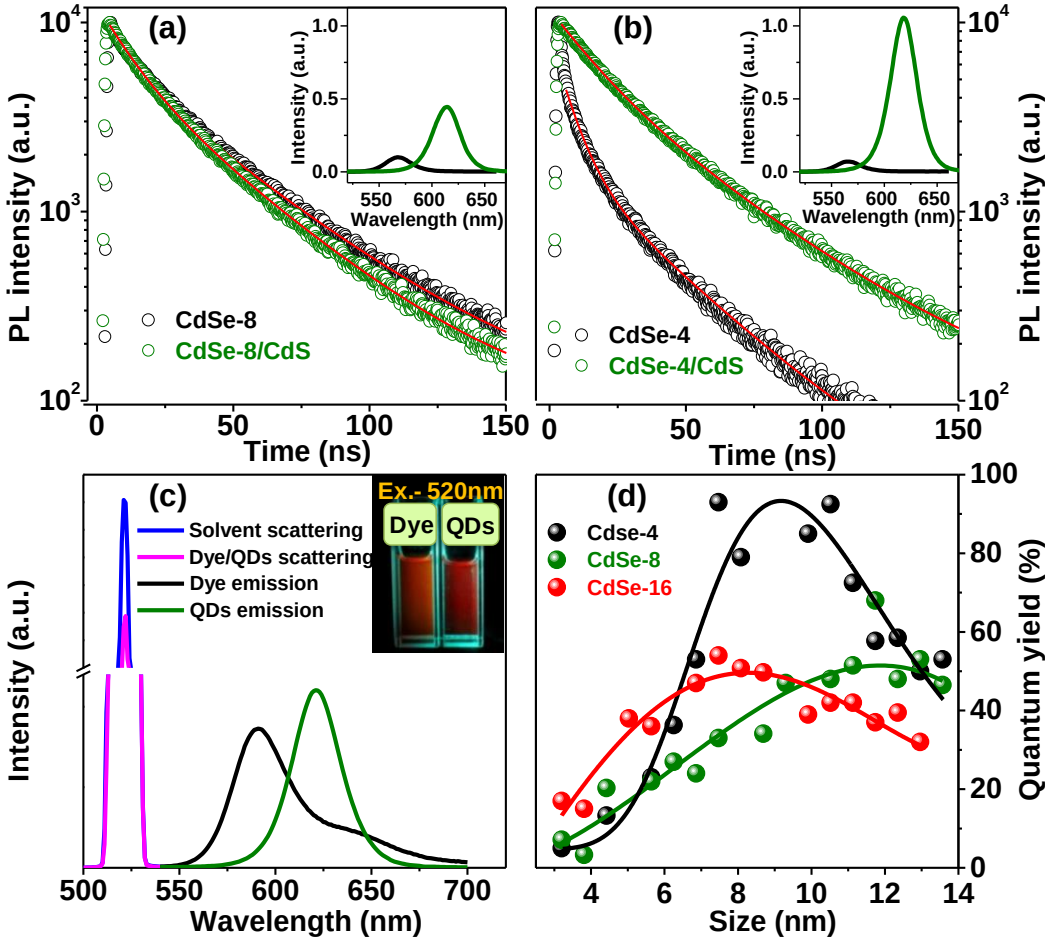

Figure 3.3: Engineering of core-shell interface and its effect on QY: The main panel shows the lifetime decay plots for CdSe-8 (a) and CdSe-4 (b) (black circles) and their corresponding core/shell structure (Green circles). Red lines show a bi-exponential fit to the corresponding data. The insets in both (a) and (b) shows the steady state PL plots of these samples in relative units of QY showing an increase in the QY of the core/shell structure on comparison with the core. (c) The absolute QY of the sample as well as the Rhodamine-101 dye obtained using integrating sphere measurements. The inset shows the photograph of the fluorescence of the dye as well as CdSe-4/CdS nanostructure obtained using excitation light of 520 nm showing similar brightness. (d) The variation of the QY as a function of shell thickness starting from three different cores with decreasing defects (CdSe-4 (Black), CdSe-8 (green), CdSe-16 (red) (Dots are experimental points and the curves are a guide to the eye).

The variation of QY as a function of shell thickness both for the surface defective (CdSe-4) and smooth core (CdSe-8) is shown in Figure 3.3(d) suggesting that the core with lower concentration of ligands produces more efficient core/shell structures. Consistent with this surprising trend, as is seen from the compiled results in Table 3.2, CdSe-16 that had a highest QY of 16% produced a rather low QY of 40% when overcoated with thick CdS shell material.

In addition, it is also interesting to note that the QY increases with the increasing thickness of the shell material followed by a decrease. This is not surprising given that PL QY is a complex interplay between various ligands. This is already evident in Figure 3.3(d) where the QY peaks at about 7.5 nm when the ligands tri-butylphosphine and octadecylamine were used, while this was shifted to much higher sizes upon the use of appropriate amounts trioctylphosphine, trioctylphosphine oxide and oleylamine. In fact, our own studies have shown that with different shell overcoating procedures we can only reach a maximum of 30% QY by varying the concentration of the ligands. This has been already studied in recent literature[25 27]and the optimal concentration of the ligands have been obtained. However the most counterintuitive observation that is so far not explained is the high QY of core/shell structure starting from low QY cores in spite of exactly similar overcoating procedures with identical ligands. In order to understand these unforeseen results we performed a study of microstructure to explore the interfacial defects and correlate their physical properties to these defects. Though low PL efficiency in presence of surface defects is well documented and it is well known that large lattice mismatch between the core and the shell material is instrumental for the absence of improvement in PL efficiency, the effect of a sharp interface in the presence of a rather low lattice mismatch of 3.9% on the PL efficiency has not been studied till now.

Table 3.2: Influence of different CdSe cores on its shell formation.

Core	Avg. lifetime of core (ns)	QY of the core (%)	Avg. lifetime of core/shell (ns)	QY of core/shell (10.6 nm) (%)
CdSe-4	8.08	4	30.2	94
CdSe-8	27	8	26	60
CdSe-16	29	16	25.1	40

3.4.2 Microstructure Study

While it is not possible to microscopically observe structural defects at the surface, the consequences of surface defects would be easily visible when overcoated with a thin CdS layer. When CdS is overcoated on a highly surface defective core, the random direction of the defects is reflected even after overcoating giving rise to internal defects radiating in random directions.

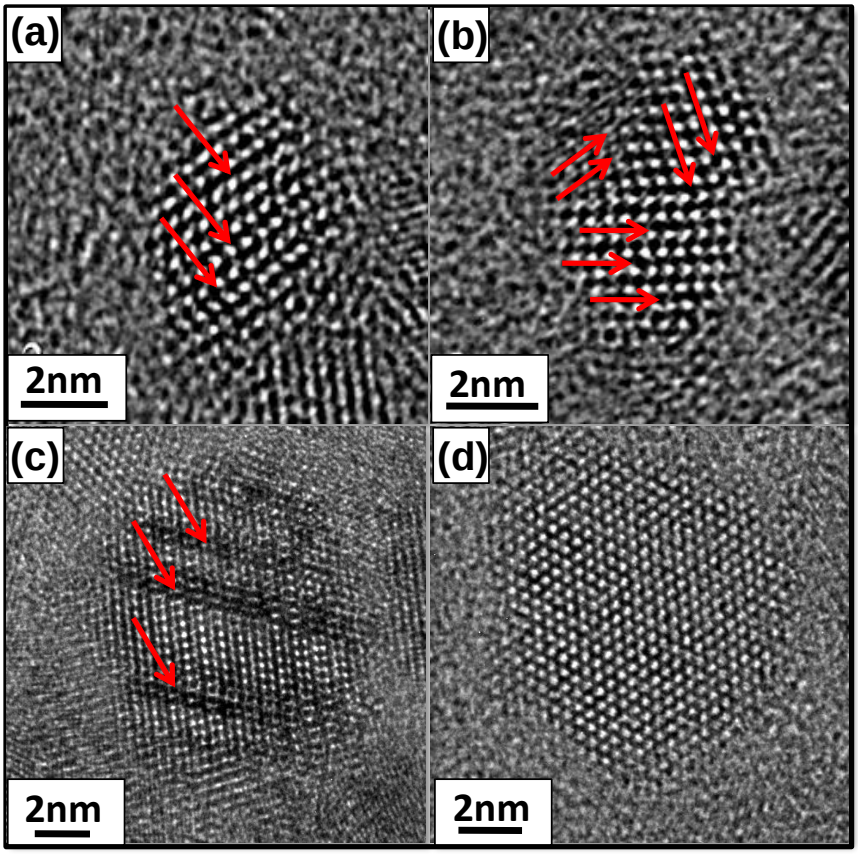

Figure 3.4: Study of defects: The high resolution TEM images of (a) CdSe-8/2ML CdS showing interface defects, (b) CdSe-4/ 2ML CdS showing defects in random directions, (c) CdSe-8/12ML CdS showing interface defects and (d) CdSe-4/12ML CdS showing a perfect defect free crystal. Defects are shown by red arrows.

However, when the surface is relatively smooth, we observe only a uni-directional defect at the interface of core and shell. The high resolution image of the two monolayers CdS overcoated material obtained from low surface defective core (CdSe-8) is observed to have a large percentage of nanostructures characterized by line defects along one single direction as shown by the red arrows in Figure 3.4(a). On the other hand the HRTEM image obtained after overcoating 2 monolayers of CdS on surface defective core (CdSe-4) shows defects radiating in random directions as shown by the red arrows in Figure 3.4(b). Not surprisingly, the line defects present in the case of CdSe-8 shown in Figure 3.4(a) were retained in spite of further overcoating with a thick shell of CdS followed by annealing as shown by the image in Figure 3.4(c). However, a similar procedure carried out for the case of CdSe-4 shown in Figure 3.4(b)

amazingly shows that most of the NQDs were found to be perfectly defect free as shown in Figure 3.4(d).

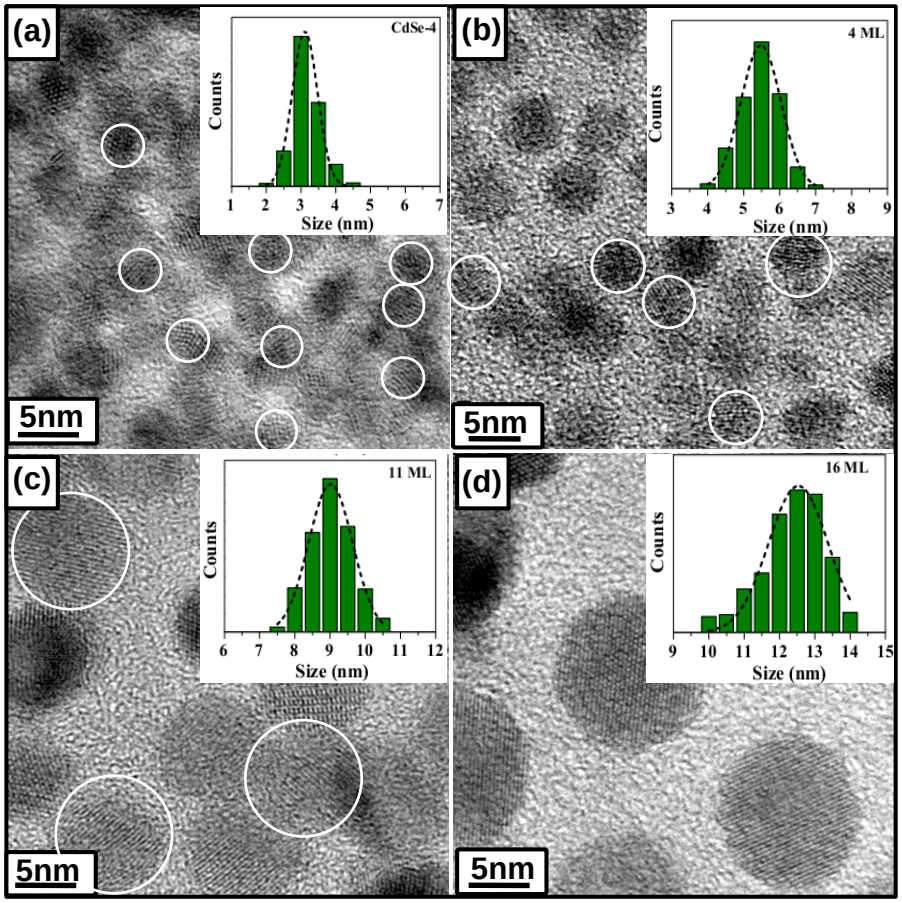

Figure 3.5: (a-d) High resolution TEM images showing the formation of defective and non-defective thick shell core/shell nanostructures. The insets show the size distribution histogram obtained by measuring the sizes of about 300-400 nanostructures. Circles show the defective particles.

In order to make sure that this is not just an anomaly but indeed the statistical trend, we performed a defect analysis on 350-400 particles. Moreover, an analysis of the HRTEM images as a function of shell thickness (shown in Figure 3.5 and Table 3.3) shows that the defects indeed are annealed out, paving way for the increase in QY as a function of shell thickness as well. Thus both the observations in Figure 3.3(d) can be explained by studying the microstructure. However, though microstructure is shown to dictate the PL QY in these materials, it is known that obtaining a defect-free crystal is a delicate balance between long annealing time at high temperature and optimal retention of the ligands on the surface at this high temperature.

Table 3.3: Results from the particles in Figure 3.5 showing the various sizes, size distribution, percentage of non-defective particles as well as the quantum yield.

Panel	**(a)**	**(b)**	**(c)**	**(d)**
monolayer	core	4	11	16
size (nm)	3	5.5	9.01	12.5
σ	0.36	0.56	0.62	0.62
non-defective particle (%)	49	63	79	85
QY (%)	4	24	86	51

From a fundamental perspective, though the results discussed above proves that the defect free NQDs gives near unity QY, the defective particles may either be completely "dark" or have a lower than unity QY. A direct correlation of defects with the QY of the sample with similar shell thicknesses but with different number of defective particles may be expected to provide more insight into this fundamental issue. Accordingly, we used the different CdSe 3 nm cores defined in Table 3.1 and overcoated them with CdS shell to obtain a total size of about 8.5 +/- 1 nm particles. The results of this study are summarized in various panels of Figure 3.6 and in Table 3.3. The panels of Figure 3.6(a)-(d) shows the typical HRTEM images of samples obtained from thick shell samples with differing defective particles (CdSe-14, CdSe-16, CdSe-8, CdSe-4 respectively). The size and size distribution obtained from the analysis of about 300-350 particles in every case is shown in the corresponding insets. The percentage of size distribution in all cases is found to be below 10% and mostly spherical particles. The percentage size distribution as well as the number of defective particles and the QY of the sample is tabulated in Table 3.3. Similar to the studies discussed earlier, the extent of surface defects, as quantified by the percentage of non-radiative decay was proportional to the number of defective particles. CdSe-14 was overcoated using slightly different overcoating procedure resulting in particles with defects along different directions as seen in the HRTEM image in Figure 3.6(a). This is indicative of low crystallinity of the nanostructure that is also reflected in the extremely low QY (~ 8%) of these samples. Nevertheless, more interestingly, from the Table 3.3, it appears that though the particles have almost same size of core and shell, with a small decrease in the percentage of defective particles, we observe a rather large change in the QY of the samples. While this information seems indicative of not completely dark defective particle, this cannot be assumed to be completely convincing. Statistically only

about 27% of defective particles are normally in the right orientation to observe these defects. With small changes like 25% to 20% defective particles as observed from our data here, due of the statistical error bar, it would be difficult to exactly estimate the number of defective structures and hence a direct quantitative correlation to QY is not possible. Thus from our analysis of the emission properties we show that the defects of different types form a major contribution to the quenching of QY, although it is known that QY is a convoluted response of various factors. The defect-free core/shell NQDs obtained from a surface defective core have been shown for the first time to have highly stable, near unity QY, in spite of their wurtzite crystal structure.

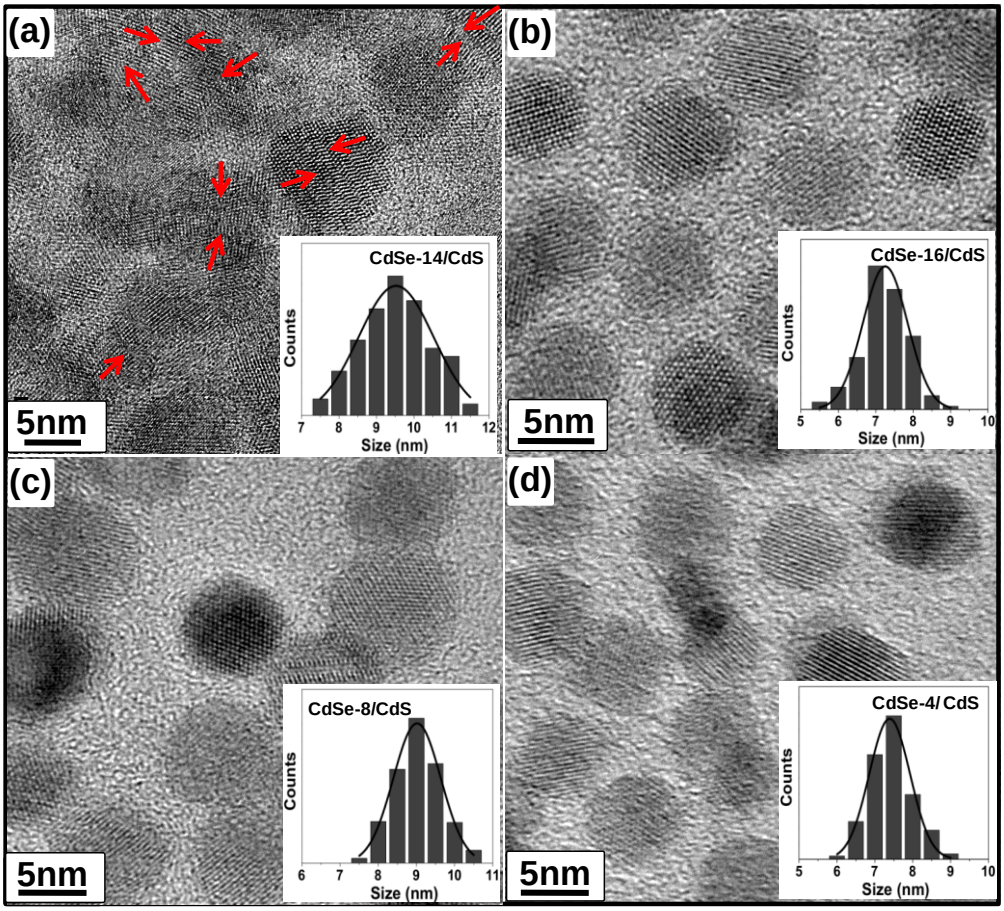

Figure 3.6: Nanostructure characterization using high resolution TEM: High resolution TEM images showing the formation of defective and non-defective thick shell core/shell nanostructures for (a) CdSe-14/CdS (b) CdSe16/CdS (c) CdSe-8/CdS and (d) CdSe-4/CdS. Red arrows in Figure 3.6 (a) point to the directions of the defects. The insets show the size distribution histogram obtained by measuring the sizes of about 300-400 nanostructures.

3.4.3 Application in LED

These high QY materials, combined with low Auger recombination rate that has already been shown in literature for these samples,[13] present substantial improvements over the commercially available nanocrystals. Since the discovery of high QY, narrow band emission of NQDs, these materials have been explored for the possibility of use as active layer in LEDs. However, nanocrystal charging under LED operation renders NQDs optically inactive consequently reducing the efficiency of these devices. Recently, it has been shown that these thick shell NQDs, even with only 10-20% QY are quite efficient in LEDs.[22] Our materials retain all the previously observed advantages along with near unity QY. Specifically, the stability of the PL quantum efficiency under intense UV radiation light is shown in Figure 3.7.

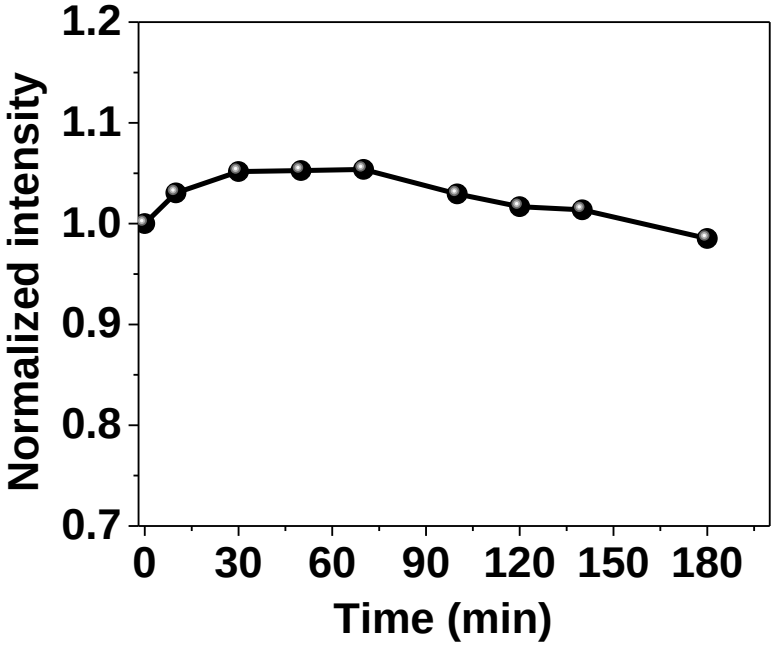

Figure 3.7: The stability of the PL quantum efficiency under intense UV radiation light. Dots show the experimental points and the curve indicates guide to the eye.

Table 3.4: The various sizes, size distribution, percentage of non-defective particles as well as the QY for the particles found panel (a) - (d) in Figure 3.6.

Panel	**(a)**	**(b)**	**(c)**	**(d)**
core	CdSe-14	CdSe-16	CdSe-8	CdSe-4
core/shell size (nm)	9.5	7.5	9	8
Size distribution (%)	10.5	8.1	7	7.4
non-defective particles	58.5	75	79	86
QY (%)	8	40	60	94

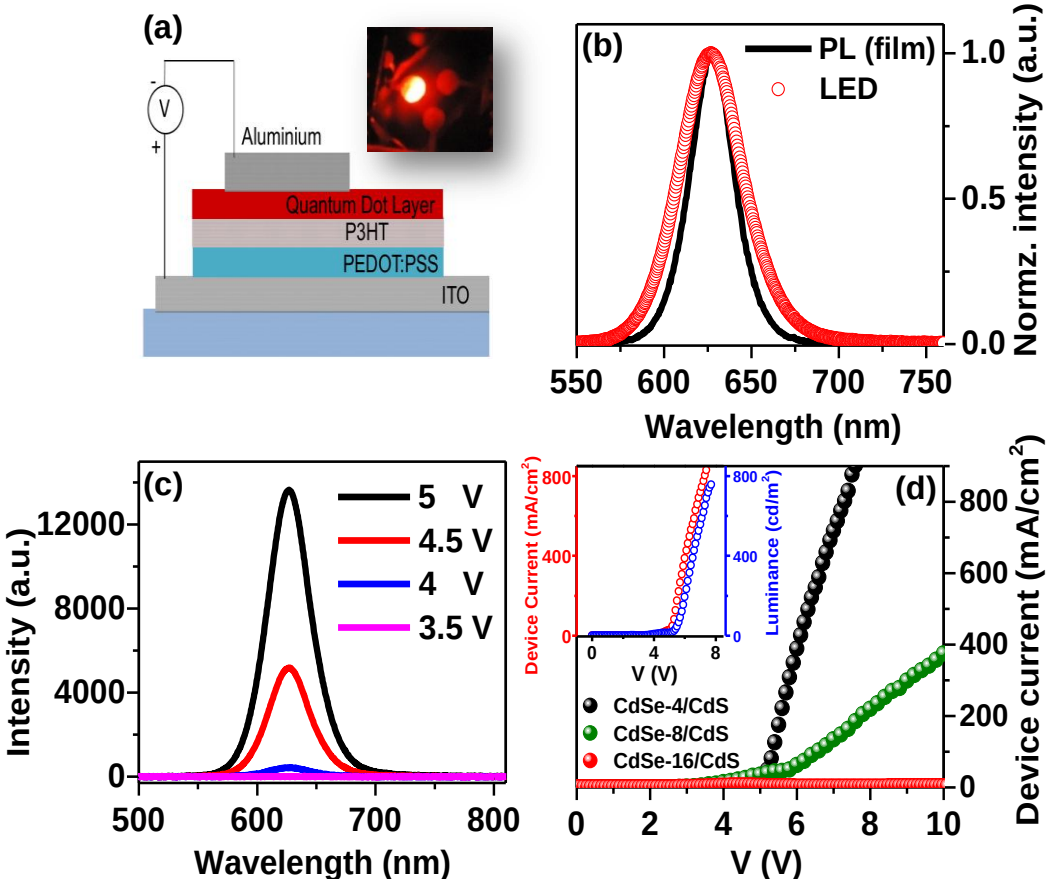

Figure 3.8: LED characterization: (a) The schematic of the device architecture. The inset shows the photograph of the LED under operation, (b) Spectral profile of the LED device and comparison with the PL of the QD film on glass, (c) LED emission spectrum with various driving voltages and (d) J-V characteristics of devices obtained from 40% (CdSe-16) and 60% (CdSe-8) QY materials in comparison with that of near unity QY (CdSe-4) materials. Maximum luminance output from 60% sample was ~20 Cd/m^2 and the luminance from 40% sample was very low. The inset shows typical J-V characteristics for the 94% QY sample (CdSe-4/CdS) and emission intensity as a function of the bias for the ITO|PEDOT:PSS|P3HT|QD|Al device.

Hence in order to translate the QY into device efficiency, we fabricated simple architecture proof-of-concept LED devices using these NQDs with different QYs (shown in Figure 3.8) as the active layer. The device architecture used in these devices is shown in Figure 3.8(a). The P3HT layer, introduced as a hole transport layer[34] (as shown from band offsets in Figure 3.9), assisted in the decrease of the threshold voltage from > 8 V to ~3 V with no change in spectral characteristics but substantial increase in the emission magnitude and stability.

Emission from a typical device is shown in the inset to Figure 3.8(a). The emission band obtained from electroluminescence (EL) was identical to that obtained from PL and was centred at 628 nm with a full width at half maximum (FWHM) < 45 nm (Figure 3.8(b)). This equivalence of PL and EL emission indicates common excitonic origin with the NQD layer as the source of emission. All the devices tested in this device configuration exhibited light emission and the emission flux showed linear dependence with current density (Figure 3.8(c)). The current density *vs.* voltage (J(V)) characteristics of these NQD based active layer devices are shown in the inset to Figure 3.8(d) and exhibited typical diode characteristics. It was possible to drive some devices to 9 V with injection current density of 0.3 A/cm^2 to result in emission exceeding 7,000 Cd/m^2. Similar devices made out of lower QY materials of identical composition were highly unstable and inefficient as shown in the main panel of Figure 3.8(d). These trends in our observations points out that the improvement in PL yields are translatable to the LED attributes. It should be pointed out that a very simple device obtained using these near unity QDs shown in this work with no state of the art, trial and error processes have shown high efficiency in every device that is tried in our laboratory so far. That is a remarkable achievement of the field of nanocrystal or other organic devices and cannot be achieved with a thin coating of CdS shell[26] though the QY can be close to unity. Further optimization of the device with a choice of different thickness of the active layers, hole injecting layers and cathodes would be expected to yield improved device characteristics.

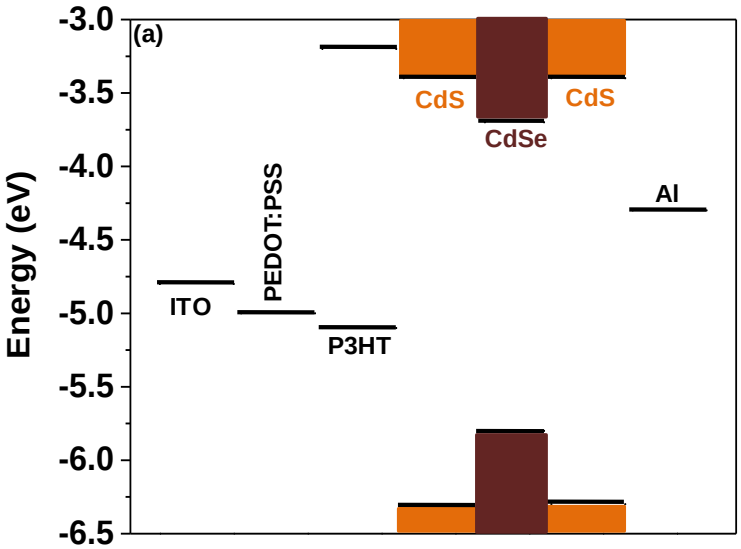

Figure 3.8: Band offsets of materials[35] used for LED discussed in the main text. The band offset for the CdS and CdSe nanoparticles were obtained from recent literature[36] for the sizes observed here.

3.5 Conclusion

We have shown for the first time that the QY of the NQDs is highly sensitive to crystal structure defects within the NQDs and that near unity QY can be obtained by synthesizing defect free nanostructures. This also establishes the relationship between the quality of the microstructure and electronic properties of the NQDs. We have also shown that these defect free core/shell structures with a smooth alloy interface can be obtained quite counter-intuitively, using cores that are highly surface defective. From a fundamental perspective, we have studied the role of defective particles in emission and find that the defect density and direction determine the efficiency of emission. These high QY NQDs have been used as an active layer in fabricating a proof of concept LED device that is shown to be quite efficient, in fact, comparable with the organic-nanocrystal hybrid device efficiencies.

Bibliography

(1) Hoy, J.; Morrison, P. J.; Steinberg, L. K.; Buhro, W. E.; Loomis, R. A. *J. Phys. Chem. Lett.* **2013**, *4*, 2053.

(2) Frederick, M. T.; Amin, V. A.; Weiss, E. A. *J. Phys. Chem. Lett.* **2013**, *4*, 634.

(3) Klimov, V. I.; Ivanov, S. A.; Nanda, J.; Achermann, M.; Bezel, I.; McGuire, J. A.; Piryatinski, A. *Nature* **2007**, *447*, 441.

(4) Aldeek, F.; Balan, L.; Medjahdi, G.; Roques-Carmes, T.; Malval, J.-P.; Mustin, C.; Ghanbaja, J.; Schneider, R. *J. Phys. Chem. C* **2009**, *113*, 19458.

(5) Peng, X.; Schlamp, M. C.; Kadavanich, A. V.; Alivisatos, A. P. *J. Am. Chem. Soc.* **1997**, *119*, 7019.

(6) She, C.; Demortiere, A.; Shevchenko, E. V.; Pelton, M. *J. Phys. Chem. Lett.* **2011**, *2*, 1469.

(7) Gomez-Campos, F. M.; Califano, M. *Nano Lett.* **2012**, *12*, 4508.

(8) Eijt, S. W. H.; van Veen, A. T.; Schut, H.; Mijnarends, P. E.; Denison, A. B.; Barbiellini, B.; Bansil, A. *Nat. Mater.* **2005**, *5*, 23.

(9) Hoy, J.; Morrison, P. J.; Steinberg, L. K.; Buhro, W. E.; Loomis, R. A. *J. Phys.Chem. Lett.* **2013**, *4*, 2053.

(10) Becerra, L. R.; Murray, C. B.; Griffin, R. G.; Bawendi, M. G. *J. Chem. Phys.* **1994**, *100*, 3297.

(11) McBride, J.; Treadway, J.; Feldman, L. C.; Pennycook, S. J.; Rosenthal, S. J. *Nano Lett.* **2006**, *6*, 1496.

(12) Chen, Y.; Vela, J.; Htoon, H.; Casson, J.; Werder, D.; Bussian, D.; Klimov, V.; Hollingsworth, J. *J. Am. Chem. Soc.* **2008**, *130*, 5026.

(13) García-Santamaría, F.; Brovelli, S.; Viswanatha, R.; Hollingsworth, J. A.; Htoon, H.; Crooker, S. A.; Klimov, V. I. *Nano Lett.* **2011**, *11*, 687.

(14) Brovelli, S.; Schaller, R. D.; Crooker, S. A.; Garcia-Santamaria, F.; Chen, Y.; Viswanatha, R.; Hollingsworth, J. A.; Htoon, H.; Klimov, V. I. *Nat. Commun.* **2011**, *2*, 280.

(15) Mahler, B.; Spinicelli, P.; Buil, S.; Quelin, X.; Hermier, J. P.; Dubertret, B. *Nat. Mater.* **2008**, *7*, 659.

(16) Spinicelli, P.; Buil, S.; Quelin, X.; Mahler, B.; Dubertret, B.; Hermier, J. P. *Phys. Rev. Lett.* **2009**, *102*, 136801.

(17) Garcia-Santamaria, F.; Chen, Y.; Vela, J.; Schaller, R. D.; Hollingsworth, J. A.; Klimov, V. I. *Nano Lett.* **2009**, *9*, 3482.

(18) Fu, Y.; Zhou, Y. H.; Su, H.; Boey, F. Y. C.; Agren, H. *J. Phys. Chem. C* **2010**, *114*, 3743.

(19) Nirmal, M.; Dabbousi, B. O.; Bawendi, M. G.; Macklin, J. J.; Trautman, J. K.; Harris, T. D.; Brus, L. E. *Nature* **1996**, *383*, 802.

(20) Park, Y. S.; Malko, A. V.; Vela, J.; Chen, Y.; Ghosh, Y.; Garcia-Santamaria, F.; Hollingsworth, J. A.; Klimov, V. I.; Htoon, H. *Phys. Rev. Lett.* **2011**, *106*, 187401.

(21) Krauss, T. D.; Peterson, J. J. *J. Phys. Chem. Lett.* **2010**, *1*, 1377.

(22) Pal, B. N.; Ghosh, Y.; Brovelli, S.; Laocharoensuk, R.; Klimov, V. I.; Hollingsworth, J. A.; Htoon, H. *Nano Lett.* **2012**, *12*, 331.

(23) Kundu, J.; Ghosh, Y.; Dennis, A. M.; Htoon, H.; Hollingsworth, J. A. *Nano Lett.* **2012**, *12*, 3031.

(24) Lin, C. C.; Liu, R.-S. *J. Phys. Chem. Lett.* **2011**, *2*, 1268.

(25) Ghosh, Y.; Mangum, B. D.; Casson, J. L.; Williams, D. J.; Htoon, H.; Hollingsworth, J. A. *J. Am. Chem. Soc.* **2012**, *134*, 9634.

(26) Chen, O.; Zhao, J.; Chauhan, V. P.; Cui, J.; Wong, C.; Harris, D. K.; Wei, H.; Han, H.-S.; Fukumura, D.; Jain, R. K.; Bawendi, M. G. *Nat. Mater.* **2013**, *12*, 445.

(27) Nan, W.; Niu, Y.; Qin, H.; Cui, F.; Yang, Y.; Lai, R.; Lin, W.; Peng, X. *J. Am. Chem. Soc.* **2012**, *134*, 19685.

(28) Cragg, G. E.; Efros, A. L. *Nano Lett.* **2009**, *10*, 313.

(29) Wang, X.; Ren, X.; Kahen, K.; Hahn, M. A.; Rajeswaran, M.; Maccagnano-Zacher, S.; Silcox, J.; Cragg, G. E.; Efros, A. L.; Krauss, T. D. *Nature* **2009**, *459*, 686.

(30) Efros, A. L. *Nat. Mater.* **2008**, *7*, 612.

(31) Cho, K. S.; Lee, E. K.; Joo, W. J.; Jang, E.; Kim, T. H.; Lee, S. J.; Kwon, S. J.; Han, J. Y.; Kim, B. K.; Choi, B. L. *Nat. Photonics* **2009**, *3*, 341.

(32) Kim, T. H.; Cho, K. S.; Lee, E. K.; Lee, S. J.; Chae, J.; Kim, J. W.; Kwon, J. Y.; Amaratunga, G.; Lee, S. Y.; Choi, B. L. *Nat. Photonics* **2011**, *5*, 176.

(33) Ning, Z.; Molnar, M.; Chen, Y.; Friberg, P.; Gan, L.; Agren, H.; Fu, Y. *Phys. Chem. Chem. Phys.* **2011**, *13*, 5848.

(34) Zhao, J.; Bardecker, J. A.; Munro, A. M.; Liu, M. S.; Niu, Y.; Ding, I. K.; Luo, J.; Chen, B.; Jen, A. K. Y.; Ginger, D. S. *Nano Lett.* **2006**, *6*, 463.

(35) Kim, J. Y.; Lee, K.; Coates, N. E.; Moses, D.; Nguyen, T.-Q.; Dante, M.; Heeger, A. J. *Science* **2007**, *317*, 222.

(36) Grandhi, G. K.; Tomar, R.; Viswanatha, R. *ACS Nano* **2012**, *6*, 9751.

Chapter 4

Interface Modeling: Photoabsorption vs. Photoemission

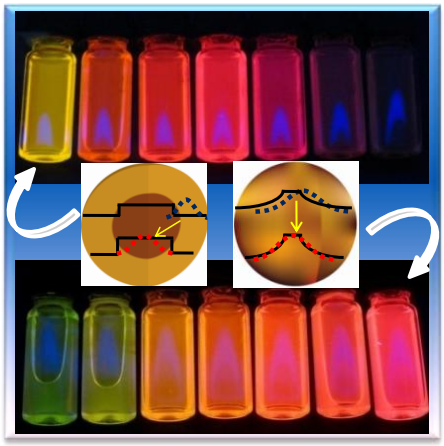

The following papers have been published based on the work presented here.

- J. Mater. Chem. C, 2014, 2, 3868.

4.1 Summary

The potential of nanomaterials arises from the fine tuning of material properties by changing composition, size and shape. Internal structure of semiconductor heterostructures has so far been only lightly explored. Herein, we show that by varying the local Cd and Te/S environment using CdTe/CdS as the host, a highly promising photovoltaic material can easily be converted to an efficient photo-emitting material. Thus we demonstrate for the first time that internal structure is extremely important in determining the properties of the semiconductor nanocrystals and can be used to tune the properties of the nanomaterial leading to competing and contrasting applications.

4.2 Introduction

The Nanocrystal quantum dots (NQDs), with an emphasis to develop novel colloidal nanomaterials for energy harvesting[1,2] and conversion applications[3], has been the subject of current research. Size, shape and composition[4] dependence of the chemical and physical properties of NQDs[5] have shown potential as promising materials for a diverse set of applications including as active materials in photovoltaics[6,7] and as size tunable phosphors[8,9] in lighting and displays.[10-13] This has propelled efforts toward controlled synthesis and in-depth characterization with programmable composition and geometric features. However, until recently, the effect of internal crystal structure of NQDs on the properties of the material is not systematically studied. In recent times, with the introduction of ultra-high resolution TEM[14] as well as X-ray photoemission,[15] the dramatic effect of lattice defects on the photo-physical properties like quantum yield, blinking *etc.* have come to light. Here in this chapter, we show that lattice defect engineering provides a playground to regulate the electron hole overlap[16] particularly in type II semiconductor interfaces[17] leading to efficient photo-absorber as well as a photo-emitter obtained from the same material. This is interesting given that photovoltaics[18] ultimately aim to absorb light, and convert the photogenerated excitons into spatially separate electrons and holes. On the other hand, the quality of the photoemitter[11,12,19] is regulated by the efficiency of the recombination of the electron-hole pair leading to the emission of the absorbed energy. This naturally implies that photo-absorptive materials are in general not efficient as active materials for a photo-emitting device and vice versa.

CdTe, with high optical absorption coefficient and optimum bandgap for solar photovoltaics,[20] is suitable for photovoltaic applications. A perfect match of electron affinity of CdS[21] in addition to the type II bandgap at the heterojunction of the CdTe and CdS have led to the widespread use of CdTe/CdS as active materials for photovoltaic devices[22] with cell efficiencies as high as 16%.[23] However, it is so far, not extensively used as a photo-emissive material for the well known reason of low quantum yield. Nevertheless, in this chapter, we observe that CdTe core NQDs synthesis dictates the photophysical properties giving rise to both photo-emitting high quantum yield (QY) materials as well as low QY, long lifetime materials suitable for photovoltaic applications. We use XRD and XAFS spectroscopy to study the long range and short range structure respectively explaining the photoluminescence properties of QY and excited state lifetime obtained from time resolved photoluminescence (TrPL).

4.3 Experimental Details

4.3.1 Synthesis

The synthesis of CdTe cores (CdTe-A and CdTe-C) were carried out using two different synthesis methods described below. Further overcoating of these core NQDs with CdS was carried out using SILAR technique[24] with alternate addition of Cd and S precursors followed by annealing at high temperature.

Synthesis of CdTe core QDs for CdTe-C: CdTe-C NQDs were synthesized after minor modification of literature method.[25] Briefly, 0.4 M TOP/Te solution was prepared by dissolving Te shots in TOP inside a glove box. In a typical synthesis method, 0.2 mmol (25.6 mg) of CdO, 0.2 ml of oleic acid, 8 ml of ODE were taken in a three necked round bottom flask. The temperature was maintained at 80°C for degassing under vigorous stirring. After degassing, temperature of the reaction mixture was raised to 310°C under constant Ar flow. After 30-40 min, as soon as a gray coloured precipitate appeared, the temperature was brought down to 290°C and a solution containing 0.13 ml of TOP/Te diluted with 1ml of TOP and 1.12 ml of ODE was quickly injected into the hot mixture. After a few seconds, the temperature was quickly quenched down to room temperature using ice bath. Samples were washed twice by centrifugation using hexane and methanol mixture.

Synthesis of CdTe core QDs for CdTe-A: In a typical synthesis, 20 mg (0.075 mmol) Cadmium acetate dihydrate, 0.3 ml of oleic acid, 0.4 g of TOPO and 5ml of ODE were taken in a three necked flask and degassed at 80°C under constant stirring. 3 ml TOP was added into this reaction mixture during this procedure. Te precursor was prepared using 0.1 ml of 0.4 M TOP/Te solution mixed with 0.9 ml of TOP and 1ml of ODE. After degassing, the temperature was raised to 320°C under steady Ar flow. At 320°C the TOP/Te was injected to the hot reaction mixture and the temperature was quenched down to room temperature using ice bath after a few seconds. Similar to the previous CdTe core, samples were washed and preserved for further use.

Overcoating of CdS shell on CdTe (CdTe-C/shell and CdTe-A/shell): SILAR technique[24] was followed to synthesize these core/shell NQDs. Firstly, 0.2 M cadmium oleate ($Cd(OA)_2$) and 0.2 M sulphur precursor were prepared using well known literature methods. The stoichiometric amount of Cd and S precursor required for each individual layer was calculated and added in a stepwise addition. In a typical experiment, CdTe cores (1×10^{-7} mol), 3 ml of OlAm and 4 ml of ODE were taken into a round bottom flask and degassed under vacuum with the temperature gradually increased to 70°C. After degassing the reaction flask was backfilled with Ar and the temperature was raised to 170°C and required amount of $Cd(OA)_2$ for the first shell was injected into the reaction mixture. After 10/15 min, the temperature was further raised to 220°C and same amount of S precursor was injected into the reaction. After 5/10 min, cycles of Cd followed by S precursors were injected and annealed at this temperature for all subsequent shell formation. The annealing conditions were very similar for both CdTe-A and CdTe-C NQDs except small changes in annealing time that was done to further exemplify the results. In both the cases, aliquots were taken out after completion of each monolayer addition. All the samples were washed by centrifugation using hexane methanol mixture and redissolved in hexane.

4.3.2 XAFS Experimental Setup

Local structure of all the samples was determined using XAFS. The Cd K-edge (26711 eV) and Te K-edge (31814 eV) XAFS measurements were carried out at the MRCAT 10-ID beam line at the Advanced Photon Source, Argonne National Laboratory.[26] The data was collected in

fluorescence Stern-Heald geometry with samples loaded in cylindrical cuvettes. Cd foil and Te powder tapes were measured in transmission geometry with help of the reference ion chamber for every scan taken at Cd edge and Te edge respectively. The spot size of the incident x-ray beam on the sample was 500 micron by 500 micron. Platinum mirror was used for harmonic rejection. Incident ion chamber had full nitrogen gas; transmission and reference ion chambers were filled with 80% Argon mixed with 20% nitrogen. Fluorescence ion chamber had Krypton gas. Data collected was processed using Athena software[27] by extracting the EXAFS oscillations $\chi(k)$ as a function of photoelectron wave number k. The theoretical paths were generated using FEFF6[28] and the models were done in the conventional way using the fitting program called Artemis.[29] Fitting parameters were obtained by modeling the EXAFS data of each sample in R-space until a satisfactory fit describing the system was obtained. Data sets were simultaneously fitted in R-space with k-weights of 1, 2 and 3.

4.4 Results and Discussion

4.4.1 Microstructure Study

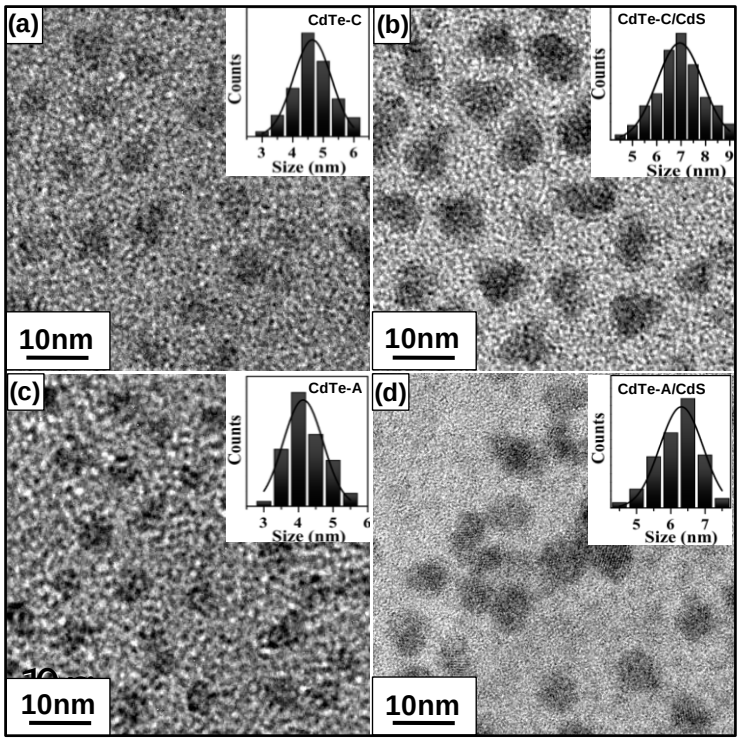

Figure 4.1. TEM images of (a) 4.5 nm CdTe-C and (b) 6.8 nm CdTe-C/CdS (c) 4.1 nm CdTe-A (d) 6.4 nm CdTe-A/CdS NQDs and their size distributions are shown in the corresponding insets showing the formation of spherical NQDs of specified sizes.

TEM images of the cores and the CdS overcoated materials along with their size distribution analysis are shown in Figure 4.1. From the figure it is evident that both the sizes of the two cores (4.1 nm and 4.5 nm) and the overcoated materials (6.4 nm and 6.8 nm) are very similar. In order to obtain the actual concentration of Te to S ratio, we performed ICP-OES measurements and found that the Te/S ratios in the two materials are very similar.

4.4.2 Optical Properties

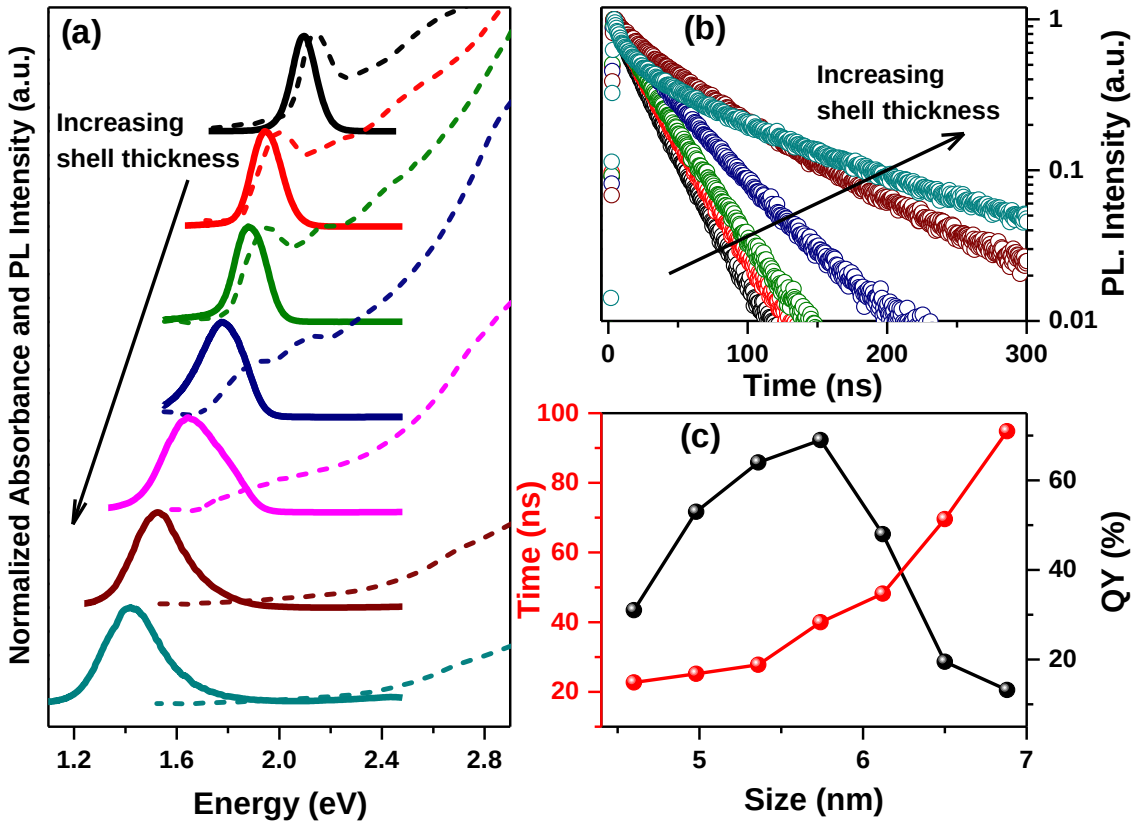

Figure 4.2: (a) Absorption (dotted line) and PL (solid lines) of CdTe-C core and CdTe-C/CdS nanocrystals with increasing CdS shell. (b) Lifetime decay plots for core CdTe-C and CdTe-C/CdS nanocrystals. (c) The variation of QY (black) and average lifetime (red) as a function of size starting from core CdTe-C to CdTe-C/CdS nanocrystals. (Dots show experimental points and lines show guide to the eye).

However, in spite of similar particle size, the absorption and photoluminescence characteristics of the two materials were unexpectedly found to be dramatically different. Figure 4.2(a) shows the evolution of absorption (dotted line) and emission spectra (solid line) of the NQDs during the growth of the CdS shell on CdTe-C cores emitting at 2.09 eV with a sharp absorption peak at 2.15 eV. As expected, CdS shell leads to broadening eventually smearing out of the

absorption feature completely along with a shift of emission peak to lower energies. The smearing is also accompanied by a significant increase in the Stoke's shift between the absorption feature and the emission energy. This observation of lower energy transitions due to weak spatially indirect transitions is consistent with the formation of a type-II structure as expected from the alignment of the energy states. Further signatures of type II semiconductors is observed in the TrPL data shown in Figure 4.2(b) as well as the evolution of QY as a function of shell formation as shown in Figure 4.2(c). The electron-hole recombination lifetime increases with increasing shell thickness as shown in Figure 4.2(b) and the average lifetime (red) plotted in Figure 4.2(c). Though the QY initially increases due to the surface protection of CdTe, it eventually decreases due to the "spatially indirect" nature of the electron-hole pair leading to lower efficiency of radiative recombination. From this it is evident that this CdTe/CdS indeed forms a type-II interface.

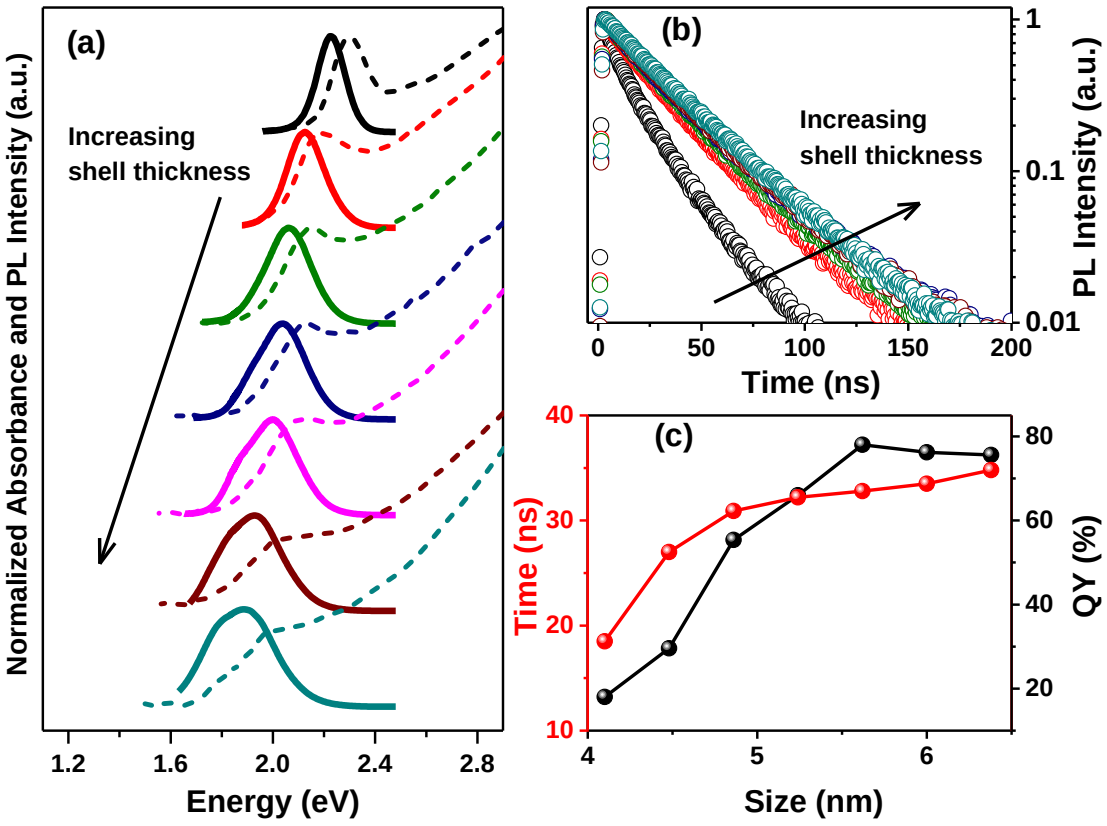

Figure 4.3: (a) Absorption (dotted lines) and PL (solid lines) of CdTe-A core and CdTe-A/CdS nanocrystals with increasing CdS. (b) Lifetime decay plots for core CdTe-A and CdTe-A/CdS nanocrystals. (c) The variation of QY (black) and average lifetime (red) as a function of size starting from core CdTe-A to CdTe-A/CdS nanocrystals. (Dots show experimental points and lines show guide to the eye)

In contrast, the optical characterization obtained from CdTe-A samples show unexpectedly different behaviour as shown in Figure 4.3. Figure 4.3(a) shows the evolution of absorption (dotted line) and emission spectra (solid line) of the NQDs during the growth of the CdS shell on CdTe-A cores. However it is obvious that the absorption edge is much sharper in CdTe-A/CdS samples compared to the CdTe-C/CdS samples, as shown by a typical example in Figure 4.4. Nevertheless, it is interesting to note that the Stokes shift in the case of CdTe-A/CdS is not as high as expected for type II systems and is contributed from both, a minute red shift of the absorption edge and a tiny blue shift of emission peak as observed in Figure 4.3(a). In addition the difference in the emission energy of 1.8 eV in 6.4 nm CdTe-A/CdS (Figure 4.3(a)) compared to 1.4 eV in 6.8 nm CdTe-C/CdS (Figure 4.2(a)) cannot be explained either by experimental error or as a consequence of small changes in the size of the nanocrystals (~0.4 nm). In fact, the small Stokes shift is suggestive of a direct transition instead of the expected indirect transition. More interestingly, the lifetime and quantum yield of these materials show drastic changes as seen in Figures 4.2(b), 4.2(c), 4.3(b) and 4.3(c). From the Figure 4.3(b) and 3c, it is apparent that the lifetime of the excitonic recombination of CdTe-A/CdS does not increase with increasing shell thickness and retains a high QY of ~ 80% in the thickest shell sample consistent with the absorption and the emission data. These changes in the absorption and emission energy as well as lifetime and QY measurements provide clear signatures of spatially direct recombination of the charge carriers within the heterostructure in an established type-II band structure alignment.[30]

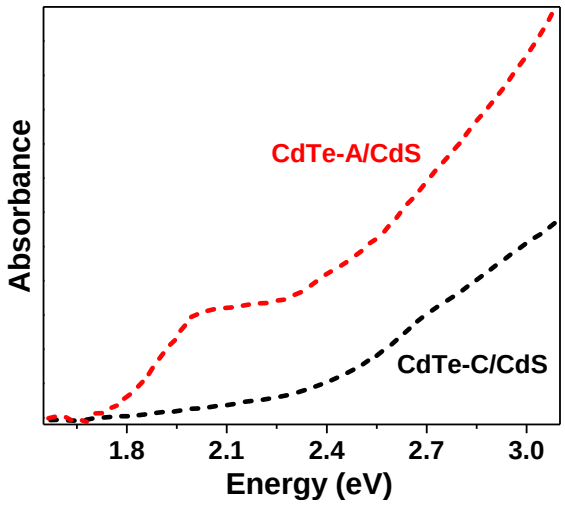

Figure 4.4. Absorption features of similar size CdTe-C/CdS (black line) and CdTe-A/CdS (red line) nanoparticles.

4.4.3 Electronic Structure

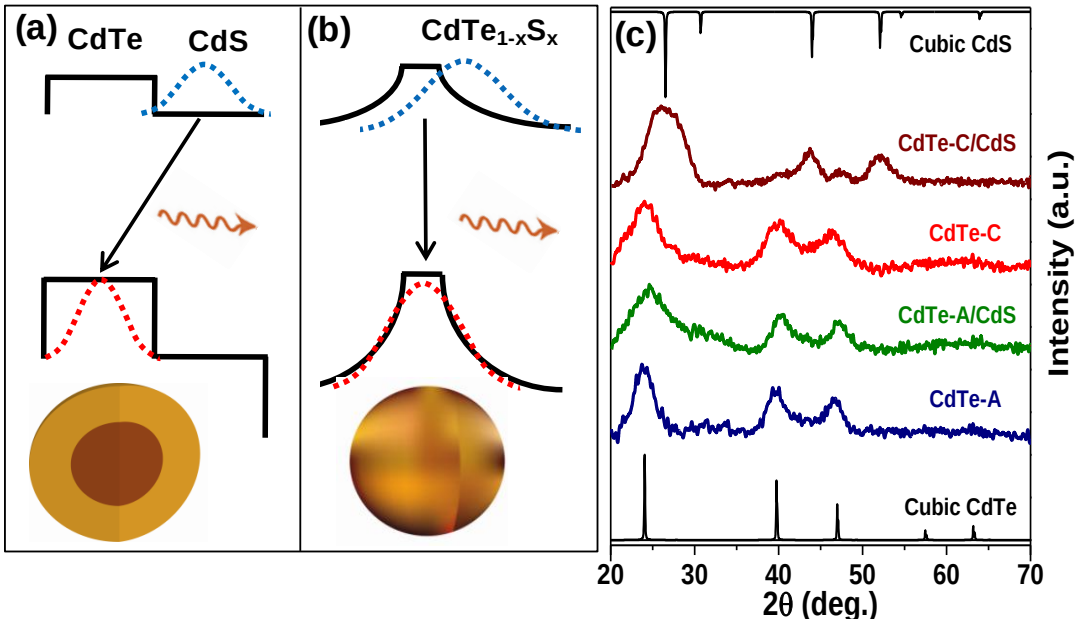

Figure 4.5. Schematics of CdTe/CdS (a) core/shell structure with spatially non-overlapping and (b) alloy interface with spatially overlapping electron (blue) and hole (red) wavefunction and their relative bandgap alignment[31] for the bulk CdTe/CdS. (c) XRD patterns of the different CdTe cores, CdTe-A/CdS and CdTe-C/CdS nanocrystals along with the bulk cubic CdTe and CdS.

These qualitative differences in the nature of the optical properties based on quantitative changes in the synthesis parameters is remarkable and could have far-reaching consequences in applications if the origin of this anomalous effect can be understood from a fundamental perspective. The recent study of the internal structures of NQDs,[14] so far only lightly explored, have shown the potential of such a study to understand these unusual photo-physical properties. In the present case, our study of the properties of the core with an average lifetime of 22.6 ns and a QY of 30.5% in CdTe-C and 18.5 ns and 18% respectively for CdTe-A suggests that CdTe-C has a lower percentage of non-radiative decay pathways and higher QY compared to CdTe-A suggesting the presence of more surface defects in CdTe-A cores. In fact, detailed analysis of the synthesis procedure suggests that in the case of CdTe-C, the cores were synthesized by heating at 310°C for 30-45 minutes until a cloudy gray precipitate of Cd^0 nanoparticles forms which reacts with TOP/Te and forms high quality QDs. This formation of Cd^0 nanoparticles in a thermodynamically slow process ensures that the surface is properly formed and well passivated upon injection of Te complex. However, in case of CdTe-A cores,

Te complex is injected as soon as the temperature of the Cd precursor reaches 320°C. In this case TOP-Te reacts with Cd-oleate complex rather than Cd^0 nanoparticles which gives rise to comparatively more surface defects than CdTe-C. However, this is only one of the factors and the formation of surface defects in NQDs depends on various factors including temperature, anealing time at high temperature, ligands[32] used and its concentration. Surface defective cores are known to be viable for efficient alloy formation[14] at the interfaces. Analogous judgment in the current scenario would lead to the formation of alloyed interface[33] in the case of CdTe-A/CdS. The results of such a variation in structure can be elucidated as shown in the schematic in the schematic in Figure 4.5(a) and 4.5(b). Formation of a sharp interface combined with a type-II alignment[31] leads to the lower overlap of e-h wavefunction resulting a "spatially indirect" recombination. However, formation of an alloy at the interface leads to a more "spatially direct" recombination due to the greater e-h wavefunction overlap. This conjecture is verified using long-range and short range crystal structure analysis as shown in Figure 4.5(c) and Figure 4.6 using X-ray diffraction and EXAFS spectroscopy. The XRD patterns shown in Figure 4.5(c) illustrate that while the crystal structures of CdTe-A and CdTe-C matches with that of cubic CdTe (bulk), the peaks of CdTe-A/CdS is only slightly shifted compared to CdTe-A with no characteristic Cd-S peaks. Contrastingly, clear signatures of both CdS and CdTe lattices are observed in CdTe-C/CdS. These observations are in agreement with an alloyed interface in CdTe-A/CdS as discussed earlier in the text.

4.4.4 Local Structure

Formation of sharp core-shell and alloyed interface was further confirmed by the local structure analysis around the Cd and Te atoms using EXAFS spectroscopy. The Fourier transform (FT) of the Cd and Te K-edge EXAFS with their corresponding fitting is shown in Figure 4.6(a) and 4.6(b) respectively while the Cd and Te K-edges with evidences of surface oxidation are shown in Figure 4.7(a) and 4.7(b) respectively. The fitting parameters are shown in Table 4.1 and 4.2. The presence of Cd-Te bond (~2.5 Å, green line) and the Cd-S (1.9 Å, magenta line) in CdTe-C/CdS (shown in Figure 4.6(a) compared to a single major peak in CdTe-A/CdS with a slightly larger bond length is in agreement with the XRD data. This suggests that CdTe-A/CdS is most likely an alloy of CdTe and CdS with its bond length close to CdS structure.

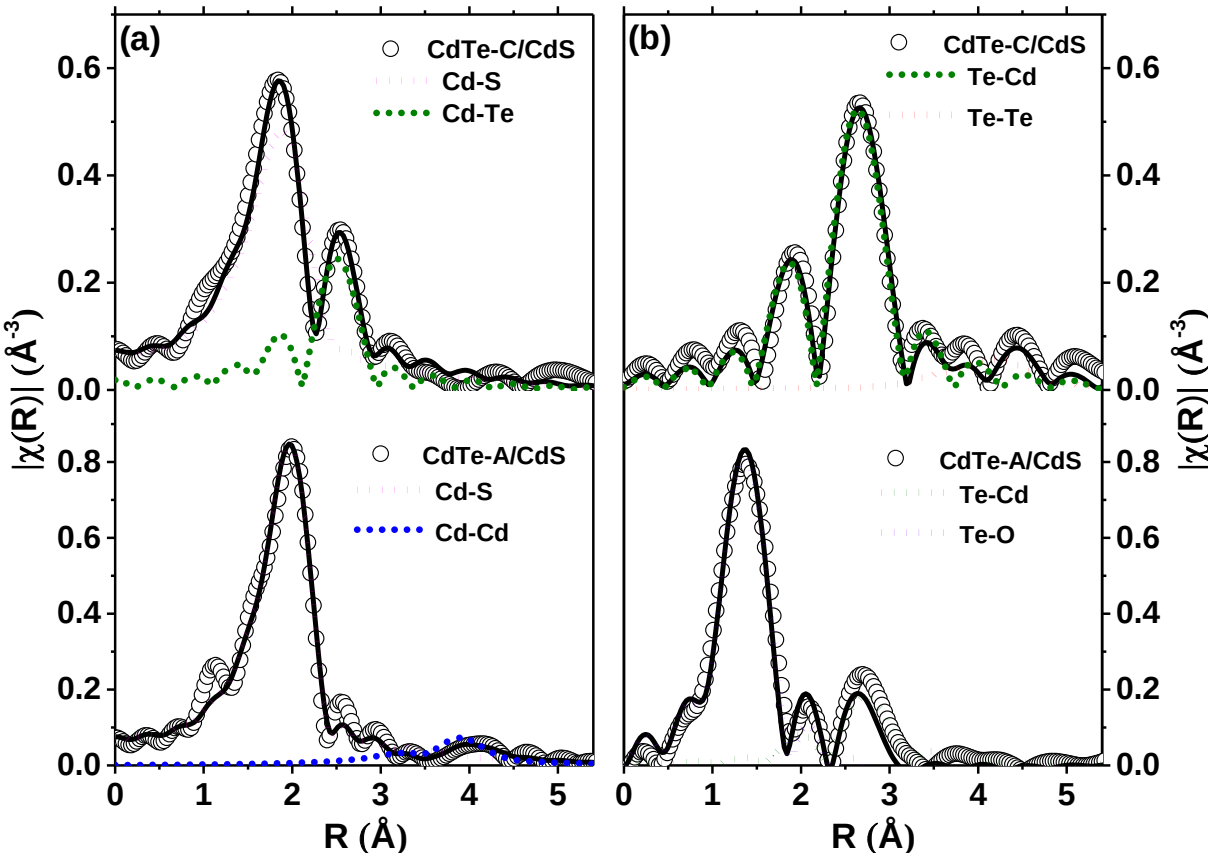

Figure 4.6: Fourier transform of (a) Cd K-edge and (b) Te K-edge EXAFS spectra (circles) and their fits (solid lines) for CdTe-C/CdS and CdTe-A/CdS. Dotted lines are different fitting paths.

This is further validated by the Te K-edge in these samples as shown in Figure 4.6(b) and Figure 4.7. CdTe-A/CdS is most likely an alloy of CdTe and CdS with its bond length close to CdS structure. The local environment around the Te in CdTe-C/CdS can be simply explained with Cd-Te bond and Te-Te bond, while Te oxidation is evident in CdTe-A/CdS suggesting that Te is exposed to the atmosphere. Figure 4.7(a) shows that the white line for the Cd edge of the alloy sample and core shell sample is higher than the Cd edge of CdS and CdTe standard samples because in both these samples, Cd atoms are slightly oxidized as some of the Cd atoms are on the surface. However, the white line for the Te edge of the alloy sample is higher than the Te edge of CdTe standard sample because this sample is slightly oxidized as shown in the table of fit parameters since some of the Te atoms of the alloy are on the surface suggesting the formation of alloy. Thus the various signatures in EXAFS are consistent with the formation of an alloy structure in CdTe-A/CdS.

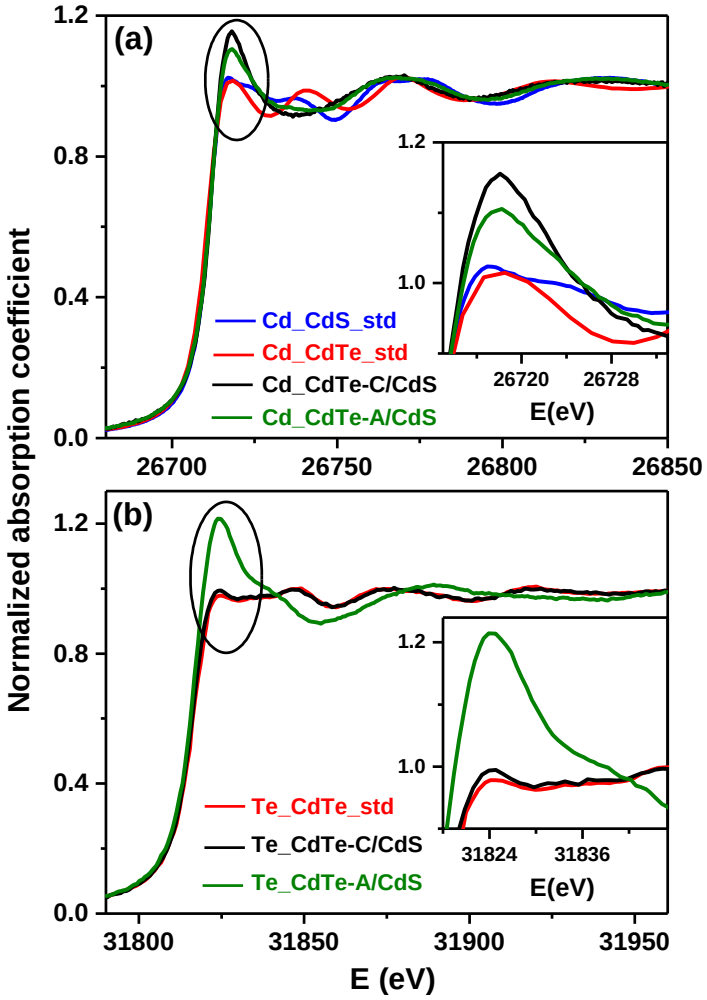

Figure 4.7: (a) Cd K-edge (b) Te K-edge X-ray Absorption Near Edge Structure (XANES) of both CdTe/CdS core/shell and alloy quantum dots.

Table 4.1: Theoretical bond lengths generated using FEFF and used for fit.

Path	Bond Length (Å)	Coordination Number (N)
TeO2 (Te-O)	1.90	2
CdS (Cd-S1)	2.52	1
CdS (Cd-S2)	2.53	3
CdS (Cd-Cd1)	4.12	6
CdS (Cd-Cd2)	4.13	6
CdTe (Cd-Te)	2.81	4
CdTe (Cd-Cd)	4.58	12
CdTe (Te-Cd)	2.81	4
CdTe (Te-Te)	4.58	12

Table 4.2: List of fit parameters obtained from modeling the data for Cd and Te edges.

Edge	Sample Name	Paths	Bond length R (Å)	Coordination Number (N)	Debye Waller Factor	Energy Shift ΔE (eV)
Cd edge S_o^2= **0.97**	**CdTe-A/CdS** R=1.0-4.5 Å k= 3.3-12.0 $Å^{-1}$	Cd-S	2.50 ± 0.01	4.1 ± 0.3	0.009 ± 0.001	-1.7 ± 0.7
		Cd-Cd	4.14± 0.03	5.6 ± 3.8	0.02 ± 0.01	
	CdTe-C/CdS R=1.2-3 Å k= 3.4-10.4 $Å^{-1}$	Cd-S	2.48 ± 0.01	4.5 ± 0.8	0.016 ± 0.002	-4.2 ± 1.0
		Cd-Te	2.77 ± 0.01	1.3 ± 0.3	0.008 ± 0.002	
Te edge S_o^2= **0.98**	**CdTe-A/CdS** R=1.0-3.2 Å k= 2.7-9.3 $Å^{-1}$	Te-O	1.90 ± 0.02	2.3 ± 0.3	0.003 ± 0.002	7.6 ± 1.4
		Te-Cd	2.79 ± 0.03	1.2 ± 0.3	0.007	
	CdTe-C/CdS R=1-4.8 Å k= 3.1-9.0 $Å^{-1}$	Te-Cd	2.77 ± 0.01	3.6 ± 0.4	0.008 ± 0.002	3.7 ± 0.9
		Te-Te	4.51 ± 0.06	12	0.03 ± 0.01	

4.5 Conclusion

Thus these data conclusively proves that surface defects in NQDs can be used to radically alter the properties of the NQDs leading to contrasting applications like photoemission and photoabsorption. Consequently, the synthesis parameters can be tuned to obtain properties necessary for the applications. These origins can be successfully traced to the lattice defects as obtained from spectroscopic techniques like EXAFS, X-ray photoemission and diffraction methods. In conclusion, we have shown in this work that lattice defects can indeed play a very important role in determining the properties of the nanomaterials and is as strong a handle as that of the size or shape of NQDs to tune the material properties. We then demonstrated this principle for specific case of CdTe/CdS semiconductor heterostructures.

Bibliography

(1) Wang, Z. L.; Wu, W. *Angew. Chem.* **2012**, *51*, 11700.

(2) Li, L.; Chen, S.; Wang, X.; Bando, Y.; Golberg, D. *Energy Environ. Sci.* **2012**, *5*, 6040.

(3) Zhang, Q.; Uchaker, E.; Candelaria, S. L.; Cao, G. *Chem. Soc. Rev.* **2013**, *42*, 3127.

(4) Ruberu, T. P. A.; Albright, H. R.; Callis, B.; Ward, B.; Cisneros, J.; Fan, H.-J.; Vela, J. *ACS Nano* **2012**, *6*, 5348.

(5) Guo, Y.; Marchuk, K.; Sampat, S.; Abraham, R.; Fang, N.; Malko, A. V.; Vela, J. *J. Phys. Chem. C* **2012**, *116*, 2791.

(6) Kamat, P. V. *J. Phys. Chem. C* **2008**, *112*, 18737.

(7) Bang, J.; Park, J.; Lee, J. H.; Won, N.; Nam, J.; Lim, J.; Chang, B. Y.; Lee, H. J.; Chon, B.; Shin, J.; Park, J. B.; Choi, J. H.; Cho, K.; Park, S. M.; Joo, T.; Kim, S. *Chem. Mater.* **2010**, *22*, 233.

(8) Lin, C. C.; Liu, R.-S. *J. Phys. Chem. Lett.* **2011**, *2*, 1268.

(9) Höppe Dr., H. A. *Angew. Chem.* **2009**, *48*, 3572.

(10) Sarma, D. D.; Nag, A.; Santra, P. K.; Kumar, A.; Sapra, S.; Mahadevan, P. *J. Phys. Chem. Lett.* **2010**, *1*, 2149.

(11) Song, W.-S.; Yang, H. *Chem. Mater.* **2012**, *24*, 1961.

(12) Kim, S.; Im, S. H.; Kim, S.-W. *Nanoscale* **2013**, *5*, 5205.

(13) Ji, W.; Jing, P.; Zhao, J. *J. Mater. Chem. C* **2013**, *1*, 470.

(14) Saha, A.; Chellappan, K. V.; Narayan, K. S.; Ghatak, J.; Datta, R.; Viswanatha, R. *J. Phys. Chem. Lett.* **2013**, *4*, 3544.

(15) Santra, P. K.; Viswanatha, R.; Daniels, S. M.; Pickett, N. L.; Smith, J. M.; O'Brien, P.; Sarma, D. D. *J. Am. Chem. Soc.* **2009**, *131*, 470.

(16) Pandey, A.; Guyot-Sionnest, P. *J. Chem. Phys.* **2007**, *127*, 111104.

(17) Li, X.; Shen, H.; Li, S.; Niu, J. Z.; Wang, H.; Li, L. S. *J. Mater. Chem.* **2010**, *20*, 923.

(18) Chen, G.; Seo, J.; Yang, C.; Prasad, P. N. *Chem. Soc. Rev.* **2013**, *42*, 8304.

(19) Ji, W.; Jing, P.; Zhao, J.; Liu, X.; Wang, A.; Li, H. *Nanoscale* **2013**, *5*, 3474.

(20) Debnath, R.; Bakr, O.; Sargent, E. H. *Energy Environ. Sci.* **2012**, *4*, 4870.

(21) Shalom, M.; Ruhle, S.; Hod, I.; Yahav, S.; Zaban, A. *J. Am. Chem. Soc.* **2009**, *131*, 9876.

(22) Yu, X.-Y.; Lei, B.-X.; Kuang, D.-B.; Su, C.-Y. *Chem.Sci.* **2011**, *2*, 1396.

(23) Kumar, S. G.; Rao, K. S. R. K. *Energy Environ. Sci.* **2014**, *7*, 45.

(24) Li, J. J.; Wang, Y. A.; Guo, W.; Keay, J. C.; Mishima, T. D.; Johnson, M. B.; Peng, X. *J. Am. Chem. Soc.* **2003**, *125*, 12567.

(25) Kloper, V.; Osovsky, R.; Kolny-Olesiak, J.; Sashchiuk, A.; Lifshitz, E. *J. Phys. Chem. Lett.* **2007**, *111*, 10336.

(26) Segre, C. U.; Leyarovska, N. E.; Chapman, L. D.; Lavender, W. M.; Plag, P. W.; King, A. S.; Kropf, A. J.; Bunker, B. A.; Kemner, K. M.; Dutta, P.; Duran, R. S.; Kaduk, J. *AIP Conf. Proc.* **2000**, *521*, 419.

(27) Newville, M. *J. Synchr. Radn.* **2001**, *8*, 322.

(28) Rehr, J. J.; Albers, R. C. *Rev. Mod. Phys.* **2000**, *72*, 621.

(29) Ravel, B.; Newville, M. *J. Synchr. Radn.* **2005**, *12*, 537.

(30) Borg, L. z.; Lee, D.; Lim, J.; Bae, W. K.; Park, M.; Lee, S.; Lee, C.; Char, K.; Zentel, R. *J. Mater. Chem. C* **2013**, *1*, 1722.

(31) Grandhi, G. K.; Tomar, R.; Viswanatha, R. *ACS Nano* **2012**, *6*, 9751.

(32) Mishra, N.; Lian, J.; Chakrabortty, S.; Lin, M.; Chan, Y. *Chem. Mater.* **2012**, *24*, 2040.

(33) Boldt, K.; Kirkwood, N.; Beane, G. A.; Mulvaney, P. *Chem. Mater.* **2013**, *25*, 4731.

Chapter 5
Core-shell to Doped Quantum Dots

The following papers have been published based on the work presented here.

- *J. Phys. Chem. Lett.* **2016**, *7*, 2420-2428.
- *J Phys. Chem. C*, **2016**, *120*, 18945-18951.
- ACS Nano, **2017**, *11*, 3347-3354

5.1 Introduction

Tunability of physical and chemical properties of QD QDs with their size leads to a wide range of applications, including optoelectronics,[1] magneto optics,[2] data storage,[2,3] bioimaging[4-6] and even biomedicine.[7] Hybrid QD heterostructure and doped QDs are an emerging class of NCs where two or more intrinsic properties can be obtained from same materials. Magnetic semiconductors are one of the best representatives in which both magnetic and semiconductor properties can be achieved from the same material. Engineering the internal structure of magnetic semiconductor QDs provides new opportunities to tune their properties. For example, magnetic/semiconductor sharp core shell heterostructure QDs[8,9] have shown properties like magneto-resistance,[10,11] high electron mobility[10] and compatibility in bio-application,[12] while a complete diffusion of magnetic core can lead to magnetic ion doped semiconductor QDs or the so called dilute magnetic semiconductor[13-16] (DMS) QDs that offers opportunities in spintronics application.

Now a days, there has been a pronounced interest in synthesis of various types of magnetic QDs and understanding their property modulation with size, shape, composition and internal structure. While there are many synthesis techniques developed to synthesize core-shell heterostructure or magnetic impurity doped QDs, the bridge between these two by changing their internal structure is missing due to lack of precise control during synthesis. Moreover, the doped QDs suffer from phase segregation of magnetic ions inside the QDs[17-19] due to thermodynamic instability, which complicates the basic understanding of their magnetic origin and thereby tunability of magnetic properties. It is interesting to note that the study of property tunability due to change in internal structure in quantum confined regime are few, even though there have obvious importance both in application and fundamental understanding. The primary bottle neck to such investigations is the lack of appropriate characterization technique to probe the internal structure evolution. While high resolution TEM and elemental mapping is the most direct probe to detect the size and morphology, the resolution is not good enough to detect minute changes in internal structure or cluster phase. In contrast to the direct probe of the structural evolution via HRTEM, QD internal structure can also be determined by high energy synchrotron X-ray absorption spectroscopy by studying the local environment.

In this chapter, we discuss about engineering the internal structure of a magnetic/semiconductor core-shell QDs and convert it into a uniformly doped DMS QDs. A complete investigation of various stages during the structural evolution and their corresponding magnetic properties has been discussed here. The chapter is divided into four sections. In section-A, we describe synthesis of uniformly doped DMS QDs by complete diffusion of magnetic core inside a semiconductor. The effects of uniform doping on QDs magnetic property in comparison with previous literature reports have also been compared. In section-B the evolution of core-shell to doped QDs has been probed by studying the local environment using XAFS. The variation of magnetic property in hybrid core-shell ferrimagnetic semiconductor heterostructure has been discussed in section-C. The role of interface in determining the properties in magnetic/ semiconductor nano-heterostructure has been discussed here. The versatility of diffusion doping technique to obtain wide size and concentration variation has been shown in section-D. Herein, we have demonstrated the effect of size and magnetic concentration in magnetic property of DMS QDs.

Section A

Synthesis and Characterization

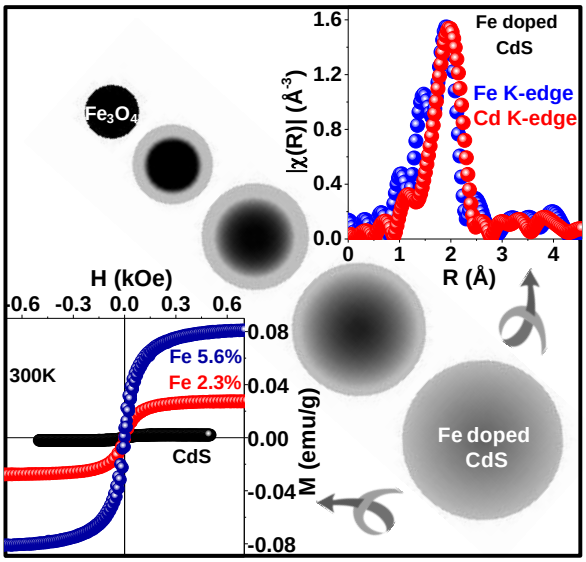

5.2 Summary

Effective manipulation of magnetic spin within a semiconductor leading to a search for ferromagnets with semiconducting properties has evolved into an important field of DMS. While a lot of research is focused on understanding, the still controversial origin of magnetism, efforts are also underway to develop new materials with higher magnetic temperatures for spintronics applications. However, so far, efforts towards QDs based DMS materials are plagued with problems of phase separation leading to non-uniform distribution of dopant ions. In this work, we have developed a strategy to synthesize highly crystalline, single domain DMS system starting from a small magnetic core and allowing it to diffuse uniformly inside a thick CdS semiconductor matrix and achieve DMS QDs. XAFS spectroscopy and STEM-EDX indicates the homogeneous distribution of magnetic impurities inside the semiconductor QDs leading to superior magnetic property. Further, the versatility of this technique was demonstrated by obtaining ultra large particles (~60 nm) with uniform doping concentration as well as demonstrating the high quality magnetic response.

5.3 Introduction

Incorporation of impurities or defects into semiconductor lattices has been realized as the primary means of controlling electrical conductivity,[20] and may also have an immense effect on the optical,[21] magnetic,[22,23] or other physical properties of the semiconductor. Transition metal doped DMS systems,[22-24] obtained by combining semiconductors and magnetic ions are a renowned class of materials known for their distinct magnetic phases ranging from anti-ferromagnetism to ferromagnetism as a function of magnetic ion concentration[25] as well as interesting low-temperature functionalities.[14] The possibility of the onset of an exchange interaction between the host and the partially-filled *d* levels of the magnetic ion allows for the control of the electronic, magnetic and optical properties of the DMS material, using external fields. Thus, these materials have attracted a lot of attention both from the viewpoint of fundamental understanding as well as applied research perspective. They have garnered comprehensive attention ranging from study of intriguing long range spin interactions to potential applications in spintronics,[26,27] magnetic recording[28] and switching.[27] However, so far, most of these experiments as well as theories have been mainly formulated for bulk materials.[27,29]

With the advent of QDs, the study of DMS properties in these QDs has been a natural extension of study. Efforts to understand extended spin interactions in the quantum confined regime has led to the revelation of host of rich physical phenomena including giant Zeeman splitting,[30,31] magnetic polaron[32] and zero field magnetizations.[33] Theory[24,32] and experiments[34] on low dimensional DMS have shown very interesting size dependent properties, specifically in achieving control over long range spin coherence and spin polarization under weak magnetic field.[35,36] In spite of this success, properties of DMS QDs have been quite controversial as it is often plagued with matters related to the uniformity of dopant incorporation and hence the origin of the ferromagnetism from the magnetic clusters. In fact, several studies in bulk, thin films and in nanowires have shown the importance of uniform magnetic ion distribution.[37-39] Though, similar studies in QDs are unavailable, statistical analysis of doping with non-uniform distribution of magnetic ions shows that the cluster formation of magnetic elements on the surface or inside the semiconductor QDs results in poor magnetic response from these QDs. In fact, few reports on QDs which claim to show DMS property have not shown any clear evidence of dopant distribution inside the QDs.[18,19] Instead, the low magnetic response from these materials supports the fact of secondary phase formation.[17]

Hence, though delicate engineering of quantum confinement to mediate carrier-spin interactions by altering the size and shape has been recognized as a possibility in solution processed QDs, it has so far been non-trivial to ensure uniform distribution of the dopants in the bulk of the QDs rather than the surface. This is further enhanced by the presence of self-purification mechanisms[36,40-42] in these QDs. Hence, even the presence of 2 mol% or lower concentration of the dopant has often proved to be detrimental to the magnetism in doped materials. Hence, there is a need to devise more effective and universal synthesis methods that would ensure uniform dopant concentration to understand the rich physics of DMS QDs.

In this study, we have reported a technique to produce transition metal doped DMS QDs. It is well known that the diffusion of dopants out of the host matrix, also known as self purification, has been the major deterrent in the earlier efforts. Hence extensive efforts have been invested to recognize and avoid this process like the reduction of lattice mismatch[41,43], lowering of temperature of the synthesis[42] and so on. However, in the current work, we have demonstrated the constructive use of the same process to diffuse a magnetic core into the semiconducting matrix to obtain a uniformly doped DMS QDs. We first synthesize a small QD

core containing oxides or sulfides of magnetic ions, like for example magnetite (Fe_3O_4), followed by high temperature annealing and growth of the semiconducting matrix. It has been seen earlier, that high temperature annealing increases the entropy of the system and provides the kinetic energy to defects and impurities to be leeched out from the QDs.[40,41] During this process of annealing, we expect ions in the magnetic core to diffuse out of the lattice due to self-purification with reduction in the core size. We carefully engineer the annealing temperature as well as the reaction coefficient of precursors such that the diffusion of the magnetic ions is slower than the growth of the semiconductor lattice leading to controlled diffusion of the magnetic ions. The controlled diffusion of Fe ions inside the thick matrix of CdS nanostructure, grown by successive ionic layer adsorption and reaction (SILAR) technique,[44] followed by the arrest of the diffusion before the complete expulsion of the dopant ions leads to formation of Fe-doped CdS QDs with excellent control over their size distribution, uniformity of dopant ions and percentage of doping. A similar principle has also been demonstrated earlier to achieve graded alloy architecture from core-shell heterostructures by varying the synthesis conditions described in chapter 3 and chapter 4. In fact, the origin of high PL quantum yields of Mn in "nucleation doping" by Peng and co-workers,[45] though claimed as a quasi core/shell structure, can be traced back to similar diffusion process.[46] However, oxides provide an interesting alternative to the sulfides and selenides due to two major reasons. Firstly the diversity of oxides that can be made into QDs is quite large and secondly the enhanced stability of the oxides plays a critical role in the growth of larger particles as well as in control of doping percentage over a larger range that will be discussed in the next chapter. However one of major hindrant to this is the stability of the Fe-O and Cd-S bonds and hence the difficulty to break these bonds and diffuse into the CdS matrix. Secondly, there exists a non-negligible lattice mismatch (4.4%) between Fe_3O_4 and CdS that creates a highly strained interface as has also been shown in earlier literature. [9,8] However, in this case, the strained interface as well as the high temperature annealing acts as the driving force to break the strong Fe-O bond and diffuse into CdS lattice and converts from an initial core-shell structure to a diffused Fe-doped CdS structure.

We used X-ray diffraction (XRD) for crystal structure information and STEM-EDX, EXAFS, XANES and electron energy loss spectroscopy (EELS) to probe the local atomic environment and study its direct correlation with magnetic property. Thermo-gravimetric analysis (TGA)

was used to obtain the weight percentage of ligands and magnetic measurements were obtained using superconducting quantum interference device SQUID magnetometer. The magnetic moment per ion was then calculated. The structural uniformity correlates with superior magnetic property from these materials which is at least an order of magnitude higher than previously reported systems.[17,18,47]

5.4 Experimental Details

5.4.1 Synthesis

Synthesis of core Fe_3O_4. Core Fe_3O_4 was prepared by high temperature decomposition of $Fe(ac)_2$ with oleic acid and oleylamine.[48] In a typical preparation 0.35 g of $Fe(ac)_2$, 2.5 ml oleic acid and 5 ml of oleylamine were taken in a three necked flask and degassed at 120°C under constant stirring. Then the temperature was raised to 220°C under constant Ar flow. After 20 min, the temperature of the reaction mixture was raised to 300°C very slowly (4K/min). This temperature was maintained for 5 min and then the reaction mixture was cooled downed to room temperature. Then the QDs were washed twice by addition of hexane-ethanol mixture and followed by centrifugation.

Synthesis of Fe doped CdS QDs. 0.2 M cadmium oleate ($Cd(Ol)_2$) was prepared using modified literature methods and 0.2 M S/ODE solution by dissolving S in ODE in inert atmosphere. SILAR technique[44] was used to synthesize these doped QDs. 12 mg of pre-synthesized iron oxide QDs (powder form), 3 ml of OlAm and 5 ml of ODE were taken in a three necked flask and degassed under vacuum at 80°C. After 2 h of degassing the reaction flask was backfilled with Ar and the temperature was raised to 250°C. The stoichiometric amount of $Cd(Ol)_2$ required for first shell formation (assumed to be a monolayer of CdS) was injected to the reaction mixture. After 40 min same amount of S precursor was injected into the system and annealed for 20 min. This cycle of Cd and followed S precursors addition were continued until an ultra thick CdS shell formed. Annealing at high temperature (250°C) for long time (1h for every CdS monolayer) along with the CdS shell formation allows the core to diffuse inside it.

Synthesis of undoped CdS QDs. Undoped CdS was synthesized using similar experimental condition described in experimental section. Here, we use CdS as core and overcoated with CdS multilayer. 0.2 M $Cd(Ol)_2$ and ODE was taken in a three necked flask and degassed at 80°C. After 90 min, temperature was raised to 280°C under constant Ar flow and required

amount of S/ODE was quickly injected into the reaction mixture. Temperature was quickly brought down to 250°C and 3 ml of OlAm was added into the reaction mixture and then CdS layers were grown similarly like other overcoating techniques.

5.4.2 XAFS Characterization

EXAFS and XANES spectroscopy were employed to probe the local structure around Fe and Cd atoms during for the Fe doped CdS QDs. Fe K-edge (7112 eV) and Cd K-edge (26711 eV) for the samples were measured at 10ID beamline at Advance Photon Source, Argonne National Laboratory.[49]

5.5 Results and discussion

While the brief method of synthesis is discussed in the experimental section, it is important to note here that the overcoating procedure was performed by annealing at high temperature (240-260°C) for long time allowing the Fe atoms to diffuse into the CdS matrix. Here, we have used so called self-purification that has been observed in several cases in literature[40-42,50] to different extents, as the driving force to diffuse the magnetic core into the semiconductor matrix. Fe_3O_4 is a stable oxide and requires long time annealing at high temperature to diffuse inside the CdS matrix. During annealing, transition metal ions is expected to diffuse out slowly through the thick CdS shell matrix while the diffusion of oxygen out of the matrix is much faster leading to a decrease and eventual absence of the oxygen content in our final QDs. We carefully monitor the reaction to stop the annealing when the magnetic ions are diffused uniformly inside the CdS. While we make sure that the transition metal has not completely reached the surface of the CdS QDs, it is clear that some of the metal ions have indeed escaped the QDs lattice as can be observed from our ICP-OES data shown in Table 5.1 and as discussed later in the text. This process provides both uniform doping as well as control over dopant percentage depending on annealing time and temperature. So the dopant incorporation depends both on kinetics as well as thermodynamics that is essential to control the amount of Fe incorporation. We have collected samples after each Cd and S cycles with differing thicknesses of CdS overcoating that is henceforth depicted as "Fe-nCdS" where n is the number of Cd and S cycles.

5.5.1 Microstructure Study

Figure 5.1 shows the representative TEM images at various stages of CdS growth of these QDs. Sizes obtained from TEM analysis as a function of growth of CdS QDs around the core range from 4.5 nm for the core Fe_3O_4 QDs (Figure 5.1(a)) to 8.5 nm, 12.6 nm and 15.4 nm (Figure

5.1(b), 5.1(c), 5.1(d)) respectively. It can be seen from Figure 5.1 that the particles are spherical and have a fairly uniform size distribution signifying a uniform growth of QDs. The high quality of these QDs with no evidence of lattice mismatch between the core and the shell are evident from the crystalline nature of these particles as shown by the HRTEM images in the insets of Figure 5.1.

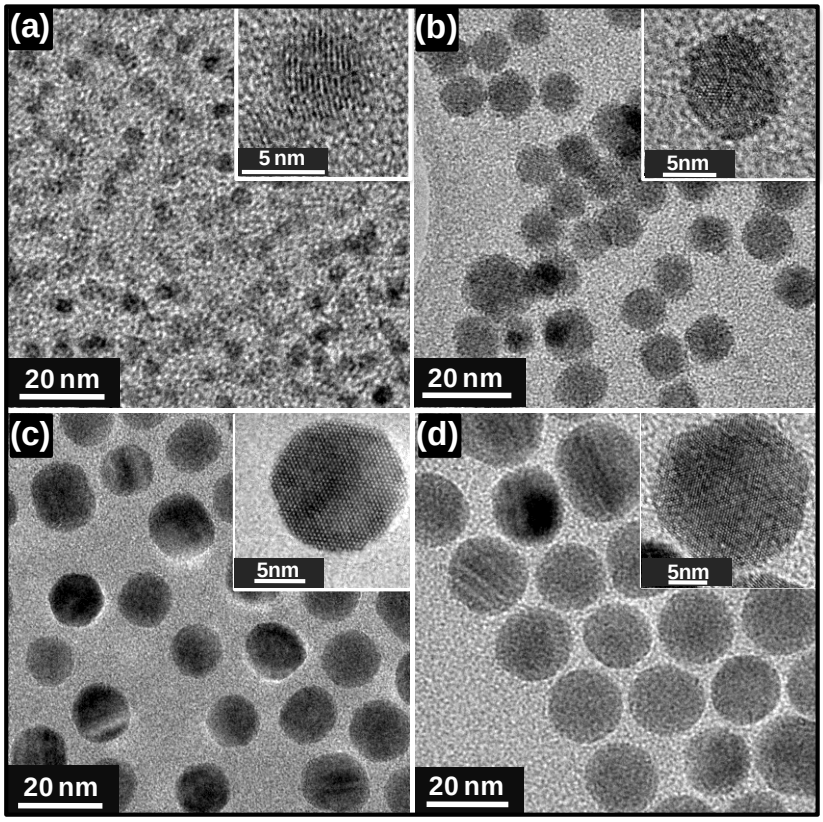

Figure 5.1: TEM images showing (a) 4.5 nm Fe_3O_4 core (b) Fe-5CdS (c) Fe-10CdS (d) Fe-14 CdS and their representative high resolution TEM in the insets.

However, as has been extensively studied earlier, HRTEM and lattice spacings do not conclusively determine the differences between alloys and/or core/shell formation in these QDs. Especially in presence of two semiconductors with no drastic differences in their TEM contrast. For comparison, CdS QDs of similar size were prepared using similar methods without doping Fe and the TEM image of the same is shown in Figure 5.2. It is shown that there is no noticeable difference between the TEM images as well as the lattice spacing of undoped CdS and Fe-doped CdS QDs. Elemental analysis using ICP-OES for all these samples at different stages along with the expected Fe percentage for a core/shell structure with 4.5 nm core and the total size as obtained from TEM have been tabulated in Table 5.1. Results show

that iron percentage monotonically decreased reaching down to 5.6% and 2.3% after 10 and 14 cycles of Cd and S additions respectively. These percentages of doping levels can now be considered to be in the dilute doping regime. Our magnetic measurement studies are going to be mainly focused on these low percentages of Fe-CdS QDs which are henceforth referred to as Fe-doped CdS QDs. In addition, it is important to note that the actual percentages are usually less than the theoretical expected percentages indicative of the leaching of the Fe atoms out of the QDs. This can be attributed to the process of self purification indicating that the Fe atoms are indeed diffusing into and out of the CdS matrix.

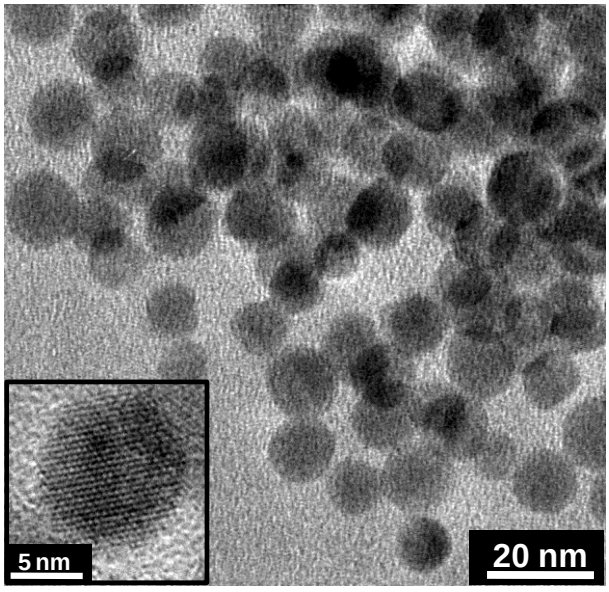

Figure 5.2: TEM image of undoped CdS QDs after 10 monolayer. Inset shows HRTEM of a single particle.

Table 5.1. Elemental analysis of Fe-CdS nanoparticles using ICP-OES.

Sample	Size (nm)	Fe (%)	Calculated Fe (%)
Core Fe_3O_4	4.5	100	100
Fe-1CdS	5.4	94.2	82.8
Fe-2CdS	6	57.7	68.5
Fe-3CdS	6.6	29.7	55.8
Fe-4CdS	7.2	20	46
Fe-5CdS	8.5	17.8	30.8
Fe-10CdS	12.6	5.6	10.6
Fe-14CdS	15.4	2.3	5.96
CdS	12	0	0

5.5.2 XRD and UV-VIS spectroscopy

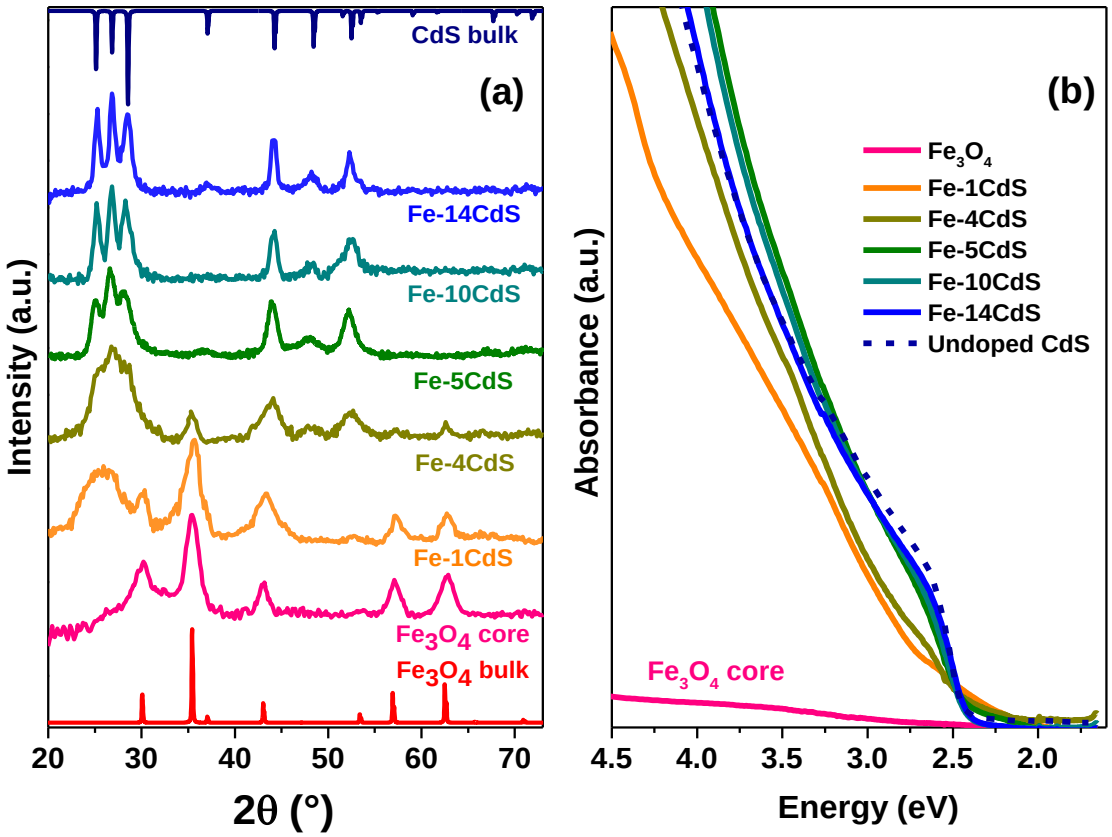

Figure 5.3: (a) X-ray diffraction patterns of Fe_3O_4 NCs core and then after different cycles (1, 4, 5, 10, 14) of Cd an S precursors additions in comparison to the XRD spectra of bulk Fe_3O_4 and CdS. (b) UV-VIS optical absorption spectra for Fe-CdS samples with increasing CdS in comparison to core Fe_3O_4 and un-doped CdS showing the evolution change from Fe_3O_4 core to doped CdS.

However a more direct evidence of the presence of Fe_3O_4 and Fe doped CdS can be studied from the XRD of these materials. In order to explore the composition and crystal structure of these QDs XRD measurements were carried out. The changes in the crystal structure of the QDs during the overcoating of CdS on core Fe_3O_4 QDs is shown in Figure 5.3. XRD pattern in Figure 5.3(a) shows that Fe_3O_4 core QDs are formed in inverse spinel structure similar to that of the bulk (also shown in the figure) as observed from the inorganic crystal structure database. The broadening of the XRD peaks is consistent with the size of the QDs as obtained from the Scherrer formula. Subsequently, with the growth of thin layers of CdS, we observe the formation of wurtzite CdS structure along with the existent inverse spinel structure of Fe_3O_4 as observed in Fe-1CdS and Fe-4CdS due to existence of core shell structure at the initial stages.

Eventually in presence of sufficiently thick shell of CdS and adequately long annealing time, signatures of spinel structure of Fe_3O_4 are completely absent. This systematic structural change from Fe_3O_4 to CdS is indicative of a diffusion of Fe from the core to the surface through the CdS matrix. In fact, unlike in other cases in literature,[45] the structures of the core and shell are substantially different, leading to clearly observable peaks in presence of iron oxide clusters or core as observed in the case Fe-4CdS. Absence of inverse spinel peaks in thicker shell CdS structures, suggest the absence of iron oxide clusters. However, it is still possible to have small clusters that are beyond the resolution of XRD, especially in such small sizes and hence cannot be a conclusive proof for absence of clustering. It is also notable that the XRD peaks, consistent with the increase in particle size have sharpened with the additions of Cd and S precursors indicating the growth of CdS shell over the existent cores rather than an independent nucleation.

The qualitative difference in the nature of optical absorption with the growth of the particles was studied using UV-VIS spectroscopy. Figure 5.3(b) shows the changes in optical absorption starting from a core to thick shell large particles in comparison to un-doped CdS. As expected, Fe_3O_4 does not absorb in this energy range. However, with the successive additions of Cd and S precursors at high temperature, CdS $1s_e$-$1s_h$ transition feature starts arising and gets pronounced after a thick CdS shell formation. Undoped thick shelled CdS also show similar absorption features as that of Fe-CdS QDs as shown by the dotted line in Figure 5.3(b).

5.5.3 Etching Experiment

In order to further confirm the distribution of Fe in CdS matrix,[51] a 15 nm Fe doped CdS QDs was etched slightly with hydrogen peroxide to remove the outermost shell of the QDs. TEM images of the samples before and after etching (Figure 5.4) shows that the average size of the QDs have reduced from 15 nm to about 11 nm. However, the ICP before and after etching to obtain the ratio of Fe to Cd show that the percentage of Fe are respectively 3.4% and 3.5%. This suggests that the percentage of Fe is unchanged within experimental error even after etching the outer shell and hence demonstrating that Fe is indeed uniformly distributed in the CdS matrix.

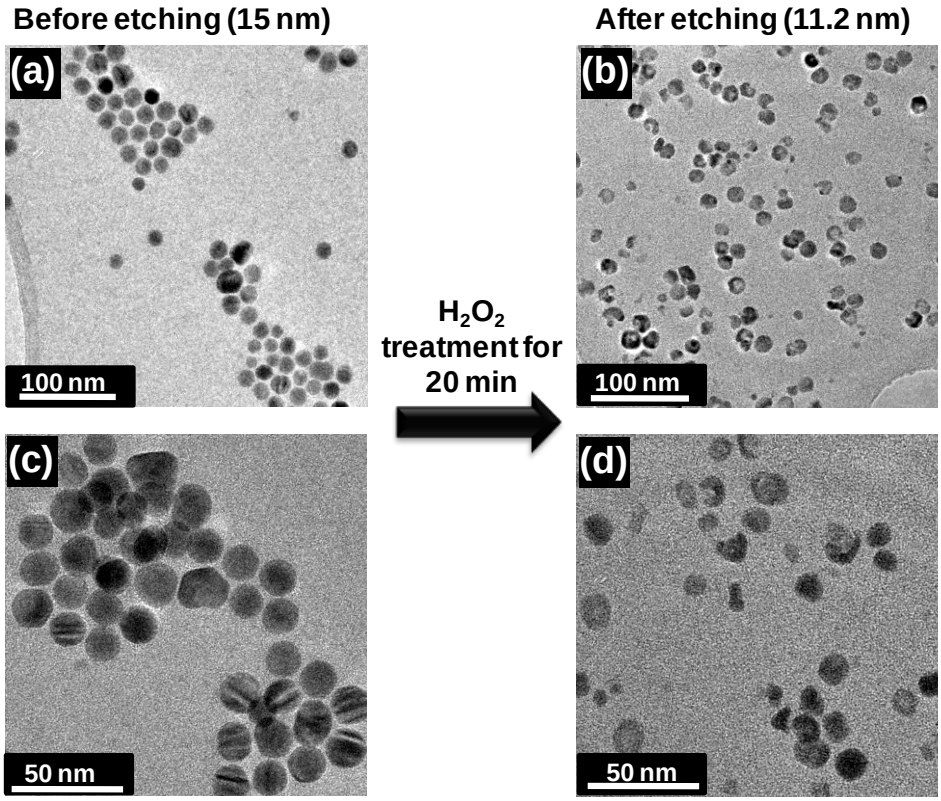

Figure 5.4: Surface etching of Fe doped CdS nanoparticles by H_2O_2 treatment. Fe doped CdS (a), (c) before etching and (b), (d) after etching.

5.5.4 Local Structure

However the ultimate proof for the distribution of Fe is obtained from the local structure investigation of the Fe atom using XAFS.[52,53] XAFS can reveal the local bonding around the atom of interest by measuring the absorption coefficient below, at and above the absorption edge of the element.

XAFS Analysis: X-ray absorption scans were collected at Fe-K edge in fluorescence mode for both Fe_3O_4 core and Fe-doped CdS (Fe-14CdS) and Cd-K edge for Fe-doped CdS QDs. The data was processed using ATHENA[54] and the Fourier transformation of Fe and Cd K-edge EXAFS spectra in real (R) space for Fe_3O_4 and Fe-doped CdS sample are respectively shown by solid lines in Figure 5.5(a) and 5.5(b). Visual inspection of the two plots makes it apparent that the local structure around Fe in Fe-CdS is very different than that of Fe_3O_4. The EXAFS of Fe in Fe_3O_4 has been extensively analysed in literature[52,55] and the various paths corresponding to Fe-O in tetrahedral and octahedral holes as well as second nearest neighbour Fe-Fe have been shown to give rise to the EXAFS pattern similar to one observed here in

Figure 5.5(a). However, EXAFS data from Fe-CdS shown in Figure 5.5(b) shows completely different pattern. In fact, upon observation of the similar data for the Cd edge, also shown in Figure 5.5(b), it is apparent that the structure around the Cd atom in Fe-CdS is very similar to that of Fe. Further verification of the absence of the clusters of iron oxide was obtained by the complete absence of the second nearest neighbour Fe-Fe contribution.

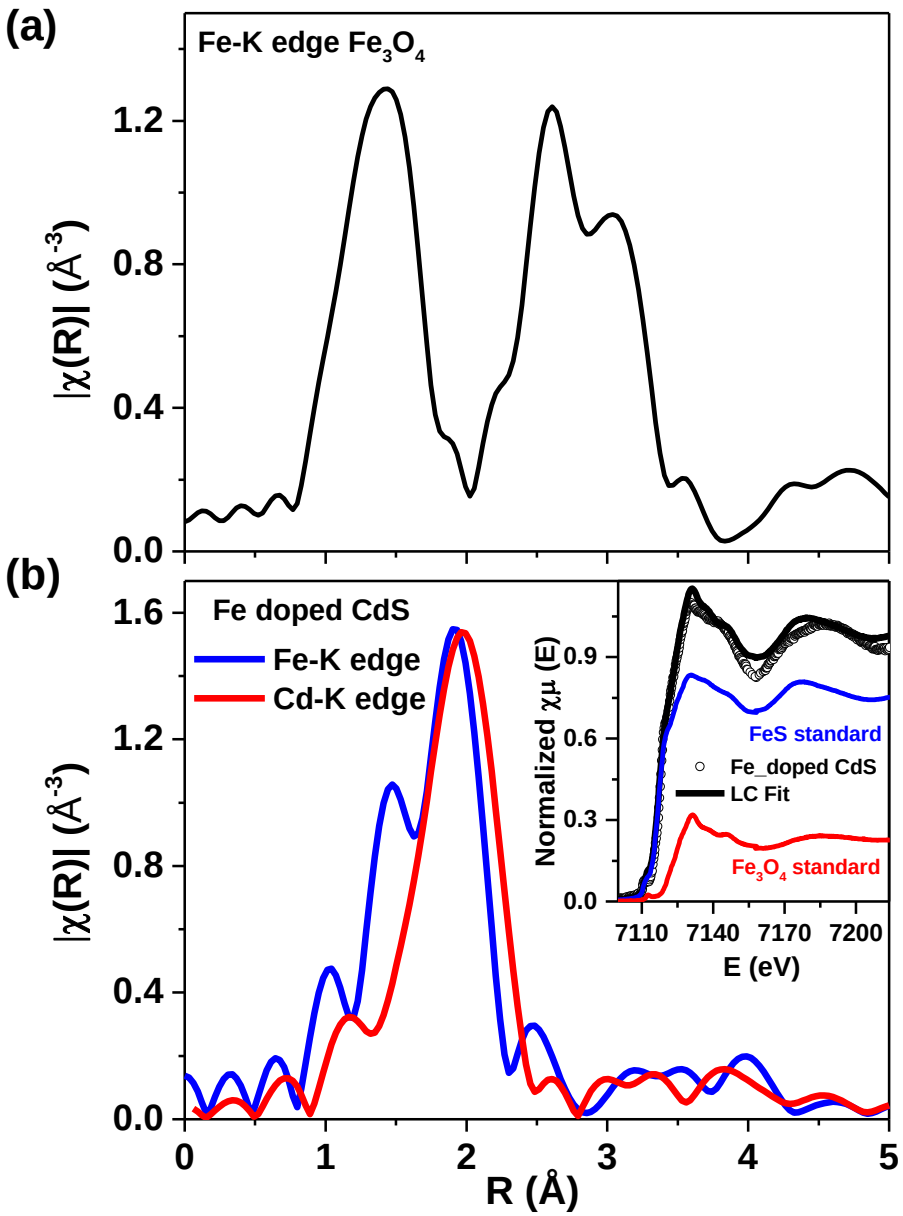

Figure 5.5: Magnitude of Fourier-transformed Fe-Kedge EXAFS spectra (open symbols) for Fe_3O_4 (a) and a comparison of Fe and Cd–K edge Fe-doped CdS (b). The linear combination fit (black solid line) of Fe-K edge XANES spectra (open symbols) with FeS (blue solid line) and FeO standard (red solid line) is shown in the inset.

The XANES spectrum of the Fe edge in the Fe-CdS is shown in the inset to Figure 5.5(b). From the figure, it is apparent that the spectra can be deconvoluted into a linear combination of Fe_3O_4 and FeS edges (also shown in Figure 5.5) with the dominant contribution arising from the FeS. This suggests that the iron has been reduced from an average oxidation state of +2.66 to +2. While this reduction in oxidation state is not surprising in presence of several reducing ligands like oleic acid, it is interesting to note that the iron has indeed reduced the oxidation state to accommodate into the CdS matrix as a dopant atom.

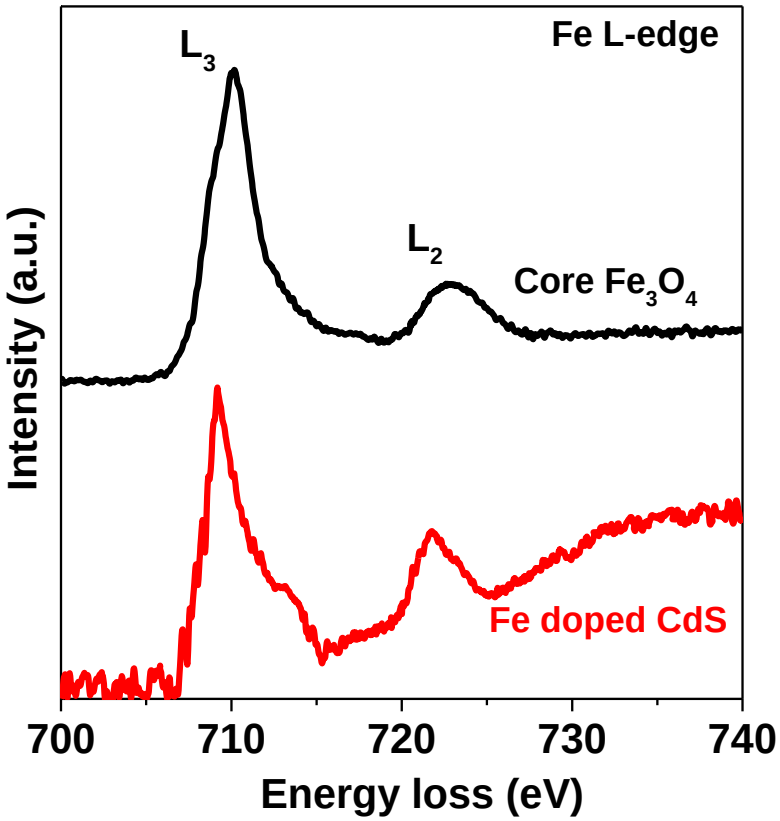

Figure 5.6: Fe $L_{2,3}$ edge electron energy loss near edge structure of core Fe_3O_4 (black line) and Fe-doped CdS (red line). The data have been normalized to the integral $L_{2,3}$ edge intensity.

Reduction in oxidation state is further confirmed by studying the ratio of $L_{2,3}$ edge in the Fe_3O_4 core as well as Fe doped CdS using EELS spectroscopy. Figure 5.6 shows the Fe $L_{2,3}$ near edge spectra after background subtraction for Fe_3O_4 core and Fe-doped CdS QDs. Consistent with the earlier literature,[56,57] we find that the Fe L_3/L_2 white line intensity ratio for the Fe doped CdS sample has reduced significantly from that of Fe_3O_4, due to a decrease in the oxidation state of Fe.

5.5.5 Elemental Mapping

However, a more direct evidence of Fe ion distribution inside these large CdS matrix has been observed by EDX elemental mapping images shown in Figure 5.7 (a-d). Large sizes of these particles allow us to capture significant resolution (STEM resolution ~1 nm) during imaging. From the spatial distribution of the elements Cd, S and Fe it is not only apparent that Fe is distributed throughout the CdS lattice, but that Cd atoms also span the complete area of the QD with no evidence of the iron oxide core suggesting the formation of uniformly distributed Fe doped CdS.

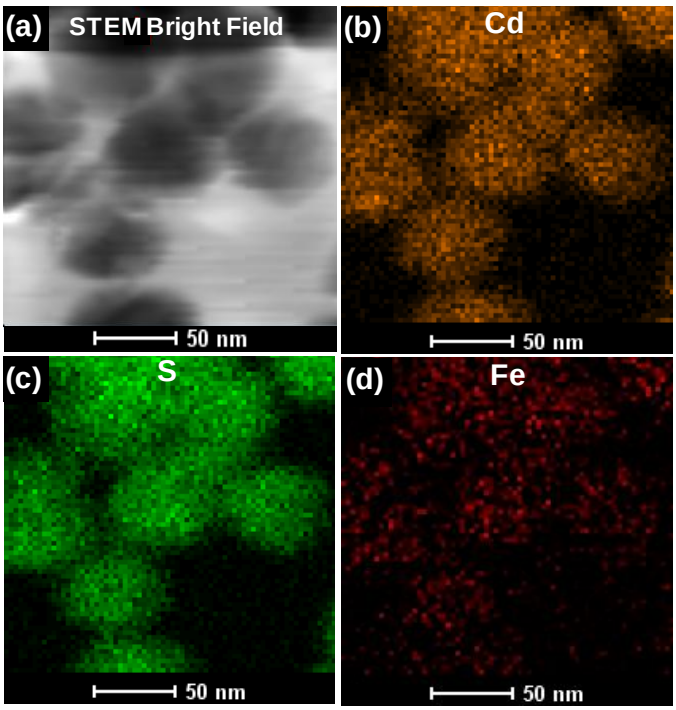

Figure 5.7: TEM elemental map of large size Fe doped CdS showing STEM (a) Bright field image (b) Cd map (c) S map (d) Fe map.

It has been seen that this technique, not only provides uniformity in dopant ions distribution, but also provides a pathway to achieve a long range size variation by controlling the reaction conditions. By appropriately tuning the core size, annealing time and other synthesis condition we have shown that it is possible to synthesize 5% Fe-doped CdS QDs with the sizes as large as ~60 nm (Figure 5.8(a)). Figure 5.8(a) and 5.8(b) showing TEM and HRTEM images respectively demonstrate that QDs have formed uniformly with no agglomeration and without any independent nucleation. Figure 5.8(c) shows the XRD pattern for these large size Fe-doped CdS QDs which matches well with bulk wurtzite structure. Absorption spectrum shown in

inset of Figure 5(c) depicts bulk CdS like absorption feature. Finally, it is worth noting that synthesis of such a large size, uniformly doped QDs having very less size distribution using a solution processed bottom up technique has not yet reported by any other group. It should also be noted that even though optical properties are sensitive to size in the quantum confined regime, magnetic properties are dictated by domain sizes. Typical domain sizes vary from about 50 nm to a few microns. Hence we obtained particles ranging upto 60 nm to study the confinement effects on the magnetic properties of the QDs. The magnetic measurement on this sample shows a large saturation magnetization as shown in Figure 5.8(d) thus substantiating the presence of confinement effects within the single domain in smaller QDs.

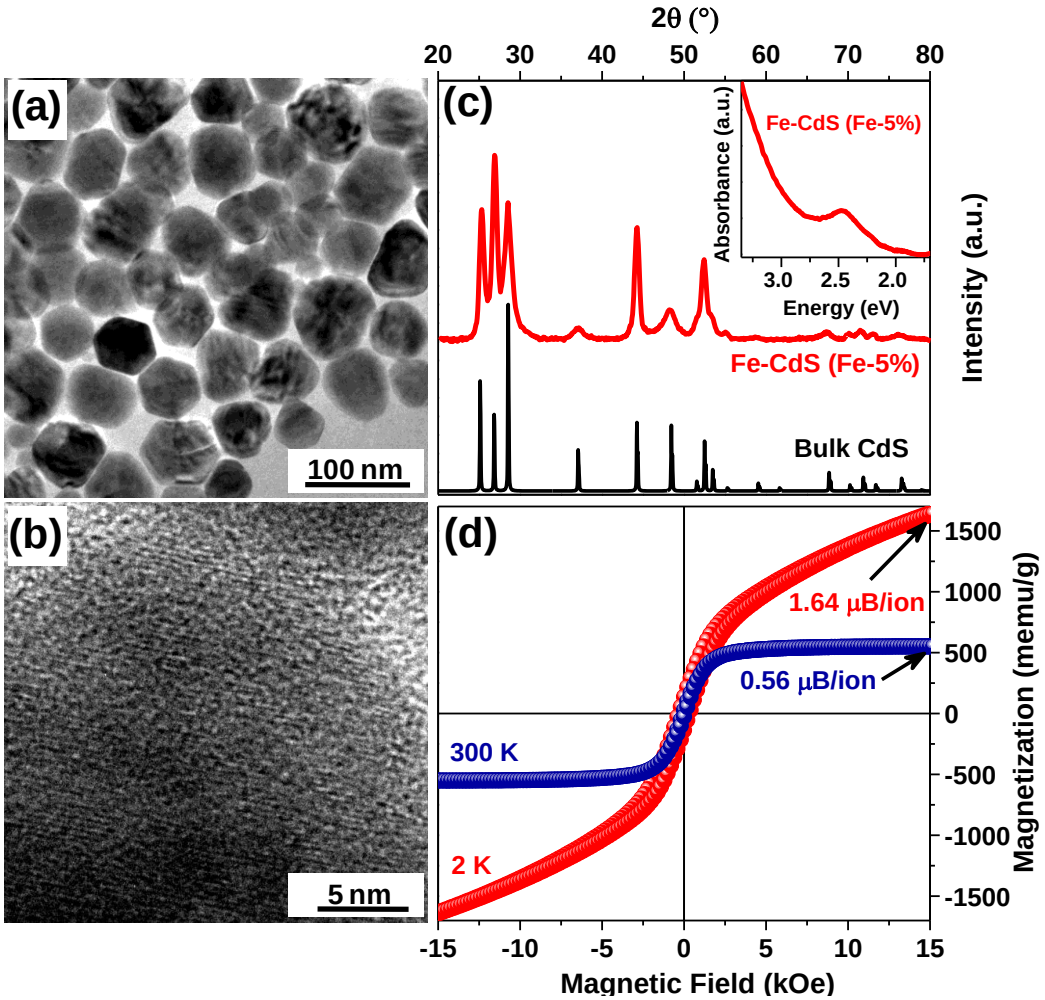

Figure 5.8: (a) and (b) are respectively TEM and HRTEM images for a large size (~60 nm) Fe-doped CdS (Fe-5%) QDs prepared by controlled synthesis. (c) X-ray diffraction patterns of these particles. Inset of (c) shows UV-VIS optical absorption spectra for the representative particles. (d) Magnetization (M) *vs.* field (H) hysteresis loop measured at 2 K (red symbols) and room temperature (blue symbols) for these particles.

5.5.6 Magnetic Properties

Magnetic properties in these materials are known to be influenced by the exchange coupling of 3d orbital electrons with the host semiconductor QDs' electronic levels.[58] Coey et al[59] showed that while conventional superexchange or double exchange cannot create long range magnetic ordering in case of dilute doping limit of transition materials inside the semiconductors, it is usually mediated by *sp-d* exchange interaction through the formation of magnetic bound polarons in the bulk systems. There have also been limited studies in the literature[35,60] on *sp-d* exchange interaction in semiconducting nanomaterials. However, a systematic understanding of these results have not been possible with varying concentrations of dopants and sizes as most of the magnetically doped QDs in the literature have a size smaller than 5 nm and very low dopant concentration (< 1%). These DMS QDs in the past have also shown several inconsistencies that is believed to be majorly due to the inhomogeneous distribution of paramagnetic dopants inside the semiconductor QDs. For example, enhanced excitonic Zeeman splitting has been observed in Mn^{2+} doped ZnSe[61] but reduced splitting has observed in Mn^{2+} doped CdS QDs[62], Co^{2+} doped ZnSe.[31] These discrepancies have been explained as due to inhomogeneous doping of magnetic ions inside DMS QDs. Gamelin group have studied the *sp-d* exchange interaction in Co^{2+} doped ZnSe QDs[13] prepared by hot injection technique and shown that excitonic Zeeman splitting is substantially smaller than its bulk counterpart which is again attributed to the absence of dopant ions inside the core or lack of homogeneous doping. It has been extensively studied and seen that, in most of the cases, these magnetic ions form magnetic islands where the spins couple anti-ferromagnetically resulting in reduced magnetic moments.[63] So, controlled synthesis and uniform doping of magnetic impurities is crucial to study magnetization leading to better magnetic properties than previously observed. So far, there have been many reports on DMS system and the observation of room temperature ferromagnetism in several of them due to magnetic impurities.[16,47,64] But the development has not improved much due to reproducibility of these materials. The lack of synthetic control leading to cluster formation in these materials results in low magnetic response as well as turn out to be useless for device applications. Our samples, shown to have a more uniform distribution with excellent control over size and dopant concentration using this synthetic technique can open up a new horizon to study the origin of magnetic interaction in DMS

systems. We performed a magnetization measurement of Fe-doped CdS obtained from this study to observe the consequences of the homogeneous distribution of dopant ions.

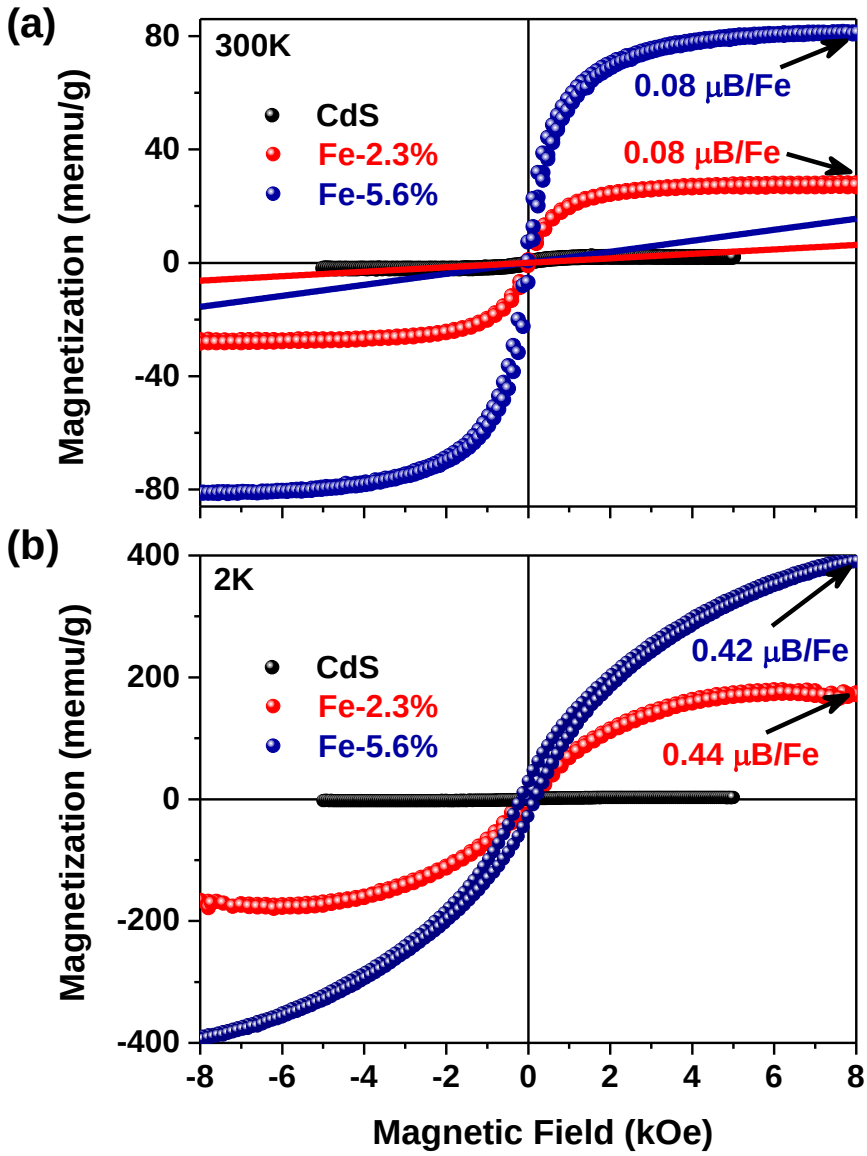

Figure 5.9: Magnetization *vs*. field plot (a) at Room temperature and (b) at 2 K for 0% (black symbols), 2.3% (blue symbols) and 5.6% (red symbols) Fe doped CdS QDs in comparison with un-doped CdS (black symbols). The solid blue (Fe-5.6%) and red (Fe-2.3%) lines are the simulated Brillouin function fit for the paramagnetic behavior of Fe-doped samples.

The results are compiled in Figure 5.9(a) and 5.9(b) showing the magnetization (M) *vs*. applied field (H) at room-temperature and at 2 K respectively for Fe doped CdS with two different percentages of Fe along with undoped CdS. The expected paramagnetic behavior of these ions simulated using Brillouin function at room temperature are also shown in Figure

5.9(a) clearly demonstrating the presence of ferromagnetic ordering rather than paramagnetic behavior. In fact, the shape of the magnetic hysteresis loop at room temperature is characteristic of the superparamagnetic behavior that arises due to the small size and single domain formation. Earlier reports[65,66] showed the presence of defect related magnetism in an otherwise non-magnetic system. Hence we studied undoped CdS QDs of similar size and the magnetic response obtained from these QDs is also shown in Figure 5.9 (a-b). Evidently the magnetism obtained in these QDs arise out of magnetic ion doping that overrides the earlier observation of defect related magnetism[65] by several orders of magnitude. Hence we tried to understand the origin of this magnetism by first studying the previously reported literature and putting our data in perspective. The results of the comparative study with other available literature reports, as expected, show almost an order of magnitude higher magnetization in these QDs compared to earlier results.[17,18] This dramatic increase should be closely related to the magnetic exchange interactions[24] between band carriers of the host CdS and magnetic ions or between magnetic ions and magnetic ions, since they control the optical, electronic, and magnetic properties of the DMS materials.

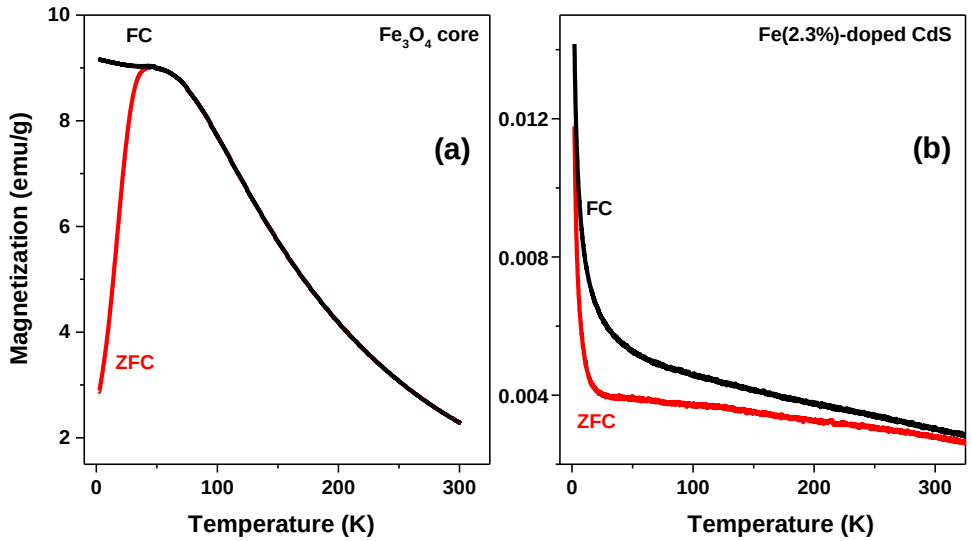

Figure 5.10: FC/ZFC magnetization curve for Fe_3O_4 core and Fe-doped CdS QDs using a field of 500 Oe.

The next step in understanding was to obtain the magnitude of this data with respect to the bulk data. Unfortunately, magnetism in quantum dots have posed a difficult challenge not only to synthesize uniformly doped QDs devoid of magnetic ion clusters but also to analyze due to the inability to express as magnetization per ion unlike in the bulk as one is not aware of the

amount of ligands attached to the QD. In addition, the size effects are also expected to decrease the magnetization though so far a systematic study of size effects is not available due to the above mentioned shortfalls. In this study, we have used TGA to study the amount of organic ligands present per gram of the sample. From these data, we have obtained an approximate value of the magnetization per ion and the saturation magnetization corresponding to the saturation value of each of these systems is indicated in the Figure 5.9 as well as tabulated in Table 5.2. It is well known that the size of the QDs contributes significantly in magnetization due to the change in domain size.[67] From the Table it is evident that as expected the magnetization increases from 0.42 μ_B/ion to 2.0 μ_B/ion at 2 K for 5% Fe as the size increases from 12.4 nm to 60 nm whereas no change is observed on changing the concentration of ions from 5% to 2.3% keeping size constant. This scaling of magnetism proportional to the concentration also provides further evidence that the magnetism is not due to the clustering effects. While this is an interesting observation, more in-depth studies with size and concentration controlled measurements have to be performed to understand the origin of this magnetism in dilute magnetic systems and will be discussed in later part of this chapter.

Finally the nature of magnetism has been studied from DC magnetic susceptibility by measuring ZFC and FC magnetization. It is observed from the Figure 5.10 that the nature of FC/ZFC curves of Fe-doped CdS QD are completely different from Fe_3O_4 core. Fe_3O_4 QDs show a clear blocking temperature at ~54 K which is a signature of transition from blocked state to superparamagnetic state. But, In the case of Fe-doped CdS FC/ZFC curves meet at very low temperature (~2K). This further tells the fact that Fe_3O_4 cluster does not exist anymore inside the CdS matrix.

Table 5.2: Magnetization value in Bohr Magneton per magnetic ion

Sample	M_s per magnetic ion at 300K (μB)	M_s per magnetic ion at 2K (μB)
Fe_3O_4 core (4.5nm)	0.64 (46.5 memu/g)	0.9 (64.1 memu/g)
Fe-10CdS (5.6%, 12.6 nm)	0.09 (0.10 memu/g)	0.42 (0.45 memu/g)
Fe-14CdS (2.3%, 15.4 nm)	0.08 (0.034 memu/g)	0.44 (0.23 memu/g)
Fe_3O_4 (7.2 nm)	1.01 (72.9 memu/g)	1.21 (87.9 memu/g)
Fe-CdS (5%, 60nm)	0.68 (0.67 memu/g)	2.0 (1.99 memu/g)

5.6 Conclusion

In conclusion, our results show a direct correlation between synthetic control and magnetic properties in magnetic semiconductor. Using the principle of self purification to our advantage, we have introduced a new generic synthesis technique to obtain uniform, doped semiconductor QDs with transition metal ions that are rid of clustering effects. We have used XAFS and XRD to prove the absence of magnetic islands in these QDs. We have also shown that this leads to better magnetic response paving way for future applications. We have chosen Fe-doped CdS quantum dot nanostructure as a model system for most of our study. This opens up a new possibility to first understand the origin of magnetism in DMS quantum dots followed by effective manipulation of the magnetic spin interaction inside any semiconductor materials. These findings will have far reaching consequence in potential application of these materials for future spintronics device.

Section B

Local Environment Study Using XAFS

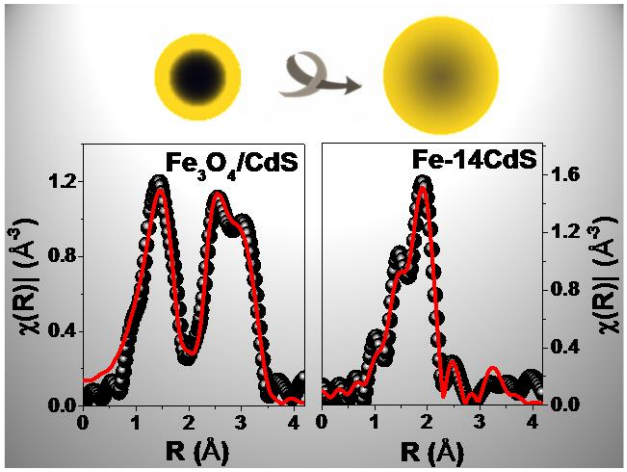

5.7 Summary

Internal structure study at an atomic level is a challenging task with far reaching consequences to its material properties, specifically in the field of transition metal doping in quantum dots. Diffusion of transition metal ions in and out of quantum dots forming magnetic clusters has been a major bottleneck in this class of materials. Diffusion of the magnetic ions from the core into the non-magnetic shell in a core/shell heterostructure architecture to attain uniform doping has been discussed in the earlier chapter and yet to be understood. In this part, we have studied the local structure variation of Fe as a function of CdS matrix thickness and annealing time during the overcoating of Fe_3O_4 core with CdS using X-ray absorption spectroscopy. The data reveals that Fe_3O_4 core initially forms a core/shell structure with CdS followed by alloying at the interface eventually completely diffusing all the way through the CdS matrix to form homogeneously Fe doped CdS QDs with excellent control over size and size distribution. Study of Fe K-edge shows a complete change of Fe local environment from Fe-O to Fe-S.

5.8 Introduction

Interest in dilute magnetic semiconductors (DMS) in bulk and quantum confined materials have increased dramatically in the past decade with its potential for applications in spintronics and other magneto-optical applications.[14,68] In this aspect, DMS quantum dots (DMSQDs) have emerged as a new class of materials having shown several interesting DMS properties like Faraday effect, giant Zeeman effect.[30,31] However, these properties, specifically their size dependence, have not been well studied in the literature as doping in QDs is rather non-trivial. Specifically, most of the QDs synthesized so far are of the order of 5 nm and larger QDs that are smaller than typical domain sizes, i.e., between 5-30 nm, have proven to be elusive. The bottleneck in the study of these systems has been the uniform distribution of transition metal within the QD. Several strategies for QD doping,[41] have been extensively studied and some techniques like nucleation doping,[69] dopant insertion at growth stage[70] or optimal use of temperature to retain the dopant,[42] interplay between the thermodynamic versus kinetic control[71] have evolved over a period of time with reasonable success in the quantum size regime. However, DMSQDs prepared using these techniques are quite small, typically around 5 nm, by the time the dopant atom is expelled from the host. Hence size dependences ranging upto typical domain sizes have not been possible. In addition, these materials are often plagued with impurity phase or clustering leading to erroneous magnetic properties.[18,47,72,73] So the

introduction of reliable synthesis strategies and proper characterization techniques are essential to study the internal microstructure of DMSQDs which is known to show significant changes in optical[50,74] and magnetic properties.[24,37]

In an effort to probe this elusive size regime, we employed the method of diffusion of dopants from inside out. It is known that core-shell QDs and modification of their interface through long time annealing show superior optical properties and promising device applications.[50,75,76] In this work, we have employed the use of magnetic cores with semiconducting shell heterostructures along with long time annealing at high temperature. Specifically, we started with a small Fe_3O_4 cluster and used high temperature to create self-diffusion [36,77,78] to diffuse it out into a thick CdS semiconductor matrix and obtain uniformly distributed Fe doped CdS QDs. It is expected that the magnetic dopant diffuses within the semiconductor matrix giving rise to uniformly doped large sized QDs as discussed in the previous section of this chapter. However, so far it has been a challenge to follow the internal structure evolution during synthesis of these systems. While X-ray diffraction can trace the change in crystal structure, smaller impurity clusters of the magnetic core cannot be detected, especially due to the broadening of the peaks due to their finite size. High resolution TEM, and elemental mapping have also failed to probe within the length scale of interest. Hence in this scenario, the investigation of the micro structural evolution by probing the local environment around impurity atoms would provide excellent insight into the local structure.

XAFS analysis is a powerful tool for the determination of local environment around the specific atoms.[20,79-81] We focused on two typical X-ray energy regions of XAFS spectrum, namely XANES and EXAFS. The XANES spectrum extends from just below absorption edge to 50 eV above and serves as a site specific probe of the local charge state and coordination geometries of the absorbing atom. Above this energy, the EXAFS is manifested as oscillations in the absorption cross section arising from constructive and destructive interference of outgoing photoelectron wave and the incoming photoelectron wave backscattered from neighboring atom, which provides quantitative information about average local coordination number, bond lengths and their distribution between the absorbing and surrounding atoms. In this section, we report a detailed analysis of local structure evolution on Fe_3O_4-CdS nanoparticles starting from core-shell heterostructure to doped systems and we correlate these findings with X-ray diffraction results.

5.9 Experimental Details

5.9.1 Synthesis

Synthesis of Fe_3O_4 core has been described in section 5.4.1 and the core has been overcoated with Cd and S precursors using SILAR method[44] at high temperature to form Fe-nCdS where n denotes the number of CdS monolayers. Aliquots were collected after completion of each monolayer for characterization.

5.9.2 XAFS Measurement

EXAFS and XANES spectroscopy were employed to probe the local structure around Fe and Cd atoms during for the Fe doped CdS QDs. Fe K-edge (7112 eV) and Cd K-edge (26711 eV) for the samples were measured at 10ID beamline at Advance Photon Source, Argonne National Laboratory.[49] Rhodium coated harmonic rejection mirror and Pt mirror were used to eliminate the higher energy photons for Fe edge and Cd edge respectively. Experiments were performed in fluorescence mode using ion chamber with Stern Heald geometry. The gases in the ion chambers were optimized for adequate absorption of photons and linearity was ensured. A mixture of 80% helium and 20% nitrogen gas was used in the initial ion chamber I_o placed before the sample and full nitrogen gas in transmission and reference ion chambers. Argon gas was used for fluorescence ion chamber. For Cd edge, pure nitrogen was used in the I_o ion chamber and a mixture of 10% nitrogen and 90% argon gas in the transmission and reference ion chambers. Kr gas was used in the fluorescence ion chamber when latter was used.

X-Ray energy was calibrated to 7112 eV with Fe metal foil before measurements were done. Relevant iron standards were measured in transmission geometry with Fe foil in front of the reference ion chamber. The spot size of the incident X-ray beam on the sample was 800 by 800 microns. The samples were initially mapped and ensured for homogeneity of particles distributions before the EXAFS measurements. Measurements were done in quick scanning mode, where undulator gap and taper were fixed for each of the edges while Bragg angle of double crystal monochromator (with Si (111)crystal) was scanned with constant speed. The EXAFS scans were taken from 6900 eV to 7900 eV with a step size of 0.35 eV and 0.03 second per step. Several scans were taken for each sample to ensure the absence of degradation of samples and averaged before fitting was done for statistics.

Data were processed using Athena software[54] by extracting the EXAFS oscillations $\chi(k)$ as a function of photoelectron wave number k following standard procedures. The theoretical model

was generated consistent with the other characterization techniques and the corresponding paths were generated using FEFF6.[82] Fitting of the theoretical model to the experimental data was carried out using fitting program Artemis[77] with FEFF6 built into it. In order to isolate the $\chi(k)$ oscillations, the atomic background was subtracted by applying a low distance cut off equal to 1Å in the Fourier transform and using a cubic spline. Fourier filtering was accomplished with a k weight equal to 2, in a range from 2 to ~10 $Å^{-1}$. Amplitude reduction factor (S_o^2) for Fe was obtained from the fitting of Fe metal foils. Fitting parameters were obtained by modeling the EXAFS data of each sample in real (R)-space until a satisfactory global fit describing the system was obtained.

5.10 Results and Discussion

The evolution of internal structure in Fe-nCdS was studied on a series of samples with varying values of n, the number of monolayers of CdS. A value of n=0 implies only Fe_3O_4 core with no CdS overcoating. In this work, we have used Fe-0CdS, Fe-2CdS, Fe-4CdS, Fe-5CdS, Fe-10CdS and Fe-14CdS to study the evolution of internal structures. The presence of Fe in these samples was determined by ICP-OES measurements and was found to be respectively 100 %, 57.7 %, 20 %, 17.8 %, 5.6 % and 2.3 %. Specifically, the presence of 5.6% and 2.3 % Fe in Fe-10CdS and Fe-14CdS respectively, indicates the dilute doping regime within QDs. These samples were then characterized by TEM and XRD.

5.10.1 Microstructure

Morphology and the particle size evolution during the growth of the nanoparticles have been studied using high resolution TEM. Figure 5.11(a) shows the HRTEM images of Fe-0CdS having average size 4.5 nm and Figure 5.11(b-f) show the differing monolayers of CdS overcoated Fe_3O_4. It is clear from the images that the particle size with increasing monolayers of CdS grows monotonically, averaging about ~0.35 nm thickness per monolayer as expected. Smaller secondary phases of pure CdS are not observed in these samples which lead to the conclusion that all the particles are overcoated as expected. Nevertheless, the presence of any magnetic islands inside the CdS matrix, due to the significant absence of contrast between Fe and Cd atoms, is not possible to observe in HRTEM even in Fe-2CdS and Fe-4CdS where there is proven evidence of clustering from XRD shown in Figure 5.3. Hence, TEM is insensitive to the presence or absence of Fe clusters within the QDs as well as Fe atoms distribution.

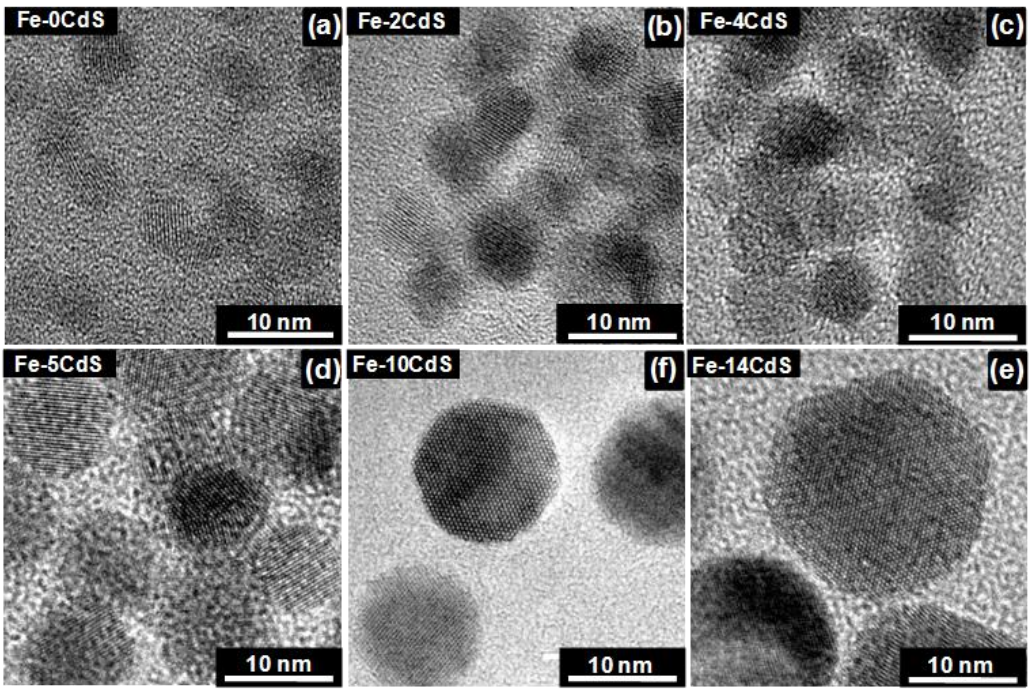

Figure 5.11: HRTEM images showing (a) 4.5 nm Fe_3O_4 core (b) Fe-2CdS (c) Fe-4 CdS (d) Fe-5CdS (e) Fe-10CdS (f) Fe-14CdS.

Typical XRD patterns are shown in Figure 5.3(a). The XRD pattern of Fe-0CdS is assignable to the contribution from a magnetite (Fe_3O_4) cubic inverse spinel structure without any impurity phase formation. With the formation of CdS layer both cubic Fe_3O_4 and wurtzite CdS peaks are visible for first few layers which eventually turns into complete wurtzite CdS structure after thick shell formation. The complete disappearance of Fe_3O_4 characteristic peaks in thick shell nanoparticles may be due to the diffusion of Fe_3O_4 inside CdS. However, given the width of the peaks, small clusters of Fe may not be seen given the broad signals with small signal to noise ratio in these materials and hence cannot convincingly prove uniform Fe distribution within the CdS matrix.

5.10.2 Local Structure Analysis

5.10.2.1 XANES

In order to investigate the evolution of the internal structure during high temperature annealing of Fe_3O_4-CdS nanoparticles at their different stages, we studied their local structure using XAFS spectroscopy. To accomplish this goal, XANES and EXAFS were employed to probe the variation of co-ordination number and different bond contribution. A series of XAFS fluorescence spectra were collected at Fe K-edges for various samples starting from Fe-0CdS to

Fe-14CdS. The data were processed using ATHENA[54] and the Fe K-edge XANES spectra are shown in Figure 5.12.

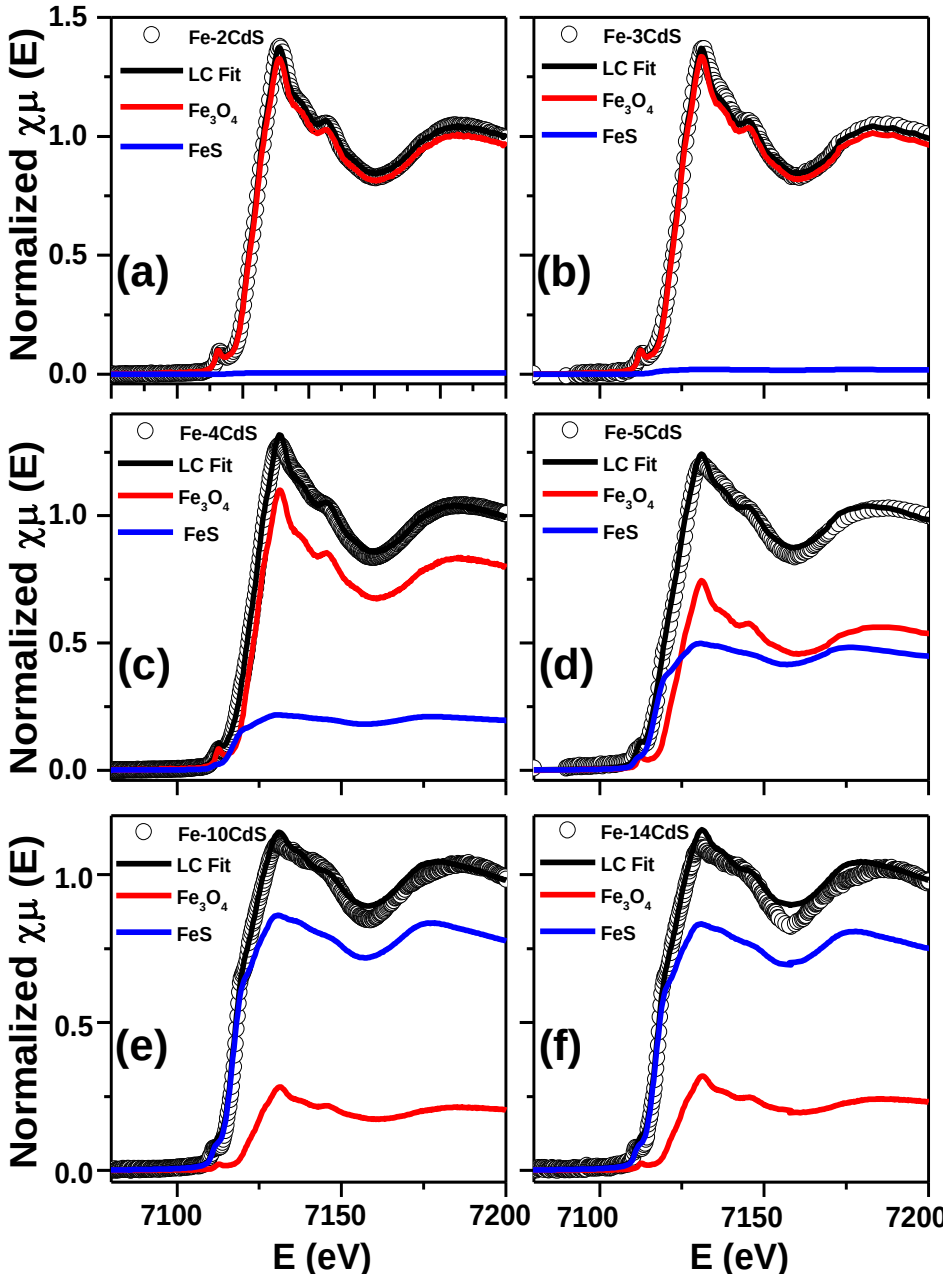

Figure 5.12: Fe K-edge XANES spectra (open symbols) for (a) Fe-2CdS, (b) Fe-3CdS, (c) Fe-4CdS (d) Fe-5CdS, (e) Fe-10CdS and (f) Fe-14CdS. All these XANES spectra were fitted with linear combination (black solid line) of FeS (blue solid line) and Fe_3O_4 standard (red solid line).

The analysis from XRD suggests that the Fe from Fe_3O_4 is migrating into the CdS lattice. This implies that the possible phases could include FeO, Fe_3O_4 and FeS. XANES data provides

insight regarding the oxidation state of the metal ion and hence we tried to obtain a linear combination fit of the experimental XANES data to the standard FeO, Fe_3O_4 and FeS data. The data were fit very well with combination of these standards, indicating the coordination environment around Fe in these samples were either similar to oxides, or sulfide. From the analysis it was evident that the FeO contribution was negligible compared to the other two phases and the results of the FeS and Fe_3O_4 contributions are shown in Figure 5.12. During the first few monolayers of CdS overcoating over Fe_3O_4, the XANES look very similar to Fe_3O_4 and the linear combination fit shows that the maximum contribution comes from Fe_3O_4 spectra with negligible contribution from FeS as shown in Figure 5.12(a) and 5.12(b) and tabulated in Table 5.3. The implications of these results translate into Fe_3O_4/CdS core/shell heterostructure with short range alloying at the interface due to the diffusion of Fe^{2+} into CdS structure at this stage of CdS overcoating. However, as we increase the CdS monolayers as well as annealing at high temperature as in the case of Fe-4CdS and Fe-5CdS as the linear combination fits show there are some significant contributions from FeS as depicted in Figure 5.12(c), 5.12(d) and in the Table 5.3. Almost 50% contribution of FeS in Fe-5CdS suggests that a major part of Fe core has diffused into CdS structure. Finally, at Fe-10CdS (Figure 5.12(e)) and Fe-14CdS (Figure 5.12(f)) the XANES data can be explained largely by the presence of Fe-S contribution (~85%) supporting the fact that Fe has completely diffused inside the CdS matrix. The small amount of Fe_3O_4 contribution could be due to small clusters of Fe core inside or the presence Fe-O-Cd bonds within the CdS matrix. This can be studied using the quantitative EXAFS analysis of the nearest neighbors.

Table 5.1: Fe_3O_4 and FeS ratio obtained from linear combination fit of XANES spectra.

Sample	Fe_3O_4 (%)	FeS (%)
Fe-2CdS	99.4(±0.6)	0.6(±0.02)
Fe-3CdS	98.1(±0.9)	1.9(±0.23)
Fe-4CdS	80(±0.7)	20(±0.5)
Fe-5CdS	54.1(±0.9)	45.9(±0.05)
Fe-10CdS	20.5(±0.8)	79.8(±0.7)
Fe-14CdS	16.4(±1.8)	83.6(±1.4)

5.10.2.2 EXAFS: k-space

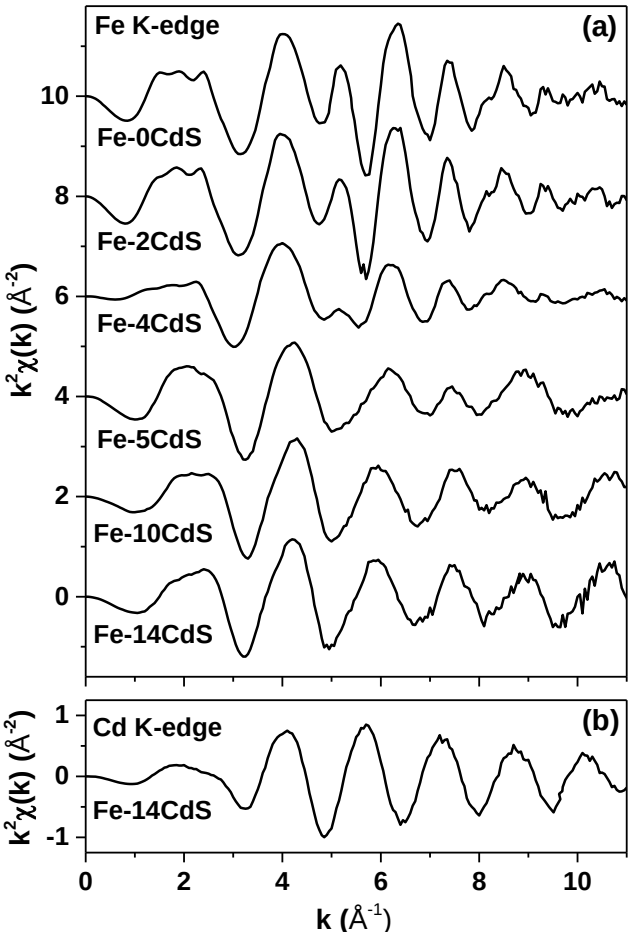

Figure 5.13: k^2-weighted $\chi(k)$ oscillations for (a) Fe K-edge for different Fe-nCdS samples and (b) Cd K-edge for Fe-14CdS sample. The Fe K-edge plots are presented with a constant offset of 2.0 units for the purpose of better viewing.

While the XANES region is known to give information about the oxidation state of the Fe ion, the information regarding the local first and second shell structure around the absorbing atom (Fe) can be obtained from analyzing the EXAFS region of the data. The evolution of the local structure around Fe with the addition of CdS shell growth at high temperature is studied by analyzing EXAFS region of the series of Fe-nCdS samples. Fe K-edge $\chi(k)$ data for all the samples have been shown in Figure 5.13(a). The k-space oscillations during the initial phases of CdS overcoating show striking changes, specifically at k values between 3-6 $Å^{-1}$ compared to the later overcoating stages suggesting an evolution in the local structure around Fe atoms due to slow Fe diffusion inside CdS matrix. However, it is also evident that the plots look very similar for the Fe edge and Cd edge (Figure 5.13(b)) for thicker CdS overcoating layers. This

result confirms that after a significant CdS shell formation at high temperature, Fe ions have uniformly distributed throughout the CdS matrix by substitution of few Cd atoms and formed uniformly doped CdS QDs.

5.10.2.3 EXAFS: R-space

For further confirmation, the data from these samples were Fourier transformed and plotted in R-space as shown by open circles in Figure 4(a)-(f). Visual inspection of these real (R) space EXAFS plots makes it evident that local structure around Fe is gradually converting from Fe_3O_4 to a completely new structure through different stages of Fe-nCdS.

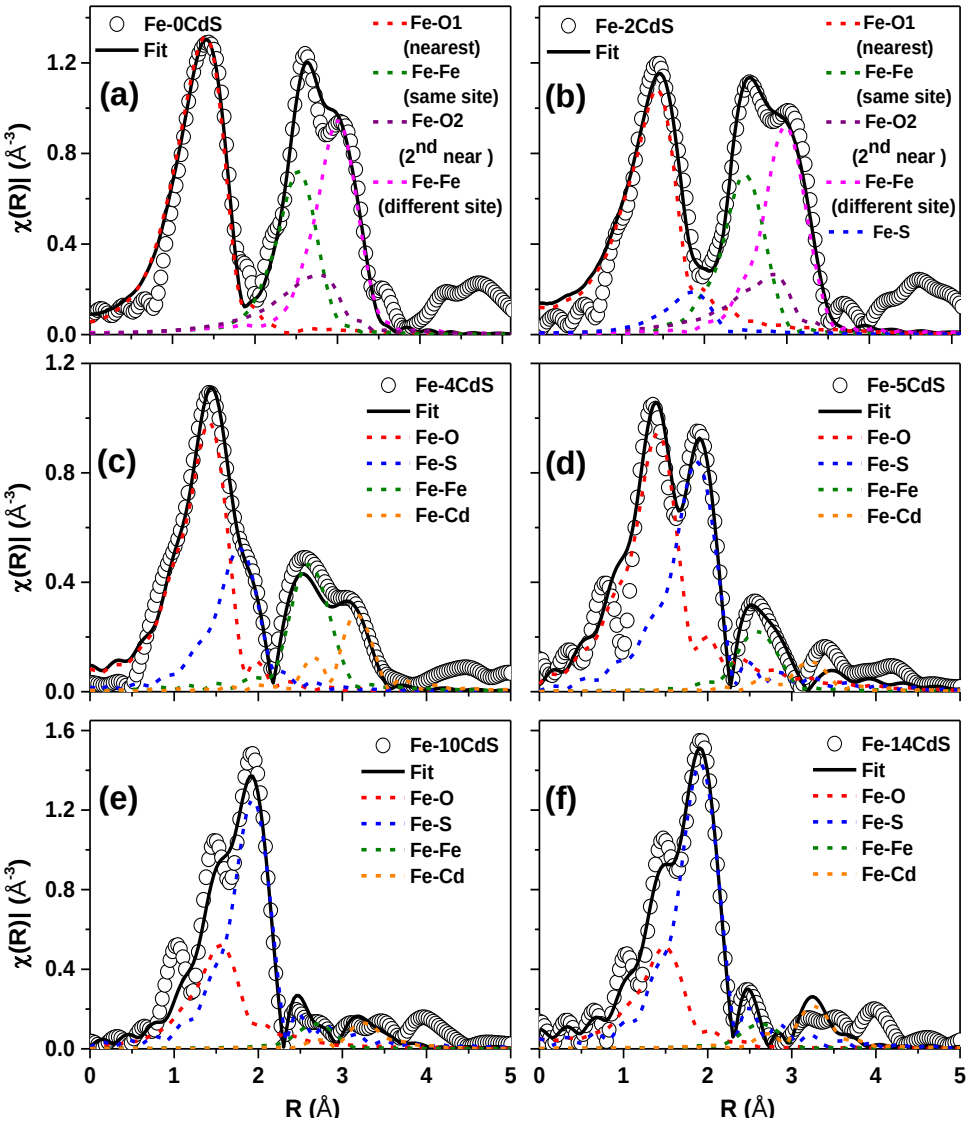

Figure 5.14: Magnitude of Fourier-transformed Fe K-edge EXAFS spectra (open symbols) and their best fit (solid line) for (a) Fe_3O_4, (b) Fe-2CdS, (c) Fe-4CdS, (d) Fe-5CdS, (e) Fe-10CdS and (f) Fe-14CdS. Dotted lines show their component fitting paths.

However, in order to obtain more quantitative information we modeled the EXAFS spectra to a theoretical model and generated the relevant paths using FEFF6 within the ARTEMIS[77] program. The theoretical model consisted of Fe_3O_4 in its cubic form with space group Fd3m (a= 8.39Å) and FeS in the wurtzite crystal structure with space group $P6_3mc$ (a= 3.43 Å, c=5.68 Å). The solid lines represent the best fit obtained from this procedure, whereas the dotted lines depict the component paths necessary to achieve this fit. Figure 5.14(a) shows the experimental data and the fit to Fe-0CdS. As expected the fit and the components are very similar to the earlier reported EXAFS spectra for Fe_3O_4 present in inverse spinel structure[52] suggesting that the small size has not affected the environment within the QDs. It is well known that Fe_3O_4 crystallizes in cubic inverse spinel structure[83] wherein oxygen ions form an fcc close packing with Fe^{3+} in one of the eight tetrahedral interstices and $Fe^{2+/3+}$ in half of the octahedral interstices. It was necessary to use different Fe-O and Fe-Fe bonding arising from tetrahedral and octahedral sites as shown in Figure 5.14(a) since Fe^{2+} and Fe^{3+} has different edge energy and thus different ΔE (approximately 5 eV). Table 5.4 provides a complete breakup of the various paths used in the fit to Fe-0CdS. The complex structure of Fe_3O_4 results in nine significant paths contributing to fit the experimental data (tabulated in Table 5.4). Similar to literature reports,[84] we also observed a 5 eV shift in energy between Fe^{2+} and Fe^{3+} ions that are octahedrally coordinated with O atoms (shown in Table 5.4). In Figure 5.14(a), the peak at 1.43 Å shown in red dotted line due to the Fe-O bond is the convolution of three different bonds arising due to the nearest oxygen whereas the peak at 2.91 Å is due to Fe-O, second nearest oxygen present in the system. Similarly, Fe-Fe bonds due to same and different interstices contribute to the peaks at 2.45 Å and 2.95 Å respectively.

Figure 5.14(b) shows the fit to Fe-2CdS where we also observe dominant contributions (as quantified by the coordination number discussed later in the text) of Fe-O and Fe-Fe paths consistent with the inverse spinel structure observed in XRD. However, it is interesting to note that along with these paths, we also require a small contribution from the Fe-S peak at 1.82 Å to obtain a good fit to the data. This small Fe-S component can be attributed to the formation of an ultrathin layer of FeS at the interface between Fe_3O_4 core and CdS shell. Systematic analysis of the EXAFS data from samples with increasing CdS shell thickness, we observe that the Fe-S path is increasingly more prominent with decreasing contribution from the inverse spinel structure of Fe_3O_4 as observed in Figure 5.14(c)-(f) for samples Fe-4CdS to Fe-14CdS

respectively. Moreover, we present the Cd K-edge data for few samples with a comparison to undoped CdS as demonstrated in Figure 5.15. It's evident that Cd K-edge looks similar in all cases and corresponds to Cd-S path in the wurtzite structure and remains unchanged with shell thickness. The similarity of the Fe-edge with the Cd-edge for thick overcoating of CdS provides further credence to our diffusion theory.

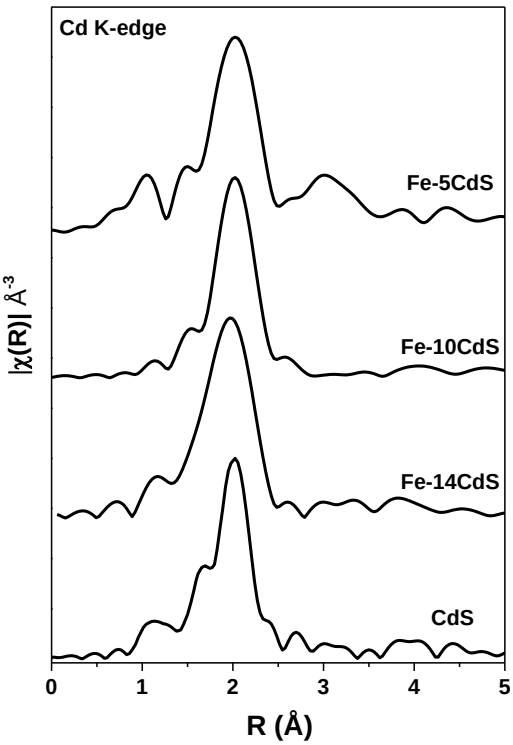

Figure 5.15: Magnitude of Fourier-transformed Cd K-edge EXAFS spectra for Fe-5CdS, Fe-10CdS, Fe-14CdS and undoped CdS.

However, the presence of a Fe-O path in the EXAFS as well as the XANES data raises the question about the presence of a small core of iron oxide. Nonetheless, we observe that there is a complete absence of the expected second nearest neighbour Fe-Fe contribution as observed in the different phases of iron oxide as shown in Figure 5.16(a). Additionally, in the thicker shells of CdS, we observe the emergence of a correlation, Fe-Cd, at 3.12 Å. However it should be noted that as expected[85] the Fe-O/Fe-S bond length is not the same as Cd-S bond length leading to some amount of disorder in the second order coordination. Due to extremely small particle size, the surface becomes an essential part of the system with highly disordered structure and coordination making it impossible to observe signals at higher k values required to obtain higher level coordination. In addition, local distortions due to differences in Fe-S and Cd-S bond lengths[85] coordination with Fe-O can give rise to highly distorted local coordination.

These large changes eventually translate into an average overall long range order which is much lower than expected average coordination number (~1) obtained for Fe-Cd bonding.

This suggests the fact that Fe_3O_4 is indeed diffusing in CdS matrix by replacing few Cd atoms with Fe atoms eventually leading to Fe as a substitutional impurity within the CdS lattice. At the final stages i.e. in the case of Fe-10CdS and Fe-14CdS, it is evident from the Figure 5.14(e) and 5.14(f) that the dominant contribution is coming from Fe-S path along with small contribution from Fe-O, Fe-Fe and Fe-Cd paths. The detailed results and the fit parameters from the entire fitting procedure are tabulated in Table 5.4.

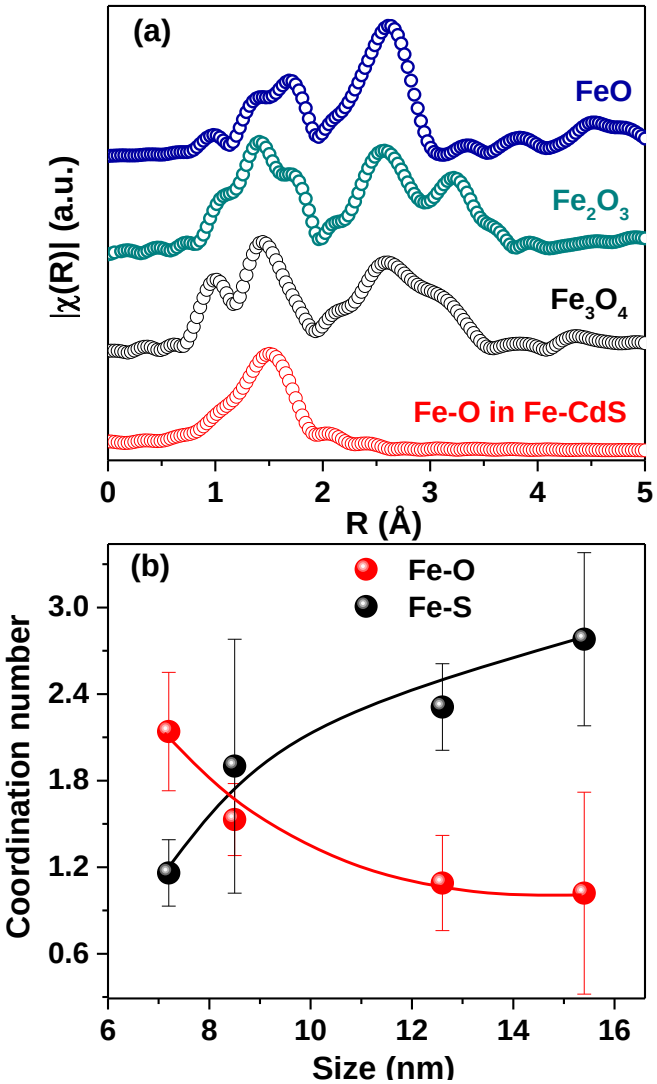

Figure 5.16: (a) A comparison of Fourier-transformed Fe K-edge EXAFS spectra of FeO (blue), Fe_2O_3 (dark cyan), Fe_3O_4 (black) with Fe-O path in Fe-doped CdS (red). (b)Variation of local coordination number around of Fe considering the nearest oxygen (red symbols) and sulfur (black) atoms from XAFS results. Solid lines are guide to the eye.

Table 5.4: List of fit parameters (Independent Points (N_{idp}) and Number of variables (N_{var}) for the fit, Bond length (R), coordination number (N), Debye waller factor (σ^2) energy shift (ΔE) and R-factor) obtained from modeling the data for Fe-K edge.

Sample	Paths		R (Å)	N	(σ^2)	ΔE (eV)	R-factor
Fe-0CdS k=1.2-13.5 Å^{-1} R=1-3.8 Å N_{idp} = 19 N_{var} = 8	Fe_3O_4 tetrahedral Fe^{3+}	Fe^{3+}-O1	1.86±0.02	1.06	0.005±0.004	-2.06 ±1.02	0.0052
		Fe^{3+}-FeOct1	3.45±0.02	3.2	0.009±0.001		
		Fe^{3+}-O2	3.47±0.02	3.2	0.006±0.007		
	Fe_3O_4 octahedral Fe^{3+}	Fe^{3+}-O1	1.98±0.07	1.6	0.006±0.001		
		Fe^{3+}-FeOct1	2.97±0.01	1.6	0.009±0.001		
		Fe^{3+}- Fe tet1	3.48±0.01	1.6	0.009±0.001		
	Fe_3O_4 octahedral Fe^{2+}	Fe^{2+}-O1	1.98±0.07	1.6	0.007±0.001	-7.06±1.02	
		Fe^{2+}-FeOct1	2.97±0.01	1.6	0.009±0.001		
		Fe^{2+}- Fe tet1	3.48±0.01	1.6	0.009±0.001		
Fe-2CdS k=2-11 Å^{-1} R= 1-4 Å N_{idp} = 19 N_{var} = 12	Fe-S		2.37±0.05	0.56±0.05	0.010	-3.25	0.0033
	Fe_3O_4 tetrahedral Fe^{3+}	Fe^{3+}-O1	1.87±0.02	1.06	0.012±0.003	-3.15±0.93	
		Fe^{3+}FeOct1	3.46±0.02	3.2	0.009±0.001		
		Fe^{3+}-O2	3.47±0.02	3.2	0.009±0.008		
	Fe_3O_4 octahedral Fe^{3+}	Fe^{3+}-O1	1.94±0.11	1.6	0.008±0.002		
		Fe^{3+}-FeOct1	2.95±0.01	1.6	0.008±0.001		
		Fe^{3+}- Fe tet1	3.47±0.01	1.6	0.008±0.001		
	Fe_3O_4 octahedral Fe^{2+}	Fe^{2+}-O1	1.94±0.11	1.6	0.008±0.002	-8.15± 0.93	
		Fe^{2+}-FeOct1	2.96±0.02	1.6	0.008±0.001		
		Fe^{2+}- Fe tet1	3.47±0.01	1.6	0.008±0.001		
Fe-4CdS k= 1-11 Å^{-1} R= 1-4 Å N_{idp} = 19 N_{var} =10	Fe-O		1.97±0.22	2.14±0.41	0.003±0.002	-2.59 ± 1.74	0.0003
	Fe-S		2.36±0.06	1.16±0.23	0.005		
	Fe-Cd		3.32±0.17	0.82±0.27	0.004		
	Fe-Fe		3.04±0.04	1.48±0.22	0.005±0.001		
Fe-5CdS k=2 -11 Å^{-1} R=1.1-4 Å N_{idp} = 19 N_{var} = 10	Fe-O		1.91±0.29	1.53±0.25	0.005±0.001	-3.76±3.06	0.0094
	Fe-S		2.33±0.10	1.93±0.91	0.007±0.001		
	Fe-Cd		3.33±0.16	0.40±0.44	0.003±0.001		
	Fe-Fe		3.00±0.02	0.72±0.50	0.005±0.002		
Fe-10CdS k=2-11 Å^{-1} R= 1.1-4.1 Å N_{idp} = 29 N_{var} = 16	Fe-O		1.98±0.22	1.09±0.33	0.008±0.002	3.16 ± 1.67	0.0052
	Fe-S		2.39±0.05	2.31±0.30	0.004		
	Fe-Cd		3.34±0.15	0.56±0.52	0.005		
	Fe-Fe		3.01±0.02	0.30±0.10	0.007±0.001		
Fe-14CdS k=2- 11 Å^{-1} R=1.0-4.1 Å N_{idp} = 30 N_{var} = 16	Fe-O		1.98±0.21	1.02±0.78	0.006±0.003	1.01 ± 4.10	0.0049
	Fe-S		2.38±0.05	2.78± 0.6	0.020±0.004		
	Fe-Cd		3.35±0.15	0.73± 1.3	0.011		
	Fe-Fe		2.99±0.01	0.32± 0.10	0.007		

A similar trend can be found by looking at the coordination numbers of Fe shown in Figure 5.16(b) as well as in supporting information Table 5.4. The total coordination numbers for Fe are found to be in the range of 3.5 to 4.5, averaging about 4, as expected. However, individually, we observe that the coordination number of Fe-O is seen to reduce from 4.26 in Fe-0CdS to 1.02 (±0.78) in Fe-14CdS as the particle size increase from 4.5 nm to 15.4 nm. Similarly, the coordination number of the Fe-S path increased from 0 in Fe-0CdS to 2.78 (±0.60) in Fe-14CdS. However, the bond lengths of the two paths remain consistent at 1.96 ± 0.2 Å and 2.36 ± 0.10 Å for Fe-O and Fe-S respectively. Figure 5.16(b) shows the variation of co-ordination number around Fe considering the nearest oxygen and sulfur atom.

In light of this, all these evidences that has been explored so far, we can now build the model that is consistent with the various observations. The decrease in Fe_3O_4 like coordination structure and increase in Fe-S coordination along with their corresponding environments systematically with increasing annealing time and the thickness of CdS monolayers suggest the slow transformation from the core/shell structure to core/alloy/shell eventually leading to uniformly Fe doped CdS matrix. This is consistent with the XAFS analysis along with TEM, XRD and ICP-OES data.

5.11 Conclusion

In conclusion, we have shown using a systematic analysis of XAFS that it is possible to study the micro structural change inside ultrafine QDs presenting a tool to understand random doping in QDs. In particular, we have demonstrated that XAFS can provide valuable information on the internal structure evolution from core-shell heterostructure to a uniformly doped QD from a site and element specific perspective. We use Fe_3O_4/CdS core shell QDs as a model system and successfully turn them into uniformly doped system through different stages and observed every step using XAFS. These findings concerning the local structure environment of the dopant have important consequence regarding optical and magnetic properties of similar systems. We expect that this idea can be generalized to probe the internal structure of other nano systems providing new insight to tune the optical and magnetic properties for different applications.

Section C

Magnetism at the Interface in Heterostructured Core/shell QDs

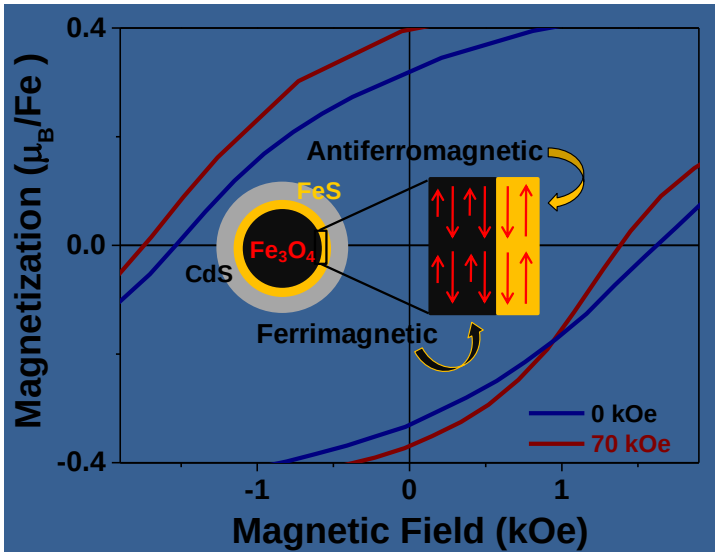

5.12 Summary

Engineering interfaces specifically in heterostructures provides new opportunities for developing multifunctional building block materials. Precise control over internal structure by chemical synthesis offers novel combination of unique properties in QDs and allows us to study their fundamental properties, depending on their structure. Herein, we studied the interface of magnetic/non-magnetic Fe_3O_4/CdS QD heterostructure. In this work, we demonstrate the decrease in the size of magnetic core due to annealing at high temperature by the decrease in saturation magnetization and blocking temperature. Furthermore, surprisingly, we observe the presence of substantial exchange bias in spite of the non-magnetic nature of CdS QDs. The presence of exchange bias was proved by the increase in magnetic anisotropy as well as the presence of exchange field during the field cooled magnetic measurements. This exchange coupling leads to enhanced anisotropy and exchange bias in this system that was eventually traced to the presence of thin anti-ferromagnetic FeS layer at the interface as verified by the study of Fe local structure using XAFS spectroscopy demonstrating the importance of interface engineering in QDs.

5.13 Introduction

Well controlled interfaces between bulk heterostructures have given rise to interesting new properties arising out of the surface interaction of the constituent materials at the interface. One of the extensively studied text-book like example of the interfacial phenomena is the $LaAlO_3$ and $SrTiO_3$ perovskite oxides.[86-90] Electronic reconstructions of these oxides have shown the presence of interfacial conductivity and a large negative magneto-resistance in these otherwise non-magnetic insulating oxides.[86,89,91] Similarly, other materials studied for interface induced phenomena include magnetism at the interface of half metallic ferromagnet $La_{2/3}Ca_{1/3}MnO_3$ and superconducting $YBa_2Cu_3O_7$ as well as characteristics of a ferromagnet/oxide interface in Fe/MgO system.[92,93] Management of the magnetism and magneto-resistance arising out of interfaces is key to the development of multiferroic and spintronics applications.[94] Hence it is important to study these interfaces especially as the devices approach quantum limit where the effects are enhanced and compete with their corresponding bulk properties. Atomic level manipulation of spin and charge of an electron in magnetic and non-magnetic heterostructures can lead to the development of quantum dot based spintronics[26,27] devices and hence need to be explored. However, except for a few recent

studies on atomically controlled interfaces like linear chain of three Fe atoms on monatomic copper nitride layer,[95] interface magnetism has not been extensively studied. Specifically, quantum dot heterostructure interfaces[11,78,96] that lie in between bulk and atomic limits that play a key role in miniaturization of devices have not been explored for interface induced properties.

Fundamental understanding of nanomagnetism, specifically single domain magnetism in confined domains, superparamagnetism have been identified as important areas in the field of magnetic quantum dots. Recently, studies have been carried out on magnetic quantum dots to optimize saturation magnetization, magnetic anisotropy, coercivity and other properties for applications in magnetic data storage,[3] MRI contrast agents,[97,98] magnetic hyperthermia[67,97,99] etc. However, interface between magnetic and non-magnetic materials have largely been ignored. Recent work[92] in bulk Fe/MgO have shown interesting results at the interface due to the proposed presence of FeO interactions at the surface. However, in these bulk materials, these effects are very small and largely not observed in bulk magnetic measurements. In fact, the authors had to perform magnetization induced second harmonic generation to selectively probe the interface to observe small changes at the interface. In this chapter, we present the study of the magnetic property at the interface of ferromagnetic Fe_3O_4 and non-magnetic CdS heterostructure quantum dots with decreasing magnetic cluster size. While encapsulation of Fe_3O_4 lattice in a non-magnetic matrix has been extensively carried out[8,100,101] for various applications including bio-compatibility, the interface of this magnetic/nonmagnetic heterostructure has not been probed. In this system the magnetic exchange interaction would be more strongly perturbed due to the spatial confinement compared to its bulk counterpart. This can affect the electronic structure and give rise to the exchange of charge carriers between ferromagnetic and semiconducting phases by injecting spins from ferromagnetic to semiconducting phase without requiring the atomic layer precision that has become the hallmark necessary to observe these effects.

In this work we have used colloidal synthesis SILAR (successive ionic layer adsorption and reaction) method[44] to obtain Fe_3O_4 QDs (NCs) overcoated with CdS. Magnetic ion localization inside the semiconductor matrix is a very crucial factor both for the fundamental understanding and application point of view. The samples were characterized using high resolution transmission electron microscopy (HRTEM) and x-ray diffraction (XRD) measurements. The magnetism at the core and at the interface of this ferromagnetic/nonmagnetic quantum dot have

been studied using standard magnetization measurements using superconducting quantum interference device (SQUID) magnetometer. Variation of magnetic cluster size is determined from their corresponding variation of blocking temperatures (T_b). Further to investigate the origin of anomalously high coercivity, we have studied the hysteresis loop shift as a function of field leading to the discovery of an exchange bias at a magnetic/nonmagnetic interface. The origin of this exchange bias field has been proposed to arise from the interfacial antiferromagnetic FeS formation. Indirect proof for this interfacial structure has been obtained by modifying the size and annealing temperature to maximize the interface and hence the increase in coercivity. Additionally, a more direct proof is achieved by a local environment study of Fe ion using X-ray absorption fine structure (XAFS) for a series of CdS overcoating and annealing temperatures.

5.14 Experimental Methods

5.14.1 Synthesis

Fe_3O_4 QDs having size of 4.5 nm were first synthesized as magnetic core by following section 5.4.1. Successive ionic layer absorption and reaction (SILAR) technique[44] was involved to overcoat CdS at high temperature (240-260 °C) which allowed us to control both the growth of semiconducting layer as well as the diffusion of magnetic core inside the semiconductor matrix precisely. Self-purification effect[36,41] is expected to diffuse the core in the semiconductor matrix in a controllable manner. We carefully monitor the reaction and collect samples at different stages during QDs growth to arrest the diverse internal structure from core shell Fe_3O_4/CdS and probe their magnetic properties. We have also synthesized a larger core having size of 7.3 nm and overcoated CdS following the similar procedure to increase the coercivity of the heterostructure.

5.14.2 Characterization

X-ray Absorption Fine Structure (XAFS) spectroscopy was employed to probe the local structure around Fe atoms for all the QDs. Fe K-edge (7112 eV) for the samples were measured at beamline 2-2 at Stanford Synchrotron Radiation Lightsource, SLAC National Accelerator Laboratory. The gases in the ion chambers were optimized for adequate absorption of photons. For Fe K-edge, a mixture of 80% Helium and 20% Nitrogen gas was used in the initial ion chamber I_o placed before the sample and full Nitrogen gas in transmission and reference ion chambers. Argon gas was used for fluorescence ion chamber. Data collected was processed

using Athena software[54] by extracting the EXAFS oscillations $\chi(k)$ as a function of photoelectron wave number k following standard procedures. The theoretical model consistent with the other characterization techniques and the corresponding paths were generated using FEFF6[82] followed by fitting to the experimental data using fitting program Artemis.[77] In order to isolate the $\chi(k)$ oscillations, the atomic background was subtracted by applying a low distance cut off equal to 1Å in the Fourier transform and using a cubic spline. Fourier filtering was accomplished with a k weight equal to 2, in a range from 2 to ~10 $Å^{-1}$.

5.15 Results and Discussion

5.15.1 XRD and TEM

XRD measurements in Figure 5.3(a) for these systems show a clear evidence of magnetic core/non-magnetic shell heterostructures in these systems, specifically with thin CdS shells. However, though the study of internal structure using HRTEM is the most straight forward proof, HRTEM shows the presence of only single lattice spacing in Fe_3O_4/nCdS as shown in the Figure 5.11. While it is evident that the particle size grows systematically with increasing CdS monolayers, clusters of Fe_3O_4 cannot be distinguished from the lattice parameters due to the presence of a very thin shell. Hence study of even thinner interface using HRTEM is clearly beyond the accuracy of the TEM. Hence interfaces have not received enough interest in literature due to the lack of characterization techniques in spite of their interesting properties.

5.15.2 Magnetic Properties

Property driven characterization wherein a specific change in property, induced by the interface is observed along with its bulk properties or the indirect methods like modeling to fit variable emission photoemission data[102] or XAFS data are some of the possible means of studying the interface. In this work, we have studied magnetic properties of a series of samples with increasingly thicker shell of CdS to propose the nature of the interface. This is then further evaluated by the study of EXAFS of the Fe edge for these materials. The evolution of magnetic properties has been studied on a series of samples of Fe_3O_4/nCdS with varying values of n, the number of monolayers of CdS at room temperature and 2K are shown in Figure 5.17 and Figure 5.18(a).

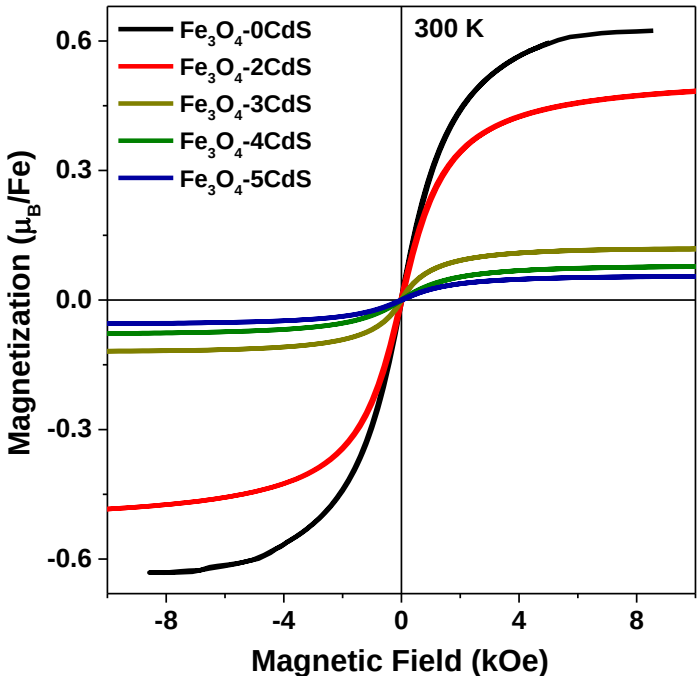

Figure 5.17: M *vs.* H hysteresis loop of different Fe_3O_4-CdS during initial shell growth, measured at 300 K.

At room temperature these particles show superparamagnetic behavior with no coercivity (Figure 5.17) as they are above the blocking temperature. However at 2 K all these NCs showed ferromagnetic behavior with significant coercivity (H_c). Figure 5.18(a) shows the magnetization (M) versus applied field (H) plots at 2K for Fe_3O_4-nCdS samples for differing values of n while the Figure 5.18(b) shows the DC magnetic susceptibility measured from M *vs.* temperature (T) curves following zero field cooled (ZFC) and field cooled (FC) protocols using an external field of 500 Oe. The inset to Figure 5.18(b) shows the zoomed plot of the same to demonstrate the blocking temperature (T_b). From the Figure 5.18(a), we can observe that as the thickness of CdS increases the saturation magnetization per magnetic ion decreases dramatically. This is not surprising as the overcoating of CdS is done at high temperature for extended periods of time. Hence as the annealing time increases, the magnetic core slowly diffuses into the CdS matrix leading to an effective decrease in the magnetic cluster size. This is also further substantiated in Figure 5.18(b) showing a blocking temperature to be 54 K, 30 K, 27 K, 21 K respectively for Fe_3O_4, Fe_3O_4-2CdS, Fe_3O_4-4CdS, Fe_3O_4-5CdS. In the case of single domain magnetic quantum dots, the size of the magnetic domain affects the energy barrier and T_b, reducing T_b with decreasing size, [67,97] that is observed in our QDs due to decrease in the magnetic cluster size in spite of an overall size increase.

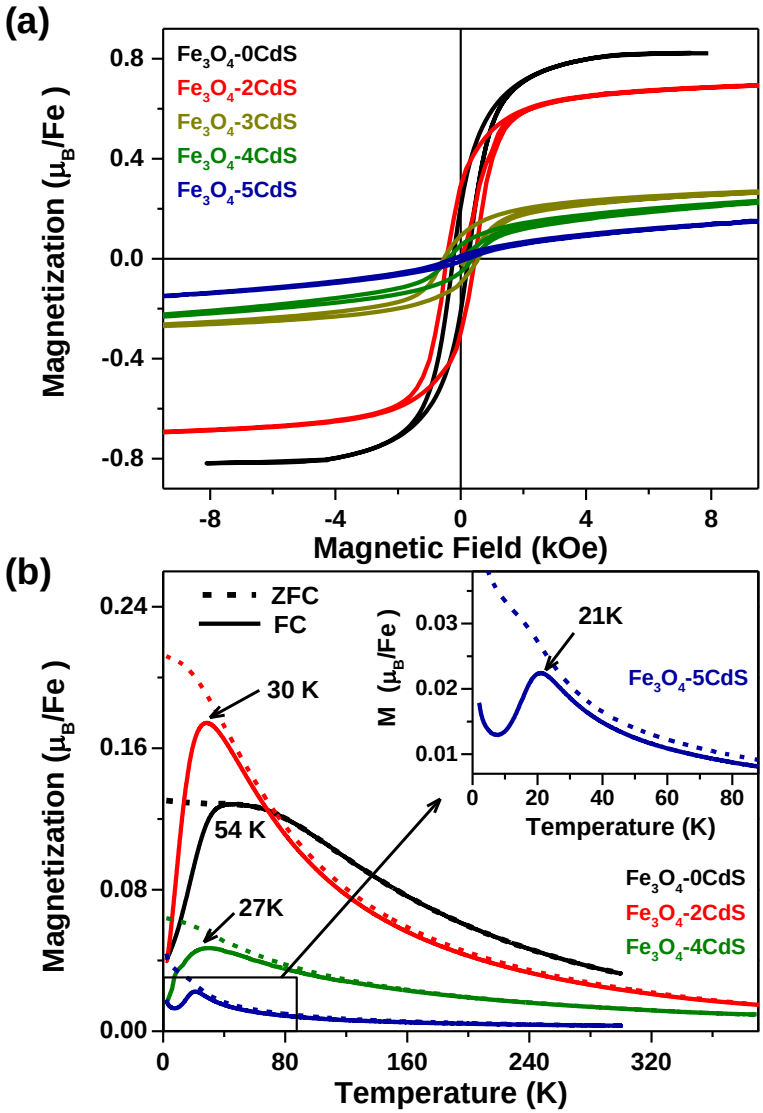

Figure 5.18: (a) M *vs.* H hysteresis loop of different Fe_3O_4-nCdS QDs during initial shell growth, measured at 2K. (b) Zero field cooled (solid line) and field cooled (dotted line) magnetization measured using a field H= 500 Oe for all the Fe_3O_4-nCdS samples, Inset shows the zoomed view of FC-ZFC curve of Fe_3O_4-5CdS at lower temperature.

However, surprisingly, the evolution of magnetic anisotropy inside the QD during CdS shell growth quantified by the coercivity (H_c) of these QDs does not decrease monotonically as expected. Figure 5.19(a) shows the M *vs.* H curve for Fe_3O_4 and Fe_3O_4-3CdS and the inset show the variation of coercivity with the increase of CdS shell growth. There is a clear enhancement of coercivity from Fe_3O_4 (H_c= 240 Oe) to Fe_3O_4-3CdS (H_c = 540 Oe). This anomalous increase in H_c is surprising as CdS is a nonmagnetic semiconductor and hence would not affect the magnetic behavior of the core. In order to investigate the validity and the

generality of this effect, we synthesized a larger magnetic Fe_3O_4 core (~7.3 nm) overcoated with a thin shell of CdS. These particles were characterized by TEM images shown in Figure 5.20. The M *vs.* H plots for these larger samples at 2K are shown in Figure 5.19(b). From the figure it can be observed that the core QDs have larger coercivity (~310 Oe) at 2K as expected due to the increase in size. Similar to the earlier case, we not only observe an increase in the coercivity with the overcoating of a thin shell of CdS but actually observe almost five-fold increase in coercivity (~1570 Oe) that is clearly above the normal error limit.

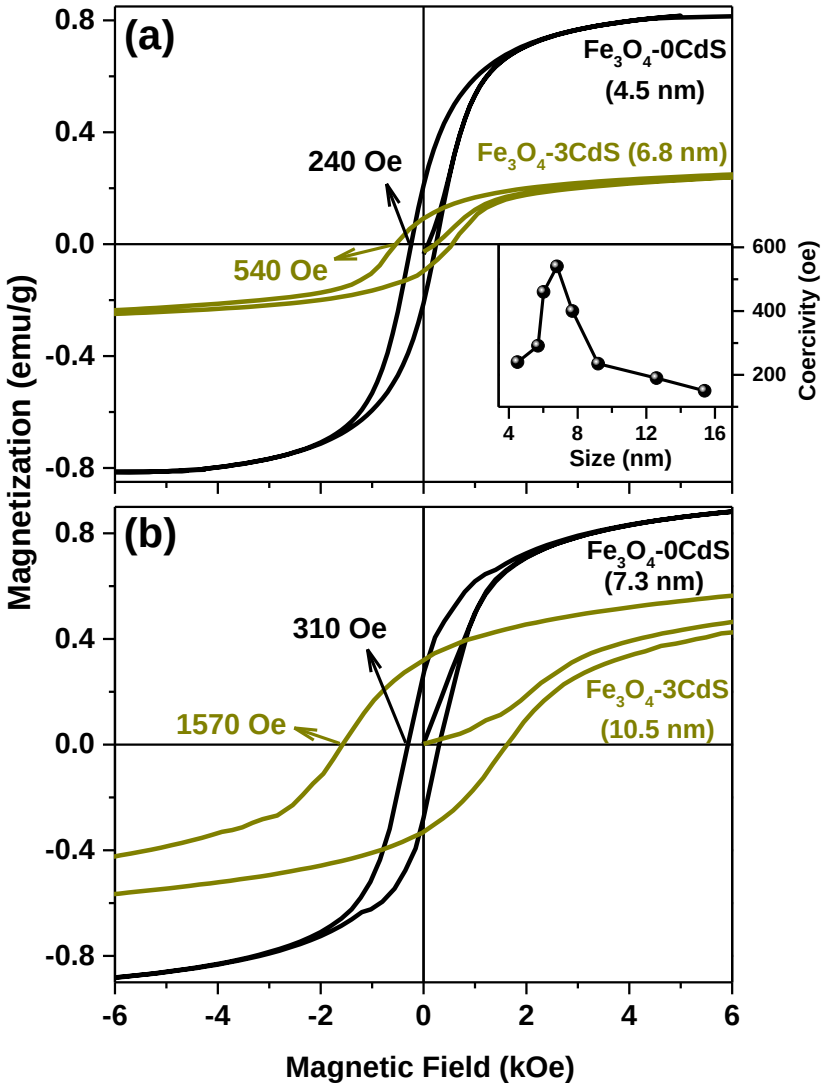

Figure 5.19: Magnetization (M) *vs.* Field (H) (zoomed view at low field) hysteresis loops of Fe_3O_4-0CdS and Fe_3O_4-3CdS QDs measured at 2 K and the inset shows the variation of coercivity obtained from M *vs.* H hysteresis loops for all the Fe-CdS samples obtained from 4.5 nm Fe_3O_4 core. (b) M *vs.* H hysteresis loop for Fe_3O_4-0CdS having size 7.3 nm and overcoated the same with 3 monolayers of CdS.

Study of the origin of coercivity, points towards an increase in the anisotropy energy inside the QD. This has been attributed in the literature[67] to exchange interactions between the core and the shell at the interface. In fact, it has been shown that in the case of a magnetic/anti-ferromagnetic interface, increase in anisotropy can be the effected due to pinning of the domain wall on the surface of the magnetic core giving rise to the so called "exchange bias" effect.[103-109] Further, these data also suggests that the effect is enhanced in presence of larger interfacial surface as in the case of 7.3 nm Fe_3O_4 attributing these changes to an interfacial phenomenon.

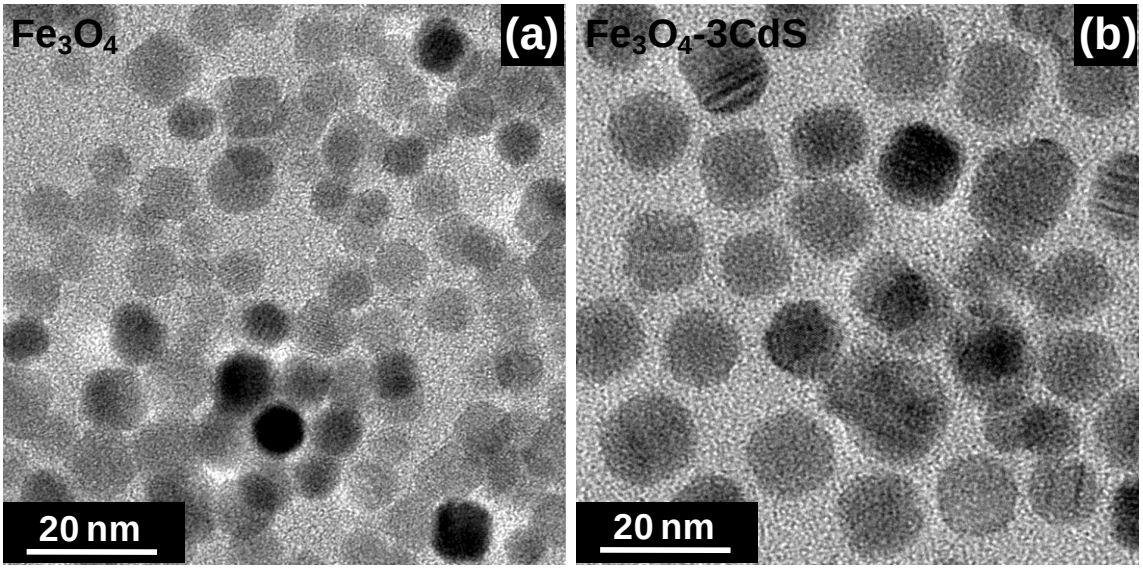

Figure 5.20: TEM images showing 7.3 nm Fe_3O_4 core and (b) 10.5 nm Fe_3O_4-3CdS.

Typical signatures of the presence of such an exchange coupling in literature is the as symmetric shift in the hysteresis loop by an amount quantified by the exchange shift H_E that is dependent on the cooling field, when the measurements are carried out in presence of field cooling. The comparison of M *vs*. H plot for the ZFC and FC plots at 70 kOe for the larger Fe_3O_4-3CdS are shown in Figure 5.21(a) and the relevant region has been zoomed in the inset I for clarity. Quantitatively, we observed a H_E of ~200 Oe using a field 70 kOe during FC measurement. The variation of H_E with different cooling field is shown in the inset II demonstrating a clear monotonic dependence of the exchange field with the applied field during the cooling. In addition, the exchange field obtained for the smaller particles is also plotted in the same inset showing the presence of a much smaller H_E values as expected. These observations suggests the presence of an anti-ferromagnetic (AFM) layer at the core shell interface as shown in the schematic Figure 5.21(b) responsible for this exchange bias.

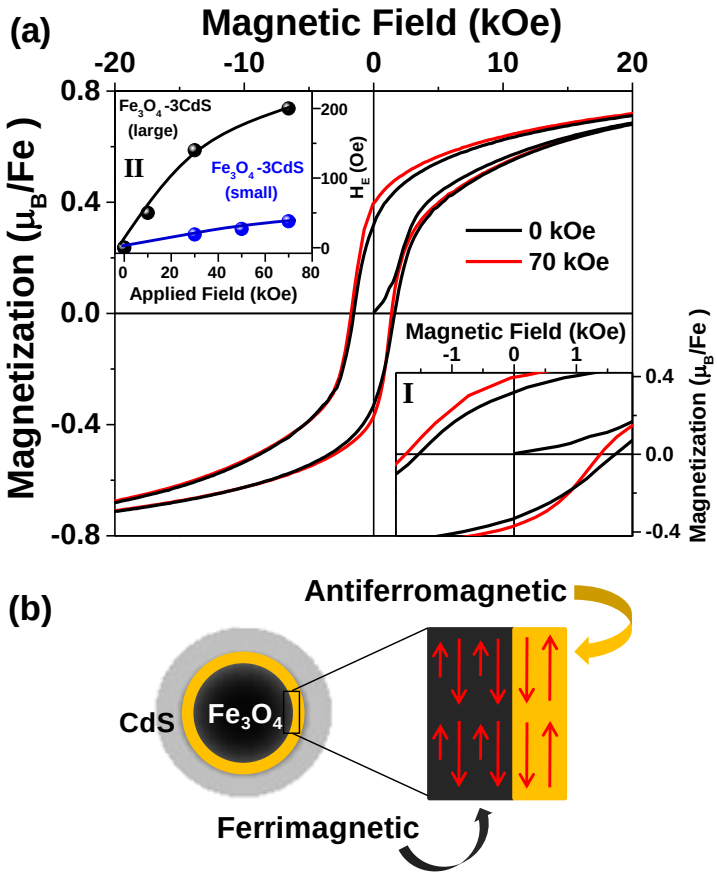

Figure 5.21: (a) M *vs.* H hysteresis loop for Fe_3O_4/CdS (larger) sample, measured at 2K using 7 kOe field cooled (red) and zero field cooled (black) condition. Inset I zoomed view of M *vs.* H hysteresis loop and Inset II variation of H_E with various cooling field for Fe_3O_4-3CdS large (black) and Fe_3O_4-3CdS small (blue) nanoparticles obtained from 7.3 nm and 4.5 nm core respectively. (b) Schematic showing formation of a thin AFM layer at the interface.

Upon survey of bulk literature, it was observed that in the case of Fe/MgO, there exists a small exchange bias (~19 Oe) at the interface as observed from magnetization induced second harmonic generation measurements even though no bulk exchange fields were observed.[92] This exchange bias was eventually traced to the presence of AFM FeO layer at the interface. Similarly, in our case, in order to trace the origin of the antiferromagnetic ordering, giving rise to the exchange anisotropy, internal structure at the interface is important. In the current case, XRD and magnetism point towards the diffusion of Fe into the CdS lattice. Based on the observed data and the synthesis methods, we propose the formation of thin FeS layer at the interface before Fe diffuses into the CdS lattice. If this is indeed true, study of local structure around the Fe atom in these structures using XAFS should show the presence of larger Fe-Fe second order interactions.

5.15.3 Local Structure Analysis

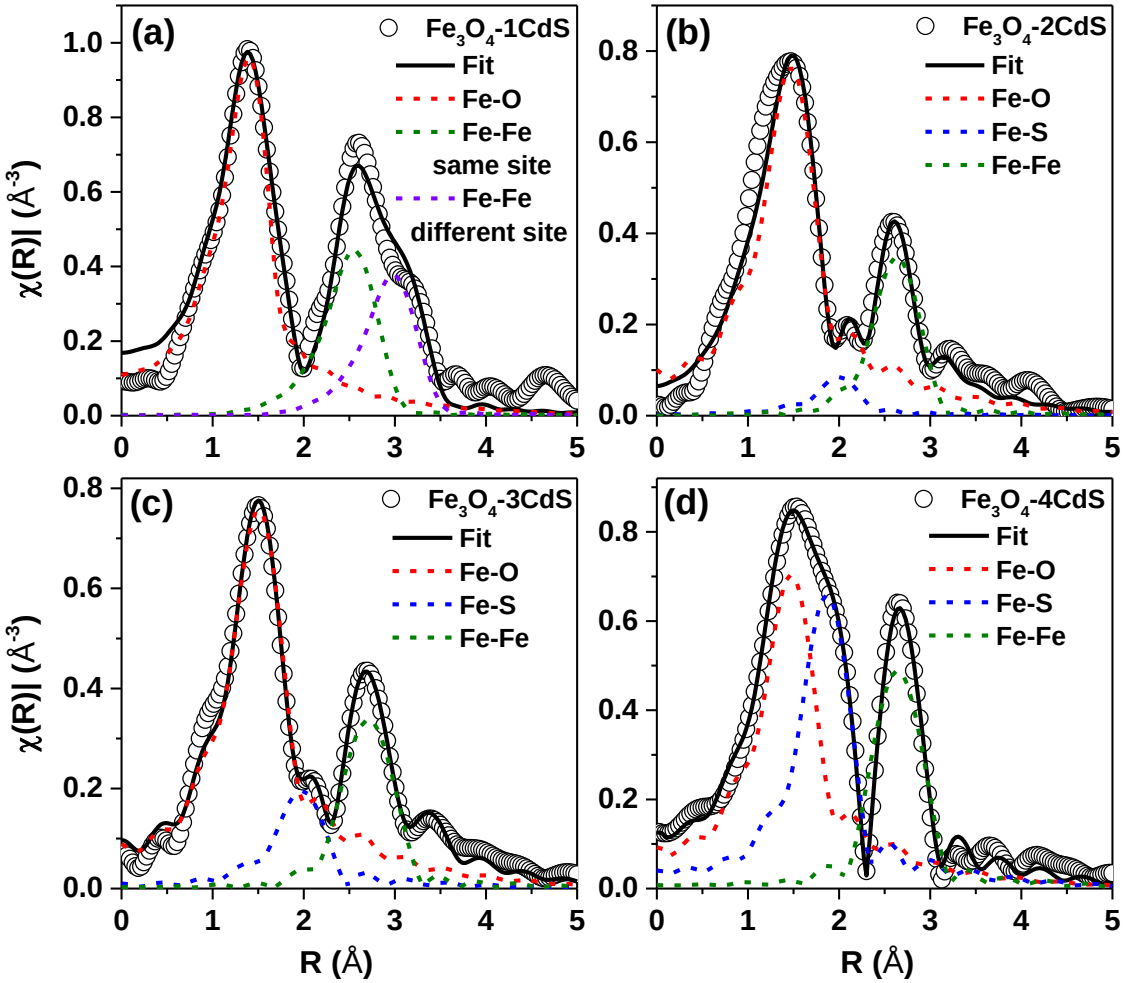

Figure 5.22: (a) Magnitude of Fourier transformed Fe K-edge EXAFS spectra (open symbols) and their best fit (solid black line) for (a) Fe_3O_4-1CdS (b) Fe_3O_4-2CdS (c) Fe_3O_4-3CdS and (d) Fe_3O_4-4CdS, synthesized using Fe_3O_4 core having size 7.3 nm. Dotted lines show their component fitting paths.

In order to verify the presence of FeS layer, we measure the Fe K-edge for a series of samples and trace the local environment change around Fe atoms. We specifically measured those Fe_3O_4-nCdS samples in which the starting core was larger in size (7.3 nm) in order to observe a higher signal to noise ratio for the second order interactions. These data were processed using ATHENA and then fitted using the theoretical proposed model and generating relevant paths using ARTEMIS FEFF 6 program. Figure 5.22(a)-(d) shows the Fe K-edge experimental data and their corresponding fits for Fe_3O_4-1CdS, Fe_3O_4-2CdS, Fe_3O_4-3CdS and Fe_3O_4-4CdS. The results obtained from these fits are tabulated in Table 5.5. It can be observed from the spectra

(Figure 5.22(a)) that Fe_3O_4-1CdS data looks very similar to Fe_3O_4 as observed in the earlier section and fitted using Fe-O and Fe-Fe bonding originating from tetrahedral and octahedral interstices in a cubic inverse spinel structure. The peak at 1.4 Å in Figure 5.22(a) is due to the Fe-O bond arising with the nearest oxygen atoms whereas the peak at 2.52Å and 3.01Å are from Fe-Fe bonds due to same and different interstices respectively. With the increase of CdS shell thickness an Fe-S path arises at 1.96 Å, due to the formation of Fe-S bonds at the core shell interface due to the diffusion of Fe from core to the shell. Fe-S peak dominates as the core starts to diffuse inside the CdS matrix as shown in the Figure 5.22(a) through 5.22(d) and Figure 5.23. The supporting information Figure 5.23 shows the Fourier transformation of Fe K-edge XAFS data of Fe_3O_4-8CdS where the most of the contributions comes from Fe-S with very little amount of Fe-O which suggest a complete dispersion of the core inside the thick CdS matrix.

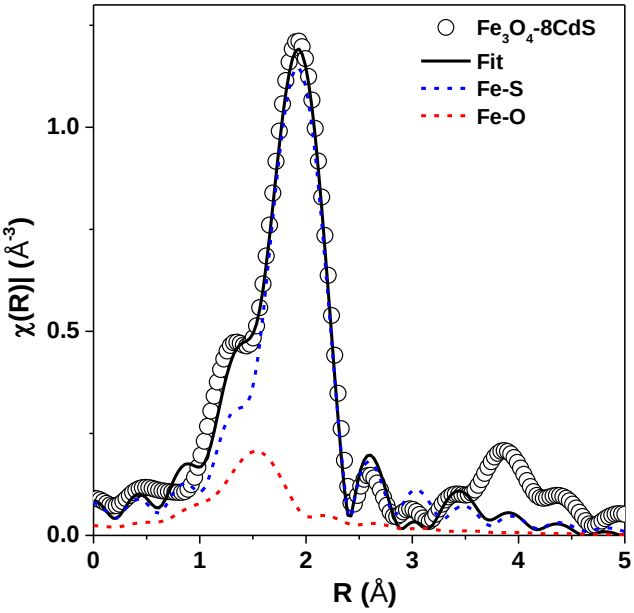

Figure 5.23: Magnitude of Fourier transformed Fe K-edge XAFS spectra (open symbols) and its best fit for the Fe_3O_4-8CdS sample obtained from 7.3 nm core.

More importantly, it is important to observe that as the Fe starts to diffuse into the CdS matrix, we expect an increase in the FeS layer thickness in the proposed model. This increase in the FeS layer can be observed in the coordination number of Fe-Fe interactions which is plotted in Figure 5.24. The total coordination number for Fe-O and Fe-S is found to be in the range 3.5 to 4.2 which is in good agreement with the expected value of 4. Individually, Fe-O decreases from 4.08 to 0.6 whereas Fe-S increases from 0 to 2.8 as expected due to Fe diffusion

inside CdS. However, interestingly Fe-Fe second shell coordination number at the initial stages is found to be almost constant in spite of the Fe-S formation suggesting the formation of FeS layer and not the diffusion of Fe in CdS. However as the annealing increases, it eventually drops down to zero after much thicker CdS shell formation. This is also in agreement with the peak observed for H_c values that is also plotted in Figure 5.24 for comparison. It is observed that the coordination number of this second shell is much smaller than the theoretically expected value of 12 due to small size as well as the in-built randomness due to the large surface to volume ratio. However, in spite of this quantitative disagreement, it is interesting to note that this Fe-Fe second shell contribution initially arising from the ordered Fe_3O_4 core does not decrease as the cluster size decreases and in spite of diffusion of Fe ions into the CdS lattice. This suggests the presence of ordered Fe-S-Fe interactions along with Fe-O-Fe at the interface. This significant contribution of Fe-Fe second order path from ordered phase in case of Fe_3O_4-3CdS and Fe_3O_4-4CdS, along with the Fe-S path suggests the fact that the Fe_3O_4 core is covered on its surface with a thin layer of Fe-S which is acting as the origin of AFM centre.

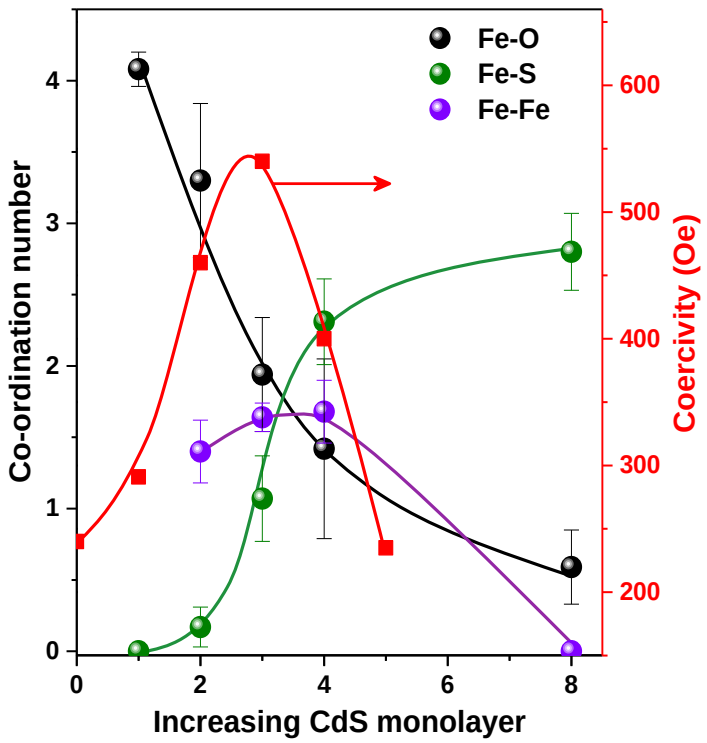

Figure 5.24: Variation of local coordination number around of Fe considering the nearest oxygen (black symbols), sulfur (green symbols) and iron (violet symbols) atoms from XAFS fittings. Red symbols show the variation of coercivity H_c as a function of CdS overcoating. Solid lines are guide to the eye.

Table 5.5: List of fit parameters (Independent Points (N_{idp}) and number of variables (N_{var}) for the fit, bond length (R), coordination number (N), Debye waller factor (σ^2), energy shift (ΔE) and R-factor) obtained from modeling the data for Fe-K edge.

Sample	Paths		R (Å)	N	(σ^2)	ΔE (eV)	R-factor
Fe_3O_4-1CdS k=2.8-12 $Å^{-1}$ R=1.1-4.0 Å N_{idp} = 17 N_{var} = 8	Fe_3O_4 tetra Fe^{3+}	Fe^{3+}-O1 Fe^{3+}-Fe oct1	1.85±0.03 3.44±0.03	0.92±0.07 0.92±0.07	0.002 0.01±0.001	-1.93 ±1.77	0.0046
	Fe_3O_4 octa Fe^{3+}	Fe^{3+}-O1 Fe^{3+}-Fe oct1 Fe^{3+}- Fe tetra1	1.99±0.06 2.99±0.02 3.50±0.02	1.56±0.04 1.56±0.04 1.56±0.04	0.008±0.002 0.01±0.001 0.01±0.001		
	Fe_3O_4 octa Fe^{2+}	Fe^{2+}-O1 Fe^{2+}-Fe oct1 Fe^{2+}+- Fe tetra1	1.99±0.06 2.99±0.02 3.50±0.02	1.6 1.6 1.6	0.008±0.001 0.01±0.001 0.01±0.001	-6.93±1.77	
Fe_3O_4-2CdS k= 2.8-11 $Å^{-1}$ R= 1-4 Å N_{idp} = 16 N_{var} =10	Fe-O		1.99±0.20	3.30±0.54	0.003±0.002	-3.48 ± 1.22	0.0067
	Fe-S		2.54±0.10	0.17±0.15	0.002		
	Fe-Cd		3.25±0.24	0.50±0.18	0.01		
	Fe-Fe		3.04±0.04	1.40±0.22	0.008±0.001		
Fe_3O_4-3CdS k=3 -11 $Å^{-1}$ R=1-4.2 Å N_{idp} = 16 N_{var} = 12	Fe-O		1.98±0.21	1.94±0.40	0.005±0.001	-2.59±1.26	0.0014
	Fe-S		2.39±0.04	1.07±0.30	0.005		
	Fe-Cd		3.33±0.16	0.42±0.14	0.004±0.001		
	Fe-Fe		3.06±0.06	1.64±0.1	0.008±0.001		
Fe_3O_4-4CdS k=2.8-11 $Å^{-1}$ R= 1.1-4.1 Å N_{idp} = 16 N_{var} = 11	Fe-O		1.99±0.20	1.42±0.63	0.006±0.003	4.09 ± 0.78	0.0013
	Fe-S		2.37±0.06	2.31±0.30	0.005		
	Fe-Cd		3.28±0.28	0.16±0.11	0.004		
	Fe-Fe		3.08±0.08	1.68±0.20	0.005±0.002		
Fe_3O_4-8CdS k=2.8- 11 $Å^{-1}$ R=1.0-4.0 Å N_{idp} = 24 N_{var} = 13	Fe-O		1.97±0.22	0.59±0.26	0.006±0.003	2.10 ± 1.67	0.0123
	Fe-S		2.37±0.05	2.86± 0.25	0.005		
	Fe-Cd		-	-	-		
	Fe-Fe		-	-	-		

5.16 Conclusion

Thus, based on the structure property correlation obtained from local internal structure through XAFS and magnetic property measurements, we observe the presence of FeS AFM interface layer in an otherwise magnetic core/non-magnetic shell heterostructure. The presence of this AFM layer gives rise to a substantial exchange bias that has so far not been observed in bulk

measurements and can be used in hyperthermia or magnetic storage like applications. In addition we show that even though growth of core/shell interfaces in quantum dots has so far been largely ignored, these interfaces, unlike in bulk, can be responsible for large number of interesting properties that has not been noticed and/or understood. We believe that the fundamental understanding of the internal structure and magnetic property in QDs reported in this work will provide a stepping stone to understand a wide range of properties of magnetic heterostructure QDs.

Section D

Effect of Doping Concentration and Size in Doped Quantum Dots

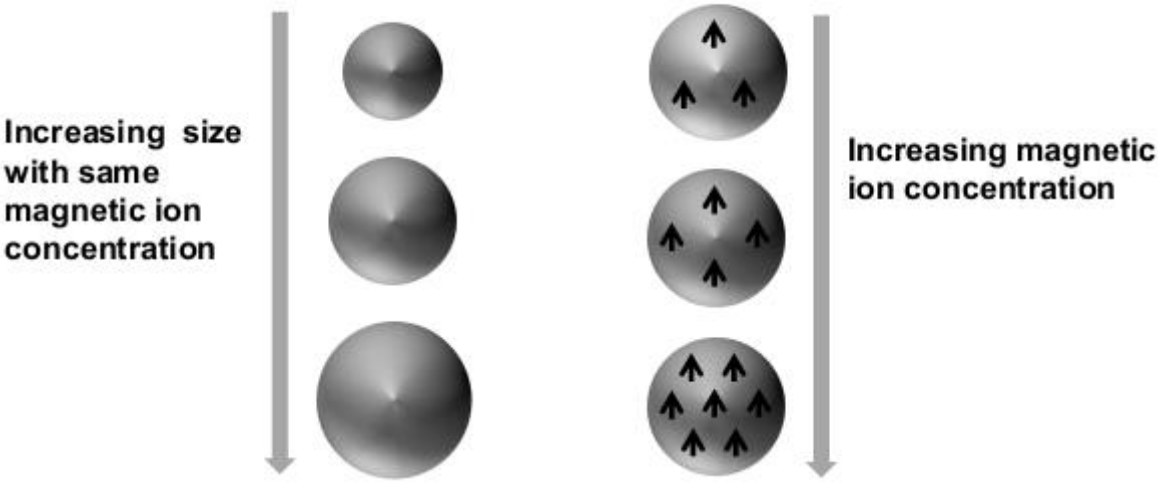

5.17 Summary

Investigation on ideal dilute magnetic semiconductors with tunable magnetic behavior by changing particle dimensionality and doping concentration and its complete understanding is a major step towards their application in multifunctional devices. Diffusion doping has shown potential in achieving controlled size and doping concentration in QDs. Following this technique, herein, various size and concentration has been achieved and an explicit dependence on magnetic properties of Fe-doped CdS QDs due to their particle size and doping concentration have been demonstrated. We observe that magnetization/dopant ion concentration is insensitive within dilute doping regime. However, the effect of domain size and disordered spin on the surface leads to a change in magnetization/ion as well as magnetization reversal.

5.18 Introduction

Nanoscale magnetism has received enormous attention in the last decade, especially in the case of DMSs[110,111] due to their unique magnetic properties as well as magneto-optical[2,31,60,112] and magneto-electrical effects[13] leading to the formation of building blocks for future sensors, data storage and communication technology. This remarkable phenomenon is a result of subtle interplay between intrinsic properties and inter-particle interactions. Fundamental understanding of this field as well as potential applications like magnetic storage devices,[3,113] magnetic resonance imaging,[114-116] requires an understanding of the effect of domain sizes, role of particle volume, finite size and surface effects in addition to addressing the issues of localization of magnetic states and the effect on these states due to quantum confinement.

Finite size effects in DMS QDs has largely been unexplored except for a few theoretical studies,[15,117] primarily due to the lack of appropriate synthesis methods to control the size and dopant concentrations in these QDs. Though wet chemical synthesis of colloidal nanoparticles has spurred a tremendous scope to engineer QDs with control over size, shape, internal structure and doping, there are often a multitude of microscopic forces that exert the fine control over these systems. Hence though an extensive post-synthetic study may reveal the forces responsible for the final size and shape of QDs it is often non-trivial to tailor-make DMSQDs with required size and dopant concentration. Additionally, synthesis of larger QDs with dopant ion retention is not well studied. It is well known that though the quantum

confinement effects are most prominent below 10 nm, the effects of volume, surface effects and domain sizes are applicable up to much larger sizes, typically up to about 100 nm. It was observed that below the critical size (D_c) the size of ferromagnetic domain in single ferromagnetic nanoparticles has great impact in determining their magnetic property. Furthermore, the study of magnetism in nanoscale systems is further complicated by the probable presence of small magnetic clusters within a non-magnetic matrix. However, unlike other ferromagnetic systems, magnetism in DMS materials arises due to long-range *sp-d* exchange interaction[118] between paramagnetic dopant ions and semiconductor charge carriers through the formation of bound polarons.[59] Thus the wish list of properties required for successful study of size effects in DMSQDs include (a) proven methodology for the formation of clustering free doped QDs, (b) ability to control size and shape with required dopant percentage up the critical domain size and (c) dopant concentration control to study the origin of magnetism.

We have shown earlier in this chapter that it is possible to obtain magnetic cluster free QDs using the diffusion of magnetic core into the semiconducting matrix within a particular size and dopant range. Further studies have shown that by appropriately modifying the thermodynamic parameters such bond strength and diffusion constant, it is possible to vary the size and dopant percentages (demonstrated in chapter 6 section A). Based on these studies, we have obtained DMS QDs with required sizes and dopant concentration meeting all the three conditions specified above by modifying the core size, annealing conditions as well as the choice of appropriate core material. We have obtained Fe-doped CdS QDs having various Fe percentage (up to 14.5 %) and various sizes (12-55 nm) to study nanoscale magnetism in QDs. The samples were characterized using TEM and ICP-OES measurements. The amount of ligands was estimated using TGA. Variation of magnetic property of Fe doped CdS quantum dot has been studied using standard magnetization measurements using SQUID magnetometer. Magnetic parameters such as the variation of coercivity (H_c), saturation magnetization (M_s), remanent magnetization (M_r) with particles dimensionality have been analyzed. Moreover, the magnetic scaling per dopant ion as a function of concentration of magnetic ions has been established. Finite size and surface effects such as canted spin have been identified and systematically quantified as a function of particle size.

5.19 Experimental Section

5.19.1 Synthesis

Various Fe doped CdS have been synthesized by diffusing Fe_3O_4 magnetic core inside a thick CdS semiconducting matrix following the synthesis technique described in section 5.4.1. In brief, Fe_3O_4 QDs having different sizes 4.5 nm, 5.6 nm, 6.2 nm and 7.3 nm have been synthesized by following previous method. We have annealed longer time at high temperature (300 °C) to achieve larger QDs. SILAR technique[44] was used to overcoat CdS at high temperature (240-260 °C). All the samples were annealed for required amount of time to obtain the required thickness of CdS shell growth as well as close to complete diffusion of Fe_3O_4 core. Samples were collected at different stages of CdS growth to monitor the reaction and to arrest growth to obtain the required sizes and concentration of Fe ions inside the system.

5.20 Result and Discussion

5.20.1 Magnetic properties

Figure 5.25(a) shows the M *vs.* H curves at 2 K for Fe-CdS during formation of the thick shell of CdS for Fe-nCdS with varying values of n, the number of monolayers of CdS and with a core size of 4.5 nm. The magnetic core is known to diffuse into the CdS matrix within about 5 monolayers of CdS at the given annealing temperature with no signatures of magnetic clustering as observed from XAFS as discussed earlier. From the figure, it is observed that, as expected, at low temperature all these QDs showed ferromagnetic behavior due to spin blocking. However at room temperature (Figure 5.26) these particles show superparamagnetic behavior with zero coercivity (H_c). Secondly, it is observed that in spite of the correction from the ligand weight, a significant reduction of absolute magnetization from the bulk value ($4\mu_B$) has been observed (Figure 5.25(a)), possibly due to decrease of domain size and increase of canted surface spins.

The variation of saturation magnetization (M_s) with the shell thickness as well as Fe concentration is shown in the Figure 5.25(b). From the figure, it can be observed that the M_s decreases upto about 4-5 monolayers of CdS which then slowly increases. So it is evident from the experimental observation that there are two significant origins, controlling the magnetization of these QDs. In the first part, magnetism is dominated by the magnetic

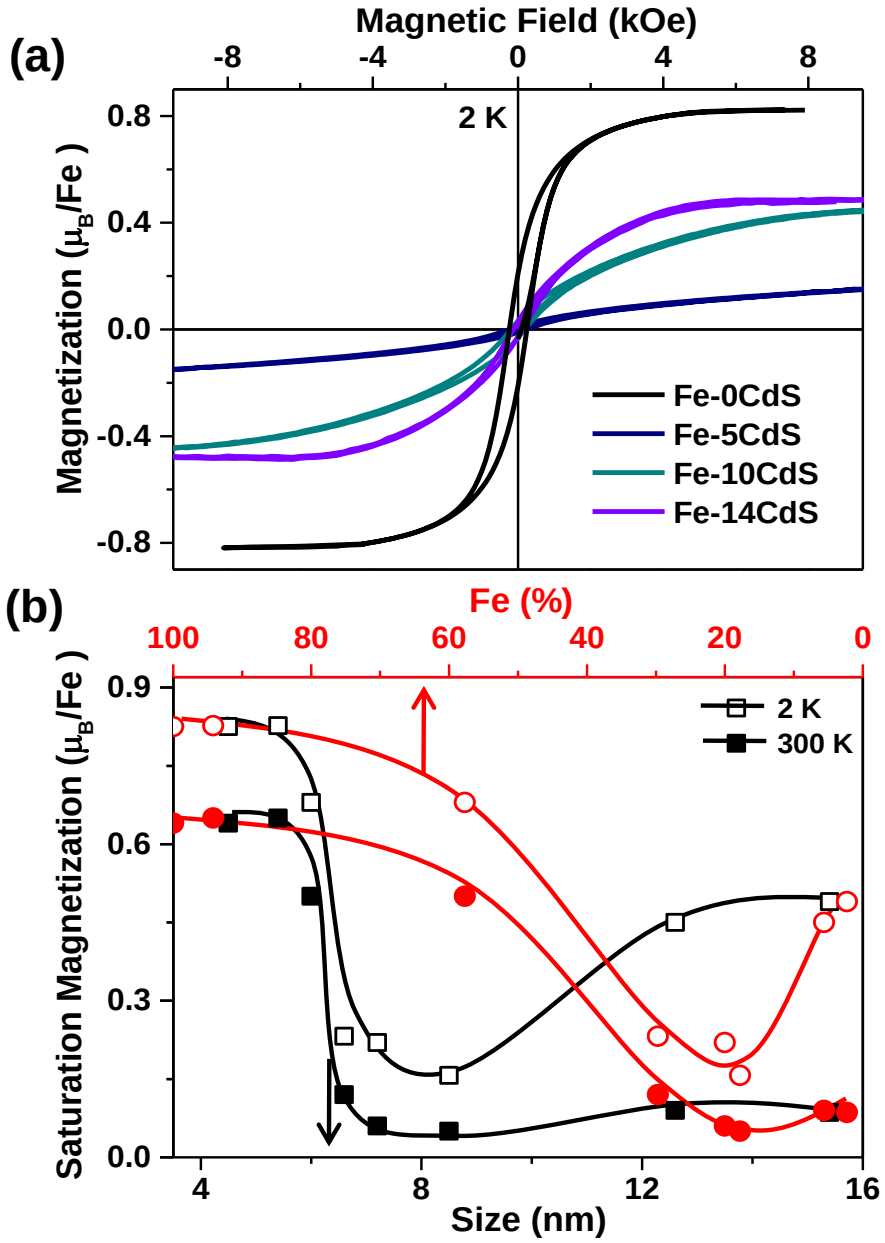

Figure 5.25: (a) A comparison of M *vs.* H hysteresis loop (2K) for different Fe-CdS QDs (b) variation of Magnetization/Fe with increasing Size (black symbols) and percentage of Fe (red symbols) measured at 2 K and 300K. Solid lines are guide to the eye.

core that is well known to contribute to the ferromagnetism due to strong short-range ferromagnetic coupling between magnetic spins. With the increase in annealing time, this cluster slowly diffuses into the lattice and hence decreases the core size resulting in a decrease in M_s. This decreasing cluster size is further demonstrated by the decrease in blocking temperature as obtained from the M *vs.* T plots as shown in the inset to Figure 5.25(b). After

the core diffuses completely magnetization of these QDs solely depends on percentage of magnetic ions and the size of the QDs. Hence in the latter part of the graph showing a small increase, wherein TM impurity ions existing as dopants inside semiconductor host, dominates due to sp-d exchange interaction between magnetic ions and the semiconductor host. Apart from these two factors, defects induced magnetism is also well known in these kinds of small QDs as has been reported earlier.[65,119] However, we can rule out this effect here as the magnitude of the magnetism arising from defects is several orders of magnitude smaller as observed from almost zero line graph of CdS shown in Figure 5.9.

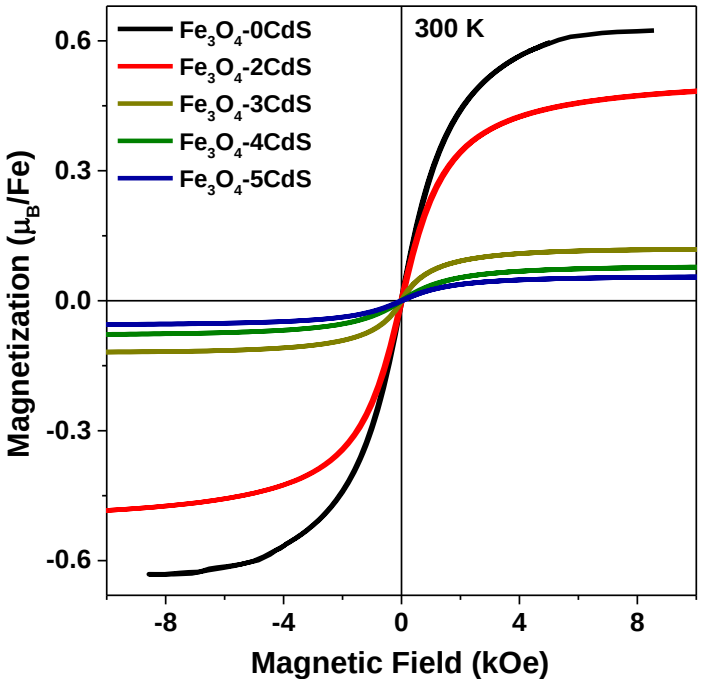

Figure 5.26: A comparison of M *vs.* H hysteresis loop (300K) for different Fe-CdS QDs.

However, it is interesting to note that even though there is high percentage (18%) of doping in Fe-5CdS (size-8.5 nm), M_s is lower than with lesser percentage (2.3 %) of ions in Fe-14CdS (15.4 nm). From these results, it is evident that these set of samples cannot isolate the effects of size as well as dopant concentration as both these variables are simultaneously changing. Hence in order to investigate the effect of magnetic ion concentration and size individually on the magnetic property, we used different core sizes to obtain two sets of samples. The first set was obtained with differing magnetic ion concentrations with similar sizes (12 nm) and the second set with varying sizes and dopant concentration of 5 % and the magnetism of these two sets are then studied.

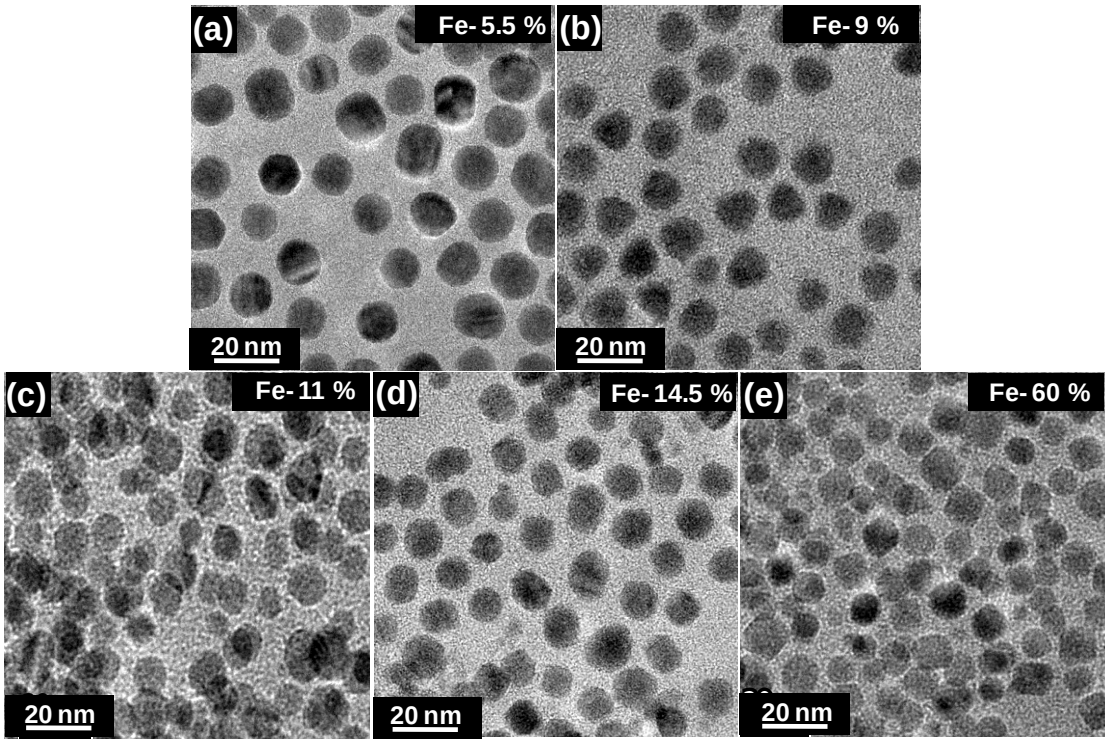

Figure 5.27: TEM images of (a) 5.5 % (b) 9 % (c) 11 % and (d) 14.5 % (e) 60 % Fe doped CdS QDs having 12 nm sizes.

Magnetic impurity concentration dependence on the magnetic properties (magnetization, Curie temperature) of a DMS material is known to be an important and a direct approach for our understanding of the origin of magnetism. It is well known that magnetism scaling with increasing dopant concentration is important to ensure that the magnetism is not arising out of clusters of magnetic islands but rather from the interaction of magnetic dopant with that of the host. However, so far, this systematic dependence has been established only in very few bulk systems, like Mn doped GaAs[120] or InAs.[121,122] This shortfall in quantum dots can be attributed to the inability to obtain the weight of ligands and hence the actual contribution from the DMS material as well as the inability to tune the percentage of dopant ions for a given size.

However, in our technique, wherein we overcome both these shortcomings, we chose five different 12 nm Fe doped CdS QDs with differing Fe ion concentrations ranging from 5-60% to investigate the effect of magnetic ion concentration on M_s and blocking temperature (T_b). The sizes of these particles were observed to be uniform (12 ± 1.5 nm) as characterized by TEM and shown in Figure 5.27(a)-(e). Figure 5.28(a) shows the M *vs.* H hysteresis loop at 2K while the variation of M_s/ Fe ion contribution with the increasing Fe ion concentration is demonstrated in Figure 5.28(b). The M_s value remains invariant upto ~10% of Fe

concentration, above which it starts to increase. This can be simply explained by the presence of a strong ferromagnetic interaction most likely arising from Fe_3O_4 cluster that has not diffused completely into the semiconducting matrix. Secondly, it is also important to note that the overall magnetization arising out of smaller magnetic clusters is much smaller than the bulk value of 4 μ_B/Fe. In a uniformly doped QD, the magnetization, possibly arising out of *sp-d* exchange interactions of the dopant with the host is of similar order of magnitude compared to the magnetism from the small cluster making it non-trivial to point to the origin of magnetism. Therefore, it is important to study the magnetic scaling for varying concentrations of the dopant ion.

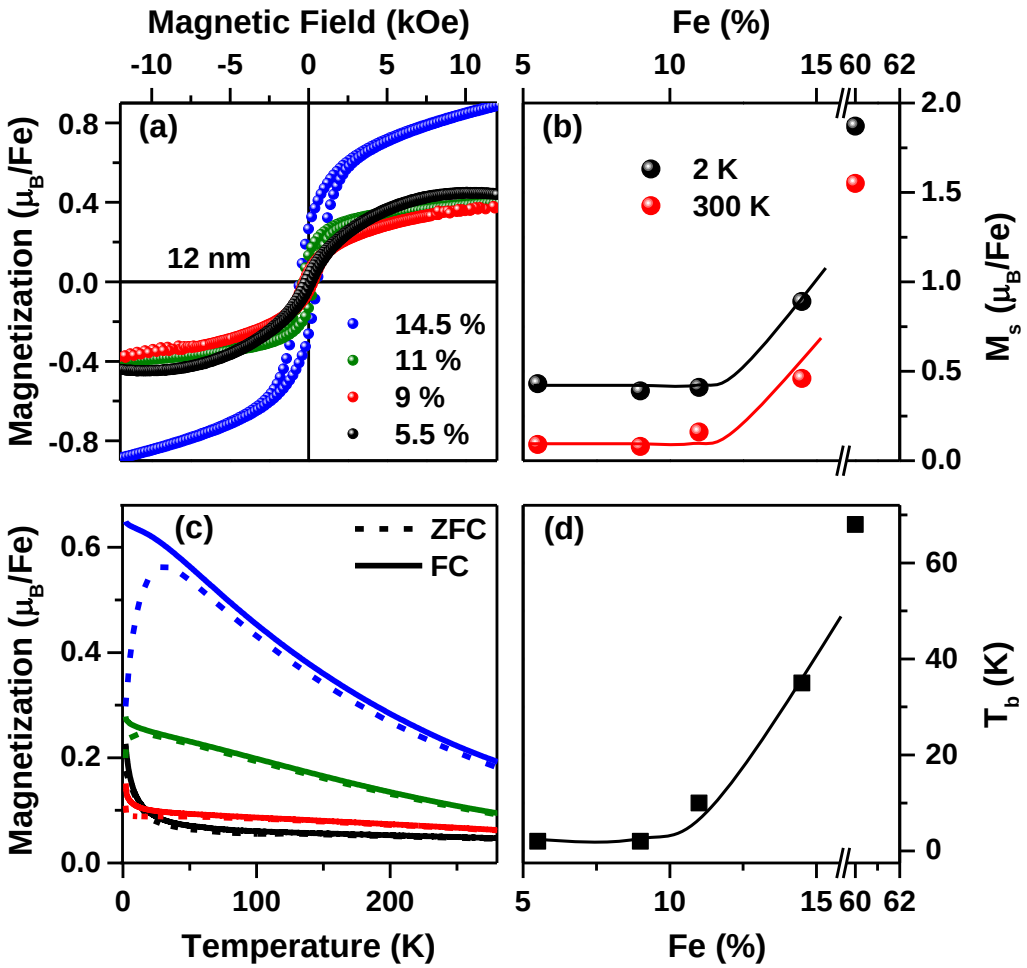

Figure. 5.28 (a) M *vs.* H hysteresis loop (2 K) and (b) variation of saturation magnetization (M_s) of Fe-doped CdS QDs having different Fe percentage. (Solid lines are guide to the eye). (c) Field cooled(solid line) and Zero Field cooled (dotted line) magnetization(Field 200 Oe) for 5.5 % 9 % 11 % and 14.5 % Fe-doped CdS QDs having same size (12 nm)(d) Variation of blocking temperature (T_b) with percentage of Fe.

Table 5.6. Variation of blocking temperature (T_b) and saturation magnetization of 12 nm Fe-doped CdS QDs having different Fe percentage.

%Fe (Size=12 nm)	T_b	M_s (μ_B/Fe)	
		2K	300K
5.5	~2 K	0.44	0.09
9	~2 K	0.32	0.07
11	10 K	0.37	0.18
14.5	35 K	0.93	0.46
60	68 K	1.87	1.55

Hence it is important to further characterize by determining the blocking temperature (T_b) from the temperature dependence of DC susceptibility by measuring zero field cooled (ZFC) and field cool (FC) magnetization measurement as shown in Figure 5.28(c). The blocking temperatures were determined from the peak of ZFC curve and tabulated in Table 5.6 as well as plotted in Figure 5.28(d) as a function of Fe concentration. It's evident that T_b remains constant for small percentage of Fe ions (<10%) due to uniformity in dopant distribution inside the CdS matrix. However, due to existence of central core in case of high Fe% samples T_b increases gradually. The two points that is evident from this study is the range of dilute concentration regime obtained from this synthesis technique and more importantly, the existence of magnetic ion concentration scaling providing further proof for the origin of magnetism in these DMS materials.

Having confirmed two different origins, we proceed to study the size dependence in both magnetic core/shell materials as well as the uniformly distributed magnetically doped semiconductors. Figure 5.29(a) and 5.29(b) shows the magnetic properties of two different sizes 30% Fe/CdS QDs. From the figure, it is evident that even though the magnetism is largely contributed by the magnetic core, the smaller core/shell system of 6 nm has lower M_s (0.3 μ_B/Fe) and T_b (32 K) compared to the 8.5 nm core/shell system with values of 0.5 μ_B/Fe and 48 K respectively. This suggests that even though there exists a magnetic core, the non-magnetic CdS matrix also contributes substantially to the magnetism possibly due to the dopant ions diffused into the CdS lattice. Hence in order to obtain contributions only from the DMS material as a function of size, we prepare different sizes of 5 % Fe doped CdS and the corresponding TEM images are shown in Figure 5.30. The sizes of the QDs are obtained from TEM images range from 12 to 60 nm.

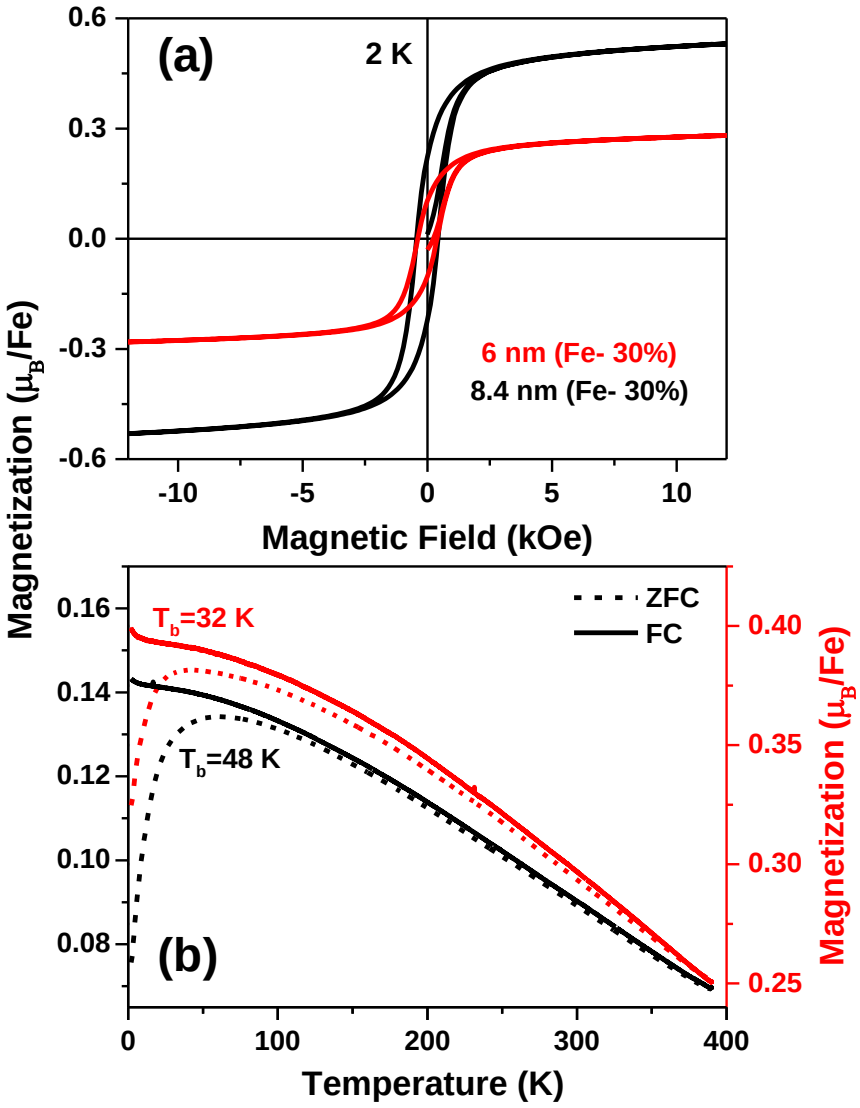

Figure 5.29: M *vs.* H hysteresis loop at 2K Fe-CdS (Fe-30%) samples having size 6 nm and 8.4 nm and (b) their corresponding variation of FC/ZFC curves using a field of 200 Oe.

Magnetic properties of these QDs are shown in Figure 5.31(a)-(d). The M_s values range from 0.44 μ_B/Fe to 1.65 μ_B/Fe as the size increases from 12 nm to 55 nm as shown in Figure Figure 5.31(a) measured at 2K. The variation of saturation magnetization/ion obtained from M *vs.* H hysteresis curve has been shown in Figure 5.31(b) demonstrates an increase of magnetization/ion as particle size increases and saturates for large size (55 nm) particles. It is notable that the M_s value for all these nanoparticles are very much comparable to the bulk value of Fe ion of 4 μ_B/Fe in spite of their small size. Due to their small size, DMS QDs exist as single domain magnet in which spins of free electrons within the QDs are aligned in one

direction. Moreover, at this size regime, physical properties of QDs are strongly influenced by the high surface to volume ratio that changes drastically with the size. As the particle size decreases, the percentage of disordered surface atoms in a QDs increase, which implies that the surface and interface effect are more relevant. In multidomain particles, magnetization reversal is proportional to both the anisotropy energy given by the product of anisotropy constant, K and the volume of the domain, V as well as the energy for the domain wall motion. However, in single domain particle the magnetization reversal is explicitly dependent only on KV. With the decrease of particle size in a single domain nanoparticle KV decreases, thus leading to a decrease in blocking temperature T_b as it requires lesser thermal energy given by k_BT to flip into a superparamagnetic state with spontaneous magnetization reversal leading to significant M_s value but no coercivity H_c. Further confirmation of the size effect is obtained by studying the effect of particle size on magnetization reversal dynamics by measuring temperature dependence of magnetization.

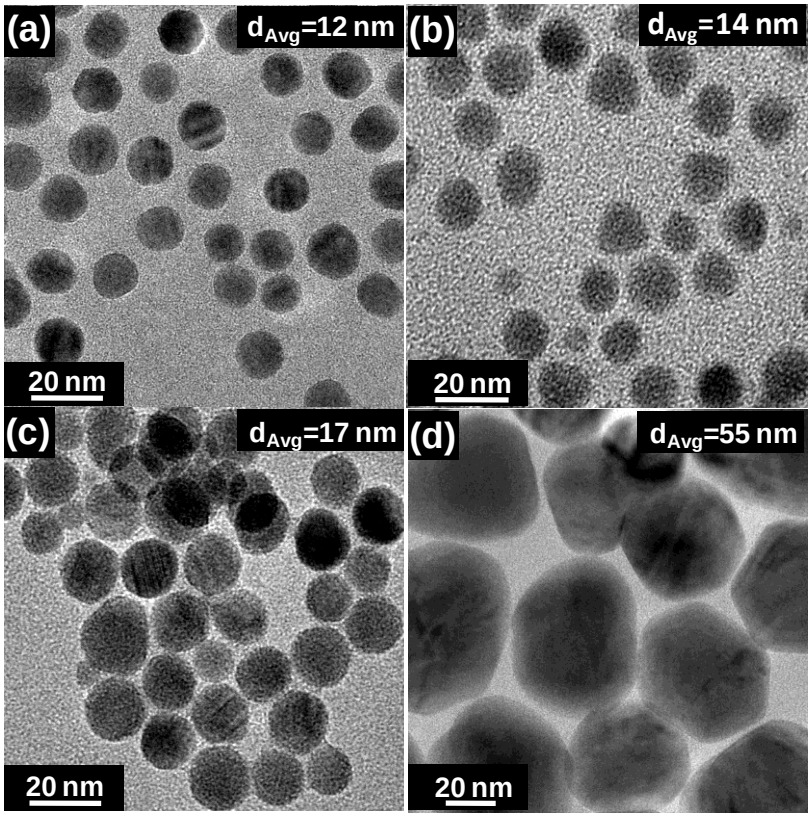

Figure 5.30. TEM images of Fe doped CdS QDs having size (a) 12 nm, (b) 14 nm, (c) 17 nm, and (d) 55 nm.

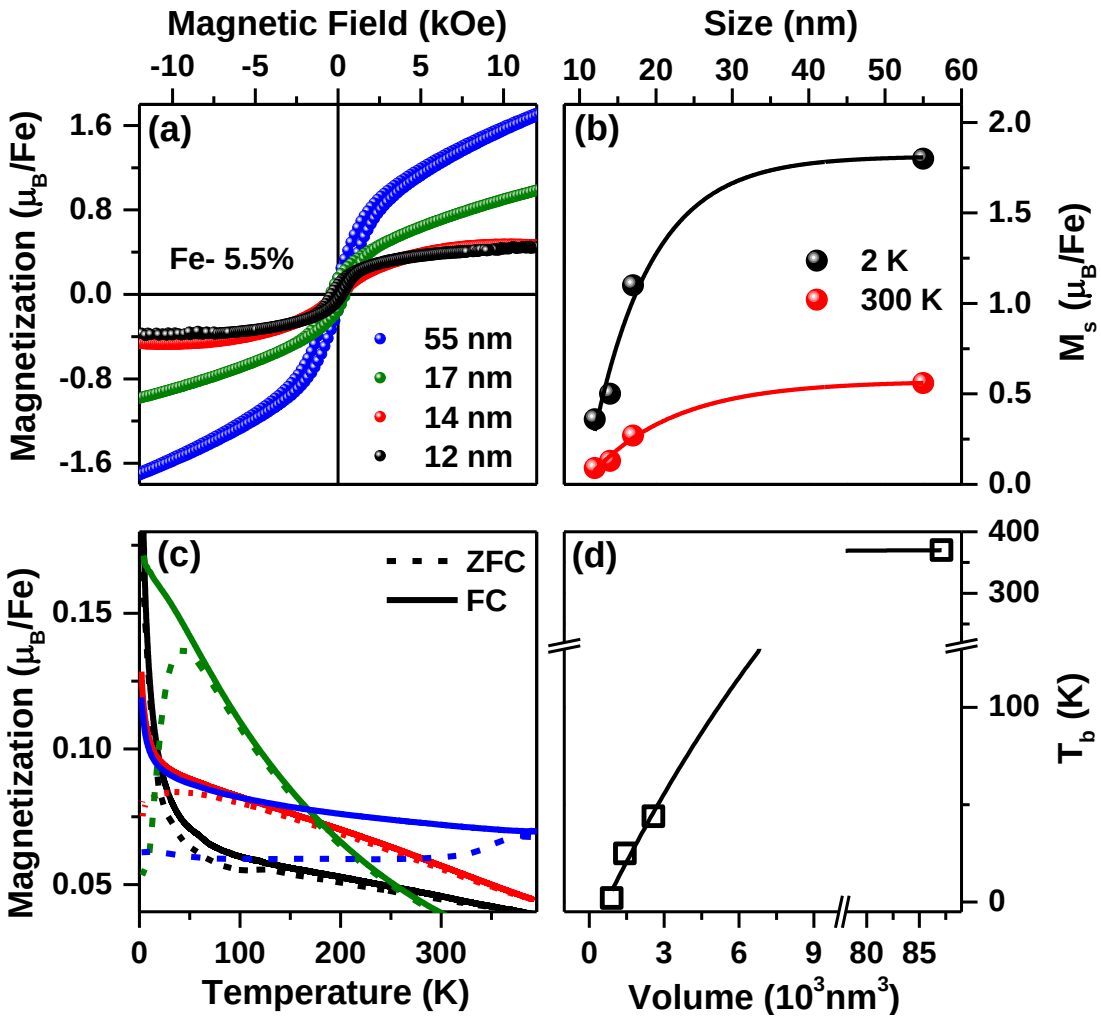

Figure 5.31: (a) M *vs.* H hysteresis loop (2 K) and (b) variation of saturation magnetization (M_s) of Fe-doped CdS QDs having various size. Field cooled and Zero Field cooled magnetization for (c) 12 nm (black) 14 nm (red) 17 nm (green) and 55 nm (blue) Fe-doped CdS QDs having same Fe percentage (5.5%)**.** (d) Variation of blocking temperature (T_b) with particles volume.

Table 5.7: Variation of blocking temperature (T_b) and saturation magnetization of 5.5 % Fe-doped CdS QDs having different size.

Size (Fe=5.5%)	**Tb**	**M_s (μ_B/Fe)**	
		2 K	**300 K**
12 nm	~2 K	0.44	0.09
14 nm	25 K	0.51	0.13
17 nm	44 K	1.12	0.30
55 nm	370 K	1.65	0.64

Variation of magnetization reversal has been studied DC susceptibility from FC/ZFC magnetization as demonstrated in Figure 5.33(c) and the variation of T_b as a function of volume is shown in Figure 5.33(d). As expected, T_b increases with increase in volume and saturates for the large size close to the bulk value of about 370 K similar to the M_s value further confirming the origin of magnetism in this DMS materials. The relevant values for varying sizes are tabulated in Table 5.7.

5.21 Conclusion

Thus we have successfully shown the effect of doping concentration and size variation on the magnetic properties of DMS QDs. These studies highlight the necessity to study the size effects and concentration scaling that provides evidence for the DMS nature of the origin of magnetism. This class of materials have provided a large number of evidences towards the formation of high quality DMS QDs. External control over these parameters in uniform doped DMS gives rise to the progress in the field of spin based electronics and its high potential can be foreseen for the development of spintronics devices. However, the ultimate evidence still relies on the magneto-optical effects that are not discuss in this thesis.

Bibliography

(1) Wang, X.; Sun, G.; Li, N.; Chen, P. *Chem. Soc. Rev.* **2016**, *45*, 2239.

(2) Greidanus, F. J. A. M.; Klahn, S. *Adv. Mater.* **1989**, *1*, 45.

(3) Dee, R. H. *Proc. IEEE* **2008**, *96*, 1775.

(4) Zhang, Y.; Wang, M.; Zheng, Y.-g.; Tan, H.; Hsu, B. Y.-w.; Yang, Z.-c.; Wong, S. Y.; Chang, A. Y.-c.; Choolani, M.; Li, X.; Wang, J. *Chem. Mater.* **2013**, *25*, 2976.

(5) Bharali, D. J.; Lucey, D. W.; Jayakumar, H.; Pudavar, H. E.; Prasad, P. N. *J. Am. Chem. Soc.* **2005**, *127*, 11364.

(6) Deng, D.; Chen, Y.; Cao, J.; Tian, J.; Qian, Z.; Achilefu, S.; Gu, Y. *Chem. Mater.* **2012**, *24*, 3029.

(7) Nagy, A.; SteinbrÃ¼ck, A.; Gao, J.; Doggett, N.; Hollingsworth, J. A.; Iyer, R. *ACS Nano* **2012**, *6*, 4748.

(8) McDaniel, H.; Shim, M. *ACS Nano* **2009**, *3*, 434.

(9) Kwon, K.-W.; Lee, B. H.; Shim, M. *Chem. Mater.* **2006**, *18*, 6357.

(10) Son, J. S.; Lee, J.-S.; Shevchenko, E. V.; Talapin, D. V. *J. Phys. Chem. Lett.* **2013**, *4*, 1918.

(11) Lee, J.-S.; Bodnarchuk, M. I.; Shevchenko, E. V.; Talapin, D. V. *J. Am. Chem. Soc.* **2010**, *132*, 6382.

(12) Depalo, N.; Carrieri, P.; Comparelli, R.; Striccoli, M.; Agostiano, A.; Bertinetti, L.; Innocenti, C.; Sangregorio, C.; Curri, M. L. *Langmuir* **2011**, *27*, 6962.

(13) Dietl, T. *Nat. Mater.* **2003**, *2*, 646.

(14) Dietl, T. *Nat. Mater.* **2010**, *9*, 965.

(15) Huang, X.; Makmal, A.; Chelikowsky, J. R.; Kronik, L. *Phys. Rev. Lett.* **2005**, *94*, 236801.

(16) Xiong, S.-J.; Du, Y. W. *Phys. Lett. A* **2008**, *372*, 2114.

(17) Murali, G.; Amaranatha Reddy, D.; PoornaPrakash, B.; Vijayalakshmi, R. P.; Reddy, B. K.; Venugopal, R. *Physica B* **2012**, *407*, 2084.

(18) El-Hagary, M.; Soltan, S. *J. Appl. Phys.* **2012**, *112*, 043907.

(19) Kaur, K.; Lotey, G. S.; Verma, N. K. *J.Mater. Sci: Mater. Electron.* **2014**, *25*, 2605.

(20) Shanker, G. S.; Tandon, B.; Shibata, T.; Chattopadhyay, S.; Nag, A. *Chem. Mater.* **2015**, *27*, 892.

(21) Grandhi, G. K.; Tomar, R.; Viswanatha, R. *ACS Nano* **2012**, *6*, 9751.

(22) Hanif, K. M.; Meulenberg, R. W.; Strouse, G. F. *J. Am. Chem. Soc.* **2002**, *124*, 11495.

(23) Bonanni, A.; Dietl, T. *Chem. Soc. Rev.* **2010**, *39*, 528.

(24) Yan, W.; Liu, Q.; Wang, C.; Yang, X.; Yao, T.; He, J.; Sun, Z.; Pan, Z.; Hu, F.; Wu, Z.; Xie, Z.; Wei, S. *J. Am. Chem. Soc.* **2014**, *136*, 1150.

(25) May, J. W.; McMorris, R. J.; Li, X. *J. Phys. Chem. Lett.* **2012**, *3*, 1374.

(26) Sarma, S. D. *Nat. Mater.* **2003**, *2*, 292.

(27) Wolf, S. A.; Awschalom, D. D.; Buhrman, R. A.; Daughton, J. M.; von Molnar, S.; Roukes, M. L.; Chtchelkanova, A. Y.; Treger, D. M. *Science* **2001**, *294*, 1488.

(28) Chappert, C.; Fert, A.; Van Dau, F. N. *Nat. Mater.* **2007**, *6*, 813.

(29) Chambers, S. A.; Yoo, Y. K. *MRS Bulletin* **2003**, *28*, 706.

(30) Sarkar, I.; Sanyal, M. K.; Kar, S.; Biswas, S.; Banerjee, S.; Chaudhuri, S.; Takeyama, S.; Mino, H.; Komori, F. *Phys. Rev. B* **2007**, *75*, 224409.

(31) Norberg, N. S.; Parks, G. L.; Salley, G. M.; Gamelin, D. R. *J. Am. Chem. Soc.* **2006**, *128*, 13195.

(32) Cheng, S. J. *Phys.Rev. B* **2008**, *77*, 115310.

(33) Gurung, T.; Mackowski, S.; Jackson, H. E.; Smith, L. M.; Heiss, W.; Kossut, J.; Karczewski, G. *J. Appl. Phys.* **2004**, *96*, 7407.

(34) Feltin, N.; Levy, L.; Ingert, D.; Pileni, M.-P. *Adv. Mater.* **1999**, *11*, 398.

(35) Viswanatha, R.; Pietryga, J. M.; Klimov, V. I.; Crooker, S. A. *Phys. Rev. Lett.* **2011**, *107*, 067402.

(36) Erwin, S. C.; Zu, L.; Haftel, M. I.; Efros, A. L.; Kennedy, T. A.; Norris, D. J. *Nature* **2005**, *436*, 91.

(37) Yuhas, B. D.; Fakra, S.; Marcus, M. A.; Yang, P. *Nano Lett.* **2007**, *7*, 905.

(38) Segura-Ruiz, J.; Martinez-Criado, G.; Chu, M. H.; Geburt, S.; Ronning, C. *Nano Lett.* **2011**, *11*, 5322.

(39) Keavney, D. J.; Cheung, S. H.; King, S. T.; Weinert, M.; Li, L. *Phys. Rev. Lett.* **2005**, *95*, 257201.

(40) Karan, N. S.; Sarkar, S.; Sarma, D. D.; Kundu, P.; Ravishankar, N.; Pradhan, N. *J. Am. Chem. Soc.* **2011**, *133*, 1666.

(41) Dalpian, G. M.; Chelikowsky, J. R. *Phys. Rev. Lett.* **2006**, *96*, 226802.

(42) Chen, D.; Viswanatha, R.; Ong, G. L.; Xie, R.; Balasubramaninan, M.; Peng, X. *J. Am. Chem. Soc.* **2009**, *131*, 9333.

(43) Hazarika, A.; Pandey, A.; Sarma, D. D. *J. Phys. Chem. Lett.* **2014**, *5*, 2208.

(44) Li, J. J.; Wang, Y. A.; Guo, W.; Keay, J. C.; Mishima, T. D.; Johnson, M. B.; Peng, X. *J. Am. Chem. Soc.* **2003**, *125*, 12567.

(45) Pradhan, N.; Peng, X. *J. Am. Chem. Soc.* **2007**, *129*, 3339.

(46) Barrows, C. J.; Vlaskin, V. A.; Gamelin, D. R. *J. Phys. Chem. Lett.* **2015**, *6*, 3076.

(47) Singh, S. B.; Limaye, M. V.; Date, S. K.; Gokhale, S.; Kulkarni, S. K. *Phys. Rev. B* **2009**, *80*, 235421.

(48) Hou, Y.; Xu, Z.; Sun, S. *Angew. Chem. Int. Ed.* **2007**, *46*, 6329.

(49) Segre, C. U.; Leyarovska, N. E.; Chapman, L. D.; Lavender, W. M.; Plag, P. W.; King, A. S.; Kropf, A. J.; Bunker, B. A.; Kemner, K. M.; Dutta, P.; Duran, R. S.; Kaduk, J. *AIP Conf. Proc.* **2000**, *521*, 419.

(50) Saha, A.; Chellappan, K. V.; Narayan, K. S.; Ghatak, J.; Datta, R.; Viswanatha, R. *J. Phys. Chem. Lett.* **2013**, *4*, 3544.

(51) Battaglia, D.; Blackman, B.; Peng, X. *J. Am. Chem. Soc.* **2005**, *127*, 10889.

(52) Signorini, L.; Pasquini, L.; Savini, L.; Carboni, R.; Boscherini, F.; Bonetti, E.; Giglia, A.; Pedio, M.; Mahne, N.; Nannarone, S. *Phys. Rev. B* **2003**, *68*, 195423.

(53) Sun, Z.; Yan, W.; Yao, T.; Liu, Q.; Xie, Y.; Wei, S. *Dalton Trans.* **2013**, *42*, 13779.

(54) Newville, M. *J. Synchrotron Rad.* **2001**, *8*, 322.

(55) Zhang, M.; Pan, G.; Zhao, D.; He, G. *Environ. Pollut.* **2011**, *159*, 3509.

(56) Colliex, C.; Manoubi, T.; Ortiz, C. *Phys. Rev. B* **1991**, *44*, 11402.

(57) Sparrow, T. G.; Williams, B. G.; Rao, C. N. R.; Thomas, J. M. *Chem. Phys. Lett.* **1984**, *108*, 547.

(58) Frost, J. M.; Harriman, K. L. M.; Murugesu, M. *Chem. Sci.* **2016**, *7*, 2470.

(59) Coey, J. M. D.; Venkatesan, M.; Fitzgerald, C. B. *Nat. Mater.* **2005**, *4*, 173.

(60) Beaulac, R.; Schneider, L.; Archer, P. I.; Bacher, G.; Gamelin, D. R. *Science* **2009**, *325*, 973.

(61) Norris, D. J.; Yao, N.; Charnock, F. T.; Kennedy, T. A. *Nano Lett.* **2001**, *1*, 3.

(62) Hoffman, D. M.; Meyer, B. K.; Ekimov, A. I.; Merkulov, I. A.; Efros, A. L.; Rosen, M.; Couino, G.; Gacoin, T.; Boilot, J. P. *Solid State Commun.* **2000**, *114*, 547.

(63) Ghosh, A.; Paul, S.; Raj, S. *J. Appl. Phys.* **2013**, *114*, 094304.

(64) Huang, J. C. A.; Hsu, H. S.; Hu, Y. M.; Lee, C. H.; Huang, Y. H.; Lin, M. Z. *App. Phys. Lett.* **2004**, *85*, 3815.

(65) Madhu, C.; Sundaresan, A.; Rao, C. N. R. *Phys. Rev. B* **2008**, *77*, 201306.

(66) Lorite, I.; Kumar, Y.; Esquinazi, P.; Zandalazini, C.; de Heluani, S. P. *Small* **2015**, *11*, 4403.

(67) Noh, S.-h.; Na, W.; Jang, J.-t.; Lee, J.-H.; Lee, E. J.; Moon, S. H.; Lim, Y.; Shin, J.-S.; Cheon, J. *Nano Lett.* **2012**, *12*, 3716.

(68) Schuler, T.; Stern, R.; McNorton, R.; Willoughby, S.; MacLaren, J.; Ederer, D.; Perez-Dieste, V.; Himpsel, F.; Lopez-Rivera, S.; Callcott, T. *Phys. Rev. B* **2005**, *72*, 045211.

(69) Pradhan, N.; Peng, X. *J. Am. Chem. Soc* **2007**, *129*, 3339.

(70) Pradhan, N.; Goorskey, D.; Thessing, J.; Peng, X. *J. Am. Chem. Soc.* **2005**, *127*, 17586.

(71) Vlaskin, V. A.; Barrows, C. J.; Erickson, C. S.; Gamelin, D. R. *J. Am. Chem. Soc.* **2013**, *135*, 14380.

(72) Bogle, K. A.; Ghosh, S.; Dhole, S. D.; Bhoraskar, V. N.; Fu, L.-f.; Chi, M.-f.; Browning, N. D.; Kundaliya, D.; Das, G. P.; Ogale, S. B. *Chem. Mater.* **2008**, *20*, 440.

(73) Popa, A.; Toloman, D.; Raita, O.; Biris, A. R.; Borodi, G.; Mustafa, T.; Watanabe, F.; Biris, A. S.; Darabont, A.; Giurgiu, L. M. *Cent. Eur. J. Phys.* **2011**, *9*, 1446.

(74) Saha, A.; Chattopadhyay, S.; Shibata, T.; Viswanatha, R. *J. Mater. Chem. C* **2014**, *2*, 3868.

(75) Hoy, J.; Morrison, P. J.; Steinberg, L. K.; Buhro, W. E.; Loomis, R. A. *J. Phys. Chem. Lett.* **2013**, *4*, 2053.

(76) Seo, G.; Seo, J.; Ryu, S.; Yin, W.; Ahn, T. K.; Seok, S. I. *J. Phys. Chem. Lett.* **2014**, *5*, 2015.

(77) Ravel, B.; Newville, M. *J. Synchrotron Rad.* **2005**, *12*, 537.

(78) Saha, A.; Shetty, A.; Pavan, A. R.; Chattopadhyay, S.; Shibata, T.; Viswanatha, R. *J. Phys. Chem. Lett.* **2016**, *7*, 2420.

(79) Zhang, P. *J. Phys. Chem. C* **2014**, *118*, 25291.

(80) Asakura, H.; Shishido, T.; Yamazoe, S.; Teramura, K.; Tanaka, T. *J. Phys. Chem. C* **2011**, *115*, 23653.

(81) Liu, T.; Xu, H.; Chin, W. S.; Yong, Z.; Wee, A. T. S. *J. Phys. Chem. C* **2008**, *112*, 3489.

(82) Rehr, J. J.; Albers, R. C. *Rev. Mod. Phys.* **2000**, *72*, 621.

(83) Krylov, A. S.; Poliakoff, J. F.; Stockenhuber, M. *Phys. Chem. Chem. Phys.* **2000**, *2*, 5743.

(84) Toyoda, T.; Sasaki, S.; Tanaka, M. *Am. Mineral.* **1999**, *84*, 294.

(85) Mukherjee, S.; Nag, A.; Kocevski, V.; Santra, P. K.; Balasubramanian, M.; Chattopadhyay, S.; Shibata, T.; Schaefers, F.; Rusz, J.; Gerard, C.; Eriksson, O.; Segre, C. U.; Sarma, D. D. *Phys. Rev. B* **2014**, *89*, 224105.

(86) Ohtomo, A.; Hwang, H. Y. *Nature* **2004**, *427*, 423.

(87) Kalisky, B.; Bert, J. A.; Klopfer, B. B.; Bell, C.; Sato, H. K.; Hosoda, M.; Hikita, Y.; Hwang, H. Y.; Moler, K. A. *Nature Commun.* **2012**, *3*, 922.

(88) Brown, K. A.; He, S.; Eichelsdoerfer, D. J.; Huang, M.; Levy, I.; Lee, H.; Ryu, S.; Irvin, P.; Mendez-Arroyo, J.; Eom, C.-B.; Mirkin, C. A.; Levy, J. *Nature Commun.* **2016**, *7*, 10681.

(89) Brinkman, A.; Huijben, M.; van Zalk, M.; Huijben, J.; Zeitler, U.; Maan, J. C.; van der Wiel, W. G.; Rijnders, G.; Blank, D. H. A.; Hilgenkamp, H. *Nature Mater.* **2007**, *6*, 493.

(90) Chan, N. Y.; Zhao, M.; Wang, N.; Au, K.; Wang, J.; Chan, L. W. H.; Dai, J. *ACS Nano* **2013**, *7*, 8673.

(91) Mathew, S.; Annadi, A.; Chan, T. K.; Asmara, T. C.; Zhan, D.; Wang, X. R.; Azimi, S.; Shen, Z.; Rusydi, A.; Ariando; Breese, M. B. H.; Venkatesan, T. *ACS Nano* **2013**, *7*, 10572.

(92) Fan, Y.; Smith, K. J.; LupkeG; Hanbicki, A. T.; GoswamiR; Li, C. H.; Zhao, H. B.; Jonker, B. T. *Nature Nanotech.* **2013**, *8*, 438.

(93) Sa de Melo, C. A. R. *Phys. Rev. Lett.* **1997**, *79*, 1933.

(94) Zanolli, Z. *Scientific Reports* **2016**, *6*, 31346.

(95) Yan, S.; Choi, D.-J.; Burgess Jacob, A. J.; Rolf-Pissarczyk, S.; Loth, S. *Nature Nanotech.* **2015**, *10*, 40.

(96) Saha, A.; Chattopadhyay, S.; Shibata, T.; Viswanatha, R. *J. Phys. Chem. C* **2016**, *120*, 18945.

(97) Wu, L.; Mendoza-Garcia, A.; Li, Q.; Sun, S. *Chem. Rev.* **2016**, *116*, 10473.

(98) Lartigue, L.; Hugounenq, P.; Alloyeau, D.; Clarke, S. P.; Levy, M.; Bacri, J.-C.; Bazzi, R.; Brougham, D. F.; Wilhelm, C.; Gazeau, F. *ACS Nano* **2012**, *6*, 10935.

(99) Fortin, J.-P.; Wilhelm, C.; Servais, J.; Menager, C.; Bacri, J.-C.; Gazeau, F. *J. Am. Chem. Soc.* **2007**, *129*, 2628.

(100) Roychowdhury, A.; Pati, S. P.; Kumar, S.; Das, D. *Mater. Chem. Phys.* **2014**, *151*, 105.

(101) Liu, X.; Fang, Z.; Zhang, X.; Zhang, W.; Wei, X.; Geng, B. *Cryst. Growth Des.* **2009**, *9*, 197.

(102) Santra, P. K.; Viswanatha, R.; Daniels, S. M.; Pickett, N. L.; Smith, J. M.; O'Brien, P.; Sarma, D. D. *J. Am. Chem. Soc.* **2009**, *131*, 470.

(103) Meiklejohn, W. H.; Bean, C. P. *Phys. Rev.* **1956**, *102*, 1413.

(104) Nogues, J.; Schuller, I. K. *J. Magn. Magn. Mater.* **1999**, *192*, 203.

(105) Nogues, J.; Sort, J.; Langlais, V.; Skumryev, V.; Surinach, S.; Munoz, J. S.; Baro, M. D. *Phys. Reports* **2005**, *422*, 65.

(106) Lottini, E.; Lopez-Ortega, A.; Bertoni, G.; Turner, S.; Meledina, M.; Tendeloo, G. V.; de Julian Fernandez, C.; Sangregorio, C. *Chem. Mater.* **2016**, *28*, 4214.

(107) Wetterskog, E.; Tai, C.-W.; Grins, J.; Bergstrom, L.; Salazar-Alvarez, G. *ACS Nano* **2013**, *7*, 7132.

(108) Son, J. Y.; Kim, C. H.; Cho, J. H.; Shin, Y.-H.; Jang, H. M. *ACS Nano* **2010**, *4*, 3288.

(109) Meiklejohn, W. H.; Bean, C. P. *Phys. Rev.* **1957**, *105*, 904.

(110) Ogale, S. B. *Adv. Mater.* **2010**, *22*, 3125.

(111) Munekata, H. *Adv. Mater.* **1995**, *7*, 82.

(112) Liu, W. K.; Whitaker, K. M.; Kittilstved, K. R.; Gamelin, D. R. *J. Am. Chem. Soc.* **2006**, *128*, 3910.

(113) Weller, D.; Mosendz, O.; Parker, G.; Pisana, S.; Santos, T. S. *Phys. Status Solidi A* **2013**, *210*, 1245.

(114) Casula, M. F.; Floris, P.; Innocenti, C.; Lascialfari, A.; Marinone, M.; Corti, M.; Sperling, R. A.; Parak, W. J.; Sangregorio, C. *Chem. Mater.* **2010**, *22*, 1739.

(115) Bauer, L. M.; Situ, S. F.; Griswold, M. A.; Samia, A. C. S. *J. Phys. Chem. Lett.* **2015**, *6*, 2509.

(116) Malyutin, A. G.; Easterday, R.; Lozovyy, Y.; Spilotros, A.; Cheng, H.; Sanchez-Felix, O. R.; Stein, B. D.; Morgan, D. G.; Svergun, D. I.; Dragnea, B.; Bronstein, L. M. *Chem. Mater.* **2015**, *27*, 327.

(117) Sapra, S.; Sarma, D. D.; Sanvito, S.; Hill, N. A. *Nano Lett.* **2002**, *2*, 605.

(118) Chekhovich, E. A.; Brichkin, A. S.; Chernenko, A. V.; Kulakovskii, V. D.; Sedova, I. V.; Sorokin, S. V.; Ivanov, S. V. *Phys. Rev. B* **2007**, *76*, 165305.

(119) Coey, J. M. D.; Venkatesan, M.; Stamenov, P.; Fitzgerald, C. B.; Dorneles, L. S. *Phys. Rev. B* **2005**, *72*, 024450.

(120) Matsukura, F.; Ohno, H.; Shen, A.; Sugawara, Y. *Phys. Rev. B* **1998**, *57*, R2037.

(121) Ohno, H.; Chiba, D.; Matsukura, F.; Omiya, T.; Abe, E.; Dietl, T.; Ohno, Y.; Ohtani, K. *Nature* **2000**, *408*, 944.

(122) Chiba, D.; Yamanouchi, M.; Matsukura, F.; Ohno, H. *Science* **2003**, *301*, 943.

Chapter 6

Diffusion Doping: A Universal Technique to Produce Multifunctional QDs

The following papers have been published based on the work presented here.

- *Nanoscale*, **2017**, *9*, 2806-2813

Section A

Role of Thermodynamics in Diffusion Doping

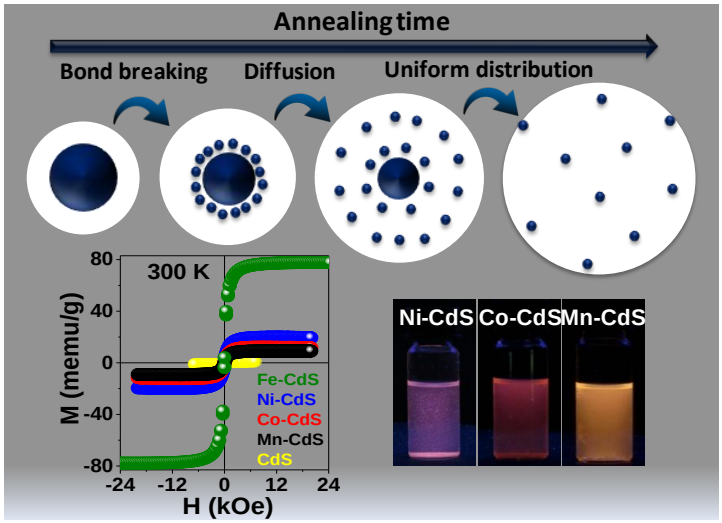

6.1 Summary

Semiconducting materials uniformly doped with optical or magnetic impurity have been useful in a number of potential applications. However, clustering or phase separation during synthesis has made this job challenging. The "inside out" diffusion doping proposed in chapter 5 of this thesis is found to be successful in obtaining large sized QDs uniformly doped with dilute percentage of dopant atoms. Herein, we demonstrate the use of basic physical chemistry of diffusion to control the size and concentration of the dopants within the QDs for a given transition metal ion. We have identified two important parameters, the bond strength of the core molecules and the diffusion coefficient of the diffusing metal ion as two important parameters in the control of size and concentration of the single domain DMSQDs with diverse dopant ions M^{2+} (Fe^{2+}, Ni^{2+}, Co^{2+}, Mn^{2+}). Steady state optical emission spectra reveal that the dopants are incorporated inside the semiconducting CdS and the emission can be tuned during shell growth. We have shown that this method enables control over doping percentage and the QDs show superior ferromagnetic response at room temperature as compared to earlier reported systems.

6.2 Introduction

The doping of paramagnetic transition metal ions in QDs have occupied center stage in nanomaterials research for a number of decades due to the unique electronic,[1,2] optical[3,4] and magnetic[5-8] properties introduced by the dopant in the host QD and its potential applications.[9,10] These unique properties are controlled by the presence of *sp-d* exchange interactions[11,12] between the dopant and the host which are enhanced by the presence of three dimensional confinements. While the presence of this multi-functionality offers unprecedented opportunities for the development of magneto-optic, magneto-switching and spintronics applications,[13-15] the actual development of these applications has not advanced much due to a bottleneck problem that is yet to be completely addressed. The main problem associated with the doped QDs is the absence of reproducible synthesis techniques promising cluster-free, uniformly distributed dopant within the host QDs. The well-known traditional techniques reported in literature are based on reaction of impurity ions with the host inside the system.[16,17] However control and optimization of the doping environment is difficult and in most of the cases forms impurity cluster or

secondary phase inside the semiconductor. As a result, a significant part of the QDs remains undoped and the doping becomes inhomogeneous. This problem was recognized in the early stages of research and several strategies have evolved over the past decade to overcome this problem. Some of the important methods include the separation of host nucleation and dopant incorporation,[18] nucleation doping,[19] reduction in the dopant concentration to avoid the formation of clusters in addition to tinkering with the synthesis parameters like temperature,[20] lattice mismatch and ligands used for the QDs synthesis. We have demonstrated in chapter 5, the use of self-diffusion to obtain uniformly doped QDs using an "inside-out" strategy for the growth of Fe doped CdS that allows for a precise control of size of the QDs and dopant concentration ranging from 0.1-10% with uniform doping. This has shown to significantly improve their magnetic properties. However, the universality of this technique is not established and extending doping chemistry to other hosts and dopants is not straight forward, as different impurity ions behaves differently depending on multitude of factors determining energetics dictated by surface morphology, crystal structure, surfactants in growth solution among many others. For example, Mn can be incorporated in ZnSe[21,22] or in CdS[23] easily by addition of Mn precursor but not in CdSe. It has been observed that Mn can be doped only at the surface by use of MnSe organometallic precursor.[24]

In this chapter, we have studied the thermodynamic parameters responsible for an efficient diffusion of the given dopant ion within the host matrix leading to required sizes, not limited to larger QDs to obtain uniformly doped multifunctional QDs.[25] Specifically, we have addressed two important factors that could be critical in determining the tunability of this technique, namely, (a) the nature of the interface of the metal atom with the solid to originate diffusion followed by (b) the diffusivity of the metal atom within the solid to propagate diffusion. The choice of these two parameters are based on study of transport of metal ions and atoms in solids under different effects like thermal, electric or magnetic stress in bulk literature.[26,27] We have studied these two effects using core molecules of differing bond strengths and hence the interface as well as different metal ions with different diffusing power in the quantum confined regime. In general the metal sulfide (M-S) bonds are known to be less stable than the metal oxide (M-O) bonds. Here we have studied the effect of use of less stable Fe_7S_8

and more stable Fe_3O_4 core on the size and doping percentage when it is allowed to diffuse into CdS matrix. Secondly, we have studied the effect of diffusion of different transition metal ions within the CdS lattice. It is well known that while Fe doping is primarily interesting for their magnetic properties, doping with other transition metals are important both for their optical as well as magnetic properties. The best manifestation of optical properties can be observed in QDs, whose sizes are typically 5-6 nm. In order to achieve this, we have used transition metal (Fe^{2+}, Mn^{2+}, Ni^{2+}, Co^{2+}) sulfides as core instead of their oxide counterparts as the diffusion of the sulfides core into the host lattice is more facile. This allows for the formation of smaller QDs (~5 nm) with uniform doping of the transition metal ions demonstrating not only the universality of the technique but also the capability to tailor-make QDs with required size and dopant concentration.

These QDs are characterized using transmission electron microscopy (TEM) to determine the size, X-ray diffraction (XRD) for crystal structure information and UV-VIS absorption and photoluminescence (PL) for optical properties. Thermo-gravimetric analysis (TGA) was used to obtain the weight percentage of ligands and the magnetic measurements were obtained using superconducting quantum interference device SQUID magnetometer. The magnetic moment per ion was then calculated. The structural uniformity correlates with superior magnetic property from these materials which is at least an order of magnitude higher than previously reported systems.[28-30]

6.3 Experimental Details

6.3.1 Synthesis

Synthesis of Precursors: 0.2 M cadmium oleate, 0.2 M nickel oleate and 0.2 M cobalt oleate. Three separate syntheses were performed to prepare $Cd(Ol)_2$, $Ni(Ol)_2$ and $Co(Ol)_2$. Cadmium Oxide (1.6 mmol) or Nickel acetate tetrahydrate (1.6 mmol) or cobalt acetate (1.6 mmol), ODE (7 ml) and OA (1.13 g) were taken in a three necked flask and degassed at 70°C. After degassing for 1 hour, the temperature was raised to higher temperature (180-220°C) under Ar atmosphere until a clear solution of respective oleates (Cadmium/Nickel/Cobalt) are formed. The solutions were cooled down to room temperature and stored in Ar atmosphere.

Manganese stearate. Manganese stearate ($MnSt_2$) was synthesized similar to literature reports.[19] Briefly, stearic acid (0.02 mol) was dissolved in methanol and heated up to 50°C to get a clear solution. TMAH solution was obtained by dissolving TMAH (0.02 mol) in methanol and was then added to stearic acid solution. The obtained reaction mixture was stirred followed by the slow addition of $MnCl_2$ (0.01 mol) in methanol with constant stirring. This results in the formation of white precipitate of manganese stearate. The resultant precipitate was washed with methanol and acetone.

Synthesis of Fe-doped CdS from oxide core: Similar synthesis of Fe-doped CdS has been done using Iron oxide (Fe_3O_4) as core. The details of synthesis can be found section 5.4.1 in chapter 5. In brief, Fe_3O_4 core was synthesised and overcoated by SILAR technique using Cd and S precursor at 240°C. High temperature annealing during overcoating results in diffusion of Fe ions inside thick CdS forming Fe-doped CdS.

Synthesis of Fe-doped CdS from sulfide core: At first Fe_7S_8 core was synthesized at high temperature. Briefly, $Fe(acac)_3$, S-powder, 2 ml of oleic acid and 6 ml of oleylamine were degassed at 80 °C for an hour and raised to 200 °C under constant argon flow. After 10 min, the temperature of the reaction mixture was raised to 250 °C gradually (3K/min) maintaining it for another 10 min. Then, the as synthesized QDs were isolated by centrifugation, washed once with ethanol-hexane mixture and a few drops of acetone, and used for further synthesis of doped QDs. These sulfide cores were overcoated following similar process as maintained for Fe_3O_4 QDs.

Synthesis of Ni/Co/Mn doped CdS from sulfide core. For the core synthesis, $Ni(Ol)_2$ (100 µL)/ $Co(Ol)_2$ (100 µL)/ $MnSt_2$ (0.03 g) was taken in a three necked flask with 8 ml of ODE and degassed at 80°C. 0.5 ml of 0.2 M S/ODE solution was mixed with 0.2 g of ODA and further diluted with 1 ml of ODE in a vial. The temperature of the reaction mixture containing oleate was raised to 240°C under Ar-atmosphere. As the temperature reached to 240°C, the precursor solution S/ODA/ODE is quickly injected and the reaction mixture is quenched to 140°C.

0.2 M cadmium oleate and 0.2 M sulfur dissolved in ODE were used as precursor to overcoat CdS matrix over these transition metal sulfide core QDs. SILAR technique[31] was used to grow the CdS matrix at annealing temperature of 140°C. In these cases

overcoating was carried on in-situ without the isolation of metal sulfide cores. The stoichiometric amount of $Cd(Ol)_2$ required for a monolayer of shell formation was injected to the reaction mixture. After 15 min same amount of S precursor was injected into the system and annealed for 10 min. This cycle of Cd followed by S precursors addition were continued until required CdS shell thickness is formed. The samples were collected after completion of each cycle. All the samples were washed by centrifugation using hexane methanol mixture and redispersed in hexane.

Undoped CdS. Undoped CdS was synthesized using similar experimental condition described for doped CdS without taking any transition metal core. We first synthesize CdS at 240°C without any transition metal precursor, and overcoated at 140°C as stated above.

6.4 Results and Discussion

6.4.1 Effect of Core Stability

Precise control of doping fraction and the final size of the doped QDs using different transition metals (Fe^{2+}, Ni^{2+}, Co^{2+}, Mn^{2+}) in the "inside-out" diffusion phenomena depend on the penetration capability of the core metal ions into the CdS lattice followed by the diffusivity of metal ions within the CdS lattice. Penetration capability, in turn depends on the interfacial stability and the bond dissociation energies of the core molecules. During overcoating and simultaneous annealing at high temperature, thermal stress created due to continuous heating and the crystal strain due to lattice mismatch from core-shell interface help to break the bonds inside the core and then the metal ions diffuse inside the semiconducting matrix as determined by its diffusivity. To study the effect of core stability we have carried out the synthesis using ~5 nm transition metal oxide (Fe_3O_4) and sulfide (Fe_7S_8) as core materials in two different reactions for the purpose of doping Fe into CdS matrix. Figure 6.1 shows the XRD (6.1 (a)) and TEM images of these core materials (Figure 6.1 (b) and 6.1(c)) demonstrating the formation of Fe_3O_4 and Fe_7S_8 phases. These core materials were overcoated with CdS and the so obtained materials were designated respectively as Fe(O)-CdS and Fe(S)-CdS. XRD patterns obtained from these two different syntheses are shown in Figure 6.2 (a). From the figure, it is evident both the samples crystallize in wurtzite form of CdS with no impurity peaks arising either from the inverse spinel structure of Fe_3O_4 or the trigonal

structure of FeS. This suggests that the Fe from the core is completely dissociated and diffused into the CdS lattice.

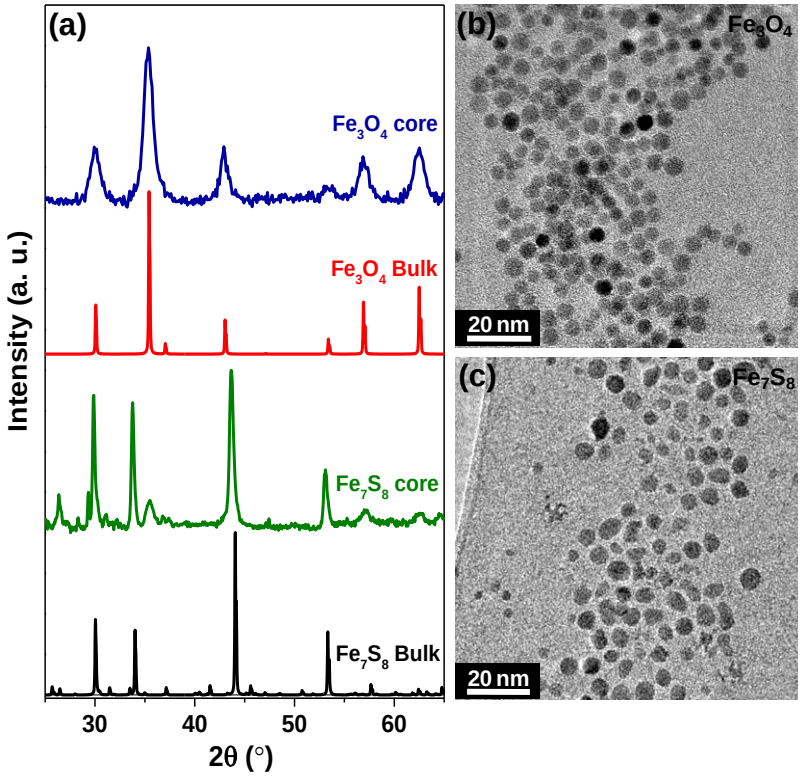

Figure 6.1 (a) XRD pattern of Fe_3O_4 and Fe_7S_8 core. TEM images of (b) Fe_3O_4 and (c) Fe_7S_8 core nanoparticles.

Further, TEM images shown in Figure 6.2 (b) and 6.2 (c) respectively for Fe(O)-CdS and Fe(S)-CdS (Size distribution Figure 6.3) show that the sizes are about 9.5 nm and 9.1 nm respectively. Both the samples were heated at high temperature for about 7.5 hours to facilitate diffusion of Fe in CdS. However, the percentage of transition metal ions inside the QDs as monitored using ICP-OES were found to be widely different. It was found to be about 10.5% in the case of Fe(O)-CdS while that in Fe(S)-CdS was found to be ~2%. Given that all other conditions were kept constant, this change in percentage can be purely attributed to the difference in their bond dissociation energies and hence penetration into the interface of CdS and the core. It is found in literature that Fe_3O_4 is more stable than Fe_7S_8 as given by their respective bond dissociation energies, i.e., bond dissociation energy of 407.0±1.0 kJ/mol for Fe-O compared to 328.9±14.6 kJ/mol for the Fe-S case.[32] In fact, it is worth mentioning that in order to reduce the Fe to 2% in the case of Fe(O)-CdS, one observes that it is necessary to heat for about 14

hours and with an increase in size from about 9 nm to 15 nm, thus increasing the distance travelled in the matrix by about 3 nm. The XRD and TEM of this sample is shown in the Figure 6.4. Hence practically, if one requires a larger size with higher doping concentration, it is necessary to use a core system with large bond dissociation energy.

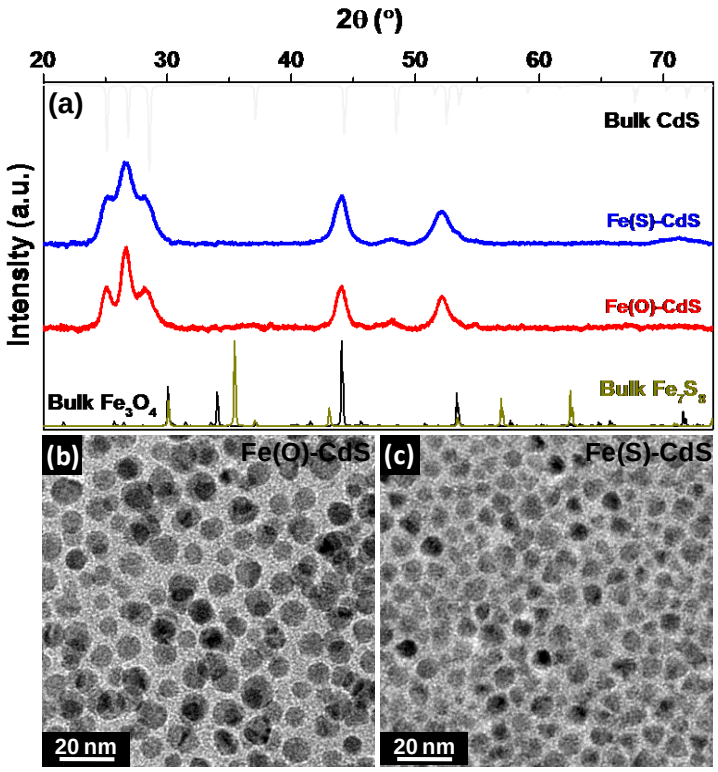

Figure 6.2: XRD spectra of Fe-(O)-CdS and Fe(S)-CdS QDs. TEM images (b) Fe(O)-CdS, (c) Fe(S)-CdS

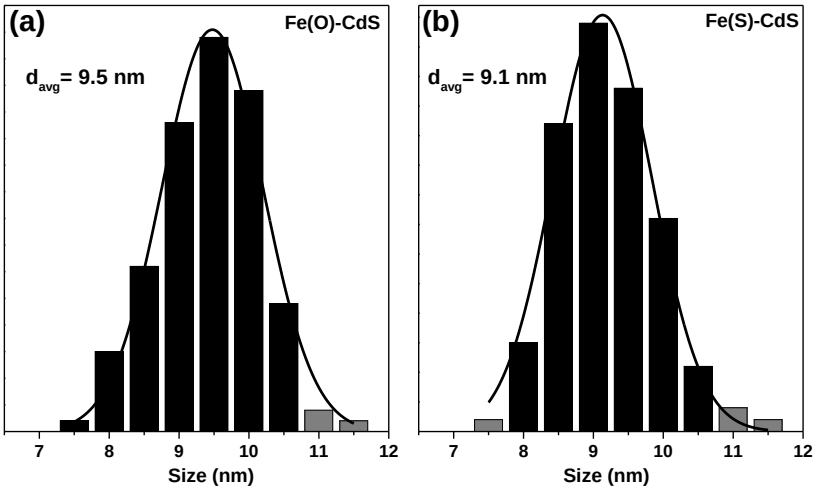

Figure 6.3 Size distribution histogram of (a) Fe(O)-CdS and (b) Fe(S)-CdS nanoparticles.

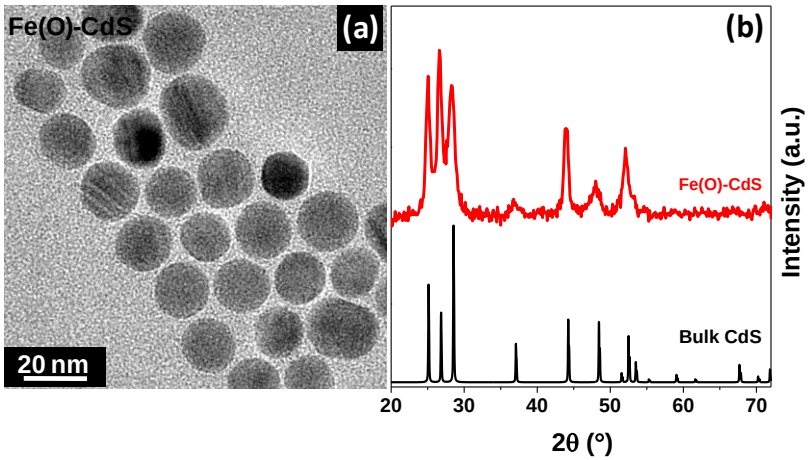

Figure 6.4: (a) TEM image of Fe(O)-CdS (Fe-2%) and its corresponding (b) XRD spectra.

6.4.2 Effect of diffusivity

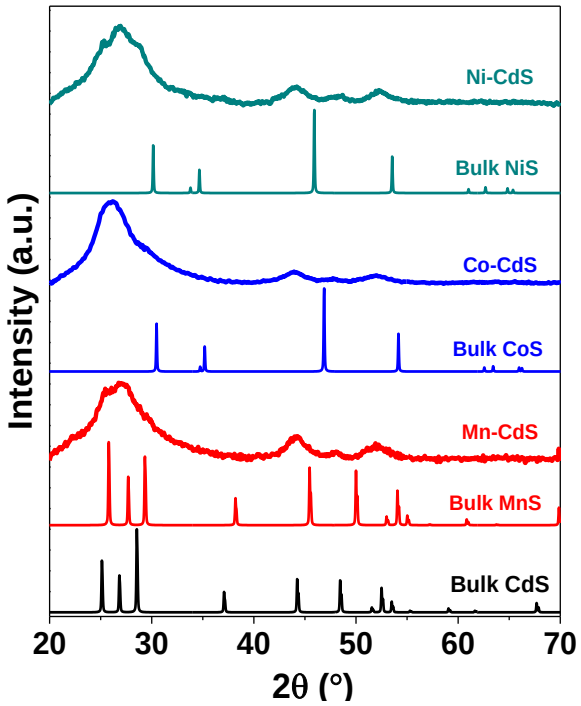

Figure 6.5: X-ray diffraction spectra of Ni^{2+} (cyan), Co^{2+} (blue) and Mn^{2+} (red) doped CdS QDs and comparison with different standard bulk spectra obtained from ICSD database.

However it is important to note that once penetration into the CdS lattice has been achieved, the diffusion of these metal atoms are completely governed by their diffusivities within the semiconductor solid. In order to study the diffusion dynamics or the diffusivities of metal ions inside the host semiconductor, we have chosen various

transition metal based sulfides (FeS, MnS, NiS, CoS) cores and allowed them to diffuse under similar condition. Keeping the final ion concentration very similar and below 5%, we study these QDs using TEM and XRD.

Figure 6.5 shows the XRD spectra of Ni^{2+} (2.5%), Co^{2+} (1.5%) and Mn^{2+} (4%) doped CdS QDs in comparison with their respective metal sulfide core. It is apparent from the figure that all the transition metal M^{2+} (Ni^{2+}, Co^{2+}, Mn^{2+}) doped CdS particles are formed with wurtzite crystal structure similar to the bulk CdS (also shown in figure) with no impurities from the metal sulfide core, suggesting a complete dissociation and diffusion of the core QDs and the absence of detectable clusters of transition metal sulfides. The broadening of the XRD peaks is characteristic of the small particle size of these NCs in accordance with the Scherrer formula.

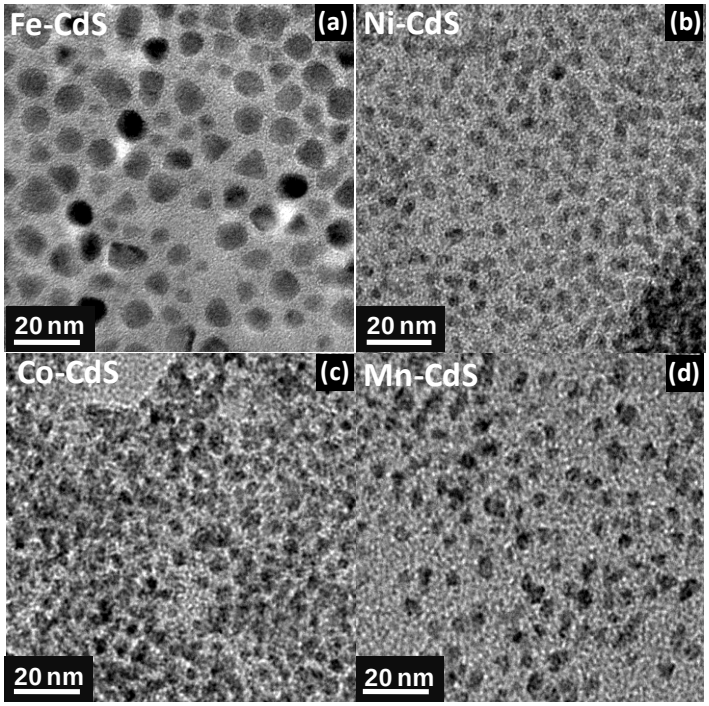

Figure 6.6: TEM image of (a) Fe^{2+}, (b) Ni^{2+}, (c) Co^{2+}, (d) Mn^{2+} doped CdS.

Figure 6.6 (a-d) shows the TEM images of typical samples of transition metals M^{2+} (Fe^{2+}, Ni^{2+}, Co^{2+}, Mn^{2+}) doped CdS respectively. Undoped CdS QDs were synthesized using similar reaction condition without any transition metal precursor for comparison with the doped CdS. Here, the average particles size for, Fe^{2+}, Ni^{2+}, $Co^{2+}$and Mn^{2+}doped QDs were found to be 10.2 nm, 5.5 nm, 5 nm and 5.8 nm respectively, calculated from histogram (shown in Figure 6.7) of the TEM images and their respective dopant

percentage 5%, 2.5%, 1.5% and 4% as obtained from ICP-OES. It is important to note that while Fe doping was synthesized at 240 °C, the other dopants were synthesized at 140 °C and heated for similar times. In spite of this higher temperature and similar bond dissociation energies (330 ± 20 kJ/mol),[32] the size and dopant concentration of Fe is much larger than the other metal atoms suggesting that the diffusion constant of Fe is substantially smaller than the other transition metal ions used here. While there is no literature on the diffusion constants of these metal ions in CdS, the diffusion of these dopants in GaAs[33] and Si[34] is instructive. It is found that Fe in GaAs has a diffusion constant (2×10^{-7} m^2/s) that is two orders of magnitude smaller than that of Mn ($6 \times 10^{-5} m^2/s$) and several orders of magnitude smaller than that of Co (1.5×10^{-2} m^2/s). Similarly, the diffusion constant of Fe in Si ($\sim 10^{-14}$ m^2/s) was several orders of magnitude smaller compared to Ni and Co in Si ($\sim 10^{-9}$ m^2/s). Hence the diffusion of the metal ions, specifically Fe <Mn < Ni < Co would be important in designing efficient doping in QDs. It is also interesting to note here that the Cu ion would be the fastest diffusing dopant and would be ejected out shortly after heating to this temperature.

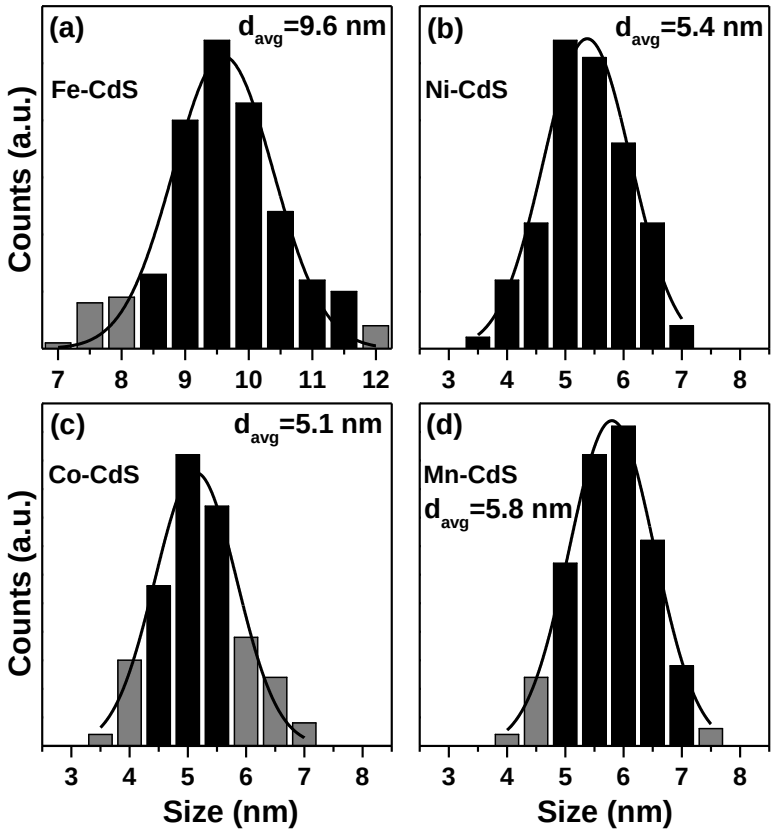

Figure 6.7: Size distribution histogram of (a) Fe-CdS (b) Ni-CdS (c) Co-CdS (d) Mn-CdS.

Hence, incorporation of Cu in CdS lattice would require a much lower temperature and has not been included in this study. Also, the higher diffusivity of transition metal ions results smaller size doped QDs. In order to achieve larger size doped QDs one can use oxide core for these ions, which have higher bond dissociation energy and can hence give rise to larger sized doped QDs. Thus the stability of the transition metal core as well as the diffusivity of the metal ions in the host matrix, combined with temperature, length of time exposed to this temperature can provide us a good handle to obtain custom-made sizes with any dopant concentration for any transition metal.

6.4.3 Optical Properties

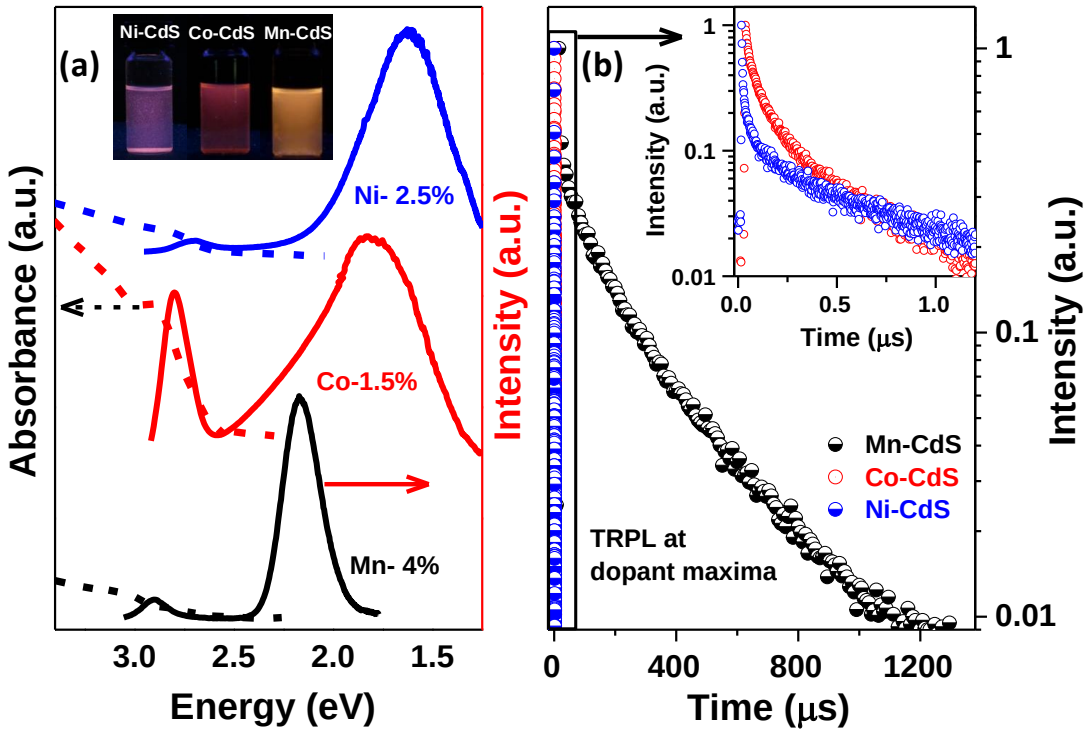

Figure 6.8: (a) Steady state PL (solid line) and Absorption (dashed line) of Ni^{2+} (blue), Co^{2+} (red) and Mn^{2+}(black) doped QDs. Inset of (a) shows photographs of the samples under UV light. (b) Lifetime decay plots for Ni^{2+}, Co^{2+} and Mn^{2+} doped CdS collected at the maxima of the broad dopant peaks. Inset of (b) shows the enlarged portion of lifetime decay of Ni^{2+} and Co^{2+} doped CdS.

While it is indeed easy to control either the percentage of doping or the size of the QDs using this synthesis methodology demonstrating the versatility of this technique, it is interesting to study the efficiency of this method by observing the effects on optical and magnetic property due to transition metals doping in comparison with earlier literature. The quality of the above

samples and their influence of uniform doping obtained by fine tuning the thermodynamic properties using the above technique on its optical and magnetic properties were then studied and compared with available literature. It is well known that while magnetic properties can be interesting even for larger sizes, optical properties are primarily interesting in the quantum confined regime, typically smaller than 6 nm in size. The optical characteristics of these QDs are summarized in various panels of Figure 6.8 (a-b) and Figure 6.9. While the absorption spectra show a single peak due to band gap transition of CdS QDs, the PL steady state spectra show a broad dopant emission peak at lower energy with quantum yields in the range of 15-20% (actual images being shown in the inset to Figure 6.8 (a) as obtained from integrating sphere measurements along with their corresponding band edge peak at higher energy consistent with the earlier studies.[28,35] The evolution of steady state photoluminescence spectra along with their absorption spectra in the dilute regime (<5%) is shown in Figure 6.9. The small but sharp peaks at higher energy in PL spectra for every sample are associated with the band edge emission of CdS. This peak is relatively intense in Co doped CdS QDs which may be due to the interplay of energetics of the host band gap with that of the dopant emission peak. The broad, tunable, intense and stable emissions, which exist in doped CdS samples but not in undoped CdS, suggest that this emission arises due to dopant states and are not related to surface states. Surface states are specifically known to be less intense and non-tunable. The red shift in band edge and dopant emission (Ni^{2+} and Co^{2+}) as a function of growth of the QDs with each subsequent addition of Cd and S precursors suggests that these bands are indeed dopant emission bands associated with localized, atomic-like dopant state to the host QDs. However in case of Mn^{2+} ion doped QDs, no emission shift in dopant peak was observed despite the increase in particle size. This has been extensively studied in literature[36,37] and can be attributed to the transition between two mid band gap atomic-like states ($^4T_1$-$^6A_1$) of Mn^{2+} ions. For further confirmation we measured time resolved photoluminescence (Tr-PL) spectra at the dopant peaks and is shown in Figure 6.8 (b). The dopant peaks are known to be much more long lived and show lifetimes of 278 ns, 184 ns and 223 μs (Table 6.1) for Ni^{2+}, Co^{2+} and Mn^{2+} respectively, which are in good agreement with earlier reported literature.[12,28] These high lifetime values further confirm that the broad emissions are due to the states originating from metal impurities doped successfully inside CdS QDs. Fe doped CdS, as expected, do not show any PL emission as well as effectively killing even the band edge emission.

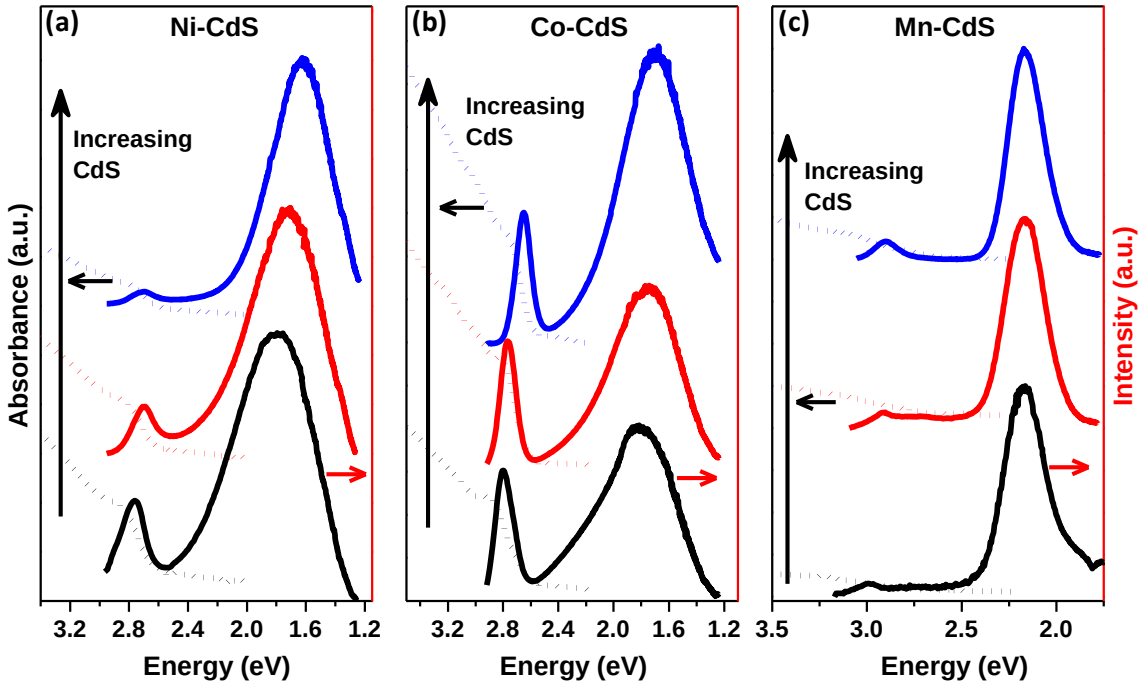

Figure 6.9: Evolution change in steady state PL (solid line) and absorption (dotted line) of (a) Ni^{2+}, (b) Co^{2+} and (c) Mn^{2+} doped nanocrystals with increasing addition of Cd and S cycle.

6.4.4 Magnetic Property

The second property of interest that is typically studied in transition metal doped QDs is their magnetic behavior. Theory predicts a ferromagnetic long range ordering due to *sp-d* exchange interaction between 3*d* orbital electrons with the host semiconductor QDs electronic level in II-VI bulk semiconductors doped with M^{2+} ion.[11,38,39] Our investigation of the magnetic properties of these M^{2+} ions (Fe^{2+}, Ni^{2+}, Co^{2+}, Mn^{2+}) doped CdS samples is shown in Figure 6.10. The field dependent magnetic behavior (M vs H) recorded for all these samples shows superparamagnetic nature at room temperature (Figure 6.10 (a)) while the particles go to blocked state at 2 K (Figure 6.10 (b)), which is due to the extremely small size and single domain formation. It is important to note that this magnetization is several orders of magnitude higher than the defect related magnetization[40] in undoped CdS QDs which is also shown in the figure as almost a straight line at zero field and hence cannot account for this behavior without the presence of dopant driven magnetism. Nonetheless, comparison of magnetism with the bulk theoretical value, in the case of QDs, is non-trivial. Magnetization has usually been expressed in emu/g instead of the more standard μ_B/ion due to the absence of knowledge on the quantitative amount of ligands present on the surface of the QDs. In this work, we have used TGA to estimate the number of moles of ligand present in the sample and determine the

approximate molecular weight of the QDs. Using these techniques, the approximate saturation magnetization obtained for different ligands at 300K and 2K is tabulated in Table 1. We note that while the magnetization is comparable to the theoretically expected magnetization of 5 μ_B/ion, 4 μ_B/ion, 3 μ_B/ion and 2 μ_B/ion for Mn^{2+}, Fe^{2+}, Co^{2+} and Ni^{2+} respectively, it is significantly lower than the expected value. This could be due to the small size of the QDs. As the particle size decreases, domain size decreases with an increase of surface spins, which are canted in different directions and hence reduce the overall magnetization significantly.[41] It is also remarkable to note that the Mn^{2+} ion, even though, theoretically the largest moment, does not magnetize easily suggesting that it is indeed more paramagnetic than the Fe^{2+} or Co^{2+}, which is in agreement with the earlier literature.[12]

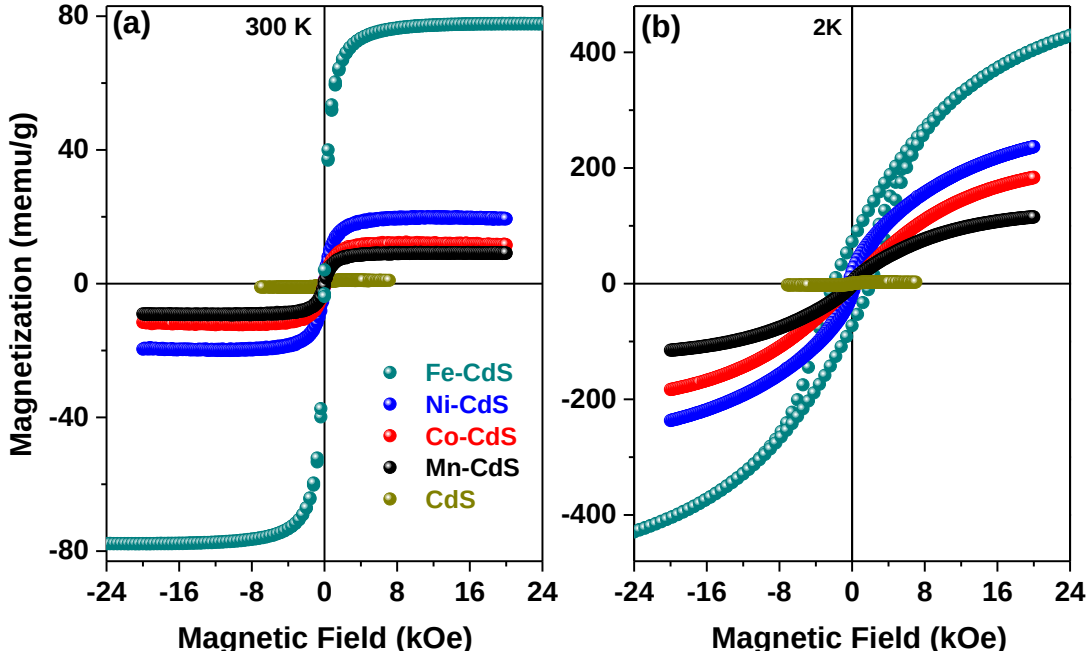

Figure 6.10: A comparison of magnetization vs field plot for different transition metal doped CdS QDs at (a) room temperature and (b) 2K.

In our study, we have then compared the saturation magnetization with the earlier literature (Table 6.2) in order to obtain an understanding of the quality of the doping. It has been observed in earlier reports[42,43] that non-uniformity in paramagnetic dopants distribution in QDs leads to reduction of excitonic Zeeman splitting and consequently results in low magnetic ordering. In this work as the particle sizes are very small, (5-6 nm) it is not possible to observe direct evidence of dopant distribution from EDAX-STEM or TEM. However, a strong magnetic response from all these nanocrystals

suggests the formation of uniform doping distribution of magnetic ions inside the QDs. A comparison with previous studies in literature shows that our samples show significantly higher M_s value in case of all the magnetic ions. Thus we demonstrate that the thermodynamics of a material can be effectively used in the synthesis of DMS QDs with varying transition metal ions that show superior optical and magnetic property compared to the other similar materials due to the absence of clustering of magnetic ions and an exchange interaction.

Table 6.1: Percentage of doping from ICP-OES, TrPL lifetime and saturation magnetization value in Bohr Magnetron per magnetic ion for various doped QDs.

M^{2+} doped CdS	M^{2+} % (ICP)	PL Life time (μS)	QY (%)	M_s (memu/g)	
				300 K	2 K
Fe-CdS	2	-	-	77 (0.15 μB/ion)	430 (0.88 μB/ion)
Ni-CdS	2.5	0.278	18	20 (0.05μB/ion)	240 (0.6 μB/ion)
Co-CdS	1.5	0.184	15	12 (0.05 μB/ion)	182 (0.76 μB/ion)
Mn-CdS	4	223	20	9 (0.028 μB/ion)	116 (0.18 μB/ion)

Table 6.2: A comparison of magnetic response in our current work with the previous literature reports on of various DMS systems.

Group name	Sample	Transition Metal (%)	M_s (memu/g)	T (K)
Jana et al.[28]	Ni^{2+} doped CdZnS nanocrystals	< 1	3	300
Current work	Ni^{2+} doped CdS	2.5	18	300
			240	2
Bogle et al.[29]	Co^{2+} doped CdS nanocrystals	3	4	300
Giribabu et al.[30]	Co^{2+} doped CdS nanocrystals	4	8.7	300
Current work	Co^{2+} doped CdS nanocrystals	1.5	12	300
			182	2
Ghosh et al.[12]	Mn^{2+}- doped CdS nanocrystals	0.14	~4.5	300
			18	5
Current work	Mn^{2+} doped CdS	4	9	300
			116	2

6.5 Conclusion

In conclusion, we report here a universal technique to obtain high quality luminescent, ferromagnetic, semiconducting multifunctional QDs which give strong tunable fluorescent emission in visible and NIR region and show room temperature ferromagnetic property. We achieve this by diffusing different transition metal sulphide and oxide cores, inside semiconducting shell matrix within the constraints of their thermodynamic properties. Based on our experimental results, we showed that two factors majorly influence diffusion doping of transition metal ions during thermal annealing which are bond dissociation energy of the core and the diffusivity of the transition metal ions inside the semiconductor matrix. Control over these parameters highlights several unique features with the extraordinary fine composition tunability and can provide uniform doping with desirable size and dopant concentration in QDs. All these QDs displays broad and intense optical emission due to doping and comparatively superior magnetic response compared to earlier studies which elucidate the direct correlation between internal doping with their magnetic property. This work demonstrates a universal technique to engineer multifunctional doped QDs with precise control over size and doping percentage which have far reaching consequence in potential application in spintronics and optoelectronics devices.

Section B

Effect of Transition Metal Codoping in QDs

6.6 Summary

Uniformity in dopant distribution in DMSQDs have shown to improve the magnetic property. In this present section, we have shown in addition to the uniform doping, simultaneous doping or "codoping" can provide an additional handle to modulate the magnetization further. Herein, we have synthesized (Mn, Ni) codoped CdS by "diffusion doping" technique and study their structural, optical and magnetic properties. The optical property confirms the presence of both the dopants, which take part in electronic transition during exciton recombination. Interestingly, in presence of similar percentage of magnetic ion (Mn, Ni) codoped CdS QDs show enhanced magnetic response compared to their individual doped counterparts.

6.7 Introduction

Partial substitution of cations from conventional semiconductor materials by transition metal ions leads to the formation of DMS[44-47] materials, which has great potential in application in spin based electronics devices.[13,48,49] Efficient spintronics[13,14,49] application demands room temperature ferromagnetism having an intrinsic origin (not from cluster phase) with a large magnetic response. However, thermal instability of transition metal ions inside the semiconductor matrix has made it challenging to synthesize cluster free, uniformly doped, semiconductor materials by traditional synthesis techniques. In previous section of this chapter we have demonstrated a universal "diffusion doping" technique, which offers uniformity in dopant distribution in DMS QDs. Using this technique, we have explored the codoping of Mn and Ni in this section.

Study of magnetism in DMSQDs in literature shows highly conflicting properties. For example, the DMS property of Codoped ZnO,[50,51] Ni-doped ZnO, and Mn-doped ZnO[52] were reported to be paramagnetic, while other reports of ferromagnetism in some samples of Codoped ZnO,[53] Ni-doped ZnO,[54-56] Mn doped ZnO[56-58] are found in both bulk and thin films. There are several reports, which show that ferromagnetism observed in nanoparticles depends on synthetic methods and condition maintained during synthesis.[56,58] Additionally, it has been shown that the transition metal based codoped semiconductors have shown high quality optical and ferromagnetic response and stability in ferromagnetic behavior.[59] For example, individually Cu and Co doped ZnO show diamagnetic and antiferromagnetic interactions while (Cu, Co)-codoped ZnO show ferromagnetic interaction.[60] Sluiter *et al.* demonstrated both theoretically

and experimentally ferromagnetic behavior from (Co, Li) codoped ZnO.[61] Similarly, (Co, Al) codoped ZnO,[62] (Mn, Ni) codoped SnO_2[63] also shown superior magnetic property due to codoping. In most of these cases it was found that increase in free carrier density due to codoping leads to ferromagnetic interaction.[61,62]

Therefore along with the size, concentration of dopant and the uniformity in dopant distribution, transition metal dual doping in semiconductor is one more parameter which can tune the magnetic property of DMS QDs significantly. However, not much research has been performed on codoped QDs based on transition metals due to challenges involved in synthesizing them due to large driving force for phase segregation. Therefore, a detailed study on uniformly codoped QDs and the effect of this simultaneous doping on their electronic and magnetic properties is required. Following the similar technique as discussed in the earlier section, we have synthesized (Mn, Ni) codoped CdS by diffusion of MnNiS core inside CdS and compared their magnetic properties with individual doped QDs.

We used XRD for crystal structure information, TEM to find out the size and morphology and ICP-OES for elemental analysis of the QDs. Optical characterization was studied using UV-Visible and PL spectroscopy. TGA was used to obtain the weight percentage of ligands and magnetic measurements were obtained using SQUID magnetometer (Quantum Design). The magnetic moment per ion was then calculated and compared between doped and codoped QDs. A significant enhancement in magnetization/ion was observed in case of codoped QDs compared to singly doped QDs.

6.8 Experimental Details

6.8.1 Synthesis

We followed very similar synthesis procedure as described in previous section to synthesize these QDs. Cadmium oleate $Cd(Ol)_2$, 0.2 M sulfar/ODE, manganese stearate($Mn(St)_2$) and Nickel oleate ($Ni(Ol)_2$) were used as different precursors and their synthesis have been discussed in previous section.

Synthesis of Ni/Mn doped CdS. Ni and Mn doped CdS were prepared following the similar procedure described in previous section. We have collected different samples at different stages of CdS overcoating and chosen 5% and 6% doped samples for the study presented in this section.

Synthesis of (Mn, Ni) codoped CdS: (Mn,Ni) codoped nanocrystals were synthesized using the similar technique described in section 6.3.1. The only difference is that, in this case, we have used MnNiS as the core instead of NiS or MnS. In brief, Manganese stearate, Nickel oleate (depending upon the Mn:Ni ratio) were taken together in a three necked RB flask with 12 mL ODE. This reaction mixture was kept for degassing at 80^{o}C for 2 h 0.5 mL of 0.2 M S/ODE solution was mixed with 0.2 g of ODA and further diluted with 1 mL of ODE in a vial. The temperature of the reaction mixture in RB flask was raised to 240 °C under constant Ar flow. As soon as the temperature reaches 240 °C the precursor solution of S/ODA/ODE was injected quickly into the system. The temperature is then decreased to 140 $^{\circ}$C, for overcoating of the CdS layers. The cadmium oleate (150 μL) was added into the reaction mixture at a regular interval of 15 minutes. Aliquots have been taken before the addition of Cd precursor each time. Samples were washed using hexane ethanol mixture by centrifugation and then re-dispersed in hexane for characterization.

6.9 Results and discussion

In order to investigate the extent of dual doping, we have chosen Mn(x%) Ni(x%) codoped CdS QDs (where x = 2.5% and 3%) and compared with Mn (5% and 6%) doped CdS and Ni(5% and 6%) doped CdS QDs. These percentages of dopants were determined from ICP-OES. Keeping the sizes of all the QDs similar (~7 nm), we characterize these QDs using XRD and TEM.

6.9.1 Structural Characterization

Figure 6.11 shows the XRD spectra of Ni (5%), Mn (5%) doped and (Mn (2.5%)+Ni(2.5%)) codoped CdS QDs in comparison with bulk CdS spectrum. It is apparent from the figure that all the doped and codoped CdS QDs are formed with wurtzite crystal structure similar to the bulk CdS (also shown in figure) without presence of any impurity peak from the metal sulfide core, suggesting a complete dissociation and diffusion of the core QDs and the absence of detectable clusters of transition metal sulphides. The broadening of the XRD peaks is characteristic of the small particle size of these QDs in accordance with the Scherrer formula.

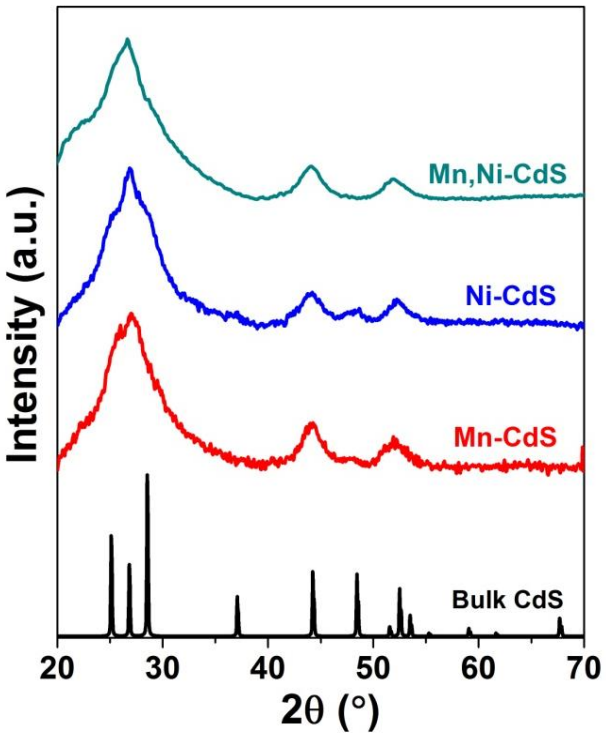

Figure 6.11: X-ray diffraction spectra of Mn and Ni doped and (Mn,Ni) codoped CdS QDs and comparison with different standard bulk spectra obtained from ICSD database.

In order to confirm the size and morphology of the QDs we performed TEM. Figure 6.12 shows the TEM images of Mn (5 %) doped CdS, Ni (5%) doped CdS and Mn (2.5%)+Ni(2.5%) codoped CdS nanocrystals. Here, the average particles size for Mn doped CdS, Ni doped CdS and Mn,Ni codoped CdS QDs were found to be 6.7 nm, 6.9 nm, and 7 nm respectively.

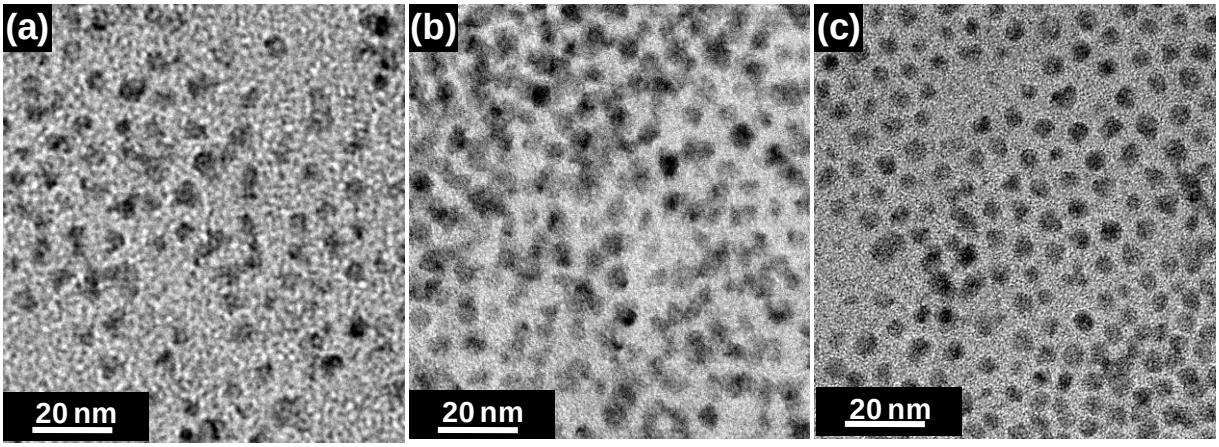

Figure 6.12: TEM image of (a) Mn doped (b) Ni doped (c) (Mn, Ni) codoped CdS

6.9.2 Optical Properties

XRD and TEM showed the crystal structure and morphology of the synthesized QDs. ICP-OES shows the presence of dopants exist in QDs. However none of these techniques conclusively suggests whether both the transition metals are indeed doped into the QDs or not. Study of electronic structure and optical property can shed light on this aspect. The presence of more than one impurity states in the semiconductor QDs generates the possibilities of multiple recombination pathways and the actual pathway can either be selective, combined or the totally new pathway giving rise to a different emission. Figure 6.13 (a) shows the absorption and emission spectra of the Mn doped and Ni doped CdS QDs. In spite of similar particle size (~6.8 nm) and absorption spectra, the photoluminescence characteristics of singly doped and codoped spectra are remarkably different. Steady state emission spectra of Mn-doped CdS show an intense peak at 2.1 eV which is the characteristics peak of manganese doping. Similarly for Ni-doped CdS, a peak observed at ~1.7 eV has been attributed to the CB to Ni transition. However, in case of (Mn, Ni) codoped CdS, PL emission spectra look very similar to Ni-doped CdS. So the presence of Mn doping is not evident here. In order to confirm that, we have taken gated PL emission spectra using a delay time of 100 µs. It is known that Mn emission arises due to the $^4T_1$to $^6A_1$, atomic like spin forbidden transition that occurs in millisecond time scale (Figure 6.14 (b)). However the band edge and the Ni transition in µs time scale. So, the gated PL, PL obtained after 10 µs is sensitive to only the Mn-doped characteristics peak shown in Figure 6.13(b).

Therefore dual emission observed here due to existence of both Mn and Ni dopant contribution; however the Mn emission is suppressed due to intense Ni emission peak, which might be due to partial transfer of energy from Mn state to Ni state. This suggests that the excitons are decaying through both channels available in the codoped system. In order to get more insight into this, we study the time resolved photoluminescence decay dynamics for all the different 5% doped samples at their respective dopant emission maxima. Figure 6.14 depicts the TrPL decay curve of (Mn, Ni) codoped CdS collected at 1.7 eV is entirely different from both Mn or Ni doped CdS as shown in figure 6.14 (a), (b). The average lifetime calculated for (Mn Ni) codoped CdS is 8 µS which is much lesser than that of Mn doped CdS (~500 µs) and much higher compared to Ni-CdS (300 ns). These results clearly suggest the presence of both the dopants competing in the process of electronic transition in codoped QDs.

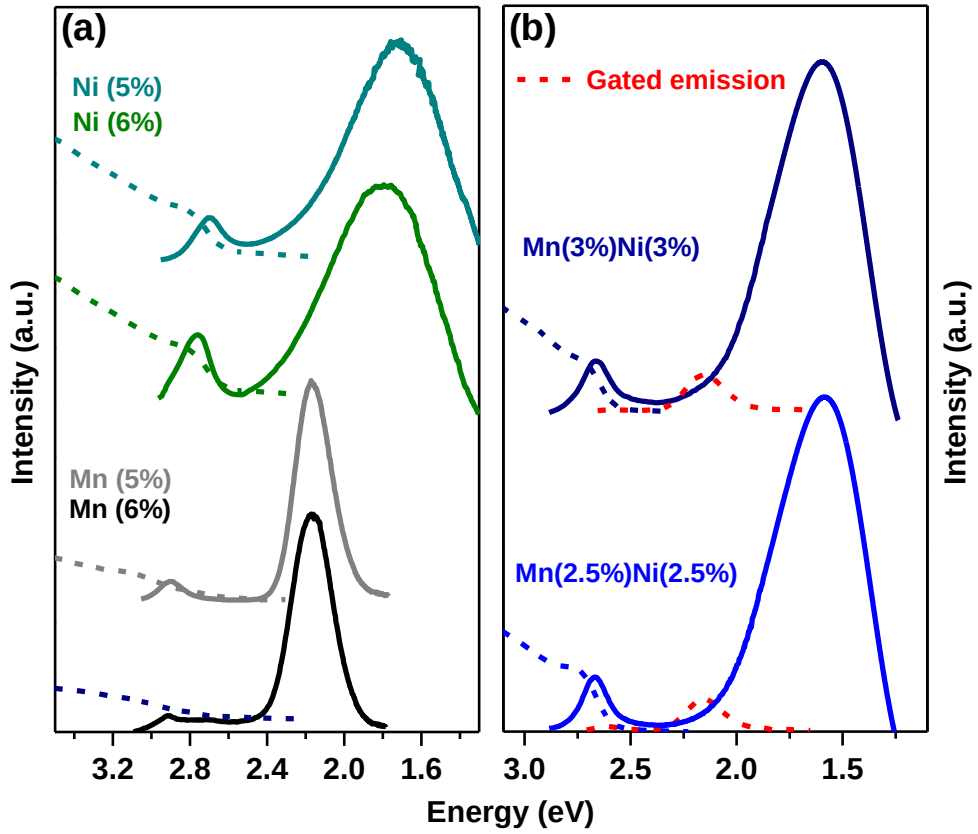

Figure 6.13: Steady state PL (solid line) and Absorption (dashed line) of (a) Mn and Ni doped CdS and (b) (Mn, Ni) codoped CdS with different magnetic ion concentration. Red dotted line shows the gated PL spectra.

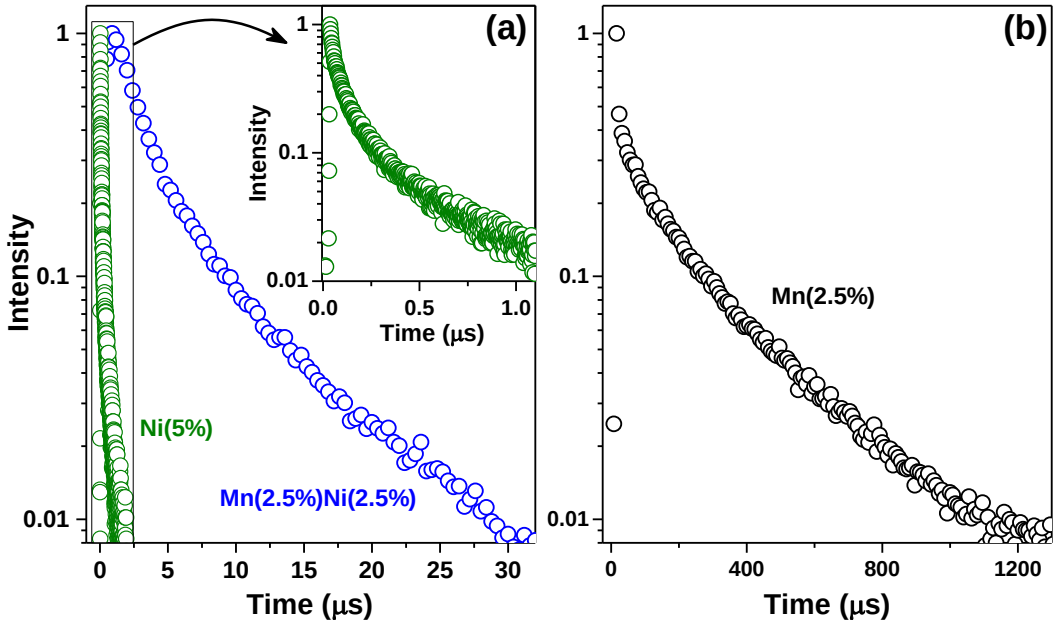

Figure 6.14: TrPL- decay plots for (a) Ni doped (green), (MnNi) codoped (blue) and (b) Mn doped (black) CdS QDs collected at the maxima of their broad dopant peak.

6.9.4 Magnetic Properties

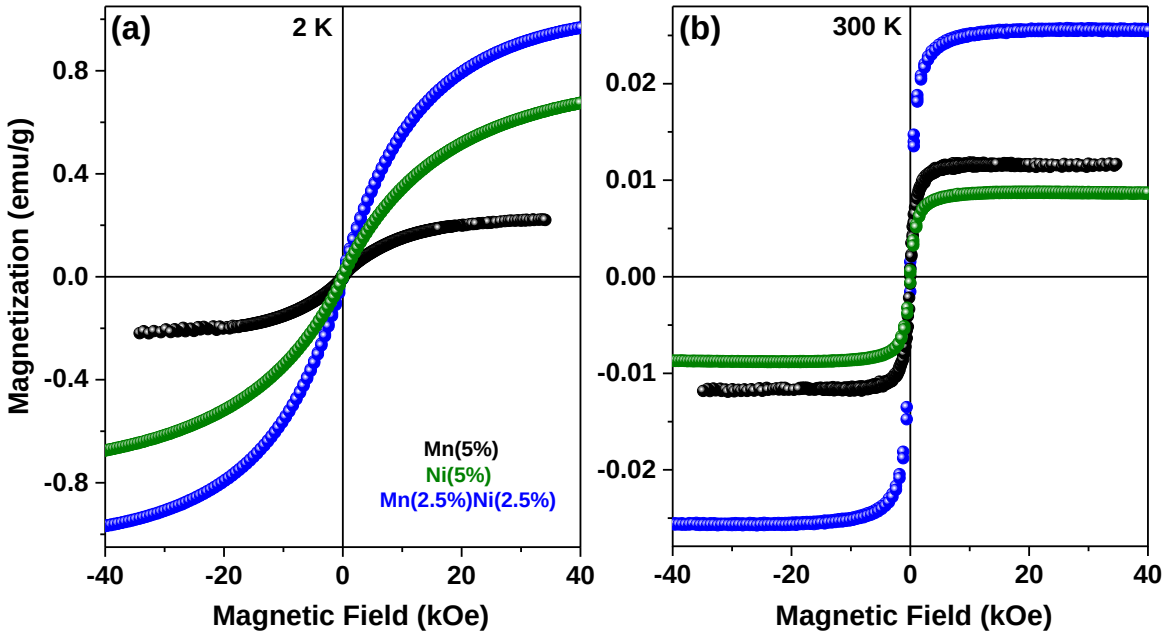

Figure 6.15: A comparison of magnetization vs field plot for different transition metal doped and codoped CdS QDs at (a) 2K and (b) room temperature.

We investigate the magnetic properties of all different doped and codoped QDs. It was predicted that magnetism in DMS systems arises due to long range sp-d exchange interaction between the 3d orbital electrons with the host semiconductor's electronic level through free charge carrier. Our results of magnetic property from these QDs are demonstrated in the Figure 6.15 and Table 6.3. A visual comparison of M vs H hysteresis curve shows an increment in saturation magnetization (M_s) value in case of codoped QDs. To get more insights into this we convert the magnetization value in μB/ion after substituting the ligand weight (calculated from TGA analysis) and the corresponding results are tabulated in Table 6.3. In chapter 5D, we have shown that in DMS QDs magnetization/ion is independent of the concentration of particular dopant percentage upto a certain limit (defined as dilute doping regime). Here also we can observe that the magnetization per ion is very similar for each individual case (doped or codoped) and does not alter as the concentration change from 5% to 6%, which agrees with the previous results. This suggests that the magnetism is arising due to uniform distribution of both the magnetic ions. However, there is a significant enhancement in magnetization/ion in codoped QDs compared to their individual counterparts. For example, magnetization in case of 5% Mn and Ni doped CdS are 0.25 and 0.8 μB/ion respectively while we observe 1.22 μB/ion

in the case of codoped CdS. This suggests that (Mn, Ni) codoping has enhanced the magnetic response which may be due to the increase of free electron in host that takes part in magnetic exchange interaction as observed in earlier codoped system reported in thin film or bulk.

Table 6.3: A comparison of saturation magnetization (M_s) for all different doped and codoped samples measured at 2K and room temperature.

Sample	2K (μ_B/ion)	300K (μ_B/ion)
Mn-CdS (5%)	0.25	0.014
Mn-CdS (6%)	0.28	0.015
Ni(5%)-CdS	0.8	0.018
Ni(6%)-CdS	0.78	0.016
Mn (2.5%)Ni(2.5%)CdS	1.22	0.035
Mn (3%) Ni(3%)CdS	1.24	0.036

6.10 Conclusion

In conclusion, we report the synthesis of free standing (Mn, Ni) codoped CdS QDs using diffusion doping technique. We prepared two different concentration of (Mn, Ni) codoping and compared their electronic and magnetic properties with individual Mn or Ni doped QDs having similar size and ion concentration. Although, all the QDs showing ferromagnetic interaction. Surprisingly the dual doped CdS QDs show a significant enhancement in magnetization/ion. Though further study is needed to understand the origin of this enhanced magnetic interaction, this work opens up a way to improve the magnetization in DMS QDs using controlled codoping.

Bibliography

(1) Grandhi, G. K.; Tomar, R.; Viswanatha, R. *ACS Nano* **2012**, *6*, 9751.

(2) Wright, J. T.; Forsythe, K.; Hutchins, J.; Meulenberg, R. W. *Nanoscale* **2016**, *8*, 9417.

(3) Proshchenko, V.; Dahnovsky, Y. *J. Phys. Chem. C* **2014**, *118*, 28314.

(4) Chen, Y.; Li, S.; Huang, L.; Pan, D. *Nanoscale* **2014**, *6*, 9640.

(5) Hanif, K. M.; Meulenberg, R. W.; Strouse, G. F. *J. Am. Chem. Soc.* **2002**, *124*, 11495.

(6) Bonanni, A.; Dietl, T. *Chem. Soc. Rev.* **2010**, *39*, 528.

(7) Yao, T.; Yan, W.; Sun, Z.; Pan, Z.; He, B.; Jiang, Y.; Wei, H.; Nomura, M.; Xie, Y.; Xie, Y.; Hu, T.; Wei, S. *J. Phys. Chem. C* **2009**, *113*, 3581.

(8) Djerdj, I.; Jaglicic, Z.; Arcon, D.; Niederberger, M. *Nanoscale* **2010**, *2*, 1096.

(9) Sung, Y.-M.; Gayam, S. R.; Hsieh, P.-Y.; Hsu, H.-Y.; Diau, E. W.-G.; Wu, S.-P. *ACS Appl. Mater. Interfaces* **2015**, *7*, 25961.

(10) Yuan, X.; Ma, R.; Zhang, W.; Hua, J.; Meng, X.; Zhong, X.; Zhang, J.; Zhao, J.; Li, H. *ACS Appl. Mater. Interfaces* **2015**, *7*, 8659.

(11) Coey, J. M. D.; Venkatesan, M.; Fitzgerald, C. B. *Nat. Mater.* **2005**, *4*, 173.

(12) Ghosh, A.; Paul, S.; Raj, S. *J. Appl. Phys.* **2013**, *114*, 094304.

(13) Sarma, S. D. *Nat. Mater.* **2003**, *2*, 292.

(14) Felser, C.; Fecher, G. H.; Balke, B. *Angew. Chem. Int. Ed.* **2007**, *46*, 668.

(15) Tian, Y.; Bakaul, S. R.; Wu, T. *Nanoscale* **2012**, *4*, 1529.

(16) Jana, S.; Manna, G.; Srivastava, B. B.; Pradhan, N. *Small* **2013**, *9*, 3753.

(17) Mahamuni, S.; Lad, A. D.; Patole, S. *J. Phys. Chem. C* **2008**, *112*, 2271.

(18) Pradhan, N.; Goorskey, D.; Thessing, J.; Peng, X. *J. Am. Chem. Soc.* **2005**, *127*, 17586.(19) Pradhan, N.; Peng, X. *J. Am. Chem. Soc.* **2007**, *129*, 3339.

(20) Chen, D.; Viswanatha, R.; Ong, G. L.; Xie, R.; Balasubramaninan, M.; Peng, X. *J. Am. Chem. Soc.* **2009**, *131*, 9333.

(21) Suyver, J. F.; Wuister, S. F.; Kelly, J. J.; Meijerink, A. *Phys. Chem. Chem. Phys.* **2000**, *2*, 5445.

(22) Norris, D. J.; Yao, N.; Charnock, F. T.; Kennedy, T. A. *Nano Lett.* **2001**, *1*, 3.

(23) Levy, L.; Hochepied, J. F.; Pileni, M. P. *J. Phys. Chem.* **1996**, *100*, 18322.

(24) Mikulec, F. V.; Kuno, M.; Bennati, M.; Hall, D. A.; Griffin, R. G.; Bawendi, M. G. *J. Am. Chem. Soc.* **2000**, *122*, 2532.

(25) Yang, J.; Yao, M.-H.; Wen, L.; Song, J.-T.; Zhang, M.-Z.; Zhao, Y.-D.; Liu, B. *Nanoscale* **2014**, *6*, 11282.

(26) Karan, N. S.; Sarkar, S.; Sarma, D. D.; Kundu, P.; Ravishankar, N.; Pradhan, N. *J. Am. Chem. Soc.* **2011**, *133*, 1666.

(27) Bicelli, L. P.; Bozzini, B.; Mele, C.; D'Urzo, L. *Int. J. Electrochem. Sci* **2008**, *3*, 356.

(28) Jana, S.; Srivastava, B. B.; Jana, S.; Bose, R.; Pradhan, N. *J. Phys. Chem. Lett.* **2012**, *3*, 2535.

(29) Bogle, K. A.; Ghosh, S.; Dhole, S. D.; Bhoraskar, V. N.; Fu, L.-f.; Chi, M.-f.; Browning, N. D.; Kundaliya, D.; Das, G. P.; Ogale, S. B. *Chem. Mater.* **2008**, *20*, 440.

(30) Giribabu, G.; Murali, G.; Reddy, A. D.; Liu, C.; Vijayalakshmi, R. P. *J. Alloys Comp.* **2013**, *581*, 363.

(31) Li, J. J.; Wang, Y. A.; Guo, W.; Keay, J. C.; Mishima, T. D.; Johnson, M. B.; Peng, X. *J. Am. Chem. Soc.* **2003**, *125*, 12567.

(32) Luo, Y.-R. *Comprehensive Handbook of Chemical Bond Energies*; CRC press: Boca Raton, 2007.

(33) Burger, D.; Seeger, M.; Zhou, S.; Skorupa, W.; Schmidt, H. *J. Appl. Phys.* **2012**, *111*, 054914.

(34) Weber, E. R. *Appl. Phys. A* **1983**, *30*, 1.

(35) Jo, D.-Y.; Kim, D.; Kim, J.-H.; Chae, H.; Seo, H. J.; Do, Y. R.; Yang, H. *ACS Appl. Mater. Interfaces* **2016**, *8*, 12291.

(36) Nag, A.; Sapra, S.; Nagamani, C.; Sharma, A.; Pradhan, N.; Bhat, S. V.; Sarma, D. D. *Chem. Mater.* **2007**, *19*, 3252.

(37) Chen, H.-Y.; Chen, T.-Y.; Son, D. H. *J. Phys. Chem. C* **2010**, *114*, 4418.

(38) Beaulac, R.; Schneider, L.; Archer, P. I.; Bacher, G.; Gamelin, D. R. *Science* **2009**, *325*, 973.

(39) Viswanatha, R.; Pietryga, J. M.; Klimov, V. I.; Crooker, S. A. *Phys. Rev. Lett.* **2011**, *107*, 067402.

(40) Madhu, C.; Sundaresan, A.; Rao, C. N. R. *Phys. Rev. B* **2008**, *77*, 201306.

(41) Noh, S.-h.; Na, W.; Jang, J.-t.; Lee, J.-H.; Lee, E. J.; Moon, S. H.; Lim, Y.; Shin, J.-S.; Cheon, J. *Nano Lett.* **2012**, *12*, 3716.

(42) Norberg, N. S.; Parks, G. L.; Salley, G. M.; Gamelin, D. R. *J. Am. Chem. Soc.* **2006**, *128*, 13195.

(43) Hoffman, D. M.; Meyer, B. K.; Ekimov, A. I.; Merkulov, I. A.; Efros, A. L.; Rosen, M.; Couino, G.; Gacoin, T.; Boilot, J. P. *Solid State Commun.* **2000**, *114*, 547.

(44) Dietl, T.; Ohno, H.; Matsukura, F.; Cibert, J.; Ferrand, D. *Science* **2000**, *287*, 1019.

(45) Dietl, T. *Nat. Mater.* **2003**, *2*, 646.

(46) Dietl, T. *Nat. Mater.* **2010**, *9*, 965.

(47) Saha, A.; Shetty, A.; Pavan, A. R.; Chattopadhyay, S.; Shibata, T.; Viswanatha, R. *J. Phys. Chem. Lett.* **2016**, *7*, 2420.

(48) Huang, X.; Makmal, A.; Chelikowsky, J. R.; Kronik, L. *Phys. Rev. Lett.* **2005**, *94*, 236801.

(49) Wolf, S. A.; Awschalom, D. D.; Buhrman, R. A.; Daughton, J. M.; von Molnar, S.; Roukes, M. L.; Chtchelkanova, A. Y.; Treger, D. M. *Science* **2001**, *294*, 1488.

(50) Lawes, G.; Risbud, A. S.; Ramirez, A. P.; Seshadri, R. *Phys. Rev. B* **2005**, *71*, 045201.

(51) Risbud, A. S.; Spaldin, N. A.; Chen, Z. Q.; Stemmer, S.; Seshadri, R. *Phys. Rev. B* **2003**, *68*, 205202.

(52) Fukumura, T.; Jin, Z.; Kawasaki, M.; Shono, T.; Hasegawa, T.; Koshihara, S.; Koinuma, H. *Appl. Phys. Lett.* **2001**, *78*, 958.

(53) Prellier, W.; Fouchet, A.; Mercey, B.; Simon, C.; Raveau, B. *Appl. Phys. Lett.* **2003**, *82*, 3490.

(54) Srinet, G.; Kumar, R.; Sajal, V. *J. Appl. Phys.* **2013**, *114*, 033912.

(55) Saravanan, R.; Santhi, K.; Sivakumar, N.; Narayanan, V.; Stephen, A. *Mater. Charact.* **2012**, *67*, 10.

(56) Ueda, K.; Tabata, H.; Kawai, T. *Appl. Phys. Lett.* **2001**, *79*, 988.

(57) Omri, K.; El Ghoul, J.; Lemine, O. M.; Bououdina, M.; Zhang, B.; El Mir, L. *Superlattice. Microst.* **2013**, *60*, 139.

(58) Sharma, P.; Gupta, A.; Rao, K. V.; Owens, F. J.; Sharma, R.; Ahuja, R.; Guillen, J. M. O.; Johansson, B.; Gehring, G. A. *Nat. Mater.* **2003**, *2*, 673.

(59) Lisenkov, S.; Andriotis, A. N.; Sheetz, R. M.; Menon, M. *Phys. Rev. B* **2011**, *83*, 235203.

(60) Viswanatha, R.; Naveh, D.; Chelikowsky, J. R.; Kronik, L.; Sarma, D. D. *J. Phys. Chem. Lett.* **2012**, *3*, 2009.

(61) Sluiter, M. H. F.; Kawazoe, Y.; Sharma, P.; Inoue, A.; Raju, A. R.; Rout, C.; Waghmare, U. V. *Phys. Rev. Lett.* **2005**, *94*, 187204.

(62) Liu, X. C.; Shi, E. W.; Chen, Z. Z.; Zhang, H. W.; Xiao, B.; Song, L. X. *Appl. Phys. Lett.* **2006**, *88*, 252503.

(63) Bhuvana, S.; Ramalingam, H. B.; Thilakavathi, G.; Vadivel, K. *Mater. Techno.* **2016**, 1.

Chapter 7

Ferrimagnetic and Antiferromagnetic Nano-heterostructure

7.1 Summary

Investigation of magnetic interactions at the heterostructure interface, specifically in core-shell magnetic QDs, has become one of the primary fields of interest in nano-magnetism research and their applications. Formation of ferrimagnetic (FiM)/Antiferromagnetic (AFM) heterostructure results in exchange bias coupling at the interface and thereby improve anisotropy that can overcome the superparamagnetic limit in small size QDs. Herein, we have demonstrated a two step synthesis of $CoO/CoFe_2O_4$ core-shell QDs using seed growth method by decomposition of metal complex at high temperature and studied the effect of magnetic interaction due to the interface. The structure of core-shell formation is characterized by X-ray diffraction and high resolution transmission electron microscopy (HRTEM). Formation of highly crystalline sharp interface results in a strong exchange coupling between AFM core/FiM shell interface leading to a large exchange bias value (H_E= 5.6 kOe) which is comparable with the largest H_E value reported for small size nanoparticles.

7.2 Introduction

The recent development of QD based technology demand for multifunctional and superior properties for numerous applications in modern nano-electronics,[1,2] sensors[3-5] and bio-applications[6-8] has resulted in extensive research into the fundamental properties of QDs. The progress in colloidal synthesis of alloy and core-shell heterostructure QDs gives the opportunities to achieve specific properties for applications. Core-shell heterostructure has been extensively studied in semiconductor QDs including extending them to magnetic QDs. It was observed that the internal microstructure of heterostructure QDs has strong dependence on their property due to the many intriguing phenomena arising from the coupling at the interface.[9-11] Transition metal based oxides with various core-shell morphologies show tunability in magnetic response according to their internal structure.[12,13] Reduction of particle size in magnetic QDs leads to thermal destabilization of magnetization due to superparamagnetic limit,[14-16] which is a drawback in applying these particles in magnetic recording devices. The idea of overcoating another magnetic layer having different anisotropy has shown higher thermal stability in small particle, due to magnetic proximity at the interface leading to exchange bias. For magnetic heterostructures, exchange bias effect[9-11,17-20] at the interface is an interesting phenomenon that has been extensively studied in the last few decades. Exchange

bias can be defined as an unidirectional anisotropy that arises due to the exchange coupling at the soft ferro (ferri) magnetic / hard antiferromagnetic(AFM) interface upon field cooling below the Neel temperature of the AFM material. During cooling below T_N the AFM spins starts couple with ferromagnetic spins. This gives rise to a new anisotropy in the system, which results in a hysteresis loop shift along the applied field axis and an increase in coercivity. It was first discovered 60 years back in Co nanoparticles due to formation of CoO layer outside the nanoparticle.[10,11] As it is an interfacial phenomenon, it has been mostly studied in thin film heterostructure.[19,21] However recently, a various core-shell FM/AFM heterostructure have been reported to show exchange bias.[12,13,22-24] Though both thin film and core-shell heterostructure shows exchange bias due to the same phenomena, it is more complicated in case of the later. This can be explained by the following reasons. Firstly, due to extremely small size, the curvature increases and the interface become very important. Secondly, increase of canted spins due to increase of surface reduce the overall magnetization. All these effects hinder the exchange coupling and results smaller exchange shift compare to the thin film layered structure. So, understanding this phenomenon in core-shell QDs has not been extensively attempted and more research is required in this direction.

Recently, there are many reports, which show that tuning of core size, and shell thickness by control synthesis can tune the exchange bias effect and give more insights into this field.[23,25,26] For example using metal nanoparticle as seed, various core-shell heterostructure have been reported like Co/CoO,[10] Ni/NiO,[27] Mn/Mn_3O_4[28] or metal oxide with different oxidation states such as Mn_3O_4/MnO.[29] Systems using different metal oxide such as Fe_3O_4/Co,[30] Fe_3O_4/FeO,[21] Fe_3O_4/CoO[24] and even Fe/Cr[31] have also been reported. The majority of these studies are based on FM core overcoated with AFM shell; however, the advent of synthesis technique offers opportunities to overcoat AFM core overcoated with FM shell, namely "inverted core-shell" heterostructure such as FeO/Fe_3O_4,[32] MnO/Mn_3O_4,[33] Cr_2O_3/CrO_2.[34] In this chapter, we have reported a simple seed growth method to synthesize CoO core embedded inside FM $CoFe_2O_4$, an inverted core-shell system, and study its magnetic property and exchange bias effect in it. This research is motivated by a recent report by Lottin et al[12] that show very high exchange bias arising from highly crystalline $Co_{0.3}Fe_{0.7}O/Co_{0.6}Fe_{2.4}O_4$ inverted core-shell structure.

Lima et al[35] and Lavorato et al[36] reported CoO/ $CoFe_2O_4$ inverted core-shell heterostructure showing high coercivity due to AFM/FM interaction. Although, there is a strong enhancement

in anisotropy, there was no exchange bias observed from these systems. In contrast, our results show a surprisingly high exchange bias effect (5.6 kOe) along with the remarkable coercivity from $CoO/CoFe_2O_4$ heterostructure, which was not observed earlier. This difference is attributed to the formation of highly crystalline sharp core-shell structure and comparatively larger size QDs obtained in this study that has enhanced the magnetic proximity effect. These samples were characterized using X-ray diffraction and high-resolution transmission electron microscopy (HRTEM). Magnetic exchange bias was studied using superconducting quantum interference device (SQUID) magnetometer, which shows that exchange bias was observed even as high as 200 K temperature from these QDs.

7.3 Experimental Details

7.3.1 Synthesis

A two-step seed growth method was employed to synthesize these QDs. In a typical synthesis, CoO nanoparticles were first synthesized by thermal decomposition of Cobalt acetate ($Co(ac)_2$) in presence of OA and OlAm at high temperature. 0.4 mmol of $Co(ac)_2$ along with 2 ml of OA and 5 ml of OlAm were taken in a three necked round bottom flask and connected with the schlenk line. The reaction mixture was degassed for 1 h with evacuation at 80 °C under vigorous stirring. The solution was then heated to 220 °C under Argon (Ar) flow maintained for 20 min. The reaction temperature was further increased to 300 °C with a heating rate 5 K/min and maintained for 10 min. The resultant CoO black solution was then cooled down to room temperature and washed by centrifugation using hexane ethanol mixture and the powder precipitate was stored in a vial for further use.

$CoO/CoFe_2O_4$ core shell heterostructure. Pre-synthesized CoO QDs were used as seed for further overcoating with $CoFe_2O_4$. 30 mg CoO powder was taken in a three necked RB flask along with 2 ml OlAm and degassed at 80 °C for 1 h under evacuation. 0.05 mmol $Co(ac)_2$, 0.1 mmol $Fe(ac)_2$, 1 ml of OA and 2 ml of OlAm were taken in a vial and degassed for 30 min at 80 °C. This was used further as Co and Fe precursor for overcoating. The temperature of the reaction mixture in RB flask was raised to 200 °C under constant Ar flow. The Co and Fe precursor prepared in the vial was slowly injected into the reaction mixture and the temperature was raised slowly to 280 °C with a heating rate of 5K/min. Samples aliquots were collected after 15 min and 30 min of annealing for different shell thickness of $CoFe_2O_4$ layer. All the

samples were washed once by centrifugation using hexane-ethanol mixture and dissolved in hexane.

7.4 Results and Discussion

7.4.1 XRD

QDs crystal structure and composition were analyzed from powder XRD techniques. Figure 7.1 show XRD spectra of as synthesized CoO and CoO/ $CoFe_2O_4$ core shell nanoparticles collected after 15 min and 30 min of annealing. It is evident from the figure that CoO QDs are formed in cubic structure similar to the bulk as observed from inorganic crystal structure database. The broadening of the XRD peaks suggests the formation of small QDs. Absence of any impurity phases suggests the formation of pure cubic phase CoO QDs formation. The XRD spectra after different annealing time (15 min and 30 min) with Co and Fe metal complexes have been shown in the figure 7.1. A comparison with the bulk data of CoO and $CoFe_2O_4$, shows an increasing trend of $CoFe_2O_4$ feature with longer annealing time suggesting a controlled slow growth of $CoFe_2O_4$ layer on CoO QDs.

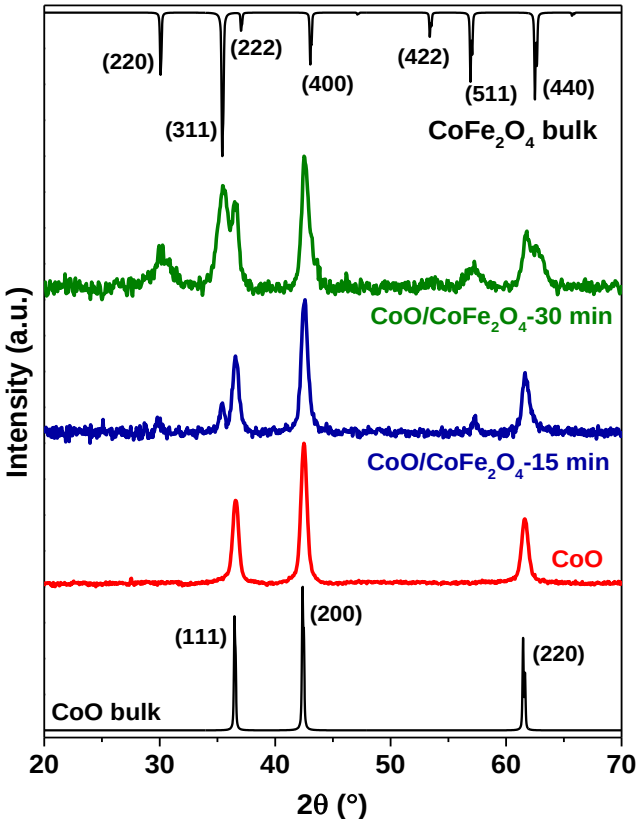

Figure 7.1: X-ray diffraction patterns of CoO core and CoO/$CoFe_2O_4$ core-shell QDs with different annealing time.

7.4.2 TEM

Although the XRD demonstrates the presence of CoO and an increased intensity of the $CoFe_2O_4$ phase with annealing time it cannot be conclusively be proven to be CoO/ $CoFe_2O_4$ core-shell and/or independent nucleation or any other heterostructure. In order to obtain a more direct evidence of the formation of core-shell heterostructure, we have carried out TEM measurement. We have chosen CoO/ $CoFe_2O_4$ sample annealed for 30 min for our rest of the measurements and the representative TEM images are shown in Figure 7.2. Figure 7.2 (a)-(b) shows the TEM images of CoO core and CoO/ $CoFe_2O_4$ QDs respectively while Figure 7.2 (c)-(d) shows their corresponding HRTEM images. It can be observed from the figure that both the particles are almost spherical in shape. The average sizes as obtained from the analysis of about 250-300 particles was found to increase from a size of 12 nm for CoO core to 15 nm for the CoO/ $CoFe_2O_4$ core/shell structure, suggesting the growth of $CoFe_2O_4$ on CoO core.

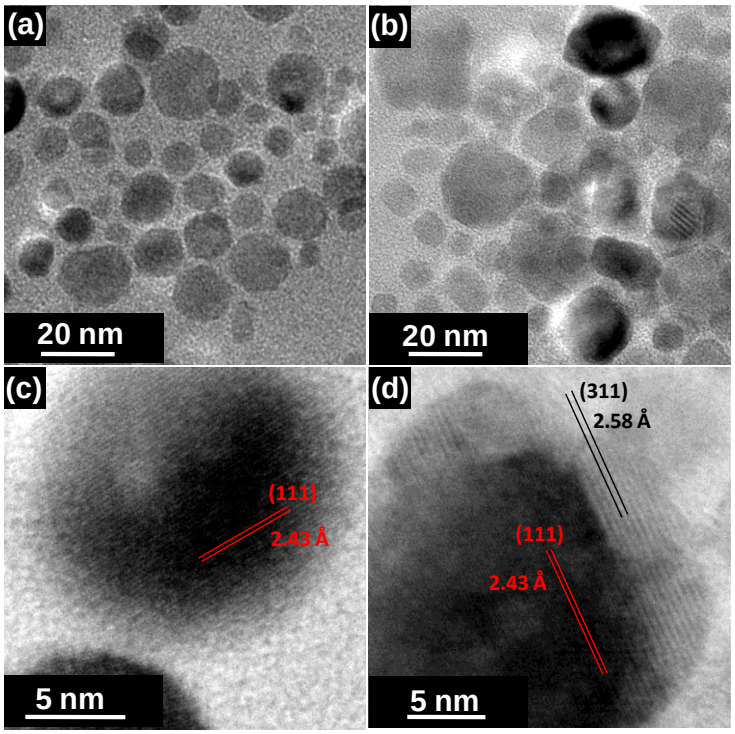

Figure 7.2: TEM image of (a) CoO and (b) CoO/ $CoFe_2O_4$. HRTEM of (c) CoO and (d) CoO/ $CoFe_2O_4$.

However the formation of sharp core-shell heterostructure was further confirmed from HRTEM images showed in Figure 7.2 (c) and 7.2(d). Figure 7.2 (d) clearly shows the presence of two different regions in the QDs, an inner core and an outer shell with different lattice fringe spacing. The interplanar spacing in the inner core (Figure 7.2 (d)) is 2.43 Å is same with CoO

core shown in Figure 7.2 (c) and corresponds to (111) plane of CoO cubic crystal structure while the interplanar distance in outer shell in Figure 7.2 (d) is 2.58 Å which is consistent with (311) planes shown in XRD. All these finding suggests the formation of crystalline $CoO/CoFe_2O_4$ core-shell QDs formation.

7.4.3 Magnetic Properties

Magnetic measurement was carried out using SQUID magnetometer. Bulk CoO is well known as AFM materials with Neel temperature (T_N) 291 K. However, below 10 K nano-sized particles show very weak ferromagnetism or superparamagnetism due to uncompensated spin on the surface.[37] Conversely, bulk $CoFe_2O_4$ (spinel) is ferrimagnetic (FiM) and nano sized particles shows superparamagnetic behavior due to single domain. Herein we have studied the magnetic properties of CoO QDs overcoated with a thin layer (~1.5nm) $CoFe_2O_4$. Figure 7.3 shows the M vs H hysteresis loop of $CoO/CoFe_2O_4$ core shell QDs at room temperature and at 2K. At room temperature the hysteresis loop shows superparamagnetic behavior. As the measurement temperature is greater than Neel temperature of CoO, the core-shell QDs shows superparamagnetic behavior at room temperature due to the presence of $CoFe_2O_4$ layer in spite of the AFM nature of CoO. M-H measurement at 2K show ferromagnetic behavior with large coercivity as the spins are in blocked state at low temperature. However it is worth noting that the low temperature hysteresis loop is not completely saturated even at high field (4T). This non-saturation behavior is due to the existence of high anisotropic AFM material.

DC susceptibility or the variation of magnetization as a function of temperature was measured using an external field 200 Oe. Figure 7.3 (b) shows the field cooled and zero field cooled curves for core-shell QDs. ZFC curve shows maxima at temperature 292 K above which magnetization decays monotonically and merges with FC curve. This behavior is a characteristic of superparamagnetic systems and the transition temperature (292 K) is known as the blocking temperature (T_b) of the material. The absence of hysteresis loop at room temperature (300 K) agrees with the value of T_b (less than 300 K) suggested by ZFC maxima peak is lower than room temperature. The observed T_B value 292 K perfectly correlates with the reported Neel temperature (T_N =291 K) of CoO.[37] Therefore, CoO/ $CoFe_2O_4$ particles go to blocked state below 292 K which is very analogous to the reported bulk state and is not influenced by nano-scale size effect.

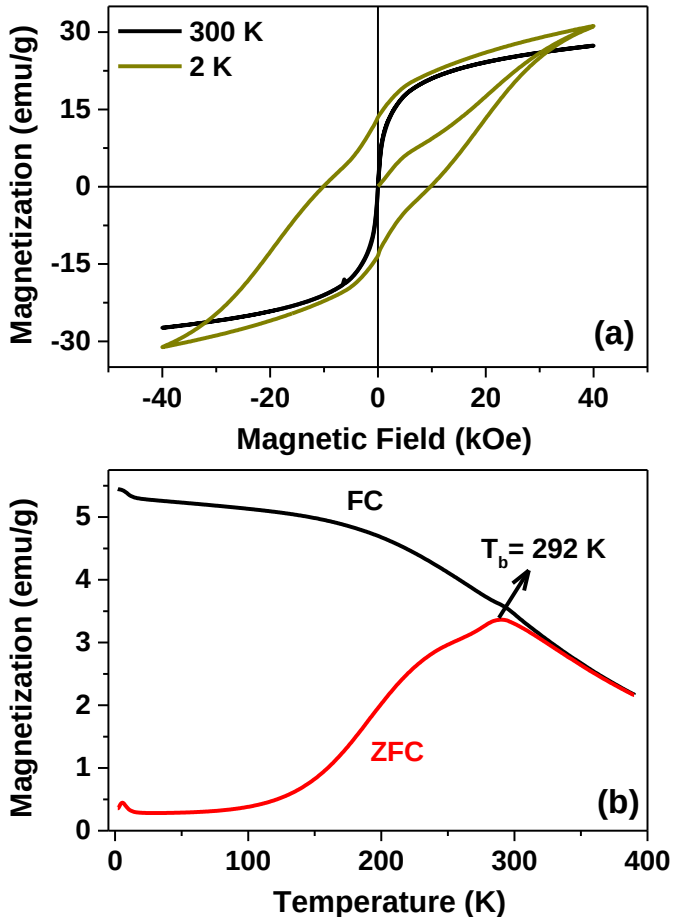

Figure 7.3 (a) Magnetization (M) vs field (H) hysteresis loop measured at 2 K (black line) and room temperature (dark yellow) (b) FC/ZFC magnetization with temperature for CoO/ $CoFe_2O_4$ core-shell nanoparticles.

In order to investigate the exchange bias effect at the AFM/FiM interface, M vs H hysteresis loops at low temperature (2K) are measured after field cooling from 400 K using different fields and are plotted in Figure 7.4 (a)-(c). All these hysteresis loops show the presence of exchange bias (loop shift along field axis). It is evident that the H_E, the exchange field, increases with increase in cooling field and reaches 5.6 kOe at 70 kOe (shown in Figure 7.5 (a). Such a strong exchange bias coupling between CoO core and $CoFe_2O_4$ shell is due to the high quality and sharp core-shell AFM/FiM interface and the stability of AFM ordering even at very high cooling field (70 kOe). The H_E value we report in this study are among the highest reported values observed in core-shell QDs and confirmed the good quality of the of the obtained CoO/ $CoFe_2O_4$ heterostructure.

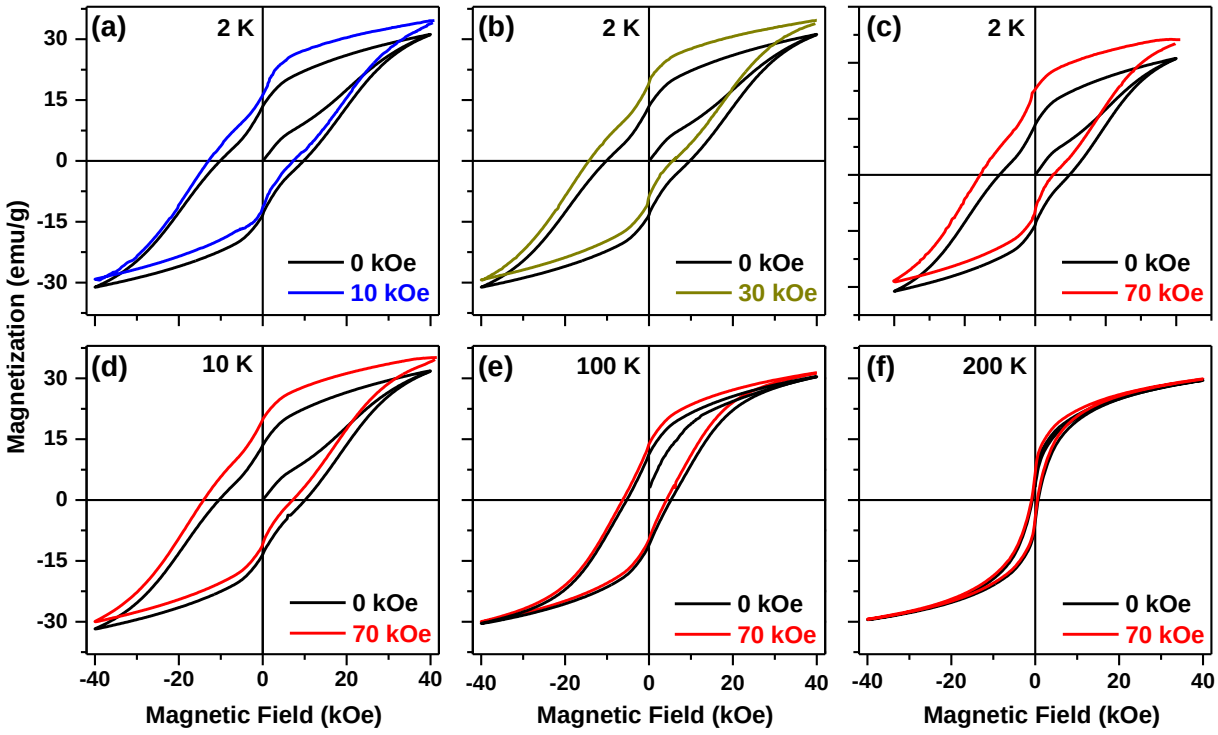

Figure 7.4: M-H hysteresis loop of CoO/ $CoFe_2O_4$ core-shell QDs recorded at 2K using cooling field (a) 10 kOe (b) 30 kOe (c) 70 kOe. M-H hysteresis loop of CoO/ $CoFe_2O_4$ measured at (d) 10 K (e) 100 K and (f) 200 K measured using FC (70 kOe) and ZFC condition.

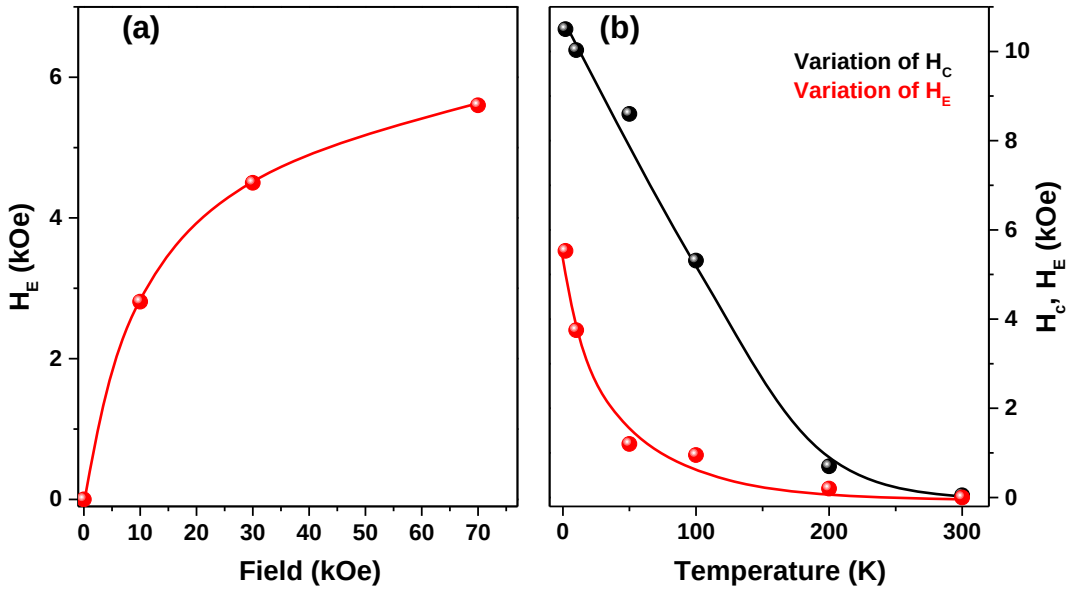

Figure 7.5 (a) Variation of H_E with different cooling field (0-70 kOe) measured at 2K. (b) Variation of H_E (red symbols) and H_c (black symbols) as a function of measurement temperature. (solid lines are guide to the eye).

In addition to the horizontal loop shift we observed very small amount of vertical loop shift for every cases, as reported in literature in various AFM/FiM core-shell QDs. This vertical shift is due to the uncompensated spins which do not follow the magnetization reversal with the applied field

The variation of exchange bias (H_E) with different cooling field has been shown in the Figure 7.5 (a) while the temperature dependence of the magnetic measurement is shown in Figure 7.5 (b). From figure 7.5 (a) it is evident that the exchange coupling is increasing with the increase of cooling field and reaching toward saturation at very high field. This suggests that the antiferromagnetic ordering of CoO exists even at high field (above 70 kOe) due to its high anisotropy energy due to crystalline nature and optimized size.

In cases of temperature variation (Figure 7.5 (a)), samples were cooled from 400 K (above the ordering temperature of the nanoparticles) using a field 7 kOe (for FC measurement). It is evident from the figure that for all different temperatures there is some significant amount of loop shift and the variation of H_E and coercivity H_c as a function of measurement temperature has been demonstrated in Figure 7.5 (b). It is interesting to note that exchange coupling of H_E between the core-shell exists even above 200 K and becomes zero below the T_N (291 K) of CoO. Similar trend was observed in the variation of coercivity which is 10.5 kOe at 2K; however becomes almost zero at room temperature. This agrees with the nature of superparamagnetic nanoparticles as the room temperature is greater than the blocking temperature and CoO behaves like paramagnetic materials as it is above Neel temperature.

7.5 Conclusion

CoO/ $CoFe_2O_4$ AFM/FiM inverted core-shell structure was designed using seed growth technique by thermal decomposition of metal complexes. Overgrowth of 3 nm thick $CoFe_2O_4$ on 12 nm CoO core leads to a sharp core-shell interface. We showed that high crystalline and sharp core-shell heterostructure leads to a remarkable value of exchange bias with a high coercivity which was not observed earlier in CoO/ $CoFe_2O_4$ system. The high coercivity and the lager value of exchange field correlates with the promising application of this materials in magnetic data storage devices or in hyperthermia application.

Bibliography

(1) Chen, L.; Wang, H.; Liu, X.; Wu, L.; Wang, Z. *Nano Lett.* **2016**.

(2) Zhang, A.; Lieber, C. M. *Chem. Rev.* **2016**, *116*, 215.

(3) Yeo, D.; Wiraja, C.; Chuah, Y. J.; Gao, Y.; Xu, C. *Scientific Reports* **2015**, *5*, 14768.

(4) Kim, Y.; Park, J. Y.; Kim, H. Y.; Lee, M.; Yi, J.; Choi, I. *Chem. Comm.* **2015**, *51*, 15370.

(5) Kuang, Q.; Lao, C.; Wang, Z. L.; Xie, Z.; Zheng, L. *J. Am. Chem. Soc.* **2007**, *129*, 6070.

(6) Zhang, Y.; Wang, M.; Zheng, Y.-g.; Tan, H.; Hsu, B. Y.-w.; Yang, Z.-c.; Wong, S. Y.; Chang, A. Y.-c.; Choolani, M.; Li, X.; Wang, J. *Chem. Mater.* **2013**, *25*, 2976.

(7) Depalo, N.; Carrieri, P.; Comparelli, R.; Striccoli, M.; Agostiano, A.; Bertinetti, L.; Innocenti, C.; Sangregorio, C.; Curri, M. L. *Langmuir* **2011**, *27*, 6962.

(8) Jiang, W.; Singhal, A.; Zheng, J.; Wang, C.; Chan, W. C. W. *Chem. Mater.* **2006**, *18*, 4845.

(9) Nogues, J.; Schuller, I. K. *J. Magn. Magn. Mater.* **1999**, *192*, 203.

(10) Meiklejohn, W. H.; Bean, C. P. *Phys. Rev.* **1956**, *102*, 1413.

(11) Meiklejohn, W. H.; Bean, C. P. *Phys. Rev.* **1957**, *105*, 904.

(12) Lottini, E.; Lopez-Ortega, A.; Bertoni, G.; Turner, S.; Meledina, M.; Tendeloo, G. V.; de Julin Fernandez, C.; Sangregorio, C. *Chem. Mater.* **2016**, *28*, 4214.

(13) Si, P. Z.; Li, D.; Choi, C. J.; Li, Y. B.; Geng, D. Y.; Zhang, Z. D. *Solid State Commun.* **2007**, *142*, 723.

(14) Skumryev, V.; Stoyanov, S.; Zhang, Y.; Hadjipanayis, G.; Givord, D.; Nogues, J. *Nature* **2003**, *423*, 850.

(15) Weller, D.; Moser, A. *IEEE Trans. Magn.* **1999**, *35*, 4423.

(16) Thompson, D. A.; Best, J. S. *IBM J. Res. Dev.* **2000**, *44*, 311.

(17) van Lierop, J.; Schofield, M. A.; Lewis, L. H.; Gambino, R. J. *J. Magn. Magn. Mater.* **2003**, *264*, 146.

(18) Binns, C.; Qureshi, M. T.; Peddis, D.; Baker, S. H.; Howes, P. B.; Boatwright, A.; Cavill, S. A.; Dhesi, S. S.; Lari, L.; Kroger, R.; Langridge, S. *Nano Lett.* **2013**, *13*, 3334.

(19) Fan, Y.; Smith, K. J.; LupkeG; Hanbicki, A. T.; GoswamiR; Li, C. H.; Zhao, H. B.; Jonker, B. T. *Nature Nanotech.* **2013**, *8*, 438.

(20) Yan, S.; Choi, D.-J.; Burgess Jacob, A. J.; Rolf-Pissarczyk, S.; Loth, S. *Nature Nanotech.* **2015**, *10*, 40.

(21) Swiatkowska-Warkocka, Z.; Kawaguchi, K.; Wang, H.; Katou, Y.; Koshizaki, N. *Nanoscale Res. lett.* **2011**, *6*, 1.

(22) Jeyadevan, B.; Chinnasamy, C. N.; Perales-Perez, O.; Iwasaki, Y.; Hobo, A.; Shinoda, K.; Tohji, K.; Kasuya, A. *IEEE Trans. Magn.* **2002**, *38*, 2595.

(23) Sun, X.; Frey Huls, N.; Sigdel, A.; Sun, S. *Nano Lett.* **2012**, *12*, 246.

(24) Baaziz, W.; Pichon, B. P.; Lefevre, C.; Ulhaq-Bouillet, C.; Greneche, J.-M.; Toumi, M.; Mhiri, T.; Begin-Colin, S. *J. Phys. Chem. C* **2013**, *117*, 11436.

(25) Salazar-Alvarez, G.; Sort, J.; Surinach, S.; Baro, M. D.; Nogues, J. *J. Am. Chem. Soc.* **2007**, *129*, 9102.

(26) Lottini, E.; Lopez-Ortega, A.; Bertoni, G.; Turner, S.; Meledina, M.; Tendeloo, G. V.; de Julian Fernandez, C.; Sangregorio, C. *Chem. Mater.* **2016**, *28*, 4214.

(27) Seto, T.; Akinaga, H.; Takano, F.; Koga, K.; Orii, T.; Hirasawa, M. *J. Phys. Chem. B* **2005**, *109*, 13403.

(28) Si, P. Z.; Li, D.; Lee, J. W.; Choi, C. J.; Zhang, Z. D.; Geng, D. Y.; Bruck, E. *Appl. Phys. Lett.* **2005**, *87*, 133122.

(29) Si, P. Z.; Li, D.; Choi, C. J.; Li, Y. B.; Geng, D. Y.; Zhang, Z. D. *Solid State Commun.* **2007**, *142*, 723.

(30) Iglesias, O.; Labarta, A.; Batlle, X. *J. Nanosci. Nanotech.* **2008**, *8*, 2761.

(31) Binns, C.; Qureshi, M. T.; Peddis, D.; Baker, S. H.; Howes, P. B.; Boatwright, A.; Cavill, S. A.; Dhesi, S. S.; Lari, L.; Kroİ̂ger, R. *Nano Lett.* **2013**, *13*, 3334.

(32) Kavich, D. W.; Dickerson, J. H.; Mahajan, S. V.; Hasan, S. A.; Park, J. H. *Phys. Rev. B* **2008**, *78*, 174414.

(33) Salazar-Alvarez, G.; Sort, J.; Surinach, S.; Dolors, B. M.; Nogues, J. *J. Am. Chem. Soc.* **2007**, *129*, 9102.

(34) Zheng, R. K.; Liu, H.; Wang, Y.; Zhang, X. X. *Appl. Phys. Lett.* **2004**, *84*, 702.

(35) Lima, E.; Winkler, E. L.; Tobia, D.; Troiani, H. E.; Zysler, R. D.; Agostinelli, E.; Fiorani, D. *Chem. Mater.* **2012**, *24*, 512.

(36) Lavorato, G. C.; Lima Jr, E.; Tobia, D.; Fiorani, D.; Troiani, H. E.; Zysler, R. D.; Winkler, E. L. *Nanotechnology* **2014**, *25*, 355704.

(37) Ghosh, M.; Sampathkumaran, E. V.; Rao, C. N. R. *Chem. Mater.* **2005**, *17*, 2348.

LIST OF PUBLICATIONS

1. "Near-Unity Quantum Yield in Semiconducting Nanostructures: Structural Understanding Leading to Energy Efficient Applications" **Avijit Saha**, Kishore V. Chellappan, K. S. Narayan, Jay Ghatak, Ranjan Datta and Ranjani Viswanatha, *J. Phys. Chem. Lett.*, **2013, *4***, 3544 – 3549.

   Highlited in C&E News: http://cen.acs.org/articles/91/web/2013/10/Understanding-Quantum-Dots- Inside.html

2. "The curious case of CdTe/CdS : photoabsorption vs photoemission" **Avijit Saha**, Soma Chattopadhyay, Tomohiro Shibata and Ranjani Viswanatha, *J. Mater. Chem. C*, **2014**, 2, 3868.

3. "Uniform Doping of in Quantum-Dots-Based Dilute Magnetic Semiconductor" **Avijit Saha**, Amitha Shetty, Pavan A.R., Soma Chattopadhyay, Tomohiro Shibata and Ranjani Viswanatha, *J Phys. Chem. Lett.* **2016**, 7, 2420-2428.

4. "Core-Shell to Doped Quantum Dots: Evolution of the Local Environment Using XAFS" **Avijit Saha,** Soma Chattopadhyay, Tomohiro Shibata and Ranjani Viswanatha, *J Phys. Chem. C*, **2016**, 120, 18945-18951.

5. "Ligand assisted digestion and formation of monodisperse $FeCoS_2$ nanocrystals" Amitha Shetty**, Avijit Saha**, Mahima Makkar, and Ranjani Viswanatha, Phys. Chem. Chem. Phys. **2016**, 18, 25887-25892.

6. "Diffusion Doping in Quantum Dots: Bond Strength and Diffusivity" **Avijit Saha**, Mahima Makkar, Amitha Shetty, Kushagra Gahlot, Pavan A.R. and Ranjani Viswanatha. *Nanoscale*, **2017**, *9*, 2806-2813.

7. "Magnetism at the Interface of Magnetic Oxide and Nonmagnetic Semiconductor Quantum Dots" **Avijit Saha** and Ranjani Viswanatha. *ACS Nano*, **2017**, *11*, 3347-3354.

8. "Magnetism in Dilute Magnetic Semiconductor Quantum Dots: Effect of Size and Dopant Concentration" **Avijit Saha** and Ranjani Viswanatha (Submitted)

9. "High exchange bias from $CoO/CoFe_2O_4$ inverted core-shell heterostructure" **Avijit Saha** and Ranjani Viswanatha (Manuscript under preparation)

List of patents

1. R. Viswanatha**, A. Saha**, K. V. Chellappan, K. S. Narayan, J. Ghatak and R. Datta, Cd-based-chalcogenide/CdS core-shell nanomaterials, defective/defect-free core nanocrystal, methods and applications thereof. (Patent Pub No. WO2014147555 A2).